Studies on design and development of Indus-2 X-ray lithography beamline and its applications in X-ray optics and Biosensor

By

Vishal P Dhamgaye

(PHYS 03 2008 04 010)

Raja Ramanna Centre for Advanced Technology, Indore

Indore – 452013, India

A thesis submitted to the
Board of Studies in Physical Sciences

In partial fulfillment of requirements
For the Degree of

DOCTOR OF PHILOSOPHY

Of

HOMI BHABHA NATIONAL INSTITUTE

October, 2014

Homi Bhabha National Institute

Recommendations of the Viva Voce Board

As members of the Viva Voce Board, we certify that we have read the dissertation prepared by Mr. Vishal P. Dhamgaye entitled "Studies on design and development of Indus-2 X-ray lithography beamline and its applications in X-ray optics and Biosensor" and recommend that it may be accepted as fulfilling the dissertation requirement of the Degree of Doctor of Philosophy.

Chairman Dr. L. M. Kukreja Date: 27.3.2015

Guide Dr. G . S. Lodha Date: 27.03.15

Member 1 Dr. V. K. Suri Date: 27.3.2015

Member 2 Dr. H. S. Rawat Date: 27/03/2015

Prof. Sudhir Chandra, IIT Delhi Date: 27.3.2015

(External Examiner)

Final approval and acceptance of this dissertation is contingent upon the candidates submission of the final copies of the dissertation to HBNI. I hereby certify that I have read this dissertation prepared under my direction and recommend that it may be accepted as fulfilling the dissertation requirement.

Date: March 27, 2015

Place: RRCAT, Indore

Guide: Dr. G. S. Lodha

STATEMENT BY AUTHOR

This dissertation has been submitted in partial fulfilment of requirements for an advanced degree at Homi Bhabha National Institute (HBNI) and is deposited in the Library to be made available to borrowers under rules of the HBNI.

Brief quotations from this dissertation are allowable without special permission, provided that accurate acknowledgement of source is made. Requests for permission for extended quotation from or reproduction of this manuscript in whole or in part may be granted by the Competent Authority of HBNI when in his or her judgment the proposed use of the material is in the interests of scholarship. In all other instances, however, permission must be obtained from the author.

Vishal P Dhamgaye

DECLARATION

I, hereby declare that the investigation presented in the thesis has been carried out by me. The work is original and has not been submitted earlier as a whole or in part for a degree/diploma at this or any other Institution/ University.

Vishal P Dhamgaye

List of publications arising from the thesis

Journals Articles

1. ***Microfocussing of synchrotron X-rays using X-ray refractive lens developed at Indus-2 deep X-ray lithography beamline***
   V. P. Dhamgaye, M. K. Tiwari, K. J. S. Sawhney, and G. S. Lodha, Pramana J. Phys., 83, 119-129 (2014**)**.
2. ***Development of high aspect ratio X-ray parabolic compound refractive lens at Indus-2 using X-ray lithography***
   V. P. Dhamgaye, M. K. Tiwari, C. K. Garg, P. Tiwari, K. J. S. Sawhney, and G. S. Lodha, Microsystem Technologies 10-11, 2055 (2014).
3. ***A micro biosensor device – application in glucose analysis***
   Gautam Bacher, **V. P. Dhamgaye**, Souvik Pal, G.S. Lodha, and Sunil Bhand, communicated.
4. ***BL07 beamline at Indus-2: a facility for microfabrication research***
   V. P. Dhamgaye, G. S. Lodha, B. Gowri Sankar, and C. Kant, Journal of Synchrotron Radiation, 21, 259-263 (2014).
5. ***Beam position measurements of Indus-2 using X-ray beam position monitor***
   V. P. Dhamgaye, G. S. Lodha and S. R. Kane, Nuclear Instruments and Methods in Physical Research A 659, 525 (2011).
6. ***Micromanufacturing: A review - Part-I***
   V. K. Jain, Ajay Sidpara, R. Balasubramaniam, G. S. Lodha, **V. P. Dhamgaye** and R. Shukla, Journal of Engineering Manufacture, Proc IMechE Part B:J Engineering Manufacture 228, 973 (2014)**.**

Book Chapter:

1. ***X-ray lithography***
   G. S. Lodha and **V. P. Dhamgaye**, In V K Jain editor, 'Introduction to Micromachining' Narosa Publishing house (2014).

Publications in edited volumes and in conference proceedings:

1. ***Indus-2 X-ray lithography beamline for X-ray optics and material science applications***
   V. P. Dhamgaye and G. S. Lodha, AIP Conf Proc, 1591, 7 (2014)**.**
2. ***Fabrication of compound refractive lens using soft and deep X-ray lithography beamline on Indus-2***
   V. P. Dhamgaye and G. S. Lodha, AIP Conf Proc 1447, 525 (2012).
3. ***Commissioning of soft and deep X-ray lithography beamline on Indus-2***
   V. P. Dhamgaye, B. Gowri Sankar, C. K. Garg and G. S. Lodha, AIP Conf Proc 1447, 527 (2012).
4. ***Beamlines on Indus-1 and Indus-2 for X-ray multilayer optics and microfabrication research***
   G. S. Lodha, **V. P. Dhamgaye,** M. H. Modi, M. Nayak, A. K. Sinha, and R. V. Nandedkar, AIP Conf Proc 879, 1474 (2007).
5. ***Effect of Various Developer Conditions on Dissolution Rates of PMMA Microstructures Fabricated by X-ray Lithography***
   V. P. Dhamgaye, S. Mukherjee and G. S. Lodha, Indo-Singapore Joint Physics Symposium, IIT Kharagpur, February 25-27, 2013.

Work done during the thesis but not included in the thesis (Journal articles):

1. ***Fabrication of high aspect ratio comb drive actuator using deep X-ray lithography at Indus-2***
   Rahul Shukla, **V. P. Dhamgaye,** V. K. Jain, P. Ram Sankar, C. Mukherjee, B. D. Pant and G. S. Lodha, Microsystem Technologies 20, 1273 (2014).
2. ***New scheme for dual readout of dose in polycrystalline Li2B4O7 irradiated with synchrotron X-rays from Indus-2***
   S. Kar, L.A. Joseph, C. Debnath, S. Verma, **V. P. Dhamgaye**, G.S. Lodha, K.S. Bartwal, Radiation Measurements 67, 55-58 (2014).
3. ***A comparative study of gamma, electron beam, and synchrotron X-ray irradiation method for synthesis of silver nanoparticles in PVP***
   Nilanjal Misra, Jayashree Biswal, **V. P. Dhamgaye**, G. S. Lodha, S. Sabharwal, Advanced Materials Letters 4(6), 458-463 (2013).
4. ***Experimental investigation of Synchrotron and Bremsstrahlung hazards at Lithography beam line of Indus-2 SRS***
   M. K. Nayak, P. K. Sahani, Mukesh Khare, T. K. Sahu, P. Haridas, Vipin Dev, S. Dashora, **Vishal Dhamgaye**, G. Haridas and P. K. Sarkar, Indian Journal of Pure and Applied Physics, 50, 829-831 (2012).

Vishal P Dhamgaye

DEDICATION

My family

(for their un-conditional love and solidarity)

Acknowledgement

In this thesis various technologies are started from scratch to its present form available at Indus-2. I took help, guidance, suggestions, criticism, and inputs from many peoples of various disciplines. I hereby take the opportunity to thank all of them who have contributed to bring these technologies and finally this thesis in its present form. I really feel very much honored for having come across brilliant teachers who not only taught me the academic subjects but also touched the deepest chords of my heart. I would like to convey my genuine appreciation and heart-felt gratitude to all of them.

It is great pleasure to express my profound sense of gratitude and indebtness towards my Guru and mentor **Dr. Gyanendra Singh Lodha,** for his inspiring and motivational guidance. He has been part of my life during all thick and thins. His humbleness and down to earth character is really appreciable. I learnt from him how accepting our weakness can makes us stronger. I am extremely glad that I had a chance to do my PhD under someone who truly practices and appreciates deep thinking. I will be forever indebted to him for all the time he has spent with me during discussions, experiments (especially at BL-16) and sharing his ideas. Thank you very much, Sir for your un-endless support which has helped me to reach my goals.

I am extremely thankful to Dr. S. K. Deb, for his support and constant encouragement. I am grateful to Dr. L.M. Kukreja, Chairman, and Dr. V. K. Suri, Dr. H. S. Rawat members of Doctoral Committee for their constructive criticism, motivation and guidance. I also want to thank Dr. P. D. Gupta for support and motivation towards X-ray lithography activity.

I would like to record my deepest appreciation and gratitude towards my Gurus, Dr. K. J. S. Sawhney, who first imbibe the art of research and science in me, time to time encouragement and help in lens measurements at Diamond; Professor V. B. Sapre for

cultivating the knowledge of X-ray physics; Professor T. M. Karade for sowing the seeds of hard work, patience and perseverance.

I am indebted to support and help received from Professor Yuichi Utsumi. His nobel and kind gestures has allowed me to learn many techniques in his laboratory. His constructive inputs and help at every stage of X-ray lithography development are appreciable. His open offer to use his laboratory just like him is appreciable. I would like to thank many people for their constructive inputs which have helped me to develop this facility. Professor Enzo de Fabrizio (for critical review on beamline design and discussions), Dr. Jost Goettert (for review the X-ray scanner design specifications and critical inputs on X-ray lithography), Dr. Juergen Mohr (for fruitful discussion on X-ray LIGA), Dr. Pascal Meyer (for constructive discussion on X-ray LIGA and DoseSim code), Dr. Matteo Alttisimo (for discussion on X-ray lithography), Dr. Franz Schaeffers (for beamline ray tracing discussion and RAY code), Dr. Rakesh Kumar (constructive discussion on X-ray lithography), Dr. Filipo Romanato and Dr. Luca Businaro (for first X-ray lithography experiment in the year 2004), Mr. Donald Johnson (for information on SUEX handling and processing) and Dr. Vladimir Nazmov (for constructive discussion on X-ray LIGA beamline). I would like to thank Diamond for providing beamtime on its B16 and I12 beamlines. In particular, I am indebted to the principal beamline scientists of these beamlines Dr Kawal Sawhney and Dr Michael Drakopoulos for performing the detailed characterisation of the lenses developed by me by the LIGA process. I also thank Toyama's CEO Katsumi(Joe) Endo and his secretary Miyuki Enamoto for instant support to beamline problems and solving the problems by even supplying spares without any hesitation.

Some works are beyond my capacity and I sincerely thank my team members, Mr. B. Gowri Sankar, Mr. Chander Kant, Dr. Rahul Shukla, Mr. Bhanu Singh Thakur, Mr. Nitin Khantwal, Mr. M Nookaraju. My special thank to Nitin, a hard working man who has taken

my attention out of Yellow room processing for students's as well as BL-07 user samples. I thank to Mr. Ramdass, a casual labor, an old man who stood with me in fixing all the vacuum flanges and many beamline components (first to last screws) and showing me the secret of working at old age. My sincere thanks to Dr Archna Sagdeo and Dr. Pankaj Sagdeo for reading the thesis draft, to Dr. R Balasubramanium, Dr. Pooja Gupta and Dr Harnath Ghosh for many discussions. Many other colleagues in the Division have helped me at various moments. Listing names of everybody is not possible but I profusely thank the entire ISUD members who have joyfully supported me in concluding my work. I also thank all M. Tech. students visiting our laboratory and keeping me on the edge by asking too many questions.

I also record my sincere thank to Dr. Tapas Ganguli and Dr. Sanjay Rai for providing dynamic discussions, reading the thesis draft and providing unlimited time for discussions out of their busy schedules. I would like to extend my sincere appreciation and thanks to many people for their help in obtaining scientific data including Mrs. P. Tiwari (for all SEM), Dr. M. K. Tiwari (BL-16 beamtime), Mr. Ajit Singh (Help in X-ay lens testing), Dr. A. K. Sinha (XRD Measurements, ANSYS calculations), Dr. M. N. Deo (Raman and IR measurements), Dr. V. Sathe (Raman measurements), Mr. H. S. Vora (for Shilankhan software), Mr. V. Bhanage (for Motor drivers and softwares), Mr. K. K. Pandey (for precision stages and high pressure XRD measurements), Dr. Ram Sankar (for electrodeposition requirements), Dr. Sunil Bhand (for constructive collaboration and characterization of bio sensor), Mr. Gautam Bacher and Mr. Souvik Pal (for constructive discussion and characterization of bio sensor).

I would not have learned many things without discussing many things with my friends all across the globe and teachers who taught in the ICTP Synchrotron School (2004) and Cheiron School (2010). These schools have not only helped me to understand SR Science but also allowed me to build relationships with X-ray lithography activities running at Italy and Japan. I would also like to thank Diamond, New Subaru and Indus-2 for providing beamtime.

I would be failing if I forget to extend my heartiest thanks to my friends and colleagues from different divisions and organisation. My friend Mr. Sandeep Sakhare who has been part of my life since my childhood and providing help at every corner of my life. My first friend at Indore, Mr. Ashoka, Ms. Trisha and Mrs. Rashmi for being constant source of togetherness and motivating me during difficult phases of my life. I also thank my friend Nageswar, Vimal, Pankaj and their families. I would like to thanks Dr. Chhayabrita for on and off scientific discussions, my trekking friend Dr. S. M. Oak for keeping me naturally happy.

No words can suffice the kind understanding, efforts, patience and perseverance of my parents and above all their high expectations from me. It is their blessings and simple questions that made this herculean task possible. Along with my parents, I would also like to sincerely thank my Grandma for having showered so much love on me since my childhood. I would like to thank my sisters, Kavita, Manjusha, Varsha, Megha, Vibha and brother Suhas his wife Archana and cute Eshin for their love and support at every stage of my life. I am also thankful to my in-laws family members for the moral support at times.

I would like to thank my wife Sonal from core of my heart, who has blossom my life and adjusted with me in all situations and providing unconditional support at every stage of my life. From the very core of my heart, I express my gratitude towards my daughter, Saanvi, who has been an inexhaustible source of strength for me. I feel sorry that I couldnot give her enough time during gestation of this thesis.

Last but not the least; I am thankful to the almighty lord for showing me the right path and teaching me to follow eight fold ways.

(V P Dhamgaye)

CONTENTS

CONTENTS i

SYNOPSIS v

LIST OF FIGURES xi

LIST OF TABLES xvii

LIST OF ABBREVIATIONS xx

LIST OF SYMBOLS xxiii

Chapter 1 1

Introduction 1

1.1 X-ray Lithography 3

1.2 Synchrotron radiation source: Indus-2 6

1.3 Beamline and X-ray Scanner 7

1.4 Attenuation of X-rays in Matter 9

1.4.1 Photo Absorption/photoelectric effect 10

1.4.2 Scattering 10

1.4.3 Pair Production 11

1.5 The Complex Index of Refraction 12

1.6 X-ray sensitive resists 13

1.6.1 Polymethylmethacrylate (PMMA) 14

1.6.2 SU-8 14

1.7 Microfocusing of X-rays 15

1.8 Introduction to Microfluidics 17

1.9 Thesis outline 19

Chapter 2 21

Design and development of X-ray lithography beamline 21

2.1 Introduction 21

2.2 Design of the beamline 22
2.2.1 Optics design of the beamline 23
2.2.2 Ray tracing simulations 29
2.3. Instrumentation for SDXRL beamline 47
2.3.1 Diagnostic devices 47
2.3.2 X-ray mirror system 51
2.3.3 X-ray exposure station or X-ray scanner 56
2.4 Commissioning of the beamline 60
2.4.1 Beam size and intensity profile 61
2.4.2 Power measurement 65
Chapter 3 70
Microfabrication of HAR structures in X-ray sensitive photoresist. 70
3.1 Development of X-ray mask 71
3.1.1 Mask membrane material 71
3.1.2 Mask absorbing material 75
3.1.3 Fabrication of X-ray mask 77
3.2 Development of HAR microstructures in X-ray sensitive photoresist 87
3.2.1 X-ray Exposure mechanism of PMMA 87
3.2.2 X-ray Exposure mechanism of SU-8 99
3.2.3 Fabrication of microstructure in PMMA 102
3.2.4. Fabrication of microstructures in SU-8 117
3.2.5. A few studies on the micro fabricated structures 122
Chapter 4 129
Design and development of X-ray refractive lens and its characterisation 129
4.1 Choice of lens materials 130

4.2 Design of parabolic refractive X-ray lenses 132
4.2.1 Focal length 134
4.2.2 Transmission 135
4.2.3 Effective aperture 135
4.2.4 Spot size 136
4.2.5 Gain 137
4.3 Design of X-ray lenses 137
4.4 Fabrication of X-ray lenses 139
4.4.1 Fabrication of PMMA lenses 140
4.4.2 Fabrication of SU-8 lenses 140
4.4.3 Fabrication of SUEX lenses 144
4.5 Performances of X-ray lenses 149
4.5.1 Experimental test setup at Indus-2 149
4.5.2 Experimental test set up at Diamond 151
4.6 Microfocussing using X-ray lenses 152
4.6.1 PMMA X-ray lenses 152
4.6.2 Characterisation of SU-8 lenses 155
4.6.3 Characterization of SUEX lenses 171
4.6.4 Comparison between SU-8 and SUEX X-ray lenses 174
4.7 Experiments using SU-8 CRLs 176
4.7.1. X-ray imaging experiment 177
4.7.2. High pressure X-ray diffraction 179
Chapter 5 185
Design and development of Bio sensor 185
5.1 Introduction to biosensors 185

5.2 Materials and methods 187
5.2.1 Microfabrication of device 187
5.2.2 Materials and instrumentation 189
5.3 Results and discussions 191
5.3.1 Optimization for Glucose sensor 191
5.3.2 Surface characterization of Cu CMEA 192
5.3.3 EIS study of glucose biosensor 193
5.3.4 Effect of surface modification 194
Chapter 6 197
Conclusions 197
6.1 Summary 197
6.2 Future studies 201

Homi Bhabha National Institute

Ph. D. PROGRAMME

1. Name of the Student	:	Vishal P Dhamgaye
2. Name of the Constituent Institution	:	Raja Ramanna Centre for Advanced Technology, Indore-13.
3. Enrolment No.	:	PHYS 03 2008 04 010
4. Title of the Thesis	:	"Studies on design and development of Indus-2 X-ray lithography beamline and its applications in X-ray optics and Biosensor"

SYNOPSIS

X-ray lithography (XRL) is a key technology used for fabricating high density and high aspect ratio (HAR) microstructures with high precision in vertical sidewall (<200 nm) and low roughness (< 20 nm). These structures find applications in various basic and applied fields. High intensity and low divergence synchrotron radiation (SR) is used as source for performing XRL. The microstructures are fabricated in X-ray sensitive resist. Detailed optical design of the XRL beamline on Indus-2 and its commissioning are presented. The XRL process optimization for micro fabrication and development of devices for hard X-ray micro focusing and bio chip are carried out.

This thesis centers on the development of XRL facility at Indus-2. The optical design was undertaken for meeting the desired features of wide energy window (1-40 keV), high flux

(>1015 photons/sec) and large horizontal beam size (>100 mm). Parameters for X-ray optical elements, beam shape and sizes, X-ray spectral width are calculated analytically followed by detailed ray tracing of the beamline configuration. Based on the optical design, the X-ray optics, X-ray mirror movement system, X-ray scanners, slits, beam position monitors etc. are custom fabricated/ developed in-house. The beamline is commissioned on Indus-2 SR source and performance compared with design specifications.

X-ray mask with unit magnification patterns, is a key technology required for developing microstructures using XRL. X-ray mask fabrication requires transferring of high X-ray absorbing (>80%) patterns (>10 micron of high Z material) on high X-ray transmission (> 60%) membrane (few tens of micron of low Z material) with low roughness, low stress and high thermal conductivity. X-ray mask design and fabrication is a costly and a time consuming process. A cost effective X-ray mask fabrication process with polyimide mask membrane and Au based absorbing material with a short turnaround time is developed. Polymethylmethaacrylate (PMMA), SU-8® and SUEX® are used as X-ray sensitive photo resists. The processing characteristics are strongly dependent on the manufacturing (specific to a supplier/ batch of production) and radiation exposure (specific to the source and beamline configuration) conditions. The exposure doses and processed depths are standardized. For PMMA, dissolution rate is determined and correlated with the microscopic changes.

X-ray micro focusing devices are required for variety of applications based on SR sources. X-ray lithography is being explored by a few groups, towards the development of refractive X-ray optical devices such as stacking many X-ray lenses in a line, known as X-ray compound refractive lenses (CRL). This is possible due to the ability to fabricate very high HAR structures with low side wall roughness using XRL. These CRLs are used for SR

experiments requiring in-line, diffraction free micro/ nano spots. CRLs fabricated in PMMA and SU-8 are reported in literature, but standard detailed fabrication process and performance (focal spot, effective aperture, gain, radiation hardness) comparison on low and moderate emittance sources are limited. In this work, CRLs are fabricated in PMMA and SU-8 and their performance at Indus-2 (moderate emittance of 58 nm-rad) and Diamond Light Source (DLS) (low emittance of 4 nm rad) is compared for developing CRLs for specific applications. SU-8 based lens are deployed for high pressure XRD and X-ray imaging experiments at Indus-2. These studies have opened up avenues towards undertaking many such micro focusing experiments using the exiting beamlines on Indus-2.

Low absorption materials are desirable for fabricating X-ray refractive lens. SU-8 has ~1% Antimony as part of photo acid generator molecule. Sb introduces extra X-rays absorption near the K and L absorption edges. Recently SUEX X-ray resist, without Sb has been developed as an equivalent of SU-8. The processing conditions for SUEX are standardized and used for fabricating CRLs. Measured performance upto 20 keV is marginally better than SU-8. The performance is expected to be significantly better as compared to SU-8 and Al in 32 - 40 keV which is above K absorption edge of Sb.

Electrochemical biosensors built as lab-on-chip, have gained importance for its simplicity, sensitivity, low detection limit, short response time, and portability. Using X-ray and photo lithography, a circular micro electrode array (CMEA) on Cu laminate printed circuit board (PCB) based SU-8 bio sensing chip is developed. The device has been tested on bio fluids using electro-impedance spectroscopy. The biosensor measures glucose concentration in 0.01-2.5 mM in aqueous solution with small integration time and found to be useful for repeated measurements.

The thesis is organized as follows:

Chapter 1 gives an introduction to XRL and its usefulness for fabrication of high aspect ratio microstructures. This chapter also introduces X-ray LIGA, type of photo resist, requirement of X-ray masks, and interactions of X-rays with matter. X-ray refractive lenses and microfluidics devices and their applications are described.

The details of XRL beamline on Indus-2 developed to fabricate HAR microfabrication are presented in Chapter 2. The design calculations for XRL beamline are provided by highlighting the major design criterion of wide lithographic window, wide beam with uniform intensity, collimated and focused beam at mask-resist stage. Brief discussion with salient features of the beamline components and the experimental considerations deciding their role for microfabrication are also presented. Each beamline component is tested for its actual performance by measuring its range and resolution in each degree of freedom. The characterization of the XRL beamline in terms of X-ray beam delivery is described.

The details towards the realization of HAR microfabrication using XRL beamline in PMMA and SU-8 resist are presented in Chapter 3. In this chapter, the description on X-ray mask development is outlined. Requirements for absorber and mask membrane materials are described. The development of polyamide based X-ray mask using photolithography and electro-deposition techniques are presented.

The capability of developed XRL beamline by producing microstructures in PMMA and SU-8 X-ray resist is discussed. Dissolution rate of PMMA as a function of X-ray exposure dose in developer solution are presented. The processing conditions of SU-8 resist using XRL beamline are described. Finally, the studies on optical characterization (depth

uniformity, sidewall roughness, effect of beam divergences) of microstructures in PMMA and fabrication of few 3D microstructures are presented.

Chapter 4 describes the development of CRLs for the creation of micro-focus spot size at Indus-2. Brief overview on the historical account of the invention of X-ray optical elements and its working principles are presented. The choice of X-ray lens materials based on the various design criteria is described. The processing conditions for fabrication of CRL with radii of curvature of 100 μm, 50 μm and 25 μm are described. The developmental details of lens characterization setup at BL-16, Indus-2 are presented. The results obtained from X-ray lenses characterized at two SR sources (Indus-2 and Diamond light source, UK) and comparison of theoretical estimates for spot size, transmission and gain with experimental results are also presented. SU-8 X-ray lenses are used for 2D X-ray focusing of hard X-rays and deployed for high pressure XRD and X-ray imaging experiments at Indus-2. Studies on SUEX X-ray lens development and comparison with SU-8 X-ray lenses are also reported.

The study and development of a lab-on- chip- device using XRL beamline is presented in Chapter 5. The processing conditions of obtaining the CMEA on Cu laminated PCB and monolithic fabrication of biochip are presented. The experimental analyses carried out to investigate response of the Cu CMEA and operating parameters for biosensor testing are highlighted. Immobilization of enzyme glucose oxidase through self assembled monolayers and covalently bonded using 11-mercaptoundeconoid acid over Cu-CMEA and its characterisation is detailed. Finally, the studies on the response behavior of biosensor to various glucose concentrations are presented.

In chapter 6, a summary of the major accomplishments and outline on scope of future works are presented.

LIST OF FIGURES

Figure 1.1: Schematic of X-ray lithography process 4
Figure 1.2: Schematic of an X-ray mask, showing mask membrane and mask absorber.....4
Figure 1. 3: Elements of X-ray LIGA process.....5
Figure 1. 4 : Attenuation of X-rays as a function of the photon energy for two X-ray sensitive photoresist (a) PMMA (b) SU-8. 11
Figure 1. 5 : Refraction of incident light in the region of (a) visible (b) X-rays and (c) total external reflection 12
Figure 2. 1 : Calculated width of the beam along the beamline length for various horizontal acceptances by the second mirror. 25
Figure 2. 2 : Possible beamline length on the basis of two geometrical errors due to vertical and horizontal divergence. 25
Figure 2. 3 : Schematic optical layout of the SDXRL beamline on Indus-2. 28
Figure 2. 4 : Point diagram of beam at various position of the beamline including at X-ray scanners. Left images (La-Le) belongs to calculations using serial number 2 parameters and right images (Ra-Re) pertains to calculations obtained using serial number 5 of table 2.2. ...32
Figure 2.5 : Calculated transmission spectra for SDXRL beamline in SXRL mode.....38
Figure 2. 6 : Calculated transmission spectra of SDXRL beamline in DXRL mode. 38
Figure 2. 7 : Calculated transmission spectra for serial number 5 (table 2.2) for obtaining the beam at height equal to height of undeviated optic axis and ± 25 mm away from it. 38
Figure 2. 8 : Point diagram of the images at mirror, scanner1 and scanner2 in case of single mirror operation and grazing angle of incidence 0.2°.....45
Figure 2. 9 : Power spectrum of Indus-2 for no reflection optics and various Be-window thicknesses at scanner2. 46
Figure 2. 10 : Spot diagram of the white beam observed at scanner1. Only two Be filters of thickness 175 μm and aperture of Be window is considered.....46
Figure 2. 11 : (a) XBPM based on photoelectric effect (b) detector blades are staggered and kept at known distances from central beam axis and (c) back view of fabricated XBPM 48
Figure 2. 12 : Indus-2 beam stability recorded by XBPM.....50
Figure 2. 13 : Schematic of wire probe scanner, Au wire is installed between two SS legs. ..51
Figure 2. 14 : Engineering design of two mirrors system.....53

Figure 2. 15 : Air based X-ray scanner with (a) mounted condition of X-ray mask and wafer (b) modified stage to create the 3-D microstructures.....58
Figure 2. 16 : (a) Internal view of X-ray scanner and (b) the mounting view of X-ray mask and wafer.....58
Figure 2. 17 : Engineering layout of SDXRL beamline 61
Figure 2. 18 : (a) Calculated and (b) measured beam sizes at X-ray scanner1 for 2.5-9 keV .63
Figure 2. 19 : Calculated and measured beam profile obtained using WPS at 18 m from source. 63
Figure 2. 20 : Horizontal intensity distribution of beam at scanner1 mask-wafer plane. 64
Figure 2. 21 : The profile of the X-ray beam recorded at scanner2 for various X-ray energy range.....64
Figure 2. 22 : Mounted view of Cu calorimeter in Scanner2 mask-wafer stage. 67
Figure 2. 23 : Temperature rise of Cu Calorimeter during exposure to the SR beam and temperature fall after closing the safety shutter. 67
Figure 2. 24 : A typical beam profile in white beam and two mirror operation geometry. 69
Figure 3. 1 : (a) Attenuation length of various X-ray mask membranes and (b) Transmission of 6.2 keV energy for few selected mask membrane materials. 74
Figure 3. 2 : (a) Attenuation length for reported mask absorber materials upto 30 keV energies and (b) absorption at 6.2 keV for few selected mask absorber materials. 75
Figure 3. 3 : Flow chart showing various route of X-ray mask fabrication.....78
Figure 3. 4 : Membrane based gold X-ray mask fabrication process: (a) photo resist is spin coated on metal substrate (b) Exposure of resist using UV source (c) the exposed resist is developed (d) resist mould is electroplated with gold (e) unexposed resist is removed and polyimide/SU-8 is spin coated on gold electrodeposited metal wafer. (f) Stainless steel ring (black) is fixed from polyimide or SU-8 side and etched in case of SU-8 membrane mask and (g) finally the metal substrate is etched to obtain X-ray mask in right side view and on left side, thin layer of SU-8 is added for protection of gold layer.....79
Figure 3. 5 : First series of developed x-ray masks at RRCAT (a) SU-8 membrane gold mask and (b) Polyimide membrane gold masks.....84
Figure 3. 6 : Schematic of X-ray mask fabrication process using photo chemical machining. 85
Figure 3. 7 : Fabricated metal foil based X-ray mask with coarser CD.....87
Figure 3. 8 : PMMA monomer unit 88

Figure 3. 9: Schematic distribution of X-ray exposure dose from top surface to bottom.....89
Figure 3. 10 : Top surface view of X-ray irradiated samples with exposure dose (a) 0 mA.min (b) 83mA.min (c) 2834 mA.min. First two samples are used for surface roughness measurements.....94
Figure 3. 11 : FTIR spectrum recorded at increasing exposed dose.....96
Figure 3. 12 : Raman spectrum recorded at increasing exposed dose. 96
Figure 3. 13 : (a) XRD patterns of the PMMA after X-ray exposure(in inset) and the enlarged first diffraction maximum (b) Raw image plate XRD data (i) for PMMA Pristine (ii) exposed at 333mA.min and (iii) exposed at 1173 mA.min. 98
Figure 3. 14 : Variation of width of first diffraction peak with increasing exposure dose.....98
Figure 3. 15 : Chemical structure of Bisphenol A Novolak epoxy oligomer contained in SU-8. Eight reactive epoxy molecules and therefore 8 in SU-8. 99
Figure 3. 16 : Typical X-ray energy-flux spectrum available for exposures at SDXRL beamline.....103
Figure 3. 17 : Schematic representation of the composition of the surface layer during polymer/solvent dissolution.....106
Figure 3. 18 : (a) Processing characteristics of SDXRL beamline at various exposure dose with constant development time, and (b) processing depth at two exposure dose as function of development time. 111
Figure 3. 19 : Depth (symbol) Vs the development time for different exposure dose and solid line shows fit for estimating the value of *a* and *b* when SS mask is used, and (b) Dissolution rate obtained from various *a* and *b* values for different exposure dose and fitted to obtain the value of *K* and φ. 115
Figure 3. 20 : Depth (symbol) Vs the development time for different exposure dose and solid line shows fit for estimating the value of *a* and *b* when polyimide mask is used, and (b) Dissolution rate obtained from various *a* and *b* values for different exposure dose and fitted to obtain the value of *K* and φ. 115
Figure 3. 21 : (a) The development depth when high exposure dose are used. (b) Dissolution rate as a function of top and bottom dose. 116
Figure 3. 22: Development of PMMA in three different conditions. 116
Figure 3. 23 : HAR microstructure of hexagonal pattern with 30 μm wall thickness and 1000 μm in deep fabricated in PMMA. 117

Figure 3. 24 : Micro-pillars fabricated in SU-8, 200 μm in diameter, 170 μm deep and 300 μm pitch. The bubbles observed on the substrate are due incomplete washing and drying of substrate. 122
Figure 3. 25 : Photograph of 6mm thick PMMA sheet showing the developed Honeycomb structure using DXRL process. 122
Figure 3. 26 : SU-8 microgears with involute profile. 124
Figure 3. 27: Measured depth profile along 80 mm wide PMMA sheet. 125
Figure 3. 28: SEM micrograph of fabricated microcoil on cylindrical substrate. 127
Figure 3. 29 : Curved neck tapered structures fabricated in PMMA. The diameter of top circular hole is 150 μm and bottom circular hole is 100 μm. 128
Figure 4. 1 : Figure of merit δ / β for various X-ray lens materials. 131
Figure 4. 2: Single parabolic lens consisting of bi-concave lens (a) 2-D view (b) 3-D view, where R is the radius of curvature at the apex and $2R_0$ defines the geometrical aperture. The thickness of the lens at the apex is d and total length of the single lens is given by ($R_0^2/R + d$) and lithographically developed depth t. 134
Figure 4. 3: Developed X-ray masks for SU-8 X-ray refractive lenses 139
Figure 4. 4 : SEM micrograph of PMMA X-ray lenses fabricated at SDXRL beamline 140
Figure 4. 5 : Fabricated SU-8 X-ray lenses (a) actual photograph of 100 mm wafer (b) SEM of series A X-ray lens. 141
Figure 4. 6 : 3D surface profilometry of X-ray lenses with radius of curvature (a) 100 μm and (b) 25μm 142
Figure 4. 7: Comparison of measured d value for X-ray lens in (a) UV mask (b) X-ray mask (c) SU-8 X-ray lens. 142
Figure 4. 8 : The fidelity in parabolic profile, measured 2-D optical image is fitted with original designed parabolic curve and enlarged 1130 times. 145
Figure 4. 9 : X-ray fluorescence data for SUEX and SU-8 resist layers 146
Figure 4. 10: Calculated attenuation coefficients for SUEX and SU-8 for E upto 100keV. . 146
Figure 4. 11 : Fabricated SUEX X-ray lens on Si wafer at SDXRL beamline 149
Figure 4. 12 : Schematic setup adopted for X-ray lens characterization at BL-16, Indus-2 .. 150
Figure 4. 13 : View of experimental setup developed at BL-16, Indus-2 for X-ray lens chracterisation 150

Figure 4. 14 : Schematic of B-16 beamline, Diamond used for PMMA and SU-8 lens characterisation. 151
Figure 4. 15 : Microfocusing of PMMA X-ray lenses (a) Incident beam impinging on X-ray lens (b) line focus measured using self developing film and (c) line focus measured using X-ray CCD. 153
Figure 4. 16 : Transmission signal from a gold wire scan (black line) in the focal plane of the planar PMMA refractive micro-focusing lens, measured at 10 keV energy. The derivative of the raw data (blue dots) and a Lorentzian fit (red line) are also shown, indicating that the beam has an FWHM of 2.0 μm.....154
Figure 4. 17 : (a) X-ray CCD Image of CRL numbers 8 to 11 at 15.9 keV, (b) Intensity profile of beam in lens focal plane measured using gold knife edge scan method. X-ray energy of 15.9 keV was focussed at focal distance of 1.07 m with N = 58 lenses. The derived derivative of the knife edge scan is also shown with FWHM = 11.2μm.....156
Figure 4. 18 : SEM micrograph showing the distinct qualitative difference X-ray lenses (a) old sets (b) new sets. 157
Figure 4. 19 : (a) X-ray CCD image of lens 4B06 and (b) the focus spot obtained using this lens at 14 keV.....158
Figure 4. 20 : (a) Measured focus spot when X-ray lens 4B06 is illuminated only with 100 μm beam (b) measured effective aperture of X-ray lens at the same energy with 460 μm horizontal aperture. 160
Figure 4. 21 : Schematic of measurement strategy for determining the performance of the X-ray lens along its depth. 161
Figure 4. 22 : X-ray lenses mounted in 2-D focussing arrangement. 163
Figure 4. 23 : SU-8 X-ray lens 2D focussing at Indus-2 (a) the crossed geometry of two lenses, tallest fabricated lense is used in horizontal dispersion geometry, (b) enlarged view 2-D focussed spot size showing uniform normal distribution.....163
Figure 4. 24 : SU-8 X-ray lenses 2D focusing characterstics (a) FWHM in vertical direction (b) FWHM in horizontal direction (c) effective aperture and transmission of vertical lens (d) effective aperture and transmission of horizontal lens 164
Figure 4. 25 : Focused beam obtained from (a) 5A08 lens at 13.4 keV, f ~ 800 mm and (b) 5B03 lens at 14.9 keV, f ~ 600 mm with 0.1 μm scan step size. 167

Figure 4. 26 : Measured transmission and effective aperture for X-ray lens (56C03) R = 25 μm, N = 19 at 15.4 keV.....167
Figure 4. 27 : SU-8 X-ray lens 2D focusing at Diamond (a) High resolution X-ray CCD image (b) Enlarged view of 2D focused spot with measured gain of 624 (c) Focused beam profile in horizontal direction. 169
Figure 4. 28 : High energy focussing using SU-8 CRL (a) incident beam (b) focused beam observed on X-ray CCD.....170
Figure 4. 29: Focused beam obtained from lens 8B06 when x-ray lens is illuminated with (a) 450 μm and (b) 100 μm horizontal slit width. 172
Figure 4. 30 : Measured effective aperture and transmission for SUEX lens 8B08. 172
Figure 4. 31 : Estimated performance between SUEX and SU-8 on the basis of their effective aperture and transmission. 176
Figure 4. 32 : Effective transmission of SU-8 and SUEX X-ray lenses measured at BL-16, Indus-2 176
Figure 4. 33 : Full field imaging of Cu TEM sample grid using X-ray refractive lenses.....178
Figure 4. 34 : (a) Cross geometry of CRLs used for XRD experiments and obtained FWHM of focused beam (b) in vertical and (c) horizontal direction.....181
Figure 4. 35 : Schematic of High Pressure XRD measurements with DAC.....181
Figure 4. 36 : Comparison of CeO_2 XRD data obtained using 2D focused CRL and without CRL.....181
Figure 5. 1 : Processing steps involved in the biosensor fabrication.....187
Figure 5. 2 : Schematic of entire fabrication process for developing biochip (a) CMEA on Cu-PCB (b) X-ray mask on Cu foil (c) SU-8 microwell and microfluidic channel over Cu-PCB using SDXRL beamline. 188
Figure 5. 3 : Cu-CMEA pattern on Cu laminate PCB. The dimensions are measured using COM and shown above.....189
Figure 5. 4 : Shows the SEM micrograph of (i) the bare Cu electrode of CMEA at magnification 80×; (ii) the 11-MUA modified electrode surface at magnification 5000×; (iii) GOD immobilized electrode surface at magnification 5000×. 192
Figure 5. 5 : Capacitive spectra for various concentrations of glucose. EIS: 10 Hz to 10 kHz, 5 mV ac potential. 193
Figure 5. 6 : Calibration curve for different glucose concentrations obtained for physisorbed enzyme on Cu electrode of CMEA. 194

LIST OF TABLES

Table 1. 1 : Major X-ray lithography facilities available worldwide some synchrotron sources 8
Table 1. 2 : Comparison of various X-ray optical elements used for microfocussing X-rays. 17

Table 2. 1 : Characteristics of Indus-2 synchrotron radiation source used for calculations 23
Table 2. 2 : Angular combinations of two mirrors for Indus-2 X-ray lithography beamline. .28
Table 2. 3 : Effect of slope error values on the image characteristics at scanner2 35
Table 2. 4 : Flux density delivered by beamline after each optical element calculated combinely from XOP and RAY software tools. 39
Table 2. 5 : Calculated horizontal and vertical divergence of SDXRL beamline.....40
Table 2. 6 : Summary of the possible grazing incidence angles for SDXRL beamline in single mirror operation mode at scanner1 and scanner2 44
Table 2. 7 : Technical specifications of X-ray mirrors used in SDXRL beamline.....52
Table 2. 8 : Overview of the measurements and technical specification of all degree of freedoms for two X-ray mirror system 54
Table 2. 9 : Salient features of X-ray scanner2 of SDXRL beamline.....59
Table 2. 10 : Beam sizes, comparison between measured and calculated at scanner1 and scanner2 65
Table 2. 11 : Measured and theoretical values of the total power available at SDXRL beamline (total power is normalized for 100mA beam current).....68
Table 2. 12 : Calculation of ratio between the photocurrent of WPS and I_R. 69

Table 3. 1 : Mask membrane and absorber thickness for SDXRL beamline.....74
Table 3. 2 : Composition of Ni electrolyte solution.....81
Table 3. 3 : Conditions for Ni electrolyte solution maintained during its electrodeposition...82
Table 3. 4 : Conditions for Neutronex 309® maintained during Au electrodeposition 82
Table 3. 5 : Composition of Cu etching solution 87
Table 3. 6 : Overview of calculation of X-ray exposure dose in 2.5-9.0 keV. 91
Table 3. 7 : Comparison of PMMA top surface roughness with exposure dose. 94
Table 3. 8 : Few physical characteristics of SU-8 resist layer 101
Table 3. 9 : Comparison of characteristic dose values of SU-8 and PMMA resist 101

Table 3. 10 : Time required for various PMMA sheet of various thickness in various energy spectrum keeping bottom dose constant D_B = 2500 kJ/cm^3 (at scanner1).....104
Table 3. 11 : Composition of GG developer and GG rinser solutions.....105
Table 3. 12 : Estimated value of K and φ in different exposure conditions. 114
Table 3. 13: SU-8 characteristic processing times (in minutes) for different variants and film thickness used in this thesis [55, 56].....119
Table 3. 14 : Exposure parameters for SU-8 at SDXRL beamline.....120
Table 3. 15 : Roughness measurement of vertical sidewall in PMMA and SU-8 126

Table 4. 1 : Overview of refractive X-ray lenses developed worldwide using different techniques. 133
Table 4. 2: List of few lens parameters chosen for design and development in this thesis. ..138
Table 4. 3: Various parameters calculated for series B lenses (01-13), f = 300mm, Source to lens distance (p) = 23 m, Indus-2 vertical source size 0.2 mm and estimated focus spot of 2.6 μm. 138
Table 4. 4: Comparison of microstructure dimensions of X-ray lenses profiles between (1) UV mask, (2) X-ray mask and (3) actual fabricated X-ray lens (for nomenclature of variables, please see figure 4.2).....143
Table 4. 5 : Measured profile of SU-8 X-ray lenses from front and back side which correlates with divergence of X-ray beam.....144
Table 4. 6: Chemical composition and weight percentage of SUEX and SU-8 145
Table 4. 7 : Exposure parameters for SUEX at SDXRL beamline.....148
Table 4. 8 : Comparative performance of X-ray lenses on two synchrotron radiation sources, Diamond and Indus-2 [180]. 154
Table 4. 9: Measured FWHM of focus beam as a function of lens depth 162
Table 4. 10: Overview of SU-8 lens characterisation at BL-16, Indus-2 162
Table 4. 11 : Overview of SU-8 lens characterisation at B16, Diamond.....168
Table 4. 12 : Microfocusing using SU-8 X-ray lenses at 60-100 keV.....170
Table 4. 13 : Overview of the SUEX X-ray lenses measurements at Indus-2.....171
Table 4. 14: Measured FWHM of focus beam as a function of lens depth at three points....172
Table 4. 15: Calculated top and bottom absorbed dose for SU-8, SUEX and PMMA in white beam. 174

Table 4. 16: Comparison between the effective aperture and transmission data of SUEX and SU-8 X-ray lenses 175
Table 4. 17: Details of the X-ray lenses used for imaging experiment..... 177
Table 4. 18 : Details of the X-ray lenses used for X-ray diffraction experiment. 180
Table 4. 19 : Comparison between three X-ray lens materials used for X-ray lens fabrication in this thesis..... 183
Table 4. 20 : SU-8 X-ray lens performance at Indus-2 and Diamond. 183

Table 5. 1 : Comparison of design, measurement technique and limit of detection in various established (reported) electrochemical sensor for glucose. 195

LIST OF ABBREVIATIONS

11-MUA : 11-MercaptoUndecanoic Acid
ALS : Advanced Light Source
ANKA : Synchrotron Radiation Facility at Karlsruhe Institute of Technology
APS : Advanced Photon Source
ATR : Attenuated Total Reflection
AXUV 100: Absolute X-ray and UV Silicon Photodiode
AZ 1518 : Claryant photoresist, series 1500
AZ400K : Claryant developer, series 400 K
AZ4903 : Claryant photoresist, series 4900
BESSY : Berliner Elektronenspeicherring-Gesellschaft für Synchrotronstrahlung
BITS : Birla Institute of Technology and Science
BL-02 : Beam Line -02
BL-07 : Beam Line -07
CAD : Computer Aided Design
CAMD : Center for Advanced Microstructures and Devices
CD : Critical Dimension
CEERI : Central Electronics Engineering Research Institute
CLS : Canadian Light Source
CMEA : Circular Micro Electrode Array
CMM : Coordinate Measuring Machine
CNC : Computer (or Computerized) Numerical Control
COM : Confocal Optical Microscope
CP : CycloPentanone
CRCA : Cold Rolled Close Annealed
CRL : Compound Refractive Lenses
CXRO : Center for X-ray Optics
DAC : Diamond Anvil Cell
DCM : Double Crystal Monochromator
DESY : Deutsches Elektronen-SYnchrotron
DI : De-Ionised
DLS : Diamond Light Source
DLSR : Diffraction Limited Storage Ring
DNA : Deoxy-ribonucleic Acid
DPI : Dots Per Inch
DRIE : Deep Reactive Ion Etching

DXF : Drawing eXchange Format
DXRL : Deep X-ray Lithography
EDC : Carbodiimide hydrochloride
EIS : Electrochemical Impedance Spectroscopy
ELSA : Electron Stretcher Accelerator
ESRF-II : European Synchrotron Radiation Facility
EXAFS : Extended x-ray Absorption Fine Structure
FTIR : Fourier Transform Infrared Spectroscopy
FWHM : Full Width at Half Maximum
FZP : Fresnel Zone Plates
GBL : Gamma-ButyroLactone
GG : Ghica and Glashauer
GOD : Glucose Oxidase
HAR : High Aspect Ratio
IC : Integrated Circuit
IMT : Institute of Management and Technology
IP : Internet Protocol
JEEP : Joint Engineering Environmental Processing
KB : Kirkpatrick Baez
KIT : Karlsruhe Institute of Technology
KSRS : Kurchatov Synchrotron Radiation Source
LASTI : Laboratory of Advanced science and Technology for Industry
LIGA : LIthographie, Galvanoformung, Abformung
LILIT : Laboratory for Interdisciplinary LIThography
LOC : Lab On a Chip
LOD : Limit Of Detection
LOQ : Limit Of Quantification
MCT : Cadmium Mercury Telluride
MEMS : Micro-Electro-Mechanical-System
MFS : Minimum Feature Size
MIBK : Methyl IsoButyl Ketone
NA : Numerical Aperture
NHS : N-HydroxySuccinimide
NIST : National Institute of Standards and Technology
NSRL : National Software Reference Library
PAG : Photo Acid Generator

PB : Phosphate Buffer
PCB : Printed Circuit Board
PCM : Photo Chemical Machining
PCR : Polymerase Chain Reaction
PDMS : Plant Design Management System
PEB : Post Exposure Bake
PEEK : PolyEther Ether Ketone
PET : Projection Transparency
PGMEA : Propylene Glycol MonoEther Acetate
PLS : Pohang light source
PMMA : PolyMethylMethaAcrylate
PSD : Power Spectral Density
PTFE : PolyTetraFluoroEthylene
SAM : Self-Assembled Monolayers
SDD : Silicon Drift Detector
SDXRL : Soft and Deep X-ray Lithography
SEM : Scanning electron microscope
SR : Synchrotron Radiation
NSRRC : National Synchrotron Radiation Research Center
SU-8 : Name of the proprietary negative resist from M/s Microchem, USA
SUEX : Name of the proprietary negative resist from M/s DJ Dev Corp, USA
SXRL : Soft X-ray Lithography
TDFS : Thick Dry Film Sheets
THF : TetraHydroFuran
UDXRL : Ultra Deep X-ray Lithography
UHV : Ultra High Vacuum
USB : Universal Serial Bus
WPS : Wire Probe Scanner
XBPM : X-ray Beam Position Monitor
XFEL : X-Ray Free Electron Laser
XOP : Name of the spectrum calculation software available from ESRF
XRD : X-ray Diffraction
XRF : X-ray Fluorescence
XRL : X-ray Lithography
XRLM1 : X-ray Lithography Beamline1

LIST OF SYMBOLS

A : Atomic mass number

$A_{1/3}$: Asymmetries in the photo current from detector blades 1 and 3

$A_{2/4}$: Asymmetries in the photo current from detector blades 2 and 4

A_{eff} : Effective Aperture

α : Fine structure constant

a_p : Attenuation parameter for X-ray lens

β : Absorption index

c_{cu} : Specific heat of oxygen free copper

C_n : Weighting coefficients

D : Absorbed dose

$D(z)$: Resist depth

D_B : Minimum/Development dose

$D_{BL}(\lambda, \psi)$:Transmission through beamline as function of wavelength and vertical angle

Δ **:** MFS or CD in proximity printing process as a function of gap

δ : Strength of refraction

Δ_{con} : Exposure contrast

$\Delta E/E$: Energy bandwidth

ΔG_m : Gibb's free energy change on mixing

ΔH_m : Enthalpy change

$\Delta\lambda/\lambda$: Spectral bandwidth

ΔS_m : Entropy change

D_{resist} : Dose rates

D_S : Threshold/Shadow dose

D_T : Top dose

E : Energy of photon

e : electron charge

E_B : Binding energy

E_{kin} : Kinetic energy

ξ : Flory-Huggins coefficient

f : Focal length

$f'$and f'' : Atomic structure factors

F_{diff} : Diffraction limited spot size

F_{total} : Total lateral spot size

g : Gap between the mask and substrate

G : Gain

Λ : Offset distance

γ : Ratio of electron energy and the electron rest energy

g_n : Random shifting of each harmonic

G_{SC} : Number of scission/crosslinking events

h : Depth

$h(t)$: Distance from the top surface at time t

I_0 : Incident flux

$I_0(E)$: Incident intensity

$I(E,z)$: Transmitted intensity

I_R : Ring current

k : Wave number

k_1 : Rayleigh resolution criterion constant

K : Function of particular beamline configuration and type of resist

K_α : k alpha absorption edge

k_{ocf} : Online calibration factor

K_ν : Modified Bessel function

L : Total length

L_α : L alpha absorption edge

L_β : L beta absorption edge

$l(E)$: Attenuation length of material

λ : Wavelength

m : mass

m_0 : Rest mass of the electron

m_{dem} : Demagnification factor

$\mu(E)$: Linear attenuation coefficient

μ_{resist} : Linear attenuation coefficient for resist

MW_D : Number average molecular weight of the exposed polymer

MW_{D_0} : Initial number average molecular weight

n : Refractive index

N : Number of lenses

N_A : Avagadro's number

$N(\lambda)$: Spectral intensity distribution

n_{quartz} : Index of refraction

p : Distance between the source and mirror or lens

P : Total power

ϕ : Diameter

ψ : Vertical opening angle

q : Distance between mirror or lens and image point

r : Sagittal radius

r_0 : Classical electron radius

R : Radius of curvature of mirror in meridional direction or lens at apex

$R(D)$: Dissolution rate

R_G : Gas constant

ρ : Density of polymer

$R_M(\lambda)$: Reflectivity of the platinum coated mirror

R_{ran} : Random number between 0 and 1

R_0^{sur} : Smooth surface reflectivity

σ : Surface roughness

σ_h : Horizontal divergence of X-ray beam

$\sigma(E)_c$: Compton Sscattering cross section

$\sigma(E)_{pair:}$: Pair production cross section

$\sigma(E)_r$: Rayleigh Scattering

$S_{source}^{x,y}$: Size of the source in lateral and transverse direction

σ_v : Vertical Divergence

t : Time

T : Temperature

T_{Be} : Transmission of the beryllium windows

T_{crl} : Transmission of CRL

$\tau(E)$: Photo absorption cross section

T_g : Glass trasition temperature

$T_{He/Air}(\lambda)$: Transmission of the gas/air filled in the exposure chamber

θ : Grazing angle of incidence

θ_c : Critical angle

θ_i : Angles of incidence

θ_r : Angles of refraction

θ_1 : Grazing angle of incidence for mirror 1

θ_2 : Grazing angle of incidence for mirror 2

$T_{mask}(\lambda)$: Transmission of mask substrate thickness

V_{ref} : Reference volume

x_{max} : First diffraction maximum from the absorber edge

$Y_{A1/3}$: Vertical beam position from current asymmetry $A_{1/3}$

$Y_{A2/4}$: Vertical beam position from current asymmetry $A_{2/4}$

y_n^0 : Initial shift values

z : Thickness of the resist or absorber material along beam direction

Z : Atomic number

Chapter 1

Introduction

Microsystem developments are driven by the need of better device performance, faster response and low fabrication cost. Miniaturization of system requires a careful selection of the materials and methods of fabrication. Application specific microsystems are fabricated by a single process or an interdisciplinary combination of microfabrication and characterisation techniques. These processes involve replication of the masters created through processes such as X-ray LIGA[#1], deep reactive ion etching, electron beam lithography, CNC machines, wet silicon bulk micromachining, UV LIGA, ultra sonic cutting, excimer laser ablation, electrical discharge machining and laser cutting [1].

X-ray lithography (XRL) is a unit magnification shadow printing process where aerial image formed by an X-ray mask is recorded as latent image in an X-ray sensitive resist. XRL can produce micron and submicron features in devices structures of few mm tall with lowest vertical sidewall roughness. X-ray lithography is now a well developed technique and available at some synchrotron radiation facilities around the world [2].

During the eighties, the field of XRL grew tremendously due to technology projections that short wavelength (X-rays) lithographic technique will replace the UV lithography to

[#1] LIGA is German word and is acronym for X-ray LIthography, Galvanoformung (electroplating) and Abformung (molding).

fabricate higher spatial resolution structures of nano dimension required for micro electronics, to keep the pace with Moore's law. Significant developments in UV lithography, with introduction of techniques for resolution enhancement, and difficulties of using XRL in micro electronics production environment, damped the initial projections of XRL deployment for microelectronics industry. However, efforts continued towards using XRL for fabrication of high aspect ratio micro structures.

Synchrotron Radiation (SR) sources, with their high brightness, continuous energy spectrum and lower divergence are attractive to achieve higher lithographic resolution. They are used for deep X-ray lithography, also known as LIGA, for producing high aspect ratio (HAR) three-dimensional (3-D) structures that opens a wide variety of potential applications in micro-electro-mechanical-system (MEMS). Lithography at the soft X-ray range (photon energies from 1 to 3 keV) achieves the high lithographic resolution (< 100nm). On the other hand, with lithography done in hard X-ray region (> 4 keV), sensitive materials of thickness, tens of microns, can be exposed [3].

The role of SR based beamline and X-ray scanner as experimental station is very important for realisation of HAR micro/nano structures. Fabrication of high density, HAR microstructures have been a challenging field. The deep penetration of X-rays, control of geometrical errors and photoelectron blurs have significant role in the production of microstructure using XRL. HAR microstructures are useful for obtaining efficient functioning of devices. HAR microstructure with steep sidewalls and low surface roughness are required particularly in the area of optical engineering. Microstructures with HAR (100-1000) are widely applied to various fields such as micro mechanics, micro-optics, sensor and actuator technology, and biological, medical and chemical engineering. XRL has been used for the fabrication of hard X-ray optics [4, 5, 6], micromachining devices [7],Ultra light-weight X-ray micro pore optics to form Wolter type-I telescope [8], photonic band-gap

crystals [9], quantum wires and quantum dots devices [10], 3D microstructures [11, 12, 13], Micromotors [14], Micro harmonic drive [15] and RF MEMS related sub-components [16, 17].

In view of the above, a need of SR based X-ray microfabrication facility at Indus-2 was felt. The main motivation behind building the X-ray lithography beamline came from the need for a national facility for the development of HAR microstructures. The objective of this thesis work is the design and set-up X-ray lithography beamline on Indus-2 bending magnet source with X-ray exposure stations and auxiliary laboratory with a capability of various pre and post processing related with X-ray lithography. The technical capabilities of the XRL facility is shown by (1) Developing X-ray refractive optics for micro/nano focusing of X-ray beams. The optics performance is evaluated on Indus-2 and Diamond Light Source, UK (Diamond). (2) Developing lab-on-chip based on electrochemical biosensing for detection of ultra low concentration of glucose. In remaining part of this chapter, various terminologies used in this thesis are briefly introduced.

1.1 X-ray Lithography

XRL was proposed in 1970's for IC patterning and was first carried out at IBM by Spiller et. al. in 1976 using DESY SR source, when they fabricated the metal structure in gold by electro deposition in 20 µm thick X-ray defined resist pattern [18]. XRL is similar to UV lithography in terms of parallel patterning process (shown in figure 1.1). Unlike UV lithography, XRL cannot be performed in projection mode due to the non-availability of suitable transmission and reflective X-ray optics. Due to reduced wavelength, the diffraction effects through X-ray mask apertures are reduced. However, reducing the wavelength and hence reduced diffraction effects does not produce submicron structures. In such case, high energy photons eject energetic photoelectron from X-ray mask and resist materials, limiting

the minimum feature size (MFS). XRL can be performed in hard contact and proximity (gap between mask and resist) modes. The MFS or critical dimension (CD) (**Δ**) in proximity printing process as a function of gap is given by [19]:

$$\Delta = k_1\sqrt{\lambda\left(g+\frac{z}{2}\right)} \qquad (1.1)$$

where k_1 is Rayleigh resolution criterion constant [20], g is gap between the mask and substrate, λ is the wavelength of X-rays, z is the resist thickness. Δ is limited by the minimum feature available on X-ray mask and illumination properties of the source and physical/chemical properties of the resist used for copying mask image.

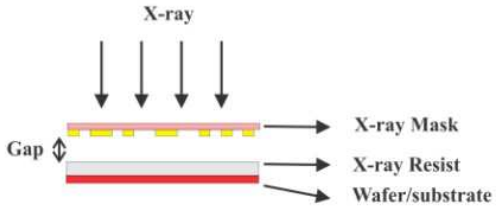

Figure 1.1: Schematic of X-ray lithography process

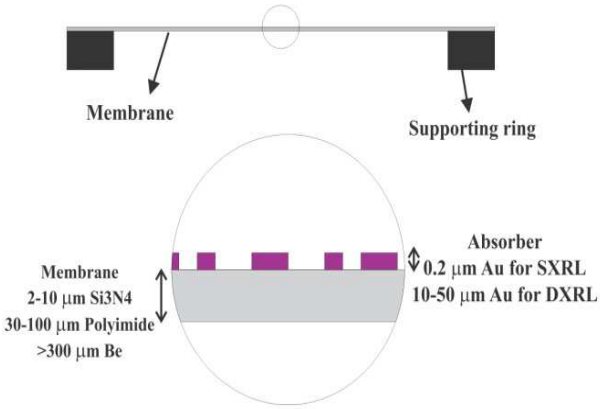

Figure 1.2: Schematic of an X-ray mask, showing mask membrane and mask absorber

X-ray mask is an essential component for XRL. A typical X-ray mask, shown in figure 1.2, is composed of patterned high Z(atomic number) material on a highly X-ray transmissive (low Z) membrane material. Depending upon the design of the structures, the mask may carry structures where feature sizes can vary from few hundreds of nm to several hundred of μm. X-ray mask should be carefully designed and optimized for obtaining the accurate patterning of desired CD.

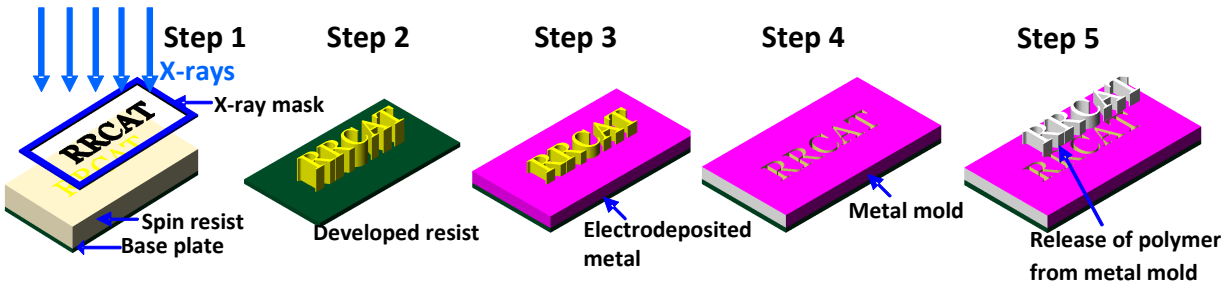

Figure 1. 3: Elements of X-ray LIGA process

Specific X-ray energies used for X-ray lithography defines HAR and high resolution microstructures which broadly classify X-ray lithography into three categories: soft X-ray lithography (SXRL) using 1-3 keV X-ray energies, deep X-ray lithography (DXRL) using X-ray energies upto 20 keV and ultra deep X-ray lithography (UDXRL) when X-ray energies are greater than 20 keV.

DXRL and UDXRL process are the core processing steps required for performing X-ray LIGA. X-ray LIGA has been first reported by Becker and his group in 1982 for the fabrication of micro nozzles for Uranium separation [21]. The processes involved in X-ray LIGA [22] are explained in figure 1.3 using micro pattern example text on mask as "RRCAT". A thick layer of photo resist (a few tens μm to a few mm) bonded on conducting substrate is exposed to high energy X-rays provided by SR source through X-ray mask pattern (step 1). The exposed resist is developed in an appropriate developer solution producing heights of X-ray mask patterned text and remaining area is removed in the case of positive resist (step 2). The structure formed in the resist is used as a parent mold for electro deposition of metal (step 3) and resist structure is later removed to obtain only metal mold. This metal mold (step 4) is used as micro structural device or else can serve as master mold for mass fabrication of polymer structure (step 5) through injection molding process. The master metal mold can also be used for ceramic filling at elevated temperature. Hence, it is

possible to fabricate 3-D shapes with steep wall structure profiles in polymers, metals and ceramics using X-ray LIGA.

1.2 Synchrotron radiation source: Indus-2

XRL can be performed using X-ray generator, laser produced plasma X-ray source and X-rays from SR source. However, synchrotron X-rays offers many advantages over the other two sources in terms of very high intensity, low beam divergence, wide X-ray energy range and better quality of microstructure.

In SR source, electrons or positrons of super relativistic speed ($v \approx c$) move in magnetic fields inside ultra high vacuum chamber, forcing them to travel in a closed path. In a storage ring the synchrotron radiation is produced either in the bending magnets which are needed to keep these particles in a closed orbit or in insertion devices (structures with alternating magnetic field) such as undulators or wigglers installed in the straight sections of the storage ring. The radiation is emitted tangentially to the curved electron orbit path. The energy is radiated in the form of electromagnetic radiation and loss of power is replenished by radio frequency (RF) cavities. The emitted radiation from synchrotron is known as synchrotron radiation. SR from bending magnet is extremely bright (several order of magnitude brighter than laboratory X-ray tubes) having continuous radiation from hard X-rays to far infra red. The SR emitted from synchrotron are linearly polarised in the plane of the electron orbit and emitted in a narrow cone. The radiation is pulsed with pulse duration of a few nano second and repetition rate of ~1 micro second. The number of electrons defines the ring current (I_R) and this is directly proportional to the flux available for experiments. Higher the energy of electron, lower the opening angle of SR and better will be collimation from source. Synchrotron accelerator complex are mega science facilities and serve as hubs for

multidisciplinary science research e.g. structural and chemical analysis, microscopy, micro-nano fabrication, medical diagnostics, photo chemical reaction etc.

The main characteristics of SR like high intensity, wide X-ray energy range and low divergence are useful to obtain better CD and higher aspect ratio with nearly perfect vertical walls (>89°) and very low surface roughness (~10-20nm) which is almost impossible with conventional micro manufacturing process. India has two dedicated synchrotron sources Indus-1 and Indus-2 [23]. Indus-1 is 450 MeV electron storage ring which provides soft X-ray and Indus-2 is 2.5 GeV electron storage ring which provides hard X-rays. Both of these sources operates in ultra high vacuum environment. Indus-2 has total circumference of ~ 172 m. The electron in one complete revolution looses ~ 186 kW of power which is replenished by RF field with frequency 505.8 MHz. Indus-2 has total 8 straight sections out of which 5 sections are available for installation of insertion devices. Eleven bending magnets provide 22 beamlines on Indus-2. Therefore total 2 beamlines can be installed on Indus-2 and maximum permission length of beamline ~ 40 m.

1.3 Beamline and X-ray Scanner

Beamline on SR sources is the setup which matches the properties of the source to the desired properties at experimental station performing particular experiment. The role of a beamline is to tune/monochromatise energy spectrum and define the beam sizes with proper beam conditioning (collimating and focusing). A typical hard X-ray beamline contains various sections, like frontend which located inside the storage ring tunnel, optics hutch containing the X-ray optical elements and experimental hutch where the experimental station is installed to carry out experiment. The beamline operates in high to ultra high vacuum conditions. For hard X-rays, the beam is brought into air if required for performing

experiments at experimental hutch. A hard X-ray beamline is shielded from all the sides using appropriate shielding materials (Steel and Pb combination) to protect the personnel working in the beamline area from highly ionising radiations.

Table 1. 1 : Major X-ray lithography facilities available worldwide some synchrotron sources

SR Source (Country)	Spectral range [keV]	Method of filtering high/low energy X-rays	Experimental station	Beamline length [m]	Ref.#
Elletra (Italy)	1-12	2 mirror (Pt), Be window (175 μm)	Stepper	20.8	[24]
	2-20	*Be window (200 μm) and filters	Scanner	20.5	[25]
ANKA (Germany)	2.2-3.3	1 mirror (Cr), Be window (175 μm)	Scanner	14.84	[26]
	2.5-12.5	1 mirror (Ni), Be window (225 μm)	Scanner	--	[27]
	2.5-15	*Be window (350 μm)	Scanner	14.89	[28]
SRRC (Taiwan)	0.5-3.0	*Be window (125 μm) and filters	Scanner	16	[29]
	0.8-2.0	1 torroidal mirror (Pt), Be (30μm)	Scanner	15	[30]
PLS (Korea)	4-20	Two mirrors Be window: beamline upgraded from white beam operation.	Scanner	15	[31]
New Subaru (Japan)	3-6	2 mirrors, Plane and Cylindrical, Be window	Scanner	25	[32]
CAMD (USA)	2-7	2 plane mirror (Cr), 2 Be window (100 μm and 120 μm)	Scanner	10.35	[33]
	2.6-7	*2 Be window (250 μm and 150 μm)	Scanner	10.7	
	2-7	*2 Be window (175μm)	Scanner	10	
ALS (USA)	3-12	*Be window	Scanner	10	[34]
APS (USA)	2-15	1 mirror (Pt) and Be window	Scanner	26	[35]
NSRL (China)	0.6-2.5	1 mirror, Be window (200μm)	Oscillating Mirror	7	[36]
Aurora–2S (Japan)	2-10	*Be window (200 μm)	Scanner	3.2	[37]
	2-10	*Be window (200 μm)	Scanner	3.39	
	2-10	*Be window (200 μm)	Scanner	3.88	
BESSY-II (Germany)	0.1-30	*2 Be window (200 μm)	Scanner	21	[38]
KSRS (Russia)	white	*Be window (200 μm)	Scanner	15	[39]
CLS (Canada)	1-15	2 plane mirrors, Be Windows	Scanner	--	[40]
Indus-2 (India)	1.5- 20	2 Mirrors, Be windows (175 μm)	Scanner	25.5	[41]

*Beamlines with only Be-windows provides white beam operation, # References

The SR beamline is one of the most important elements in SR lithography facilities. An X-ray scanner is used in experimental station in XRL beamline to hold the X-ray mask and the X-ray resist in SR beam. In case of XRL beamline, the wider beam, higher intensity and suitable X-ray energies are required to be delivered at the scanner. The use of appropriate X-

ray optics and horizontal acceptance of few mrad of SR defines the good quality of the beam for better lithography experiments in comparison to white X-ray beam without X-ray optics. It is desirable to have high brightness source like third generation source with wiggler to deliver the high intensity beam for smaller exposure time and lower horizontal divergence to reduce the runout errors at mask-wafer plane. Small runouts give small field distortions in the mask-wafer plane in the tune of few tens of nm.

Table 1.1 summarises the major XRL facilities installed on various synchrotron sources. The X-ray lithography beamlines are usually based on the bending magnet sources. Working with soft or deep X-ray lithography depends on user's requirement, i.e. spectral range of interest, spatial resolution, depth of focus and type of applications. Below 100 nm features is difficult for XRL beamline operating at higher energies (> 4 keV), however using soft X-ray spectral range (1-2 keV) a spatial resolution less than 100 nm can be achieved.

1.4 Attenuation of X-rays in Matter

X-rays interacts with matter via following interactions:

(1) Photo absorption

(2) Scattering (elastic and inelastic) and

(3) Pair production.

The absorption of X-rays in a homogenous matter with thickness '*z*' is described macroscopically by an empirical Lambert-Beer's law:

$$I(E, z) = I_0(E) e^{-\mu(E)\,z} \qquad (1.2)$$

where $I_0(E)$ is the incident and $I(E, z)$ is the transmitted intensity, E is the energy of the X-rays and $\mu(E)$ the linear attenuation coefficient. Overall attenuation coefficient $\mu(E)$ of X-ray

in a matter is function of photo absorption $\tau(E)$, scattering (Rayleigh $\sigma(E)_r$ and Compton $\sigma(E)_c$) and pair production $\sigma(E)_{pair}$:

$$\mu(E) = \tau(E) + \sigma(E)_r + \sigma(E)_c + \sigma(E)_{pair} \quad (1.3)$$

The different terms involved in μ(E) are discussed below.

1.4.1 Photo Absorption/photoelectric effect

Photoelectric effect occurs when an incident photon ($h\nu$) is absorbed by an electron in core level with binding energy (E_B) with the ejection of a photo electron with kinetic energy (E_{kin})**.** If the incident photon has higher energy than the E_B, then ejected electron will have the remaining energy as kinetic energy:

$$E_{kin} = h\nu - E_B \quad (1.4)$$

At energies from few eV to 40 keV the term τ(E) representing the photo absorption dominates the attenuation coefficient $\mu(E)$; and coefficient $\tau(E) \propto \frac{Z^4}{E^3}$.

The de-excitation of atom is either through the radiative emission or through non-radiative process (by ejection of Auger photo electron). For low *Z* material, Auger process dominates [42]. Photoelectron and Auger electron are responsible for creating the blur in X-ray resist under the shadow region of X-ray mask. This is discussed in the Chapter 2.

1.4.2 Scattering

Scattering is divided into two different processes, the elastic and the inelastic scattering.

Elastic scattering of X-ray by bound electron is described by Rayleigh scattering. In this type of scattering, X-ray photons are deflected without loss of energy or magnitude of momentum. The scattering cross section for elastic scatter is directly proportional to Z^2 in low energy limit.

Inelastic scattering: In this type of scattering, X-ray photon interacts with nearly free (weakly bound electron in atom) by transferring part of its energy and changing direction. The inelastic scattering coefficient is directly dependant on the *Z*. In case of X-ray lenses, Compton scattering creates the blur in the focal spot.

1.4.3 Pair Production

Pair production refers to the creation of an elementary particle and its antiparticle, usually when a photon interacts with a nucleus. If the photon energy is sufficiently high (> 1.02 MeV), a photon in an electric field of nucleus can produce an electron-positron pair.

In XRL, the energy range used is 1 keV – 40 keV. In this energy range the energy deposition in resist is mainly due to photoelectric effect and Compton scattering. Figure 1.4 (a and b) shows the competing interaction coefficient of various processes as function of energy for PMMA and SU-8 which are commonly used X-ray resist materials [43]. For low energy, photo electric absorption dominates. At around 30-40 keV, Compton scattering start contributing significantly for low atomic number materials. Besides, other scattering like coherent scattering plays a minor role.

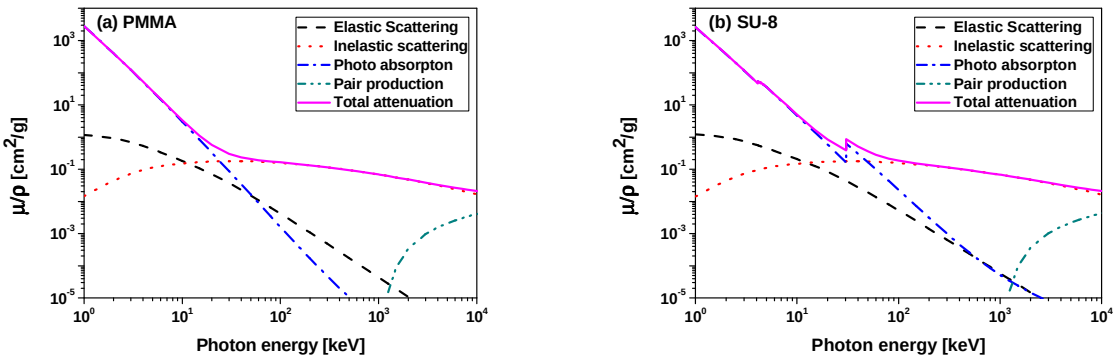

Figure 1. 4 : Attenuation of X-rays as a function of the photon energy for two X-ray sensitive photoresist (a) PMMA (b) SU-8.

1.5 The Complex Index of Refraction

The index of refraction for X-rays in matter can be written as [44]:

$$n = 1 - \delta + i\beta \tag{1.5}$$

where the refractive index decrement δ describes the strength of refraction with respect to vacuum and β describes the absorption. The value of δ and β are given by:

$$\delta = \frac{N_A}{2\pi} r_o \lambda^2 \frac{\rho}{A} (Z + f') \tag{1.6}$$

$$\beta = \frac{N_A}{2\pi} r_o \lambda^2 \frac{\rho}{A} f'' \tag{1.7}$$

where N_A is Avogadro's number and $\lambda = 2\pi\, c/\omega$ the wavelength of the incident X-rays. f' and f'' are atomic structure factors. The parameter ρ is the density of pure elements and A the atomic mass. The term $N_A\rho/A$ represents the number of atoms in the volume of interest and the value $r_0 = e_0^2 / (4\pi \epsilon_0 m_0 c^2)$ is the classical electron radius, and m_0 represents the rest mass of the electron as the scattering particle.

According to Snell's Law [45]:

$$n_1 \cos(\theta_i) = n_2 \cos(\theta_r) \tag{1.8}$$

where (θ_i) and (θ_r) are the angles between the surface and the incident and the refracted ray, respectively. It can be observed that in contrast to visible light for X-rays a beam coming from vacuum (or air) is refracted away from the surface normal (figure 1.5).

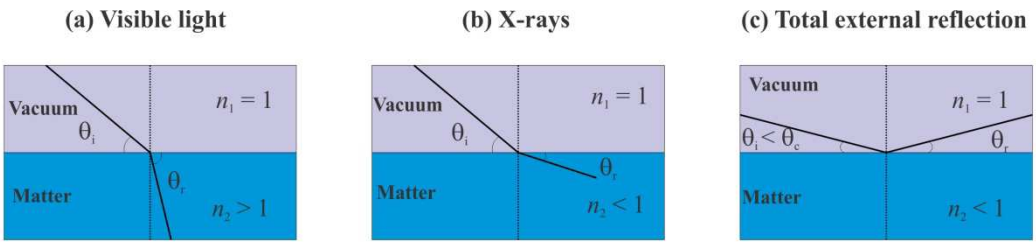

Figure 1. 5 : Refraction of incident light in the region of (a) visible (b) X-rays and (c) total external reflection

The value of δ is very small, the refraction in X-ray region is very weak. For example, at photon energy 15 keV the value of δ for SU-8 with density 1.2 g/cm^3 is δ = 1.18 x 10^{-6}. For an angle of incidence of θ_i = 20°, the corresponding angle of refraction θ_r is 19.9981°. In contrast, the corresponding refraction angle of visible light in case of glass (n =1.5) would be θ_r = 51.21°. Due to weak refraction, there were no X-ray lenses till 1990s. This topic is discussed in great detail in Chapter 5. In addition to refraction away from normal, total external reflection is observed in X-ray region in contrast to total internal reflection of visible light (figure 1.5 c). Again, by following Snell's law it can be shown that the critical angle below which total external reflection occurs is given by $\theta_c=\sqrt{2\delta}$.

The imaginary part β of the refraction index n describes the absorption of X-rays in matter. The attenuation coefficient is related to the absorption index β by:

$$\mu(\mathrm{E}) = \frac{4\pi}{\lambda}\beta \qquad (1.9)$$

1.6 X-ray sensitive resists

In typical XRL setup, X-ray sensitive photoresist is used to create the microstructures by X-ray exposures and development. Depending on the type of photoresist either exposed or unexposed part of resist is removed on developing in an appropriate developer solution. The choice of the resist material is entirely dependent on the process (SXRL or DXRL) for which it is going to use, sensitivity, resolution, contrast and good thermal and mechanical stability. The ideal resist material should have high throughput and submicron resolution. The material should also have the compatibility with electrodeposition process and it should be removable at the end of fabrication process. Most commonly used photo resists for X-ray lithography are polymethylmethacrylate (PMMA) and SU-8.

1.6.1 Polymethylmethacrylate (PMMA)

PMMA is a positive resist used for obtaining high spatial resolution and low side wall roughness. PMMA is available in the pre-casted sheet form upto very high thickness (10 mm) or in solution form which can be prepared as thin resist layer by spin coating (0.1-20 μm). Precast sheets are also commonly known with their trade names of Plexiglas® and Perspex®. Sheets are available from various suppliers worldwide, Plexiglas® from Ross GmbH, CLAREX from M/s Nitto Jushi Kogyo Co Ltd, PMMA sheets from M/s AIN Plastics, and CQ grade from M/s Vistacryl vista optics, are used for XRL process. These sheets have molecular weight in the range of few 10k to 2000k g/mole with an average of 600k g/mole [46]. Powder PMMA dispersed in Anisole or Chlorobenze available in various molecular weight (450k and 950k g/mole) solutions from Microchem Corporation, USA has been used. The resolution obtained in PMMA sheet is different and depends on its molecular weight of monomer and processing methods. These sheets are used as bare substrate for exposures referred here as uncrosslinked and sheets bonded to metal/Si substrate using bonding glue are refereed here as crosslinked PMMA.

In our studies, CLAREX sheet (molecular weight 2000k g/mole) in precast form is used for various studies and for the development of the microstructures. The preparation method, exposure mechanism and exposure dose for producing microstructure using XRL is discussed in Chapter 3.

1.6.2 SU-8

Epoxy based chemically amplified negative tone resist SU-8 has been developed by IBM (US Patent No. 4882245 (1989)) [47]. SU-8 is suitable for X-ray lithography. SU-8 photoresist is composed of SU-8 epoxy molecules dissolved in either gamma-butyloracton

(GBL) or cyclopentanone (CP) mixed with a photo-acid generator (PAG) made of a combination of triaryl sulfonium salt and sulfonium hexaflorate. SU-8 photoresist is available from two companies, M/s Microchem Corporation (USA) and M/s SOTEC Microsystems, (Switzerland).

The sensitivity of SU-8 resist is 100 times better than PMMA. The sensitivity is dependent on the percentage of PAG added to SU-8 formulation. The exposure mechanics and processing of SU-8 resist at Indus-2 XRL beamline are discussed in Chapter 3. SU-8 on exposure to X-ray, crosslinks and form polymeric structures. The unexposed part is solvable in the developer solution propylene glycol monoether acetate (PGMEA). The main problem with SU-8 is that it is difficult to remove after crosslinking and hard bake.

The fabrication in SU-8 by DXRL process is preferred where SU-8 material can itself work as structural material for the devices. However, after electrodeposition in deeper recesses, SU-8 is preferably removed by mechanical process. PMMA is still better choice for X-ray LIGA process due to the best precision and easy removability. The comparison between PMMA and SU-8 X-ray sensitive photoresist is given in Chapter 3.

1.7 Microfocusing of X-rays

Since X-rays discovered by Wilhelm Konrad Röentgen in 1895, several experimental techniques have been developed for characterisation of materials. X-rays were tried to focus to smaller spot sizes by Röentgen himself who later concluded from his experiments that X-rays cannot be focused by lenses [48]. The first observation of refraction was credited to Stenström in 1919 and reflection was observed later by Compton in 1923. Stenström's results indicated that the index of refraction of all materials with respect to X-rays was slightly less than one [49].

X-rays are used in wide applications in the area of science and technology covering atomic and molecular physics, structural biology, lithography and time resolved chemical kinetics. With increasing coherence length by the development of 3rd and 4th generation sources and deeply penetrating properties makes X-rays useful in microscopy for obtaining sample information in 2-D or 3-D using various X-ray analytical techniques such as diffraction, fluorescence and absorption spectroscopy, X-ray scanning microscopy allows one to measure local meso-scopic structures, elemental species and chemical state respectively. In association with tomography, 3-D inner structure of samples can be reconstructed. The demand of high spatial resolution and higher flux in these techniques led to the development of new X-ray sources and X-ray optics conserving source properties. With advancement of new high brightness SR source and now discussion on new version diffraction limited storage ring (DLSR) like ESRF-II, Spring-8 II, several X-ray optics element have been developed and new optics being developed to achieve better spatial resolution and obtain better signal in microscopy measurements by increasing the flux in focused beam. Several optics are used for X-ray focusing, distributed on their geometry and principle of operation for focusing X-rays such as reflective, diffractive and refractive. Among those are KB mirrors, Fresnel zone plates (FZP), curved mirrors, waveguides and refractive X-ray lenses, Multilayer Laue lens etc. These X-ray optics are capable of generating the micro/nano beams ranging from 7 nm-50 μm. The details on these optics are provided in table 1.2.

Reflective based optics is large size optics and they are manufactured by various mechanical techniques. The route for the fabrication of diffractive and refractive optics requires lithographic techniques due to micro and nano size features. Diffractive optics requires the dimension down to 10 nm and therefore it is fabricated using e-beam and complimentary techniques. For higher efficiency in hard X-ray region, zone plates are fabricated with combination of e-beam and X-ray lithography. Refractive optics has also been

fabricated using combination process of e-beam, focused ion beam, DRIE and X-ray lithography. X-ray resist, PMMA and SU-8 have been used for obtaining very high aspect ratio using X-ray lithography. In Chapter 4, design development and implementation of X-ray refractive optics are discussed.

Table 1. 2 : Comparison of various X-ray optical elements used for microfocussing X-rays.

Type of X-ray optics	**Reflective**					**Diffractive**		**Refractive**
	Kirkpatrick-Baez system		Capillaries		Waveguides	Fresnel zone plates	Multilayer Laue lens	Refractive lenses
	Mirrors	Multilayers	Multi-bounce	One-bounce				
E [keV]	< 20	< 80	< 20	< 20	< 20	< 30	< 30	< 1000
$\Delta E/E$	White beam	10^{-2}	White beam	White beam	10^{-3}	10^{-3}	10^{-3}	10^{-3}
Minimum spot size	8 nm [50], 7 x 8 nm^2 [51]	45 nm [52]	50 nm [53] 10 nm [54]	250 nm [55]	40×25 nm^2 [56] 26 nm [57]	30 nm [58]	16 nm [59]	47 nm [60]

E: energy range; $\Delta E/E$: energy bandwidth

1.8 Introduction to Microfluidics

Microfluidics is an area of micro manufacturing which centres on the miniaturization of fluid handling systems. In microfluidics, small volumes of solvent, sample, and reagents are moved through microchannels embedded in a chip. Potential benefits include reduced size, improved performance, reduced power consumption, disposability, integrated electronics and low cost. It is in fact, conceptually related with building of a small lab on a chip (LOC) where mixing, reaction, separation and manipulation of various chemicals and particles can

be carried out for example in biology for DNA sequencing, polymerase chain reaction (PCR), electrophoresis, DNA separation, enzymatic assays, immunoassays, cell counting, cell sorting, and cell culture [61, 62]. Biosensors are based on electrochemical impedance, optical and fluorescence measurement techniques [63]. Few impactful areas where LOC can be used include drug delivery, environmental monitoring, clinical diagnostics, and point of care portable sensors. LOC has generated great amount of interest in a wide variety of industries leading to tremendous growth in microfluidics. Few examples of LOC, which have been developed are for detection of various toxins, detection of nerve agent sarin in blood [64], label-free analysis of serum samples for pancreatic cancer diagnosis [65], etc. Recent review shows the use of inexpensive, easy-to-process, light-weight polymer-based materials such as polyimide, PEEK, PVDF and Parylene. These materials are biocompatible, mechanically flexible, and optically transparent as an alternative to metals and ceramics in the packaging of implantable sensors [66].

The manufacturing of microfluidics devices in various substrates in 2-D/3-D is required for sample transport, mixing, separation, and detection systems on single chip. Previously, microfluidic devices were fabricated in Si, glass or quartz. The fabrication method include photolithography on substrates using thin polymer layer (1-10 μm) followed by etching for obtaining required depth. Anisotropic etching of silicon yields V shaped grove channels in (100) oriented Si, isotropic etching of glass and Si yields U shaped grove channels and dry plasma etching produces the nearly vertical channel walls. The etched substrates are then bonded with plane wafer for sealing of the channels. The first of such devices was fabricated in Si for gas chromatography application [67]. These devices have few critical limitations including the fabrication in larger area with planer topography and low yields during bonding of substrates. The devices based on Si, glass and quartz is now being replaced by cheaper, use and throw type polymeric devices. UV LIGA, X-ray LIGA or imprint technologies are

used to produce the microfluidic systems in polymers. X-ray LIGA produces deep and vertical sidewalls in SU-8 and PMMA substrate. UV lithography is also used for preparing the microstructures in UV sensitive resist including SU-8. The structure in PMMA or SU-8 is used to convert negative profile in PDMS by casting process. The metal master either fabricated by X-ray LIGA or conventional machining technique is also used to prepare multiple polymer structures by imprint technologies. Due to the good chemical and mechanical properties of the polymerized SU-8, many novel microfluidic devices have been demonstrated [68].

There is a need to fabricate ultra-deep trenches or taller structures as a complete devices or subcomponent of the device. In obtaining HAR microfluidics/biochips, X-ray lithography plays a pivotal role. Obtaining high throughput in the micropumps is desirable and its construction requires thick substrates. These HAR structures are related with the performance of microfluidic devices (micro mixers, micro electrophoresis chips for bioanalysis, and micronozzles for generating thrust forces, etc). The high aspect ratio microchannels (35 μm width × 150 μm depth) has been used to process large input volumes (> 1mL) of blood and demonstrate capture efficiency of circulating tumor cells >97% with reasonable time of 31 minutes [69]. Impedimetric and ampereometric biosensors require microwell/microchannels of the height equivalent to the width of complete electrodes array to utilize the maximum use of field produced within the microelectrodes. Thus, microstructures in thicker polymer substrates are required.

1.9 Thesis outline

Chapter 1 begins with an introduction to the X-ray lithography, SR beamline, microfocusing of X-rays and microfluidics.

Beamline design, construction, installation and commissioning results are presented in Chapter 2. The optical design of the X-ray lithography beamline on Indus-2 is described. The design and development of beamline components, their individual testing are summarised. The performance results of the beamline in terms of beam size and beam power are presented.

Chapter 3 defines the research and development related to X-ray mask design and manufacturing, exposure mechanism of PMMA and SU-8 resist, and standardisation of HAR microfabrication process.

The details of development of X-ray refractive lenses in three different lens materials and its performance testing are discussed in Chapter 4.

Chapter 5 covers the successful fabrication and characterisation of biosensor with ultra low trace detection of glucose concentration.

Chapter 6 provides a summary of the development efforts towards X-ray lithography facility for fabrication of high aspect ratio microstructures, X-ray lenses for focusing X-ray and biosensor for detection of glucose. A recommendation for future work is proposed.

Chapter 2

Design and development of X-ray lithography beamline

2.1 Introduction

The beamline is an important element in SR based lithography facilities, required to efficiently transmit the flux from source to scanner. DXRL beamlines are based on the bending magnet sources at medium energy storage rings (ANKA, Elettra, Indus-2) or with wiggler at low energy storage ring (CAMD, BESSY-II). SXRL beamlines are operational at low energy storage ring with critical energy less than 4 keV. Appropriate choice of X-ray optics and acceptance of few mrad horizontal beam from SR source defines the good quality of the beam for SXRL and DXRL experiments in comparison to white X-ray beam with no X-ray optics. The use of X-ray optics ensures proper conditioning of beam at mask-wafer plane. High photon density and better collimation of beam are required to fabricate microstructure in reasonable time with low runout errors. Lower runouts are required to reduce overlay error in the microstructures to the tune of few tens of nm.

The XRL beamline on Indus-2 bending magnet source, is designed with an aim to fabricate HAR micro/nano structures. The beamline is planned to use a combination of X-ray mirrors for providing usable photon flux in the wide energy range from 1 to 24 keV. The

main design consideration is to have high flux in the appropriate X-ray energy range at mask wafer position. The beamline should also have a provision of white beam operation for performing UDXRL process. The selection of X-ray energy is planned using a combination of absorption edge filters and grazing incidence mirrors. The major design criteria also include providing homogenous intensity profile in horizontal plane which is required for better process latitudes when high sensitivity resist is used for obtaining HAR with good throughput. The beamline with combined SXRL and DXRL capabilities is advantageous in obtaining higher spatial resolution as well as HAR microstructures. In this chapter, optics design of the X-ray lithography beamline on Indus-2, design of individual beamline components, installation of the beamline and its measured performance are presented.

2.2 Design of the beamline

The optimum X-ray energies with peak at ~ 1.5 keV and ~ 6 keV are used for SXRL and DXRL respectively. Such energies are respectively available using low energy storage rings (0.5-1.3GeV) with critical energy 1-3 keV or medium energy storage rings (2.0-3.0 GeV) with critical energies 4-7 keV. X-rays in the desired energy window are defined using absorption edge filters and/ or high energy cut off X-ray mirrors [70,71,72]. LILIT beamline at Elettra, Italy [72], XRLM1 at CAMD, USA [73] and BL-2 at New Subaru, Japan [74] operate with two mirrors configuration. These beamlines do not support the beamline operation in white beam mode. There is a separate beamline available for white beam operation at Elettra and CAMD. Indus-2 X-ray lithography beamline optics is customized for SXRL, DXRL and UDXRL. Three scheme of operation are considered:

(1). Two mirror operation (for SXRL and DXRL)

(2). Single mirror operation (for DXRL)

(3). White beam operation (for DXRL, UDXRL)

Other major requirement is to obtain the collimation in horizontal direction and high power density beam in vertical direction at mask-wafer plane. This condition is obtained by deliberately generating astigmatism in the X-ray beam using single mirror. Astigmatism at mask-wafer plane can be achieved by using different radius of curvatures of a mirror in sagittal and meridional directions, focusing the beam in horizontal and vertical directions at different distances respectively. The profiles of the X-ray mirrors and its radius of curvature define the profile of the X-ray beam and its intensity at mask-wafer plane. The design for XRL beamline is carried out by choosing plane mirror (M1) as a first mirror and torriodal mirror (M2) as a second mirror. The ray tracing simulations for these mirrors are carried out using SR beamline ray tracing tools RAY and ShadowVUI and power calculations are simulated using XOP modules and RAY [75, 76, 77]. The properties of Indus-2 bending magnet port 7 used for design calculations are described in table 2.1.

Table 2. 1 : Characteristics of Indus-2 synchrotron radiation source used for calculations

Beam energy	2.5 GeV
Bending magnetic field	1.5 T
Ring current	100mA (designed for 300mA)
Horizontal emittance (coupling 1%)	58 nmrad
Electron beam dimension, horizontal (rms)	215 μm
Electron beam dimension, vertical (rms)	243 μm
Vertical divergence	62 μrad
Critical energy	6.24 keV

2.2.1 Optics design of the beamline

Prior to ray tracing of the beamline, analytical calculations are performed using geometrical optics to determine the distances of the optics and experimental station from the

source. The available space in Indus-2 experimental hall for Indus-2 dipole 3 (DP-3), 10°, BL-07 port is considered for these calculations. Required beam width is linked to the optics demagnification of the source at mask-wafer plane. The design is optimized for obtaining horizontal beam width of ~ 50 mm for performing SXRL and ~100 mm for performing DXRL. The width (w) of the beam at a particular distance from second mirror (q') where wafer can be placed is determined using:

$$w = \frac{p}{q}\sigma_h(q - q') \tag{2.1}$$

where p is the distance between the source and the second mirror, q is the distance between the second mirror and the focal point, $\sigma_h$is the divergence of the X-ray beam in horizontal direction incident on second mirror. Considering the mirror position at 17 m from the source and demagnification of 0.77, figure 2.1 shows the calculated beam width for three values of horizontal acceptances. The horizontal beam width reduces as distance from second mirror increases. Shorter beamline length will provide higher divergence resulting in higher runout. Considering the required beam width in SXRL, calculated beamline length is 25.5 m for 5 mrad and ~ 35 m for 10 mrad horizontal divergence. The vertical size of the beam is small in comparison to horizontal size. The vertical distribution of the beam at mask-wafer plane is Gaussian due to distribution of electron beam inside storage ring. Vertical divergence (emission angle) of X-ray is energy dependent. Also, the finite size source in vertical direction will lead to error, which in lithography terms is called penumbral blur or Penumbra. Therefore, the effect of vertical divergence is also considered in optics design of the beamline. The vertical divergence of 4 σ, calculated at 1.5 keV; 0.88 mrad is considered for calculations. Figure 2.2 shows various beamline lengths and resulting vertical and horizontal divergence when position of the second mirror is changed, keeping the fixed width (50mm) of beam at mask wafer plane. The observation from figure 2.1 and figure 2.2 are as follows.

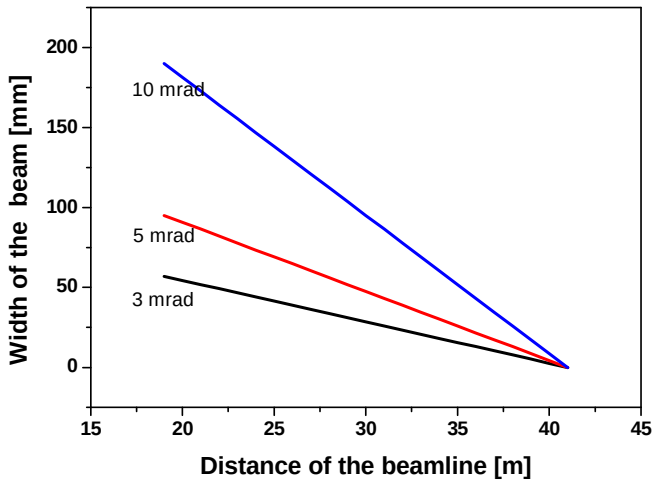

Figure 2. 1 : Calculated width of the beam along the beamline length for various horizontal acceptances by the second mirror.

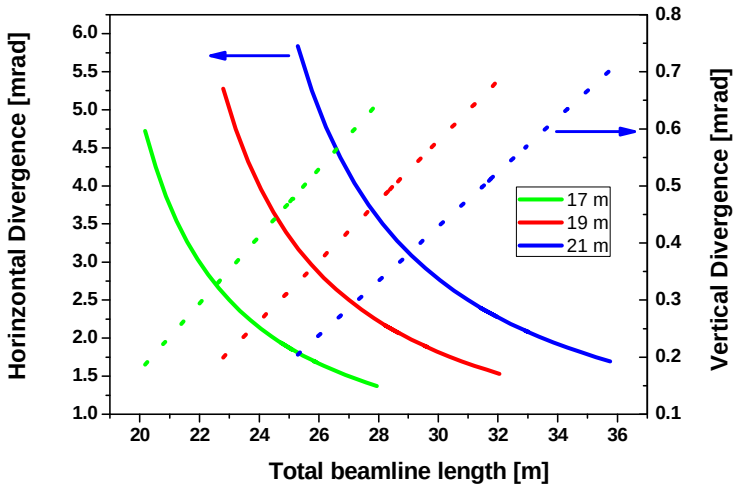

Figure 2. 2 : Possible beamline length on the basis of two geometrical errors due to vertical and horizontal divergence.

Longer beamline length is not desirable for obtaining higher flux in white beam and also in pink beam mode of operations. Shorter beamline length will results in higher horizontal divergence and higher runout as one moves away from the beam axis. A tradeoff between all

available combinations is considered and beamline length is kept ~ 25.5 m. The possibility of placing the first optics very near to shielding wall than the proposed distance is explored and found that it is not feasible due to circular radiation shielding wall. In our earlier reported results, M1 was kept at 16.35 m from source point and M2 at 0.65 m away from M1 [78]. Considering the manufacturing feasibility and to avoid the mirror optical surface collision, the distance between two mirrors is revised to 0.8 m, by placing M1 at 16.2 and M2 at 17 m from the source. In this thesis, the calculations pertaining to these mirror distance are reported.

Two mirrors geometry is selected for beamline due to following two conditions (1) beam at mask-wafer plane remains parallel with respect to the incident beam and (2) beam is available at fixed height from floor at mask-wafer plane. Two mirrors geometry allows the beam to fall perpendicular to mask and therefore, there is no requirement of tilting mask-wafer as required in single mirror operation due to each change in grazing angle of incidence. The position of X-ray beam at the mask-wafer plane is preferred to be away from the un-deviated optics axis, particularly in SXRL mode where scattered hard X-ray beam falling on the mask-wafer can produce error in submicron structures. According to condition (2) mirrors are kept at fixed distance from each other, different combination of grazing angles of incidence (θ_1 and θ_2) for M1 and M2 respectively are calculated to obtain continuous band of energies with different energy width. The proposed mirrors angular combinations and associated height of M2 from undeviated optics axis are given in table 2.2 to achieve constant position of X-ray beam at mask-wafer plane.

The beam at mask wafer plane can be kept at 0 mm, ± 25 mm and -50 mm with respect to the undeviated optic axis of SR beam. For mirror setting in serial number 1 to 3 of table 2.2, the beamline provides the energy between 1-2 keV for SXRL mode and for settings in serial number 4-9, beamline operates under DXRL mode offering energy between 2.5 keV and 24

keV (see figures 2.5 and 2.6). The beamline provides energies for SXRL and DXRL techniques and therefore christened as “Soft and Deep X-ray Lithography” (SDXRL) beamline.

In order to obtain the proper beam conditioning at mask-wafer plane, it is required to match the source properties with required properties at experimental stage using X-ray mirrors. M2 is considered as torroidal mirror which has two radii of curvatures in two orthogonal directions. The radius of curvature in sagittal (tangential) and meridional(longitudinal) direction for torroidal mirror (M2) is given by Coddington’s equations [79]:

$$\frac{1}{p} + \frac{1}{q} = \frac{2\sin\theta}{r} \tag{2.2}$$

$$\frac{1}{p} + \frac{1}{q} = \frac{2}{R\sin\theta} \tag{2.3}$$

r is sagittal radius, R is merdional radius and θ is the grazing angle of incidence.

Grazing incidence angles are different in soft and hard X-ray energies. Beamline operation in different X-ray energy regime requires different sagittal and meridional radii of curvatures. It is difficult to have optimized mirror radii for an extended energy range. SDXRL beamline optics parameters are calculated at 1.5 keV where better spatial resolution is achieved due to reduced photoelectron blur [80]. For obtaining the horizontal beam size of 50 mm and focusing in vertical direction, calculated radius of curvatures are R = 420 m and r = 0.577 m. The performance of the beamline marginally deteriorates for DXRL operation due to fixed R and r values. This is acceptable due to moderate spatial resolution requirements at higher energies. However, the power density values are comparable.

Table 2. 2 : Angular combinations of two mirrors for Indus-2 X-ray lithography beamline.

Serial No.	Angle for M1 (θ_1)[°]	M2 height from un-deviated optic axis [mm]	Angle for M2 for beam at ## mm down from optics axis at mask-wafer (θ_2) [°]			
			25 mm	0 mm	-25 mm	-50mm
1	2	-55.94	1.915	1.99	2.083	2.166
2	1.75	-48.93	1.665	1.745	1.833	1.917
3	1.5	-41.93	1.415	1.499	1.584	1.667
4	1	-27.94	0.916	0.999	1.084	1.168
5	0.6	-16.76	0.516	0.599	0.684	0.768
6	0.5	-13.96	0.416	0.499	0.584	0.668
7	0.4	-11.17	0.316	0.399	0.484	0.568
8	0.3	-8.38	0.216	0.299	0.384	0.468
9	0.2	-5.59	0.116	0.199	0.284	0.368
10	0.15	-4.19	0.066	0.15	0.234	0.319
11	0.1		No mirror	No mirror	No mirror	No mirror

Figure 2.3 shows the schematic optical layout of SDXRL beamline [81]. The beamline consist of two X-ray mirrors (M1 and M2), two slits systems, filters, two Be window assemblies, two X-ray scanner systems (scanner1 and scanner2) and vacuum hardware (gate valves, pumps, etc.). The performance of the beamline is simulated at scanner1 and scanner2 where regular experiments are planned.

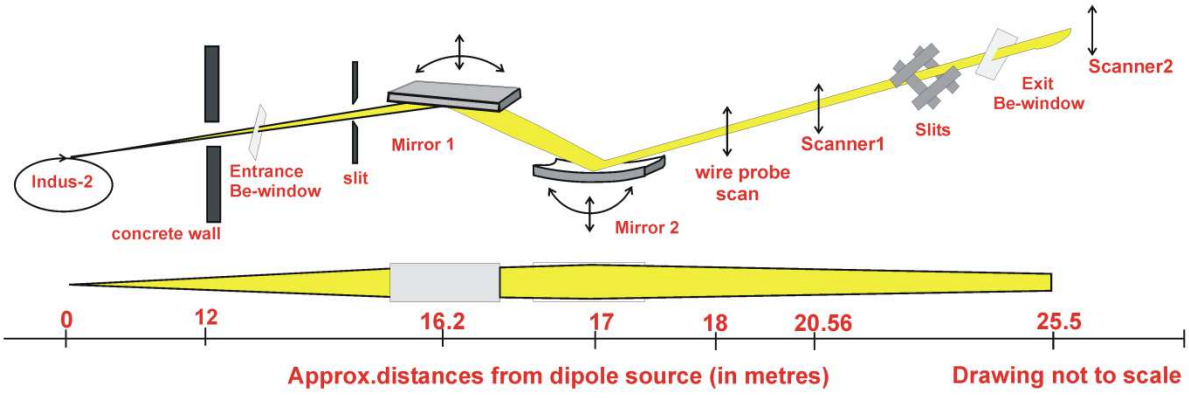

Figure 2. 3 : Schematic optical layout of the SDXRL beamline on Indus-2.

2.2.2 Ray tracing simulations

Beamline design using ray tracing simulation software allows exact planning and estimating the performance of the critical components. Ray tracing results provides key information on the flux/power transmitted through individual beamline components. The ray tracing program RAY is used for the most of simulation during this beamline design. The ShadowVUI is also used to find out the complimentary information on the design aspects, like runout and penumbra.

RAY simulates the imaging and focusing properties of a beamline. In present case, RAY generates random rays from the dipole magnet source and trace them through the optical elements (reflection mirrors and foils) according to the laws of geometric optics. A ray which traces through the optical elements are described by its coordinates and direction cosines defined with respect to a suitable coordinate system and also its energy, polarization and path length. Program simulates the complete transmission of the beamline. Geometric distribution of rays in graphical format can be visualized at the source, at all optical elements and at desired image planes. The program also gives the details on angular distribution, intensity, flux, polarization and energy resolution.

2.2.2.1 Two mirror mode

The performance of the beamline over full energy range (1-24 keV) is based on detailed ray tracing simulations [82]. Representative ray tracing results at 1-2 keV (serial number 2, table 2.2) for SXRL and 2.5-9.0 keV (serial number 5, table 2.2) for DXRL are presented along with simulated performance of the beamline.

2.2.2.1.1 Point diagram of image at optical elements

The point diagram of image formed at scanner2 and scanner1 mask-wafer plane (including at source and mirrors), by the beamline configuration are shown in a series of images in

figure 2.4 (La-Le) and (Ra-Re). The figures on left side (La-Le) shows the beamline performance in the energy range 1-2 keV and figures on right (Ra-Re) shows the performance of the beamline for energy range 2.5-9 keV.

Figure 2.4(La and Ra) shows the RAY generated source, where FWHM source sizes are 0.568 mm (V), 0.500 mm (H) and 0.565 mm (V) ,0.503 mm (H) respectively at 1.5 and 6 keV. The corresponding vertical (σ_v) divergences are 0.79 and 0.44 mrad. The source is generated uniformly with 5 mrad in horizontal divergence in both the cases, as per design considerations.

For soft X-ray energy range, the vertical acceptance is 4 σ_v (~ 95%) to determine beam footprint on the mirrors. At higher energy range 2.5-9 keV, 3 σ_v (~ 86%) and energies >10 keV 2 σ_v (~ 67%) values are considered. For vertical acceptance (>2 σ_v), at energies >10 keV, the beam footprint on mirrors is $\geq \pm$ 500 mm. Considering exit Be-window aperture (~ 10 mm (V) x ~ 80 mm (H)) through which beam shall be available and fixed mirror curvatures, beam footprint on both mirrors is limited to $\pm$ 350 mm length. Figure 2.4 (Lb and Lc) shows the foot print on M1 and M2 respectively in the soft X-ray energy. It is noted that 4 σ_v is well accommodated in 700 mm long mirror in meridional direction. Identically, figure 2.4 (Rb and Rc) shows the footprint at higher energies at M1 and M2 respectively. It is apparent that the beam is entirely filled on the mirror substrate and portion of the beam is lost. The ray tracing simulation suggests the optimum mirror surface dimensions of 100 mm (width) and 700 mm (length) are sufficient to obtain desired quality of the beam at mask-wafer plane.

The beam sizes at scanner2 are important for carrying out X-ray exposures. In case of SXRL mode, the obtained beam sizes are ~ 2 mm (V), 50 mm (H) (shown in figure 2.5(Le)). The beam size at scanner1 for same configuration (figure 2.4(Ld)) are 7.35 mm (V), 69.7 mm

(H). In DXRL mode, the obtained beam sizes at scanner1 are 2mm (V) and 90.7 mm (H) is shown in figure 2.4(Rd). The beam sizes at scanner2 in same energy range are 13 mm (V), 100 mm (H) (figure 2.4(Re)). Uniformity in horizontal intensity is required for obtaining better line width, depth control and uniform exposure. The estimated horizontal intensity uniformity is ± 3% for SXRL and ± 5% for DXRL.

SXRL mode

(La) Source at 1.5 keV

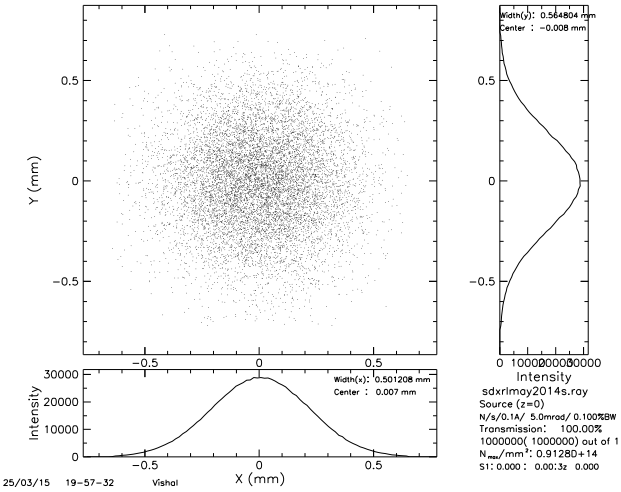

DXRL mode

(Ra) Source at 6 keV

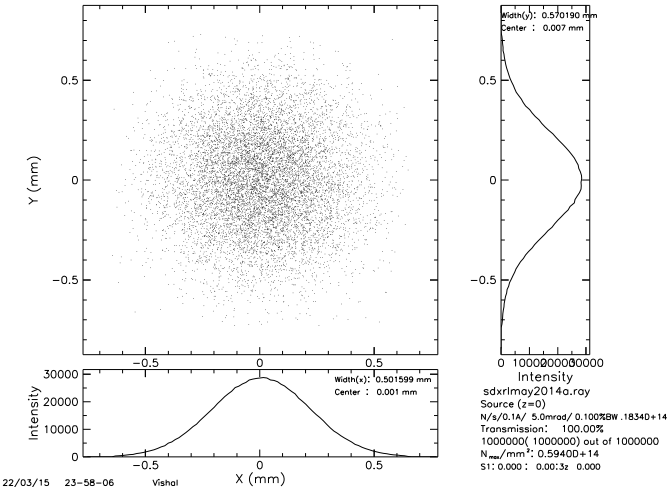

(Lb) Footprint on Mirror1

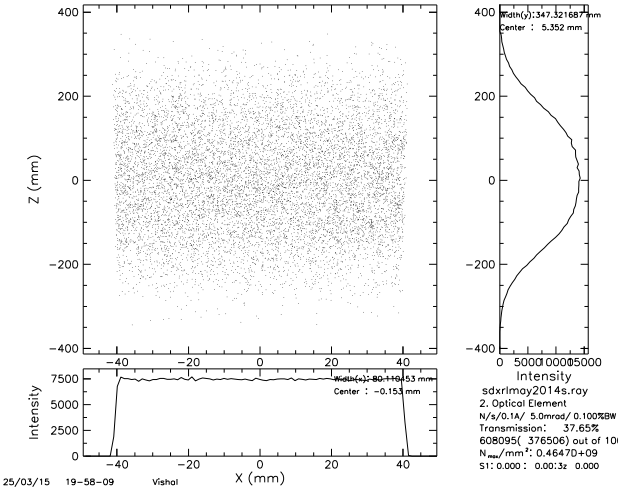

(Rb) Footprint on Mirror1

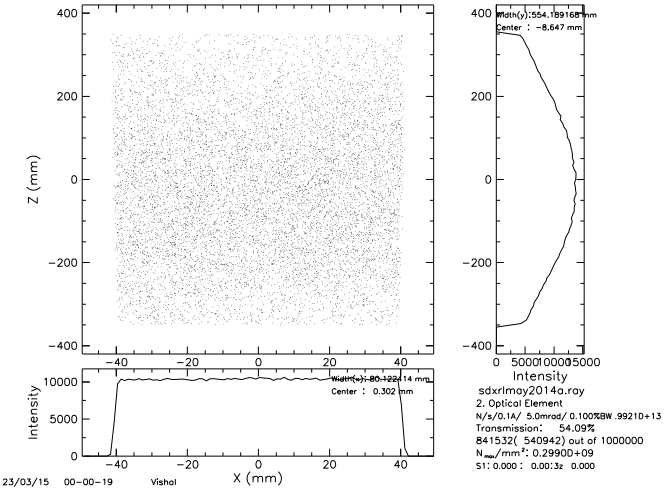

(Lc) Footprint on Mirror2 **(Rc) Footprint on Mirror2**

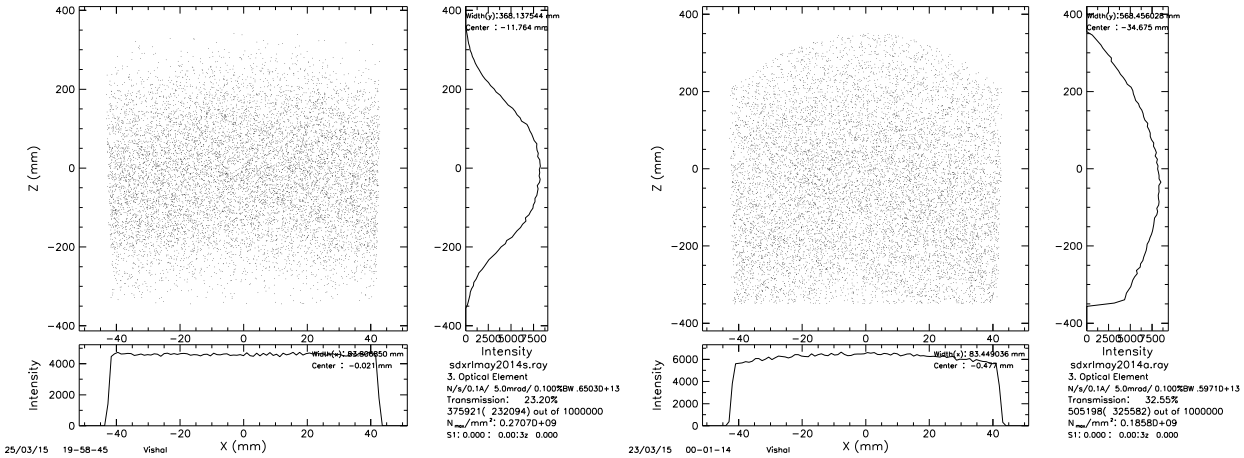

(Ld) Point diagram at scanner1 **(Rd) Point diagram at scanner1**

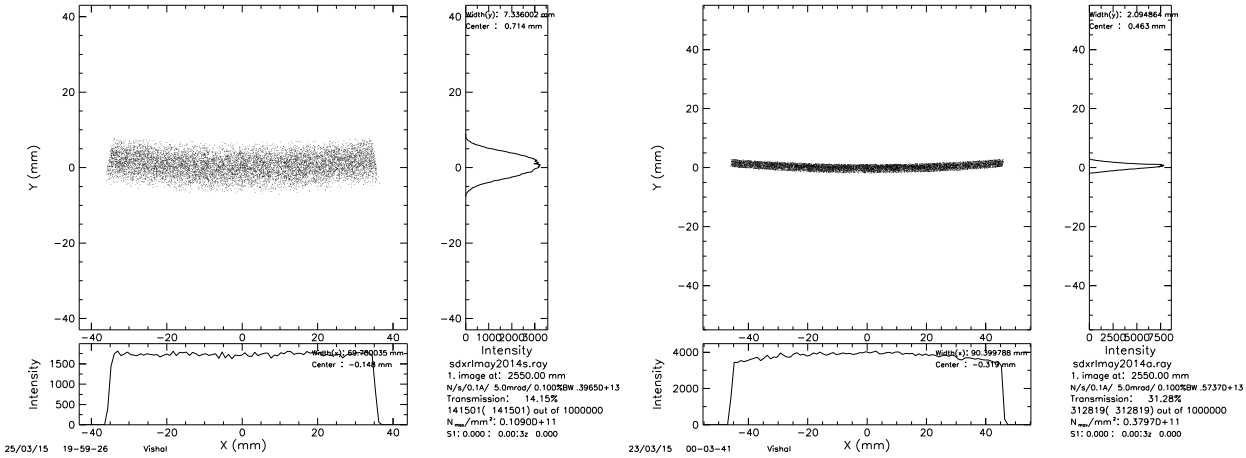

(Le) Point diagram at scanner2 **(Re) Point diagram at Scanner2**

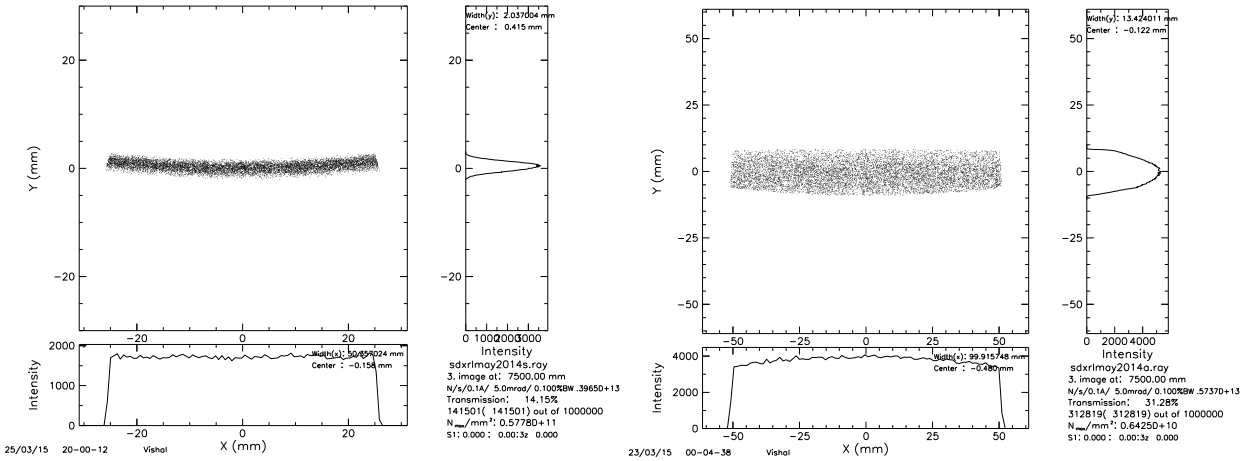

Figure 2. 4 : Point diagram of beam at various position of the beamline including at X-ray scanners. Left images (La-Le) belongs to calculations using serial number 2 parameters and right images (Ra-Re) pertains to calculations obtained using serial number 5 of table 2.2.

2.2.2.1.2 Effect of mirror surface roughness

The roughness process is incoherent. Specular reflection from the X-ray mirror is reduced with increase in surface roughness. The reduction in reflectivity at a given energy and grazing angle of incidence is:

$$R^{sur} = R_0^{sur} \exp\left[-\left(\frac{4\pi\sigma \sin\theta}{\lambda}\right)^2\right] \quad (2.4)$$

where R_0^{sur} is smooth surface reflectivity, λ is the wavelength of incident light and θ is grazing angle of incidence and σ is rms surface roughness. The term in square bracket is also known as Debye–Waller factor.

The influence of mirror roughness on the quality of the beam image is evaluated by assuming three surface roughness values of a platinum coated mirror for two energy range. In this case, the grazing incidence angles 1.75° and 0.6° and rms roughness values of 3 Å, 5 Å and 10 Å are used. No significant changes in the beam shape and uniformity in horizontal intensity profile are observed. However, the overall transmission of the beamline is reduced by 1.6% when surface roughness value is increased up to 10 Å for SXRL energy range. At higher X-ray energies where low grazing angles of incidence are employed will show high impact on beamline transmission due to high roughness. In this case for same change in surface roughness value, the transmission of the beamline is reduced by 4.4 %. The acceptable tradeoff between the performance of beamline and manufacturability of mirror with low cost is considered by choosing a surface roughness of 5 Å.

2.2.2.1.3 Effect of slope error

The effect of slope errors on X-ray mirror surfaces are considered to evaluate the beamline performance using ray tracing simulation. Slope error on mirror surface introduces the hollow in specular reflection. Real surface with slope errors is characterized by the presence of many

frequencies, few of them are directly related to variation in optical characteristics of the image thus formed. The fine scale fluctuations in the effective surface height are best determined by power spectral density (PSD) function. For real surface characterization, any shape or profile can be simulated by a series of sine or cosine signals having frequencies, which are multiples of the fundamental. By considering the limited number of harmonics n_{max}, fixing their amplitudes with function of (period, slope error) and considering the complex part of Fourier series and shifting the signal randomly, the fine scale fluctuations is given by

$$Z(y) = \sum_{n=0}^{n_{max}} A_n (-1)^n \cos \frac{(2n+1)\left(y + y_n^0 + R_{ran} g_n\right)}{L/\pi} \qquad (2.5)$$

where $A_n = \frac{C_n L \Delta_{rms}}{(0.5+n)\sqrt{2}\pi}$

where C_n are weighting coefficients, y_n^0 are the initial shift values, R_{ran} is random number between 0 and 1, g_n is a random shifting of each harmonic.

Simulation of beamline under the influences of slope errors for X-ray mirrors set at grazing angles 1.75° for M1 and 1.75° for M2 are carried out. This beamline operating setting is the most crucial to obtain the maximum spatial resolved microstructures. Rio et. al. incorporated the above algorithm in Waviness_gen subroutine of ShadowVUI [83]. A mirror surface is divided into small planar elements that individually steer the beam. An input file is generated by giving the 100 x 700 mm^2 mirror size and divided into mesh of 2 x 10 mm^2. Input values of n_{max} = 60, and Δ_{rms} are 0, 0.5, 1, 5, 8, 15, 30, 50 and 100 μrad respectively are used, and resulted slope error values are given in table 2.3. For change in the value of slope error from 0 μrad to 57 μrad, the vertical FWHM is increased by three times of initial value. For meridional slope errors < 28 μrad, horizontal intensity uniformity is within acceptable

limit. In sagittal plane, the broadening in the focal spot is relaxed by 1/sinθ. Thus large value of sagittal slope errors (≈500 μrad) does not have any appreciable effect on horizontal FWHM values.

Table 2. 3 : Effect of slope error values on the image characteristics at scanner2

Serial No.	Slope error [μrad]		FWHM [mm]	
	Sagittal	Meridional	Horizontal	Vertical
1	0.000	0.000	49.390	1.058
2	9.401	0.945	49.409	1.062
3	18.801	1.890	49.428	1.073
4	150.389	15.126	49.497	1.249
5	564.032	56.723	49.525	2.894

2.2.2.1.4 X-ray flux density at mask wafer plane

The X-ray intensity in chosen energy spectrum at mask-wafer plane is an important parameter for any XRL beamline. X-ray intensity decides the exposure time for a particular setting of SDXRL beamline. The intensity calculations of the X-ray spectral distribution from bending magnet source, through mirrors and Be window assemblies are carried out. The radiation spectra from the bending magnet source are calculated using the formula for vertical integrated beam:

$$N(\lambda)\ [\text{photons/mA/s/mrad}/\Delta\lambda/\ \lambda] = \frac{\sqrt{3}}{2\pi}\alpha\gamma\frac{1}{e}\frac{\lambda}{\lambda_c}\frac{\Delta\lambda}{\lambda}\int_y^{\infty} K_{5/3}\,(y')dy' \qquad (2.6)$$

and photon flux as a function of vertical opening angle ψ is given by:

$$N(\lambda,\psi)[\text{photons/mA/s/mrad}^2/\Delta\lambda/\ \lambda] = \frac{3\alpha\gamma^2y^2}{4\pi^2}\frac{1}{e}\frac{\Delta\lambda}{\lambda}[1+(\gamma\psi)^2]^2 \times \left[K_{2/3}^2\bar{\omega} + \frac{(\gamma\psi)^2}{1+(\gamma\psi)^2}K_{1/3}^2\bar{\omega}\right] \qquad (2.7)$$

where, $\bar{\omega} = \frac{y[1+(\gamma\psi)^2]^{\frac{3}{2}}}{2}$, e is the electron charge, γ is the ratio of electron energy and the electron rest energy, $\lambda c = 4\pi R_{BM}/3\gamma^3$, α is the fine structure constant, Δλ/λ is the spectral

bandwidth and K_ν is the modified Bessel function of second kind of fractional order ν and $y = \lambda_c/\lambda$.

The spectral intensity distribution $N(\lambda)$ of bending magnet source is a function of the electron energy, the bending radius(R_{BM}), and the circulating current (I_R) and it is given in units of Photons/mA/sec/mrad/0.1% bandwidth, integrated over the vertical direction. $N(\lambda)$ is modified by the beamline optical elements, like reflectivity $R_M(\lambda)$ of the platinum coated mirrors and the transmission $T_{Be}(\lambda)$ of the beryllium windows. Be window of thicknesses 175 μm and 15 μm filter out the radiation below 2.2 keV and 1 keV respectively. The spectral density per mrad $D_{BL}(\lambda)$ falling onto the mask-wafer plane due to various optical elements of the beamline is then given by:

$$D_{BL}(\lambda) = N(\lambda)\, T_{Be(ent)}(\lambda)\, R_{M1}(\lambda)\, R_{M2}(\lambda)\, T_{Be(exit)}(\lambda) \qquad (2.8)$$

In order to consider the exposure of the resist, transmission of mask substrate thickness ($T_{mask}(\lambda)$) and transmission of the gas/air filled in the exposure chamber ($T_{He/Air}(\lambda)$) must be accounted. Therefore the above equation modifies to:

$$D_{BL}(\lambda) = N(\lambda)\, T_{Be(ent)}(\lambda)\, R_{M1}(\lambda)\, R_{M2}(\lambda)\, T_{Be(exit)}(\lambda) T_{mask}(\lambda)\, T_{He/Air}(\lambda) \qquad (2.9)$$

XOP is used to calculate spectra for various mirrors grazing incidence of angles. The XOP does not account for optics sizes and beam loss due to the finite size of optics and its slope errors. In RAY, the optical components with their lateral sizes are taken into consideration while calculation of flux density at mask-wafer plane. All flux/power calculations are carried out by considering 100 mA ring (e-beam) current (I_R) in Indus-2 storage ring operating at 2.5 GeV. Total incident power available from bending magnet is ~ 49 W for 5 mrad horizontal acceptance and full beam in the vertical direction.

During these calculations, a mirror surface coated with platinum is used with mirror surface roughness of 5Å and slope errors values of 20 μrad in saggital and 5 μrad in

meridional direction. Platinum is chosen as mirror reflecting layer over gold or rhodium due to its higher reflectivity for wide lithographic window [84]. The energy power spectrum for selected angular combinations as per table 2.2, are calculated. Figure 2.5 shows the X-ray spectrum in soft X-ray energy region which may be used for obtaining better spatial resolution or higher density microstructures (for angular combinations described at serial number 1-2, table 2.2). In this case, Be window thicknesses of 15 μm each is considered. Figure 2.6 shows the spectra of the beamline for angular combinations given in serial number 4, 5 and 9, of table 2.2. For calculation of spectra shown in figures (2.8 and 2.9), the values of grazing angles of incidence for M2 (θ_2) are used from 5th column of table 2.2. As seen from the table 2.2, the incidence angles values for M2 is higher for placing the beam at -25mm and -50 mm at mask-wafer plane in comparison to 0 mm and +25mm. In such cases, obtained spectrum will be trimmed on higher energy side due to higher grazing angles of incidence of M2. The calculated spectra for serial number 5 for 0 mm and ± 25 mm is shown in figure 2.7. The tuned beam at 0 mm is preferred as long as the direct/scattered components of SR beam do not interfere in the line of desired beam. In SXRL mode, the beam at scanner2 is preferred away from undeviated optic axis. In this energy range the change in incidence angles does not change energy spectrum significantly.

Table 2.4 shows the power and power densities calculated in selected four mirror angular combinations at mask-wafer plane and downstream to polyimide mask membrane. The power values enclosed in the parenthesis is absorbed power at each optical element. The values of power and power densities are given at scanner1 and scanner2 position. Since the beam size after exit Be window is reduced, therefore the normalized power values are also tabulated for scanner2.

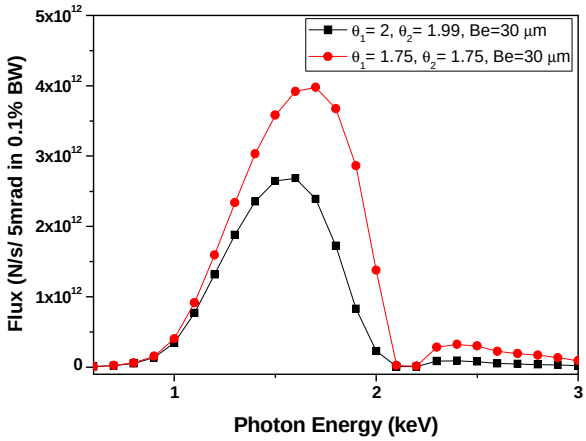

Figure 2.5 : Calculated transmission spectra for SDXRL beamline in SXRL mode.

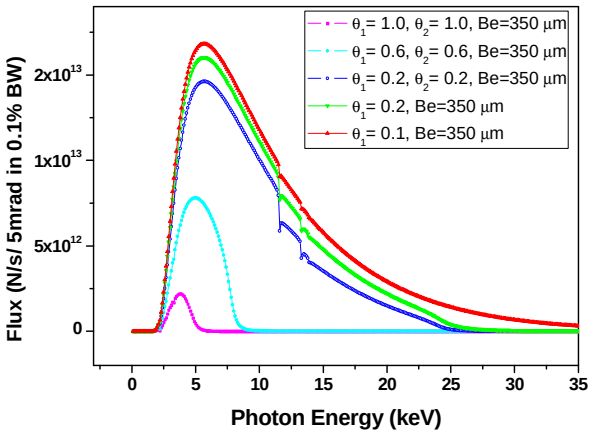

Figure 2. 6 : Calculated transmission spectra of SDXRL beamline in DXRL mode.

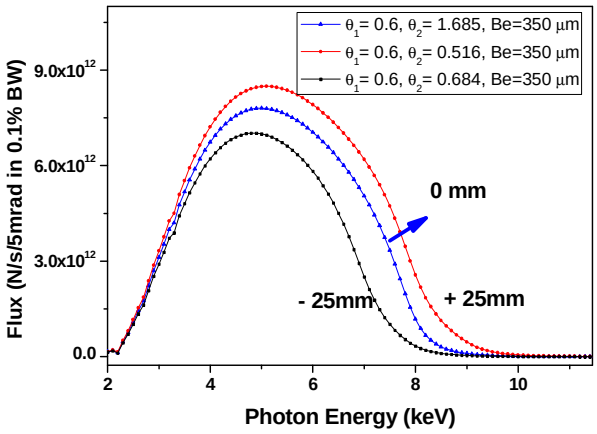

Figure 2. 7 : Calculated transmission spectra for serial number 5 (table 2.2) for obtaining the beam at height equal to height of undeviated optic axis and ± 25 mm away from it.

Table 2. 4 : Flux density delivered by beamline after each optical element calculated combinely from XOP and RAY software tools.

Serial number (Energy range [keV])	**2 (1-2)**	**4 (2.5 – 6)**	**5 (2.5 – 9)**	**9 (2.5 – 24)**
Optical elements	**Transmitted and (absorbed) spectral power in optical elements [W]**			
Source (1-50 keV), I_R =100 mA	49.4	49.4	49.4	49.4
Entrance Be Window	43.4 (6.0)	35.3 (14.1)	35.3 (14.1)	35.3 (14.1)
Mirror 1	2.0 (41.4)	2.6(27.4)	9.9(23.6)	19.4(4.6)
Mirror 2	0.9(1.1)	0.9(1.7)	6.0(3.9)	16.6(2.8)
Exit Be window	0.5(0.4)	0.6(0.4)	4.7(1.2)	14.8(1.8)
Polyimide (50μm)	0.02(0.5)	0.4(0.2)	3.9(0.8)	13.6(1.2)
Beam area at Scanner1 [cm^2]	7.0	2.4	2.7	6.3
Beam area at Scanner2 [cm^2]	1.5	5.8	14.0	20.4
Normalized power# at Scanner2 with aperture	0.48	0.56	2.42	4.05
	Power density [W/cm^2]			
Scanner1	0.069	0.230	1.59	2.36
Scanner2 (no aperture)	0.320	0.096	0.339	0.728
Scanner2# (with aperture 10mm x 80 mm)	0.320	0.096	0.242	0.380

These calculated power and power density values are used to compare with actual power measurement carried out at SDXRL beamline's scanner2.

2.2.2.1.5 Quantification of horizontal and vertical divergence of the beam

It has been discussed earlier in this chapter, the divergence in lateral profile of the beam causes error in microfabricated structures during shadow printing process. Horizontal divergence in the beam causes the lateral magnification error also known as runout. This error is higher for patterns away from the axis of the beam. Penumbra is caused due to finite source size effect which cannot be reduced for fixed source dimensions. Both these errors put the limit on spatial resolution or CD to be achieved. The values of vertical and horizontal divergence obtained during ray tracing calculations are illustrated in table 2.5 for a few energy ranges. The run out error for present beamline is optimized to ± 1.7 mrad and

penumbra is ± 0.7 mrad in SXRL mode. At higher energies the vertical divergence of the X-ray photon energies are smaller due to smaller source divergences. The obtained vertical divergence of the beam is within the limits. The effect of the run out errors on the spatial resolution during microfabrication is discussed in section (2.2.2.1.7).

Table 2. 5 : Calculated horizontal and vertical divergence of SDXRL beamline

Serial number (energy range[keV])	**2 (1-2)**	**4 (2.5-6)**	**5(2.5-9)**	**9(2.5-24)**
Horizontal divergence [mrad]	± 1.8	± 0.1	± 0.8	± 1.4
Vertical divergence [mrad]	± 0.7	± 1.3	± 1.2	± 0.9

2.2.2.1.6 Effect of mirror movement on the beam profile

The movement of the source or the optical elements affects the performance of the beamline. Particularly, if the source/optical elements is moved beyond acceptable limits, it may vary the flux and/or its uniformity. The movements of both the mirrors are taken into consideration for simulating its effect on beam performance. The mirrors are translated from 0-1000 μm in three orthogonal axes as well as rotated between 0 and 207 arcsec (0-1 mrad) during this simulation study. The translations and rotations are considered in one directions only. The beamline configuration mentioned at serial number 2 (table 2.2) is used for simulation. In ShadowVUI/RAY, *x* and *z* are horizontal and vertical axis respectively and *y*-axis is the direction of propagation of the beam.

During simulations, no significant changes in horizontal and vertical FWHM values of beam sizes are observed. Images at scanner2 for corresponding translation and rotation are translated and rotated respectively. While translating the mirror along *x*-direction from 0 to 1000μm, the beam remains at its original location. During vertical translation i.e. along *z*-direction, the beam move up by 4 mm at mask wafer plane of scanner2 for vertical translation

of 1mm. While translating mirror in the direction of propagation of the beam (*y*-axis) there is no change observed in the shape of the image and position.

The pitch movements by ± 1 mrad moved the beam vertically by ± 8.5 mm in wafer plane. This rotation can also be seen as scanning of mirror for ± 1 mrad such that a vertical exposure field (17mm) is obtained at fixed mask-wafer stage. At higher values of grazing angle of incidence, scanning mirror does not modify the energy spectrum. While at lower grazing angle, scanning mirror by ± 1 mrad will significantly change the power and energy range. The change in energy will modify the absorbed dose, even though the size of aerial image remains constant. Therefore, it is necessary to keep fixed pitch angles to obtain uniform flux in the selected energy range. When mirror is rotated along *y*-direction; parallel to beam in clockwise direction, the image gets compressed down on right side corner and vice-versa effects are observed on the other side. During counter clockwise rotation the image suppresses down on left side corner and on right side it moves up and expands. At higher values of rotation (1 mrad), the intensity at corners increase/decrease depending on the direction of rotation. No significant change is observed in image if mirror is rotated along *z*-axis by 1 mrad. At higher values of z-axis rotation, the diagonal edge (front and back side) of the torroidal mirror will modify the edge intensity at mask-wafer plane. These simulations have helped in defining the motion and motion accuracies of the two mirrors system.

Mirror movement, or mirror misalignment will vary the incidence angles of X-rays falling on mask-wafer plane. Also manufacturing defect and tolerances in two radii of torroidal mirror may introduce the change in vertical and horizontal divergence as well as vary the collimation and the focusing conditions. In proximity lithography process, this effect introduces error in the multiple of gap distance between mask and wafer. The mirror misalignment along *x* and *z* direction should be within 100 μm whereas in *y* direction such

limitation is relaxed to 1 mm. Mirror rotation in *x*-axis should be within of 5 arcsec. While roll and yaw movement can be relaxed to 50 arcsec (0.24 mrad). Radius error in sagittal direction is assumed to be 1 % and error in meridional radius is 5 %. Controlling all this parameters pertinent to the beamline will ensure less impact on the obtained feature sizes.

2.2.2.1.7 Spatial Resolution

Minimum feature size achieved is given by relation 1.1 (reproduced here):

$$\Delta = k_1\sqrt{\lambda\left(g+\frac{z}{2}\right)}$$

In proximity lithography, spatial resolution is influenced by many factors, such as illumination system (source and beamline), the mask, the interaction of X-rays with resist material and resist development. Value of k_1 depends on design of illumination system and quality of mask. For binary mask the value of k_1 is 1.44 and for phase shifting X-ray mask, k_1 is equal to 0.65. In case of phase shifting mask, at λ = 0.8 nm, resist thickness 2 μm and for gap of 10 μm, theoretical minimum feature size $\Delta \approx 56$ nm can be obtained. By using binary X-ray mask, the theoretical achievable value is $\Delta \approx 135$ nm. For hard X-ray, though wavelength is smaller, the value of Δ in the same range or smaller is not possible. It is due to the interaction of hard X-rays with resist and high Z mask absorber layer which generates the photoelectrons blur in the shadow region. This blur is combination of Gaussian distributions of photoelectron and Auger electrons. Range of photoelectron in PMMA resist material is 56 $\lambda^{-1.75}$ [85]. Range of photoelectrons in photoresist resist at λ = 0.8 nm is 82.8 nm and at λ = 0.2 nm is 936 nm.

Another blur in shadow printing process is due to diffraction effects from edge of mask layer. Therefore the dose deposition in resist, at shadow region, is not an abrupt binary fall but is smeared. The diffraction is Fresnel type. The first maximum from the absorber edge in

the resist surface is obtained by formula $x_{max} = 1.5\ (\lambda z/2)^{0.5}$; where z is the depth in resist. For 1 μm thick resist and λ = 0.8 nm, first Fresnel peak is at 30 nm from absorber edge and for λ = 0.2 nm, x_{max} is 15 nm. However, in DXRL, where thicker resist >100 μm , x_{max} ~ 150 nm.

A geometrical property of beamline, runout error and penumbral blur also limits the lower feature size. As shown in table 2.5, the values of horizontal and vertical divergence are 1.8 mrad and 0.7 mrad respectively. For a gap distance of 10 μm, a calculated value of runout error ~18 nm for 50 mm wafer exposure and penumbral blur 7 nm will be introduced in vertical direction. Considering the contributions from all the errors, the minimum feature sizes of the order of ~150 nm can be fabricated using SDXRL beamline.

2.2.2.2 Single mirror mode

In order to further enhance the power density at mask-wafer plane, there is a provision to operate SDXRL beamline in single mirror mode and white beam mode. Either of the mirrors can be brought in the path of beam to obtain the suitable beam either in focused condition (use of M2) or only higher energy rejection (use of M1). The beamline in single mirror mode cannot be operated at grazing angles of incidence higher than 0.15° (please refer to table 2.6) for delivering the beam at scanner2 due to the finite size of the beam transporting channel (150 mm) and the height (50 mm) adjustment of exit Be window. However, for scanner1, the grazing incidence angles upto 0.4° are feasible. These higher angles are possible in case of scanner1 mask-wafer plane due to shorter distance from the mirror(s). Table 2.6 shows the possible grazing angle of incidence for mirror(s) at scanner 1 and scanner2 respectively for single mirror operation. During the exposure, the mask and wafer is required to be tilted by twice the value of mirror's grazing angle incidence to allow normal incidence of beam with

respect to mask-wafer plane. At SDXRL beamline, the single mirror mode cannot be used for SXRL operation due to non availability of higher angle of incidence.

Table 2. 6 : Summary of the possible grazing incidence angles for SDXRL beamline in single mirror operation mode at scanner1 and scanner2

Serial No	Grazing angle of incidence [°]	For scanner1		For scanner2	
		M1 (4.35 m) [mm]	M2 (3.55m)[mm]	M1 (9.3 m) [mm]	M2 (8.5m) [mm]
1	0.4	60.7	49.6	Not available	Not available
2	0.3	45.5	37.2	Not available	Not available
3	0.2	30.4	24.8	64.9	59.3
4	0.1	15.1	12.4	32.5	29.6
5	0.05	7.6	6.2	32.5	29.6

Ray tracing calculations are carried out for single mirror operation. The geometrical parameters are kept identical to those used for two mirror geometry. Figure 2.8 shows the simulation results of beamline in either using M1 (left side images) or M2 (right side images) at grazing angle of incidence ~0.2°. The beam at scanner1 and scanner2 from M1 will have no focusing effects. In case of M2, three times higher beam size in vertical direction is available with comparable photon density as obtained in case of M1. The use of M2 in this case is preferred due to better collimation condition.

The power-energy spectrum of the beamline in one mirror mode is shown in figure 2.6 for grazing incidence angles of 0.2° and 0.1°. The energy spectrum for other grazing angles of incidence will remain comparable in the shown energy range.

2.2.2.3 White beam mode

The design of SDXRL beamline allows the operation in white beam mode where it delivers flux upto ~40 keV. This mode of operation of the beamline ensures the penetration

Plane Mirror at θ_1= 0.2° **Torroidal Mirror at θ_2= 0.2°**

Footprint on mirror

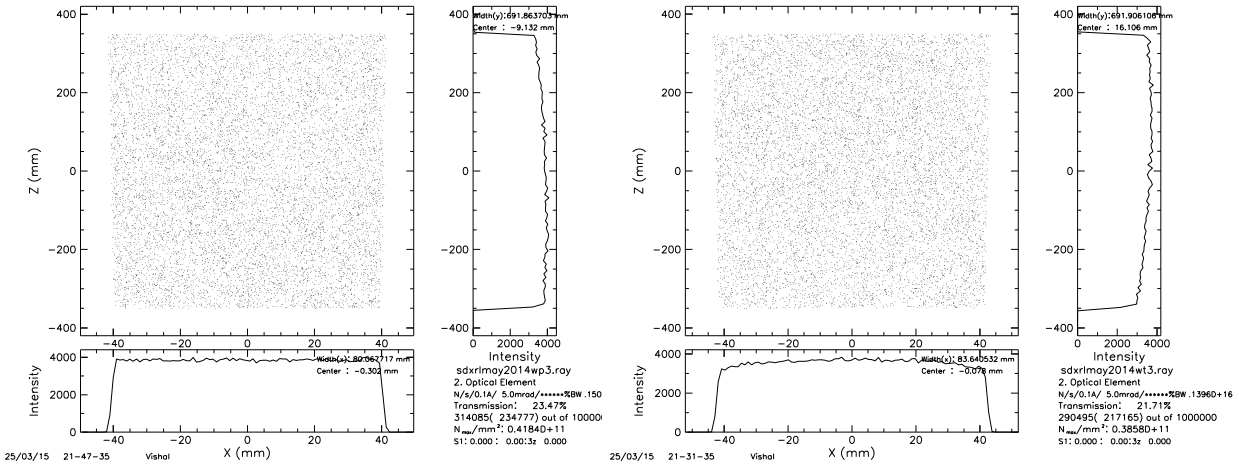

Scanner1

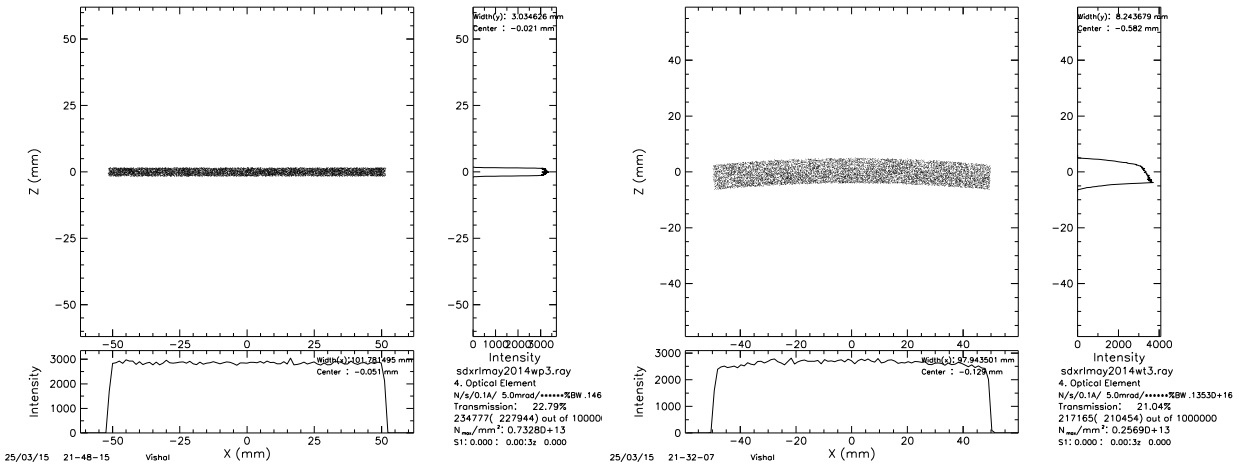

Scanner2

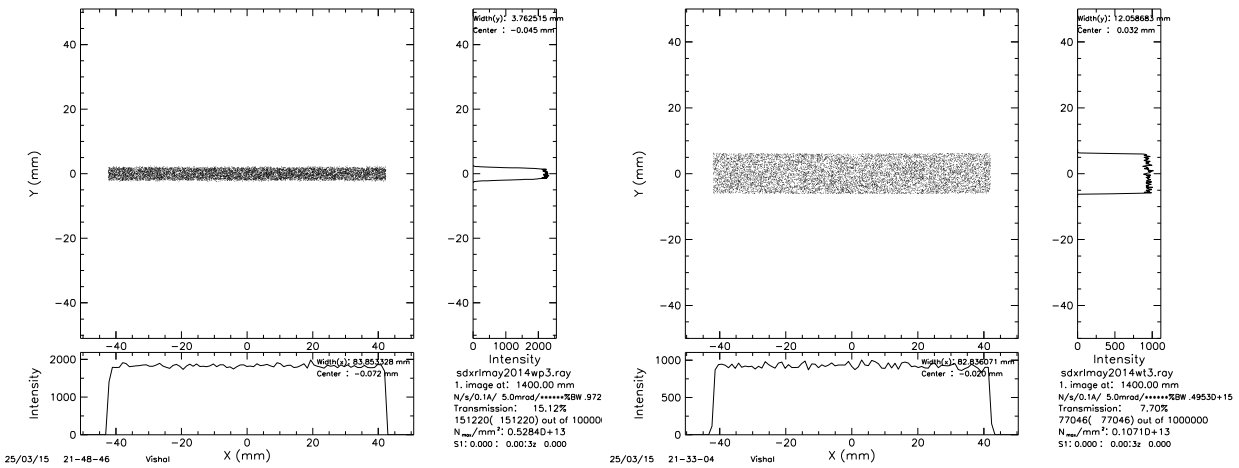

Figure 2. 8 : Point diagram of the images at mirror, scanner1 and scanner2 in case of single mirror operation and grazing angle of incidence 0.2°.

of X-ray into 5-10 mm thick photoresist for producing microstructure. The dose at top of the PMMA can quickly reach beyond the damaging values for thicker resist (please refer to table 3.10). Therefore it is necessary to remove the low energy photon from the spectrum using suitable filters. The preferred filter materials are Be, Al, Kapton and Graphite. Figure 2.9 shows the transmitted energy power spectrum at scanner2 mask wafer plane in white beam mode as function of Be window thickness. Size of the beam at scanner1 or scanner2 will depend on SR source divergence and simulated dimensions of the beam at scanner2 are shown in figure 2.10.

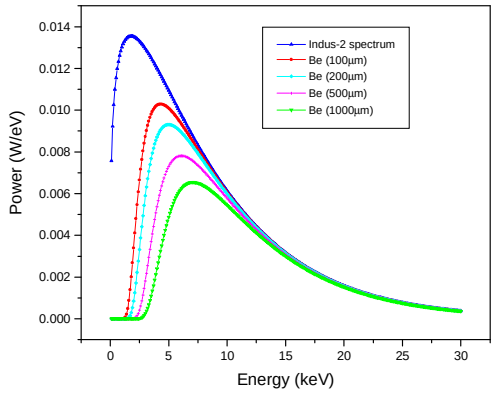

Figure 2. 9 : Power spectrum of Indus-2 for no reflection optics and various Be-window thicknesses at scanner2.

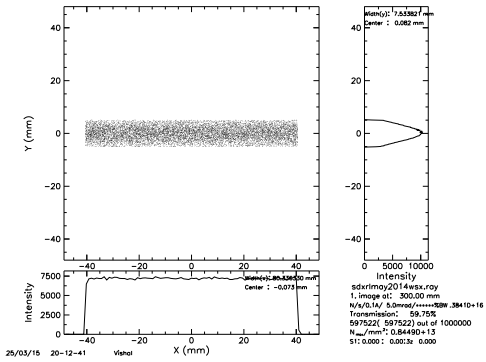

Figure 2. 10 : Spot diagram of the white beam observed at scanner1. Only two Be filters of thickness 175 μm and aperture of Be window is considered.

The white beam is useful for carrying out X-ray lithography exposure in very thick resist. SDXRL beamline in this case is similar to the DXRL beamline operation at Elettra with white beam mode [25]. Apart from the normal use in XRL, beamline can also be used for carrying out certain optics test and calibration measurements. The performance of newly developed X-ray optics can be tested at SDXRL beamline using white beam before their actual deployment.

2.3. Instrumentation for SDXRL beamline

Various SR beamline instrumentations are carried out in this thesis during the development of SDXRL beamline. Key components of the beamline include diagnostic system, two mirrors system, scanner1 and scanner2. All of these instruments are custom designed and developed components for fabrication of HAR microstructures are highlighted here.

2.3.1 Diagnostic devices

SR beam profile and its position is required during the normal operation of the beamline. Various diagnostics devices like beam position monitors, phosphor screen, wire probe scanner, photodiode and ionization chambers are used in the beamlines. Non-invasive blade type X-ray beam position monitor (XBPM) to monitor changes in source position and wire probe scanner(WPS) for obtaining beam profile during the operation of the beamline are developed as part of this thesis.

2.3.1.1 X-ray beam position monitor

The XBPM is based on the concept of staggered pair metal blade type monitor which gives online calibration for beam position measurements independent of quantum efficiency degradation [86]. The XBPM consists of a water cooled detector block on which four detector blades are mounted in vertical orientation in such a way that individual blade intercepts the tail of Gaussian SR beam in vertical direction (figure 2.11). The detector blades are made of 2 mm thick Cu [87]. The electrical connections of individual blades are isolated from each other and detector block. However, they are thermally connected with each other. The principle of XBPM and scheme of staggering and orientation of blades is shown in

Figure 2.11 (a, b) respectively. The actual fabricated XBPM (view from downstream beam direction) is shown in figure 2.11 (c).

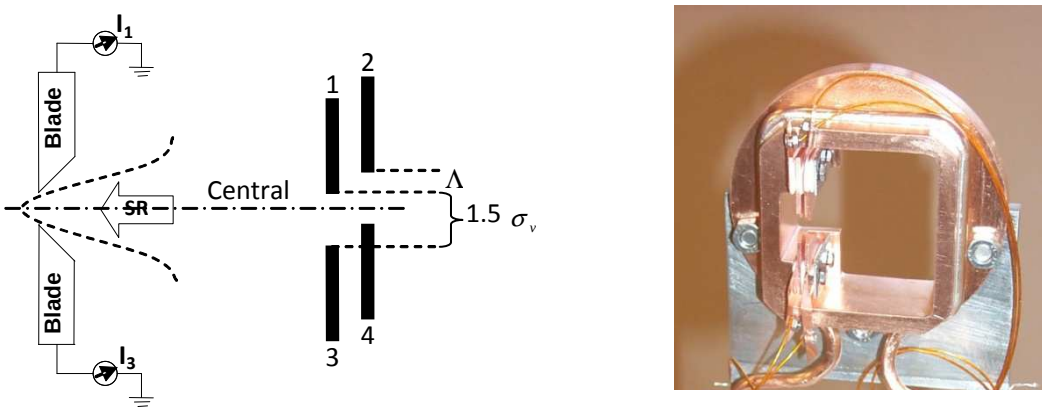

(a) (b) (c)

Figure 2. 11 : (a) XBPM based on photoelectric effect (b) detector blades are staggered and kept at known distances from central beam axis and (c) back view of fabricated XBPM .

Detector blades (blades 1, 3 and blades 2, 4) are vertically separated with each other by maintaining gap of $\pm 1.5\sigma_v$ where σ_v is vertical divergence (mrad) of X-rays. Value of σ_v is calculated for 1 keV X-ray energy where significant quantum efficiency is obtained due to 2p and 3p electrons of Cu [88]. Both the pairs of detector blades are staggered by an offset distance (Λ) of 1 mm in vertical direction. A theodolite system is used for initial alignment of distances between detector blades. The vertical gap ($\pm 1.5\sigma_v$) between the blade 1 and 3 (2 and 4) is found to be 3.8 mm at 5 m from the source and both pairs of metal blades are staggered by 1 mm. The accuracy of the alignment is ~ 50 μm. The XBPM assembly is housed inside the ultra high vacuum chamber.

The photoelectric effect produces an equal photo current in each detector blade if the beam is centred with respect to detector blades. Asymmetry in photocurrent is linearly dependent on beam position in dynamic region of XBPM. Staggered pair XBPM design allows

measurement of vertical beam position using online calibration factor. The formalism for calculating vertical beam position, $Y_{A1/3}$ and $Y_{A2/4}$ (in mm) is given by:

$$A_{1/3} = \frac{I_1 - I_3}{I_1 + I_3}\,;\; A_{2/4} = \frac{I_2 - I_4}{I_2 + I_4} \tag{2.10}$$

$$Y_{A1/3} = k_{ocf} A_{1/3} + \Lambda \tag{2.11}$$

$$Y_{A2/4} = k_{ocf} A_{2/4} - \Lambda \tag{2.12}$$

where I_1, I_2, I_3, and I_4 are the photo-currents produced in the metal detector blades 1 to 4 respectively, $A_{1/3}$ and $A_{2/4}$ are the asymmetries in the current from respective pair of detector blades and k_{ocf} is the online calibration factor given by:

$$k_{ocf} = \frac{2\Lambda}{A_{1/3} + A_{2/4}} \tag{2.13}$$

The photo currents are measured using a low current amplifier (LCAD4 synchrostar, Frank Optics [89]). All the detector blades are kept at negative potential to reduce cross talk between them.

XBPM is calibrated using two schemes, (1) vertically scanning the XBPM in the direction in stationary path of the SR beam [90] and (2) keeping XBPM position fixed, and giving controlled bump to electron beam by vertical steering coils [91].

Scanning XBPM

The XBPM assembly is scanned in vertical direction with step size of 125 µm using motorized vertical jack. Beam position is measured as a function of vertical movement of XBPM. The position values obtained from asymmetries $A_{1/3}$ and $A_{2/4}$ are identical. The linear beam position response from the XBPM vertical stage displacement (the XBPM dynamic range) is around 1.5 mm.

Electron beam bump

In second calibration method, asymmetric bump in steps of 10 μrad is generated on electron beam and shift in SR beam position is measured. Theoretical beam position values are calculated using simple arithmetic multiplication of amount of asymmetric bump given to e-beam and a distance (4.95 m) at which XBPM is installed. The average value of 49.4 μm is obtained for two measured position difference induced by incremental electron bump steps of 10 μrad which matches well with calculated average value of 49.5 μm.

The developed XBPM is used for recording the day to day stability of Indus-2 beam. One of the stability data is shown in figure 2.12 where Indus-2 beam stability of 9 μm is obtained during e-beam storage condition.

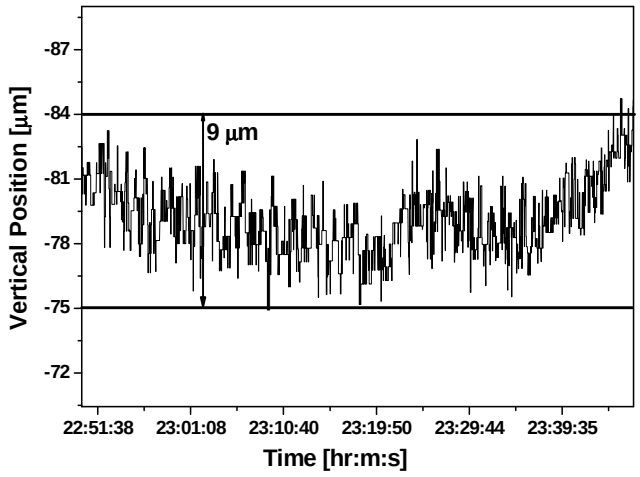

Figure 2. 12 : Indus-2 beam stability recorded by XBPM.

2.3.1.2 Wire probe scanner (WPS)

WPS is second diagnostic system developed in this thesis. It consist of UHV compatible motorized vacuum feedthrough for the movement of an electrically insulated block where gold wire of 60 μm diameter, is tightened between two spring legs made of stainless steel.

The WPS is scanned in beam in the vertical direction to obtain its profile. Figure 2.13 shows the schematic of the wire probe scanner used in SDXRL beamline.

This instrument is helpful for online estimation of change in flux coming from two mirrors system. The amount of photocurrent produced is proportional to the flux and is helpful to correlate with the flux falling on the resist during exposure. With proper calibration, WPS is helpful to indicate change in the beam position after two mirror system. Use of WPS is beneficial during alignment of two mirrors. In-situ precision angle measurement with an accuracy of 20 μrad is also possible with the help of WPS. The detailed discussion on how this instrument used for alignment is given in section 2.3.2.1 for mirror alignment and section 2.4.2 for correlating with power measurements.

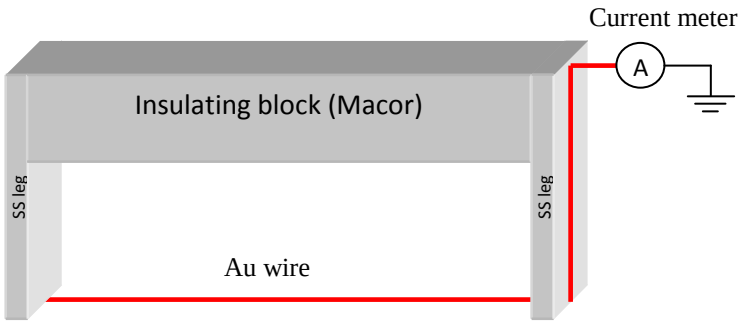

Figure 2. 13 : Schematic of wire probe scanner, Au wire is installed between two SS legs.

2.3.2 X-ray mirror system

X-ray mirror system is the heart of the SDXRL beamline. The technical specifications of two X-ray mirrors used in two x-ray mirror system of SDXRL beamline are given in table 2.7.

Figure 2.14 shows the engineering drawing of two mirrors system. The first mirror reflects the beam downward and second mirror bounces the beam in upward direction. Both X-ray mirrors are placed inside 2 m long stainless steel vacuum vessel with side cooling provisions.

Table 2. 7 : Technical specifications of X-ray mirrors used in SDXRL beamline

Parameters	**Mirror (M1)**	**Mirror (M2)**
Clear aperture [mm]	650 x 90 with ± 5 tolerance	650 x 90 with ± 5 tolerance
Geometrical area [mm]	700 x 110 with ± 5 tolerance	700 x 110 with ± 5 tolerance
Distance from tangent point [m]	16.2	17
Beam acceptance [mrad]	5 (H) x 0.83 (V) i.e. 4 σ_v at 1.5 keV	5 (H) x 0.83 (V) i.e. 4 σ_v at 1.5 keV
Mirror surface (shape)	Plane	Torroidal
Mirror radii [m]	Meridional (R) = ∞ (≥30000), Sagittal (r) = ∞ (≥1000)	Meridional (R) = 420 (±3%), Sagittal (r) = 0.57(±1%)
Compatibility for grazing angle of incidence [°]	0 to 2.0 (variable)	0 to 2.0 (variable)
Cooling option	Side cooled	Side cooled
Maximum power absorbed [W]	186	14
Power density [mW/mm^2]	7.97	0.323
Mirror substrate material	Silicon	Silicon
Optical coating (thickness [Å])	Pt (~500)	Pt (~500)
Mirror substrate thickness [mm]	50	50
Mirror orientation	Deflecting the beam vertically downward	Deflecting the beam vertically upward
Roughness [Å]	≤ 5	≤ 5
Slope error [μrad]	25 (Sagittal) x 5 (Meridional)	25 (Sagittal) x 5 (Meridional)

The optical surfaces of both the mirrors are protected with a water cooled fixed mask at front edge facing to the beam against high heat load from source. Any change in temperature at the mirror surface or upfront fixed mask is recorded by K type thermocouple. Each mirror is mounted on the base plate which is then kinematically coupled with three linear actuators. Two actuators holds the base plate, are located on the up-stream side and one of them is located on the downstream side. The distance between the linear actuators along beam direction is 600 mm. These three linear actuators provide the manipulation of a mirror to obtain suitable height and grazing angle of incidence with respect to beam. These actuators

are vacuum compatible and have a movement resolution of 1 μm and different strokes for M1 and M2 in vertical direction. The rigidity to whole mirror system is provided by the synthetic granite table with vibration damper. The mounting of mirror system is tested against any ground vibrations upto frequencies of 100 Hz and is found stable.

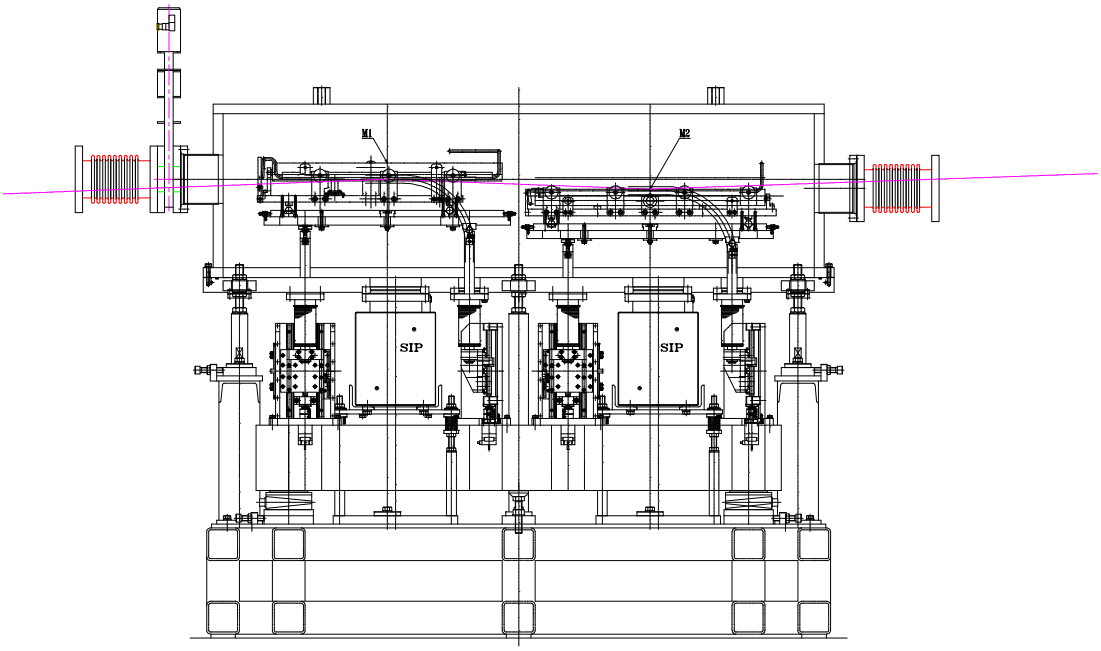

Figure 2. 14 : Engineering design of two mirrors system

The requirement of range, resolution and repeatability of the mirror system in angular and translation degrees of freedom are given in table 2.8. The design of the mirror manipulator system is such that there is minimum cross linkage in pitch-roll-yaw movements of X-ray mirrors. All mirror manipulations are operated through a LabVIEW platform.

The mirror manipulator system's range, resolution and repeatability for M1 and M2 are measured at Indus-2 using Renishaw ML10 laser system with linear and angular measurements capabilities. In the test setup, ML10 Renishaw interferometer with laser source mounted on a tripod and retro-reflector optics is fitted on the moving object (M1 and M2). By

using the path length measuring interferometer principle, this laser interferometer can be used to measure an angle up to ± 10° with a resolution of 0.05 arcsec. The accuracy of the measurement is ± 0.2 % of the displayed value. The error in the measurement is dependent on measurement environment including pressure, ambient temperature and humidity level. The measured range, resolution and accuracies are described in the table 2.8 against each design specified values. The measured value of pitch (rotation in *x*-axis) angles for M1 and M2 is found to be 0.97 and 0.67 arcsec respectively against the specified value of 1 arcsec. The roll angles (rotation in *z*-axis) accuracies are also measured for M1 and M2 and obtained results is less than the specified values. Similarly, crosstalk between the pitch rotation on roll or yaw, roll rotation on pitch and yaw for both the mirrors are measured. The crosstalk between all angular rotations is found less than 10 arcsec.

Table 2. 8 : Overview of the measurements and technical specification of all degree of freedoms for two X-ray mirror system

Direction	**Range**	**Resolution**		**Reproducibility**	
		Specified	**Measured**	**Specified**	**Measured**
Translation					
z -axis (vertical) for M1 [mm]	20	0.001	0.001	0.002	0.001
z -axis (vertical) for M2 [mm]	70	0.001	0.001	0.002	0.001
Angular					
Pitch (*x*-axis) for M1 [arcsec]	7200	1	0.5	1	0.97
Roll (*y*-axis) for M1 [arcsec]	± 3600	5	1.0	5	4.16
Pitch (*x*-axis) for M2 [arcsec]	7200	1	0.5	1	0.67
Roll (*y*-axis) for M2 [arcsec]	± 3600	5	1	5	2.31

2.3.2.1 Alignment of the mirrors

Reproducible alignment of the mirror system is crucial for efficient operation of beamline. It is difficult to align the mirror in the vacuum chamber at desired target positions and angles. The images obtained on florescence screen at mask-wafer plane have been used for mirror

alignment but this procedure is not precise. A novel in-situ, online technique is proposed in this thesis for quick alignment of the two mirrors system to obtain appropriate beam size (energy range) at the X-ray scanner(s). During installation, significant efforts were made to align the mirror system within 50 μm, with respect to plane of electron orbit. This referencing helps towards easy and quick setting up of mirrors in different beamline operation modes using reproducible vertical position and angular movement. WPS helps in estimation of mirror vertical position and angles. It is installed 1 m downstream to M2 and measures the beam profile with 10 μm repeatability. This ensures the angular placing of mirror(s) at an accuracy of 10 μrad (~2 arc sec) which is far better than using phosphor screen. At the start of the alignment, both mirrors are moved out of beam path and vertical slit is opened. WPS is used to determine beam profile and beam position of SR beam. If the beam position is at its known centre (~1400mm from experimental floor) then the height of the first mirror is fixed to 'zero'. Now referring to table 2.2 and beam height required at scanner2, appropriate M1 and M2 angles and corresponding M2 height are set. During these processes, beam profile using WPS is taken for each change (angle and height of the mirrors) and compared with standardized results. Every scan measurement provides the beam profile at each instant of alignment and helps in quick and precise alignment. Any variation in the beam profile from standardized profile hints at the revision of alignment by either changing the mirror angle or mirror height. Once both the mirrors are set at their respective height and value of grazing angles of incidence, a final wire scan is taken. The relationship between the photocurrent from WPS and mirror configuration is determined and any offset parameter to manipulate the mirror to its desired position/angle is derived. During the exposure of resist, the change in the wire scan profile/photocurrent provides information on change in mirror alignment due to change in source position or emission angle. This alignment procedure is

simple and efficient. The alignment of two mirror system for energy change in SDXRL beamline can be done in ~20 minutes.

2.3.3 X-ray exposure station or X-ray scanner

The SR beam has wider size in horizontal direction (~100 mm) and smaller in vertical direction (5-10 mm) at SDXRL beamline. The extent of vertical beam is insufficient to expose the ϕ 50-100 mm wafer. The enlargement of X-ray beam on mask-wafer plane can be obtained by using either oscillating mirror or wobbling electron beam in storage ring or using X-ray scanner. The generation of instability in the electron beam position is not desirable in multi user synchrotron facilities. The dedicated machines like Aurora-2S or Super-ALIS can be used for enlargement of beam by disturbing the electron beam in storage ring. The distance between the oscillating mirror and mask-wafer plane should be smaller to reduce the complexities in beam enlargement system. The simplest vertical enlargement scheme of SR beam is vertical scanning of mask-wafer in stationary SR beam.

In Indus-2 SDXRL beamline, an X-ray scanner is employed for scanning mask-wafer in SR beam. As highlighted earlier, the beamline is equipped with two X-ray scanners for conducting X-ray exposure either in air, vacuum or He atmosphere. In X-ray scanner, known frequency of vertical scanning of samples in the stationary path of the beam is introduced in order to impart the pre determined X-ray exposure dose to the resist. Scanner1 is installed at 20.56 m in experimental hutch1 and scanner2 is installed in experimental hutch2 at 25.5 m away from source point.

Scanner1 has a vertical scanning stage (shown in figure 2.15) with a possibility of mounting multiple samples during single exposure. Scanner1 has a movement range of 300 mm and samples of length ~ 260 mm can be exposed in X-ray beam. With ease of handling samples in air, samples viz., X-ray resists, radiochromic films, chemical solutions and

biological samples can be X-ray irradiated. Scanner1 can also be equipped with additional stages where the independent movement of mask and substrate is feasible. These additional stages give the freedom to move mask and wafers independently to tailor the X-ray exposure dose in 3-D. Such scheme has been used previously for fabrication of 3D microstructures using X-ray lithography [92]. Scanner1 stage is modified to accept the independent movement of mask and resist. This stage assembly is developed for fabrication of various 3-D featured profiles [93].

Scanner2 consists of vertical scanning stages, rotation and tilt module, water cooled mask-wafer mounting base plate and water cooled apertures housed inside vacuum chamber, vacuum system for evacuation, control system to control the entire scanner system and IR camera to record online temperature of resist and mask. The X-ray mask-wafer assembly for X-ray exposure is made up of 4 stages, two vertical scanning stages, mask-wafer tilt stage and mask-wafer rotation stage. Figure 2.16 shows the inside view of X-ray scanner2 and position where X-ray mask and wafers are mounted. A goniometer with tilt arm and rotation stage moves on two guided vertical scanning stages actuated by two synchronized stepping motors. The major parameters of scanner2 are illustrated in table 2.9. The complete stroke of scanning stage is ± 90 mm with speed and acceleration controllable between 1-30 mm/s and 1-600 cm/s^2 respectively. The variable scanning speed controls the time spent by resist during single pass, especially to reduce the thermal degradation of resist at higher electron beam current. X-ray mask and wafer upto 100 x 100 mm^2 in square or circles upto 100 mm diameter fits on mask-wafer mounting assembly. This assembly rotates by 360° and tilts between 0-90°. This feature is used for creating tapered or interwoven non-traditional (3-D) structures. The tilt stage also helps the easy loading and unloading of mask and wafer. The wafer and mask is sandwich between water cooled mask-wafer assembly stage embedded with magnet and matching MS button annular ring. The mask and substrate are also fixed

mechanically. An offline mask-wafer alignment stage with 300X stereo zoom microscope is also developed for mask-wafer alignment. This system helps to carry out multi level, multiple exposures by aligning the alignment marks of the wafer and X-ray mask. The use of optical microscope limits the alignment only in optically transparent X-ray mask.

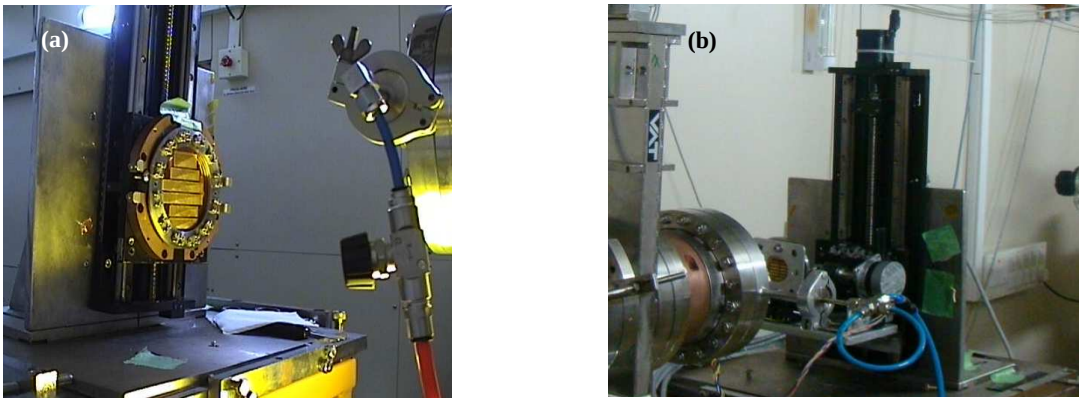

Figure 2. 15 : Air based X-ray scanner with (a) mounted condition of X-ray mask and wafer (b) modified stage to create the 3-D microstructures.

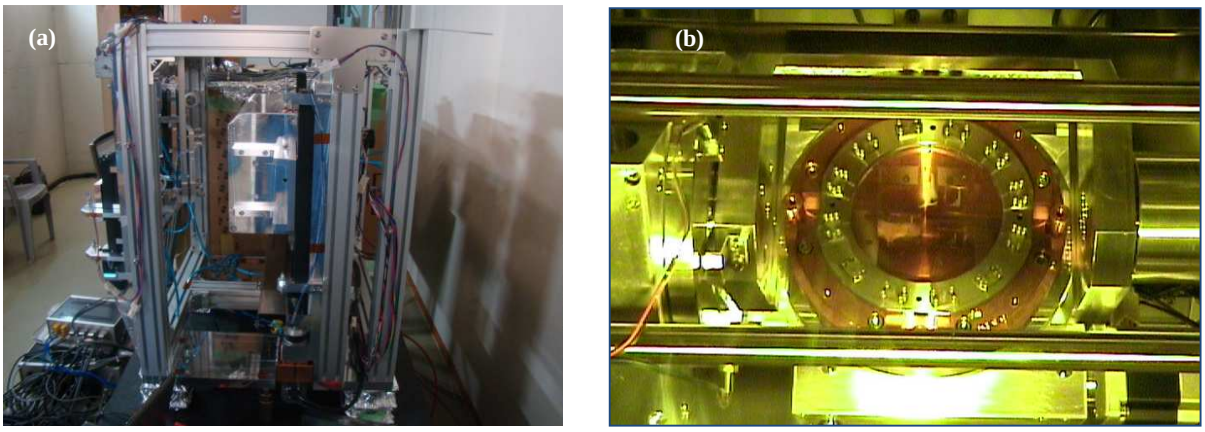

Figure 2. 16 : (a) Internal view of X-ray scanner and (b) the mounting view of X-ray mask and wafer.

In scanner2, exposures are performed in vacuum and Helium atmosphere. Due to large volume of vacuum vessel (~1000 litres), evacuation is done using combination of dry pump

(make: ULVAC, LR 60) and mechanical booster pump (make: ULVAC, PMB 001CM). Pump down time to 4 $x10^{-2}$ mbar is ~10 minutes. Higher vacuum, if required, can be achieved by using the turbo molecular pump. Helium gas can be introduced at partial pressure of 100 mbar in the chamber for cooling the mask and wafer. A high temperature setup is added to scanner2 for maintaining the resist at elevated temperatures. This attachment is used for direct etching of PTFE using SR.

Table 2. 9 : Salient features of X-ray scanner2 of SDXRL beamline.

Name/parameters	**Design specifications**	**Measured /Achieved parameters**
Exposure window	± 90 mm (V), ± 40 mm (H)	± 90 mm (V), ± 50 mm (H)
Exposure Environment	Vacuum, Helium and Air	Achieved vacuum = 1x 10^{-2} mbar He partial pressure = 100 mbar
Mask-Resist Size	Circular ϕ 100 mm and Square 100 x 100 mm^2	From 5 x 5 mm^2 to 100 x 100 mm^2 and Circular ϕ 100 mm
Resist thickness	1-5000 μm or higher	Upto 6000 μm
Mask-wafer tilt and rotation	tilt 0-90° and rotation ± 180°	tilt 0-90° and rotation ± 180° (with resolution of 0.01°)
Gap between mask and resist	0-100 μm	Hard contact to 1000 μm
Speed	1-30 mm/s	Upto 30 mm/s ± 0.5 %
Acceleration	1-650 mm/s^2	1-650mm/s^2
Resting time	30 msec-1 sec	30 msec-1 sec
Offline alignment stage	Alignment accuracy between mask and resist is < 5 μm.	2-5 μm

Scanner is equipped with two cameras, (1) IR camera (NEC 6400) for in-situ recording of change in temperature of the X-ray mask or wafer and (2) IP based surveillance camera (AXIS PTZ 214, Axis communication) to monitor the mask-wafer stage movement during the exposure. X-ray scanner stages are controlled through USB interface. Control software is in LabVIEW. The real time information on set exposure parameters, scan speed, number of scan remaining, time to finish scans, inside view of the exposure station is available on the PC. The range, resolution and repeatability of all degrees of freedom of scanner2 are

measured. The scan speed, scan acceleration, resting time, angular resolution for tilt and rotation stages are measured using Renishaw laser interferometer system as described in case of X-ray mirror system. The measured values are given in the table 2.9 against the designed values.

2.4 Commissioning of the beamline

The beamline is installed on BL-07 port of Indus-2. Engineering layout of the beamline is shown in figure 2.17. The beamline is divided into three parts, frontend, X-ray optics and experimental stations. The frontend of this beamline is situated within the shielding tunnel and comprises of beam absorber, fast shutter, Bremsstrahlung safety shutter, primary slits, entrance Be-window and other UHV components [94, 95, 96] are not shown here. The beamline optics is installed in the optics hutch and scanner1 and scanner2 is installed in experimental hutch1 and experimental hutch2. All hutches are made of 1 mm Pb sheet sandwiched between two CRCA mild steel sheets of thickness 1.2 mm and 0.9 mm. Beamline is installed with two Beryllium windows of 175 μm thickness. It should be pointed here that the low energy beam (serial no 1, 2 of table 2.2) is not characterised in this thesis and neither used for X-ray lithography in SDXRL beamline. The use of low X-ray energy is feasible only after the availability of e-beam pattern generator produced X-ray mask and optimization of windowless operation of Indus-2 beamlines.

The installations of the beamline are carried out between May 2009 and April 2011. Hot commissioning of beamline has begun in the November 2010. The first light in the beamline was observed in air through entrance Be window on November 18, 2010 and first test structure was obtained on February 19, 2011. In following section, the performance results of the beamline during commissioning are presented.

2.4.1 Beam size and intensity profile

Characterization of the beam shape, size and intensity gives an idea about the performance of the beamline. In these measurements, phosphor screens at various places (scanner1, scanner2), wire probe scanner and X-ray sensitive photodiode mounted on x-y stage are used. Due to ease in handling photodiode and phosphor screen, X-ray beam is first characterized at scanner1 mask-wafer plane and measured performance of the beamline can be extended to scanner2 mask-wafer plane. The mirrors are aligned as per the scheme mentioned in section 2.3.2.1.

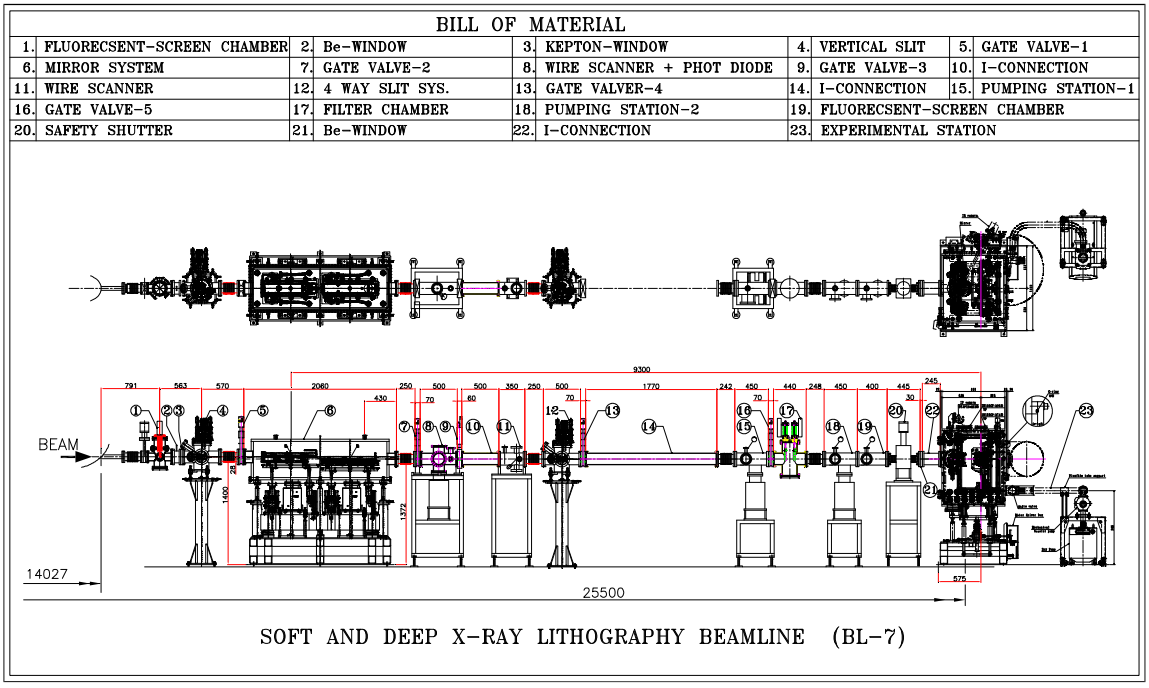

Figure 2. 17 : Engineering layout of SDXRL beamline

In two mirrors mode of operation, the highest power is available for grazing incidence angles ~ 0.1°. In a typical beamline operating condition when both the mirrors are set at 0.6°, a pink energy spectrum between 2.5 and 9 keV is obtained. A point diagram of beam at

scanner1 position simulated using “RAY” ray tracing software for this setting is shown in figure 2.18 (a). The size of the beam is 2.5 (V) and 70 (H) mm^2. The characteristics smile curve of the image is due to shape of torroidal mirror. The actual beam is recorded using radiochromic film. Beam impression on radiochromic film is measured using vernier (2.5 (V) and 68 mm^2 (H)) and correlated one to one with calculated beam size and is shown in figure 2.18 (b). The beam sizes mentioned here are different from the sizes shown in figure 2.4 (Rd) due to the smaller horizontal acceptance of the beamline than designed. This is due to error in size of fixed mask installed at BL-07 frontend which provides 4 mrad instead of its design value of 5 mrad. The vertical beam profile with horizontal integrated beam is measured using WPS with a minimum step size of 100 μm. Figure 2.19 shows the calculated beam profile and measured beam profile at 18 m from the source. The measured beam profile reasonably matches with the calculated profile curve.

A high quality microstructure with uniform depth on wafer is dependent on the dose uniformity at mask-wafer plane. Intensity variation in horizontal direction of ~ ± 12 % for two toroidal mirror geometry has been reported earlier and was reduced to ± 4 % using appropriate X-ray compensation filter [97]. In present case, calculated horizontal uniform intensity for two mirror geometry (2.5- 9 keV spectral band) is ± 5 %. The horizontal uniform intensity at scanner1 is measured with the help of X-ray sensitive photodiode (AXUV 100). The intensity (vertical integrated) is measured by placing the 1 mm slit in front of photodiode and scanning photodiode in horizontal direction with incremental step of 1 mm. The measured and calculated horizontal intensity distribution is shown in figure 2.20. The measured peak variation of intensity in the horizontal direction is ± 7% which is close to calculated value. The glitches in horizontal intensity are due to surface figure errors in M2. The higher non-uniformity in horizontal intensity uniformity can also be attributed to heavy

element impurities in Be foil and change in SR beam position due to electron beam drift inside storage ring. In case of beamline's designed energy (1.5 keV), the calculated horizontal uniform intensity is ± 3 % which could not be measured.

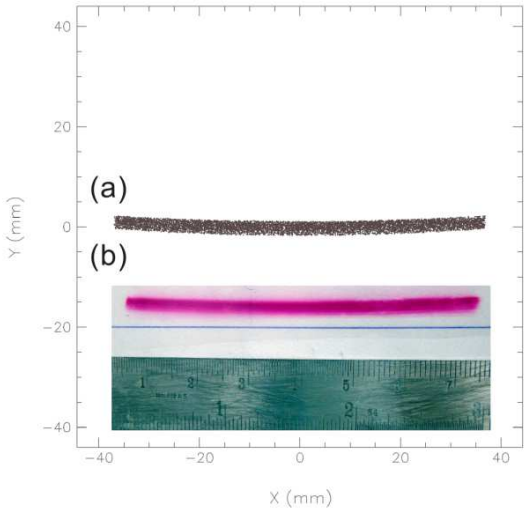

Figure 2. 18 : (a) Calculated and (b) measured beam sizes at X-ray scanner1 for 2.5-9 keV

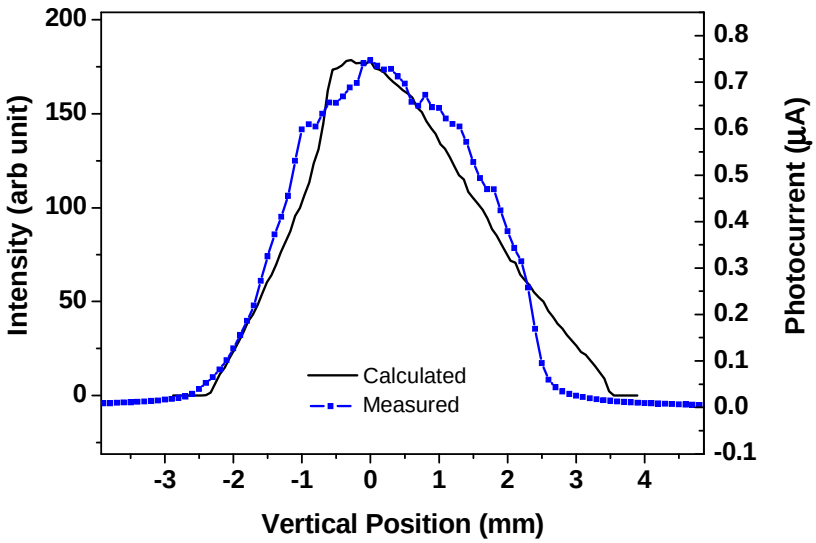

Figure 2. 19 : Calculated and measured beam profile obtained using WPS at 18 m from source.

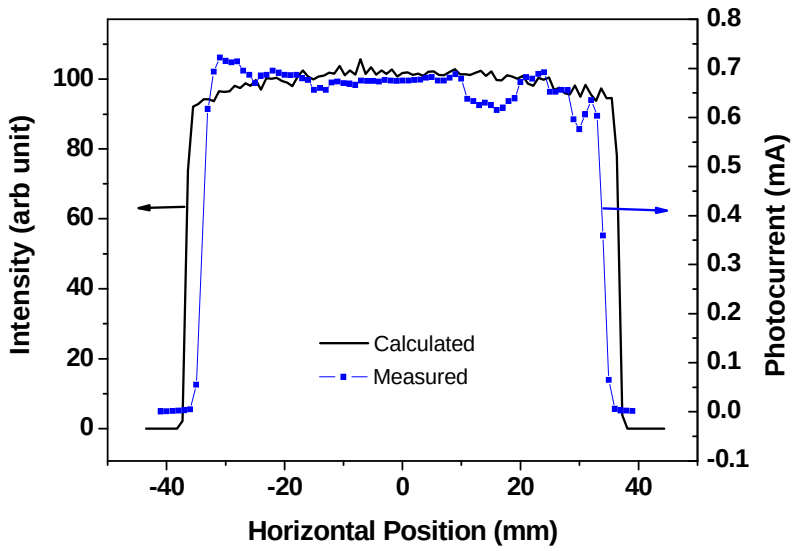

Figure 2. 20 : Horizontal intensity distribution of beam at scanner1 mask-wafer plane.

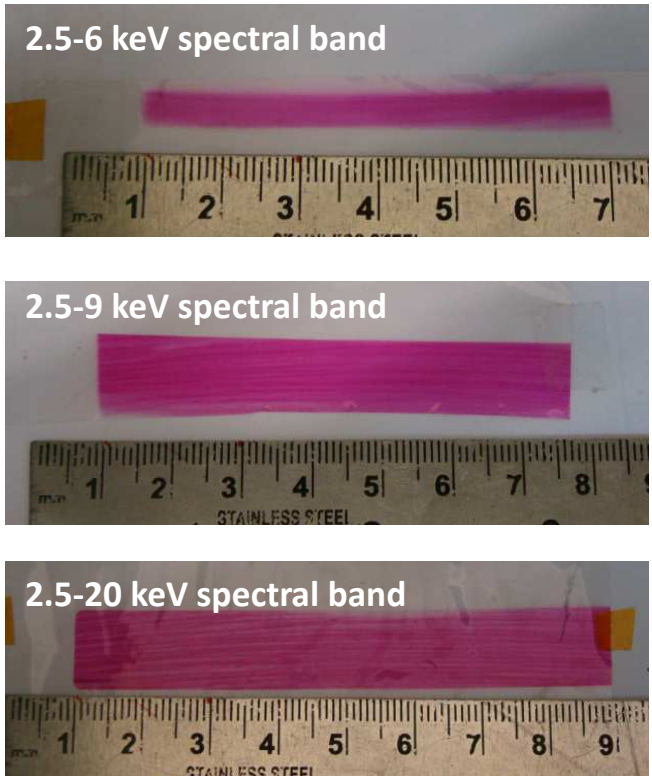

Figure 2. 21 : The profile of the X-ray beam recorded at scanner2 for various X-ray energy range.

Similarly the beam sizes in the different X-ray energy ranges are measured and compared with the ray tracing simulated sizes at scanner2. The figure 2.21 shows the beam impressions obtained on radio chromic films. The measured beam sizes are compared with their calculated values and are tabulated in table 2.10. In all cases, the measured horizontal sizes of the beam are different from the calculated. It is due to smaller horizontal beam available from frontend due to reduced aperture. If horizontal acceptance of 4 mrad instead 5 mrad is considered, then measured horizontal beam sizes matches with the calculated beam sizes. The vertical beam size at scanner2 is limited by the 10 mm vertical aperture of exit Be window. Vertical divergence of 1 mrad propagated in the beam from mirror has increased the vertical beam size by 3 mm (1.45 m is distance between exit Be window and scanner2 mask-wafer stage) in two spectral bands, 2.5-9 keV and 2.5-24 keV.

Table 2. 10 : Beam sizes, comparison between measured and calculated at scanner1 and scanner2

Energy range [keV]	**Measured beam size at scanner1, V[mm] x H [mm] (cal.)**	**Measured beam size at scanner2, V[mm] x H [mm] (cal.)**
2.5-6	3 x 60 (3 x 80)	6 x 60 (7.5 x 77)
2.5-9	3 x 68 (3 x 90)	12 x 68 (14 x 100)
2.5-24	7 x 78 (7 x 90)	12 x 80 (17 x 120)

2.4.2 Power measurement

The flux in wide X-ray spectral band for lithography beamline is measured using 20 μm pinhole and energy dispersive silicon drift detector (SDD) [74]. For SDXRL beamline, instead of measuring flux at different energies using energy dispersive detector, total power is measured using calorimetry technique and is correlated with exposure dose. A copper

calorimeter is built for these measurements. The calorimeter consists of 5 mm thick oxygen free copper which absorbs X-rays upto 40 keV. The plate is mounted on a mask wafer stage of scanner2 and thermally shielded from the cooled mask-wafer stage by thick PMMA sheet (shown in figure 2.22). The cross section of copper plate is 5 x 25 x 140 mm^3, and its weight measured using analytical balance is ~ 90.58 g. K-type thermocouple is mounted at the centre of plate back side of Cu calorimeter to measure the change in temperature.

The power measurement is carried out in X-ray energy 2.5-9 keV. The measurement is carried out twice on the same day by considering the role of all beamline optical elements and maintaining the vacuum in the X-ray scanner2 ~5 x 10^{-2} mbar. The safety shutter is opened. The temperature rise due to impinging X-ray beam is recorded with the help thermocouple at every 20 seconds. After 12 minutes the safety shutter is closed. The temperature decrease is also recorded at same rate to estimate the thermal losses of the calorimeter to the surrounding environment. The graph in figure 2.23 shows the measured time dependent temperature profile.

Initial twelve minutes of the measurement data has been differentiated in order to get the temperature increase per unit time; $\left(\frac{dT_{rise}}{dt}\right)$. The same procedure has been applied to the data of the falling temperature per unit time; $\left(\frac{dT_{fall}}{dt}\right)$. The total power deposit in Cu is estimated by equation [98].

$$P = \frac{dQ}{dt} = mc_{\mathrm{cu}}\left(\frac{dT_{rise}}{dt} - \frac{dT_{fall}}{dt}\right) \qquad (2.15)$$

where m is mass of the Cu calorimeter and c_{cu} is the specific heat of oxygen free copper is 341 J/kg/K. In this case mc_{cu} is equals to 34.87 J/K. The slope for rise in temperature with time is found to be 0.0324 ± 0.0004 K/s and slope for fall in the temperature with time (0.006 ± 0.00012 K/s) is used to correct the rising curve by accounting heat loss of the system. The total power in the calorimeter comes to 1.35 ± 0.18 W at average ring current of 74.43 mA

Figure 2. 22 : Mounted view of Cu calorimeter in Scanner2 mask-wafer stage.

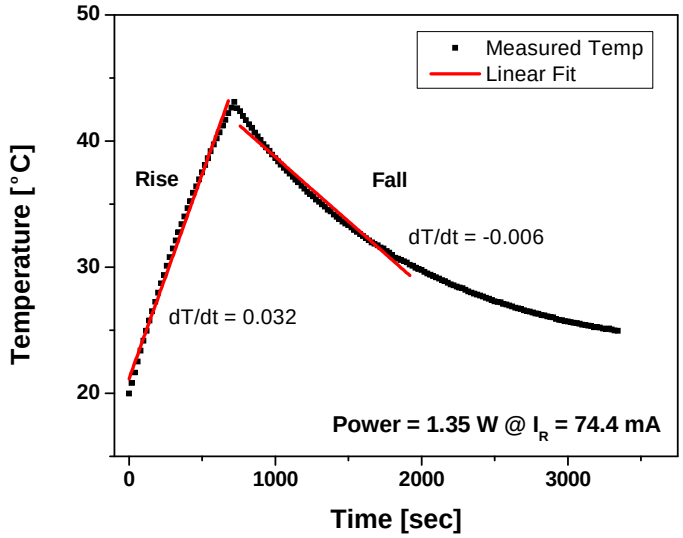

Figure 2. 23 : Temperature rise of Cu Calorimeter during exposure to the SR beam and temperature fall after closing the safety shutter.

which corresponds to 0.455 W/mrad horizontal/100 mA. The calculated value for 5 mrad is given in table 2.4 and for 1 mrad, this value comes to 0.484 W. The measured and calculated value closely match. The temperature measurement is also carried out in spectral band 2.5-6 keV and 2.5-24 keV for determining the total power. The measured value and calculated values are summarized in table 2.11. In case of low energy spectrum, the measured value is nearly half of the calculated value. The total power lost by beam due to air scattering at a pressure of 10^{-2} mbar is negligible (1 mW). Therefore, discrepancy may be due to lower

transmission of the beamline compared to the simulation and/or due to measurement errors in the present calorimeter at low power. The reasons need to be explored further. In case of high energy beam (2.5-24 keV) for all absorbers 2 x 175 µm Be, 2 mirrors, and 100% deposition 5 mrad of the beam energy in the copper shall yield a theoretical value of 4.05 W and 0.81 W/mrad. The measured power value in this energy range is 0.737 ± 0.1 W/mrad. Comparing measurements, the calorimeter has shown accuracy within 90-95% of the calculated value at SDXRL beamline for two spectral bands.

Table 2. 11 : Measured and theoretical values of the total power available at SDXRL beamline (total power is normalized for 100mA beam current)

Source : Bending magnet	**Total vertically int. power [mW/mrad/100mA]**		
Energy spectral band [keV]	2.5 - 6	2.5 - 9	2.5 - 24
Measurement using Cu calorimeter (linear fit error)	56 (± 1)	455 (± 61)	740 (± 100)
Calculated (Ref to table 2.4)	110	484	810

Online monitoring of intensity variation is essential for reliable estimation of the dose deposited in resist. A technique is proposed to observe the stability of beam or record change in the flux of source using WPS for online monitoring of change in exposure dose. Figure 2.24 shows the beam profile in terms of per mA ring current (I_R) for white beam and 2.5-24 keV. A peak current obtained in this profile is used to obtain a constant value normalized by ring current. This value is uniquely defined for particular mirror settings. These values are measured for few spectral bands and given in table 2.12. Changes in these values during exposure provide clear indication of change in flux.

Also, during power measurement, the performance of the calorimeter is correlated with this constant value measured from WPS. With change in values of determined constant can be correlated with earlier measured power and therefore is helpful to estimate the actual power absorbed in the resist. This procedure provides a good online estimation of dose rates.

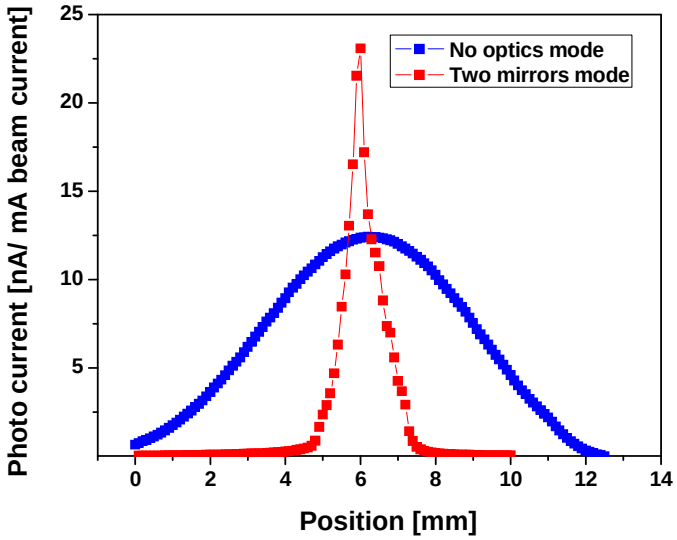

Figure 2. 24 : A typical beam profile in white beam and two mirror operation geometry.

Table 2. 12 : Calculation of ratio between the photocurrent of WPS and I_R.

Energy range [keV]	Ring Current (I_R) [mA]	Max current in the profile [nA]	Ratio [$1x10^{-6}$]
2.5-6	40	48	1.2
2.5-9	92	820	8.9
2.5-24	44.4	711	16
White beam	77	955	12.4

In conclusion, X-ray lithography facility based on two mirrors systems and two scanners has been built. The various subcomponents of the beamlines are custom designed, evaluated in terms of their optimum operation and installed at Indus-2. The beamline is commissioned and the performance results compares closely with simulated results. The total power available in different energy ranges is measured using the in-house built calorimeter. Two techniques has been proposed (1) use of WPS for quick alignment of two mirrors system (2) online monitoring of change in exposure dose/flux using WPS.

Chapter 3

Microfabrication of HAR structures in X-ray sensitive photoresist.

This chapter introduces various requirements for achieving HAR microfabrication in polymers. The various aspects of HAR microfabrication are summarised as (1) Development of X-ray mask, (2) Studying mechanism of the X-ray exposure in X-ray sensitive photoresist and (3) Development of microstructures in X-ray sensitive resist. The process of fabrication of X-ray mask and HAR microstructures are optimised for SDXRL beamline and results obtained are correlated with the reported results.

X-ray sensitive resist is generally positioned behind X-ray masks and intense, well collimated X-ray beam is used to copy the mask on the resist. The change in chemical properties of the resist depends on its tone and type of resist which is selectively dissolved in a suitable developer solution. In X-ray lithography, a unit magnification X-ray mask is critical requirement since scaling of X-ray mask onto wafer is difficult. It is important to discuss here about the properties of the X-ray mask and its fabrication before discussing HAR microfabrication using X-ray lithography. Effect of X-ray exposure on PMMA and SU-8 and their use for microfabrication is discussed in second part of this chapter.

Dedicated microfabrication laboratory is developed to carry out pre and post processing steps of X-ray microfabrication. This laboratory provide various instrumentations including UV exposure system, processing equipments for preparation of X-ray masks, spin coater, hot plates and fume hoods for handling chemicals.

3.1 Development of X-ray mask

X-ray mask is primary requirement for XRL works carried out in this thesis work. Tight tolerance X-ray masks are required for producing X-ray optical elements due to constraints of low roughness. The ideal route of mask fabrication is using e-beam pattern generator and greater details can be seen in reference [99]. The chrome coated photomasks produced using laser pattern generator and UV photolithography is used in this thesis for preparing the pattern on mask membrane. A suitable thickness of absorbing layer is grown using electrodeposition.

The engineering of X-ray mask for studies carried out in this thesis are dependent on the X-ray energy used for exposure, fabrication route and critical dimensions required on mask pattern. The general criterion used for choice of mask materials are; good X-ray transparency(> 60%), good X-ray absorption contrast (> 80-90%) due to low sensitivity of X-ray resist, good mechanical and thermal stability to sustain in high energy X-rays, high radiation resistance (~ MJ/cm^2) and compatibility to fabrication processes using UV based lithography and electrodeposition.

3.1.1 Mask membrane material

The membrane material should have low absorption and should not introduce significant scattering of incident X-ray photons. High optical transparency of membrane increases the

alignment accuracy between mask and resist. The absorption of X-rays in the high Z material patterns of the mask and in the membrane generates heat, which in turn produces temperature gradients in the mask, leading to deformation of the structures. Thus mask membrane should have good thermal conductivity. Higher Young's modulus of membrane material results in lower mask distortion. The membrane should be chemically inert, to avoid reaction during etching and mask finishing.

In first Chapter, interaction of X-ray with matter is discussed. X-ray transmission/attenuation characteristics of membrane and absorber materials can be mathematically defined by rewriting equation (1.2) as:

$$I(z) = I_0 e^{-z/l(E)} \tag{3.1}$$

I_0 incident flux, z is thickness of the membrane or absorber material and $l(E)$ is the attenuation length of material at specific energy which is inversely related to $\mu(E)$. In X-ray lithography, the wide energy ranges is used and hence the attenuation of X-ray inside material is accounted by summing attenuation lengths of all involved energies. The attenuation lengths of various mask membrane materials are computed using a web-based tool available at Center for X-ray Optics (CXRO) website [100]. Figure 3.1 (a) shows the attenuation length for photon energies upto 30 keV for reported mask membrane materials for development of X-ray masks. However, this is not exhaustive collection of data. It is observed that the attenuation length of the materials increases with increase in photon energies and at very high energy attenuation length remain same for low Z materials.

Indus-2 X-ray lithography beamline offers various photon energies spectral band for the exposures. In all such energy ranges, the choice of X-ray mask membrane material and its thickness values for transferring appropriate X-ray exposure doses are required. Figure 3.1 (b) shows the transmission of Beryllium, SU-8, Graphite, Polyimide, Silicon Nitride, and

Titanium mask membrane materials at 6.2 keV. Assuming 60 % transmission in case of DXRL process, Beryllium is one of the most suitable materials with reasonable handling thickness and desired thermal, mechanical and radiation hardness properties. However, Be is toxic and costly, which limits its extensive use as membrane material. The other reasonable choice of membrane materials are made from SU-8, Polyimide, Graphite, Silicon Nitride and Titanium. An optically transparent low cost mask can be obtained using SU-8 thin layer as membrane material which shows a good transparency to X-ray. However, optical transparency of SU-8 is lost due to absorption of very high exposure dose (> few MJ/cm^2). Polyimide, also commercially known as Kapton is better choice as it retains the optical transparency more than SU-8. These polymer based mask were earlier reported for fabrication of micro structures with reasonable precision and accuracies [101]. X-ray mask based on the Silicon Nitride and Titanium mask are very thin membrane compared to polyimide and requires careful handling while fabrication and also during X-ray exposures. Graphite masks are prepared on special grade substrate available from M/s POCO graphite. The normal graphite substrate has high porosity which makes them difficult to use as mask membrane.

In this thesis, investigation is undertaken on suitable quality of X-ray mask with low cost, fabrication feasibility, availability of materials and higher X-ray transmission. SU-8 is chemically amplified photoresist which is good proposition to use as X-ray mask membrane with better optical transmission [102]. SU-8 in polymerised form has chemical inertness towards acids and corrosive mixtures like KOH. Polyimide is generally used as dielectric material in IC industry and is easily available at reasonably low cost. The radiation resistance is very high and it can be prepared in the form of rugged thin film supported by fixture. SU-8 and Polyimide can be spin coated on the patterned gold layer and cured for polymerisation to form uniform X-ray transparent film. Table 3.1 gives the required thickness for SU-8 and

polyimide in various spectral band offered by SDXRL beamline. The thickness of 50-100 μm is easily obtained for polyimide which transmits more than 95 % of incident X-ray. It makes this material interesting due to higher transmission and more efficient for delivering exposure dose. Polyimide is already used as mask membrane in the development of X-ray mask [103]. Achenbach et. al. has compared the microstructure fabricated using polyimide and Titanium X-ray mask membranes [101].

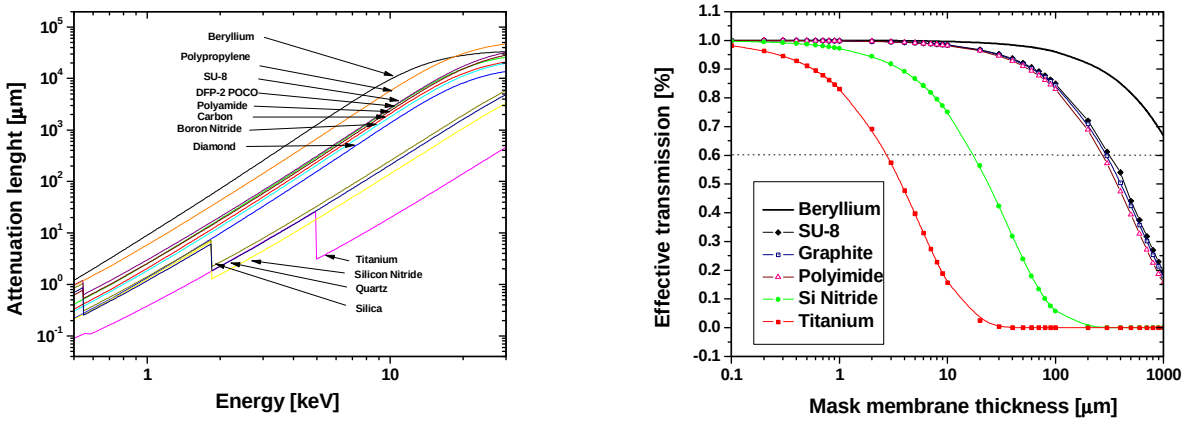

Figure 3. 1 : (a) Attenuation length of various X-ray mask membranes and (b) Transmission of 6.2 keV energy for few selected mask membrane materials.

Table 3. 1 : Mask membrane and absorber thickness for SDXRL beamline

Serial No	Spectral energy band [keV]	Energy considered for thickness calc. [keV]	Thickness for mask membrane, 60 % transmission [μm]		Thickness for mask absorber for 80 % absorption, Au [μm]
			SU-8	Polyimide	
1	1-2	2	10.6	10.6	0.75
2	2.5-6	6	280	240	2.9
3	2.5-9	9	1000	883	5.55
4	2.5-24	21	12400	11000	17.75
5	White beam	30	16000	14550	32.2

3.1.2 Mask absorbing material

High Z materials provide good attenuation of X-rays in the energy range 1-30 keV. The X-ray absorbing patterned layer on mask membrane is formed either by additive techniques (electro deposition or physical vapor deposition) or by subtractive technique (reactive ion etching or lift off). The absorber material should have low internal residual stress after deposition. Absorbers with compressive stress are preferred over tensile stress. Figure 3.2 (a) shows the attenuation length for photon energies upto 30 keV for reported mask absorber materials for development of X-ray masks. Platinum, Gold, Tantalum, Tungsten, Tin, Lead, Nickel, and Copper are suitable choice as X-ray absorbers.

Effective X-ray absorption of few selected materials at 6.2 keV as a function of material thickness is shown in figure 3.2 (b). The required thickness for Platinum, Gold, Tugnsten, Lead, and Copper mask absorber materials at 6.2 keV photon energy can be obtained by assuming 80 % absorption.

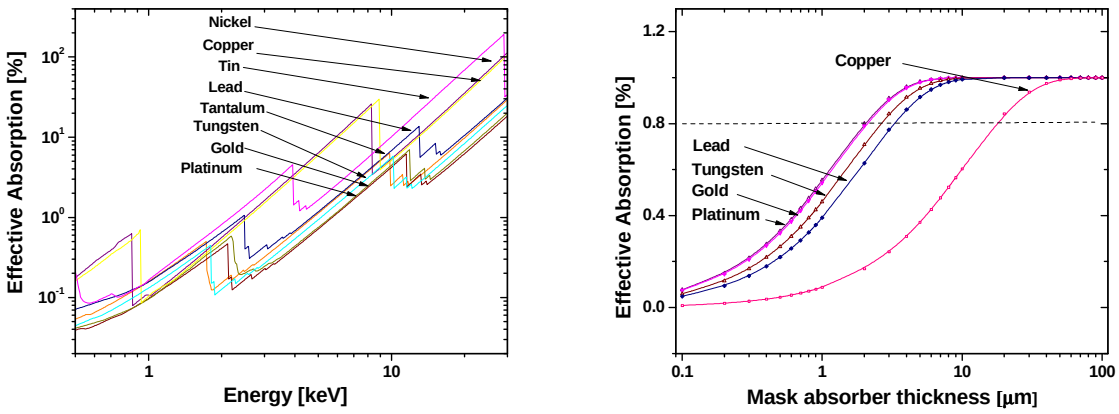

Figure 3. 2 : (a) Attenuation length for reported mask absorber materials upto 30 keV energies and (b) absorption at 6.2 keV for few selected mask absorber materials.

Materials like Nickel, Copper, Tin are easily electroplated. However, their higher attenuation length imposes the requirement of high absorbing layer thickness to obtain sufficient contrast during X-ray exposures. The contrast is defined as the ratio of the exposure dose obtained on the resist layer with and without mask absorbing material. For example, a 100 μm thick Copper is required to absorb > 95 % 20 keV X-rays. Usage of materials with long attenuation lengths adds another level of complexities during mask fabrication process by introducing the requirement of higher thickness photoresist. This type of material can be used for fabrication of standalone metal type X-ray mask with less pattern density by photolithography and wet chemical etching, popularly known as photo chemical machining (PCM) [104].

Recently, X-ray masks are developed by sputtered lead film on a Mylar sheet substrate with the lift-off process. Sputtering is selected for Pb thick film deposition due to its high sputtering yield [105]. Electrodeposition of Tungsten and Tantalum at temperature compatible with the photoresist technology is difficult due to higher (850 °C) temperature requirement. Alternatively, they are deposited on the substrate through physical vapour deposition and later are etched out selectively using reactive ion etching process. Platinum and Gold have the highest absorption among the mask absorber materials shown in figure 3.2 (b). In this case lowest thickness of absorbing layer will be required for absorption of ~ 80 % X-rays compared to other absorbing materials. Table 3.1 also shows the required thickness of gold as absorbing layer in various X-ray energies offered by SDXRL beamline. Gold is an ideal choice for the absorber material due to its good X-ray absorbing properties and compatibility to chemical process. Gold electro deposition is known from several centuries by jewelers and low stress gold deposition is easily achievable. However, electro deposition using gold cyanide solution is toxic. Nowadays, non cyanide gold solutions, based on gold sulphate chemistry, are available for electro deposition. In this thesis, non-cynaide gold

plating solution is used for preparing Au layer on conducting substrate. Fabrication steps of X-ray masks are described in next section.

3.1.3 Fabrication of X-ray mask

Fabrication of X-ray mask is one of the most difficult inputs required for XRL. Due to thin mask membrane and high Z absorbing material with high density, it is difficult to handle the substrate during its fabrication. A block diagram showing various fabrication routes for transferring the desired patterns of X-ray masks on substrate are given in figure 3.3. All membrane based X-ray masks used in this thesis are developed at RRCAT by scientific and technical exchanges with LASTI, Hyogo University, Japan. X-ray mask can be fabricated using UV lithography method [106] or electron beam lithography method [107]. A laser pattern generator (for features > 2 μm) and electron beam lithography system (for features < 2 μm) are used to direct pattern the structures on suitable resist coated on substrates. To satisfy the high contrast (>100) mask condition for DXRL process, one requires high absorber thickness (> 10 μm of gold) on mask membrane. The micro patterns produced from electron beam pattern generator is 1-4 μm thick which is not sufficient to obtain dose contrast. This mask is used as intermediate mask to fabricate working mask by patterning higher thickness positive photo resist using low energy X-rays in the beamline and electroplating of Au layer (thickness ~ 5-40 μm). A moderate resolution (CD Δ > 5 μm) X-ray mask is also fabricated using UV photolithography. In this case, a UV mask prepared by laser pattern generator is used. In present thesis, all membrane based X-ray mask are produced using UV photolithography process. In next section, the development of X-ray mask based on membrane and stand alone metal foil based mask are discussed.

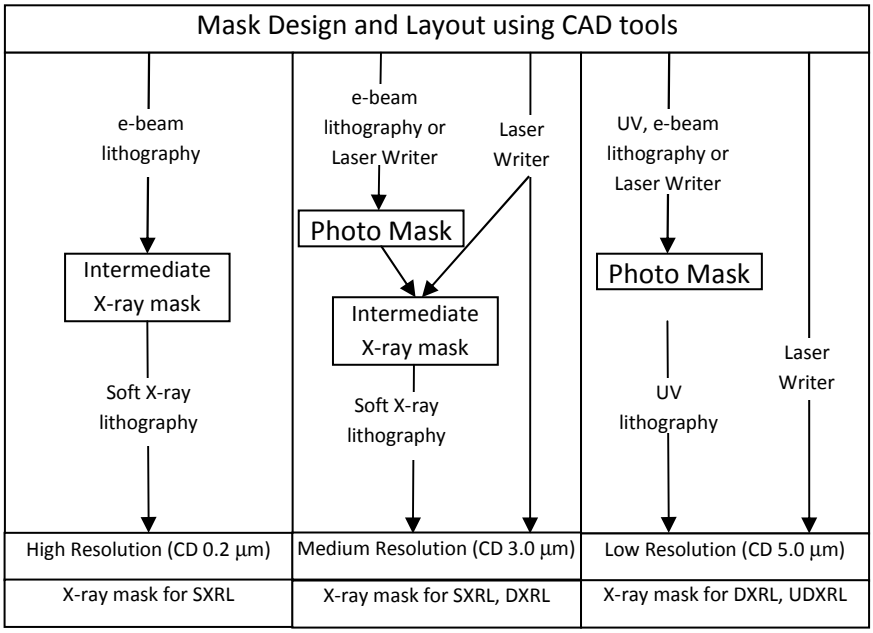

Figure 3. 3 : Flow chart showing various route of X-ray mask fabrication

3.1.3.1 Membrane based X-ray mask

The fabrication process of X-ray mask is schematically shown in figure 3.4 for two mask membrane, SU-8 (left side) and Polyimide (right side). The detail of fabrication process is explained stepwise in following text.

3.1.3.1.1 UV photo mask fabrication

UV photomask is fabricated using a laser pattern generator where suitable laser wavelength 405 nm for positive photo resist or 375 nm for negative resist is used. Depending on the desired resolution on photomask blanks, a laser with suitable objective is focused down to 0.8 µm with minimum scanning grid size 25 nm for writing the patterns. During the course of this research work and other device development work, the mask are purchased from M/s Bandwidth Foundry, Australia [108] or obtained from CEERI, Pilani under joint program of collaboration [109]. A pattern generator requires a computer aided design (CAD) drawing containing geometric coordinates of the micropatterns. The generated drawing file is

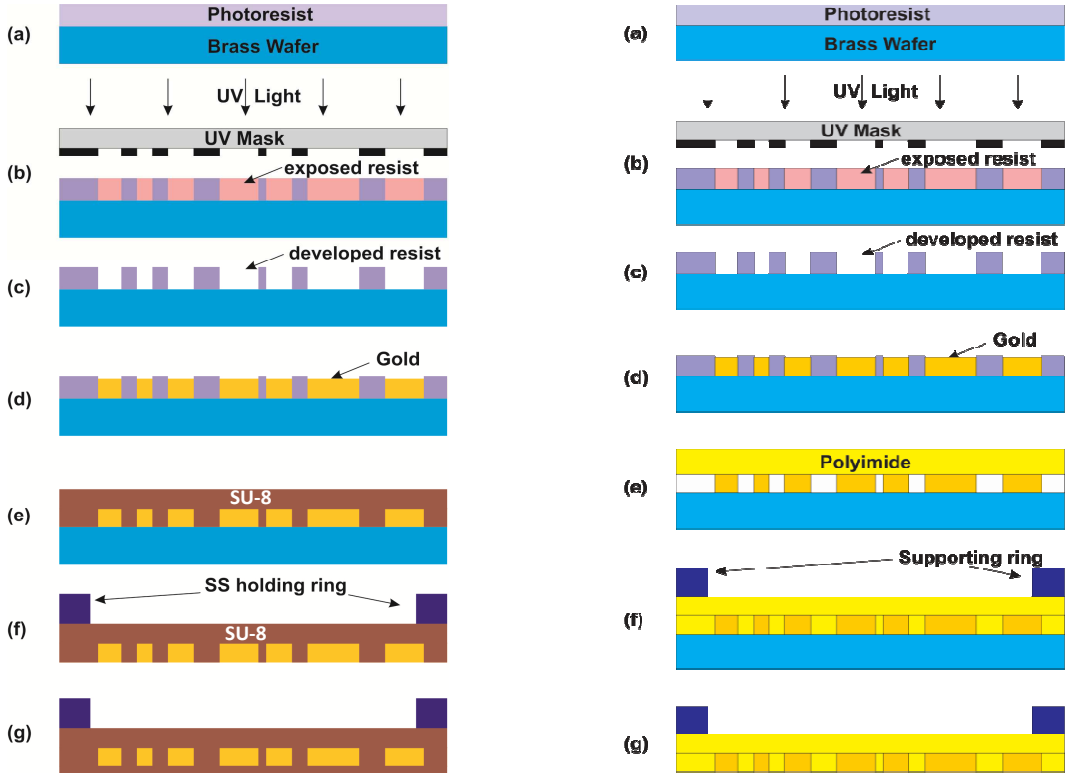

Figure 3. 4 : Membrane based gold X-ray mask fabrication process: (a) photo resist is spin coated on metal substrate (b) Exposure of resist using UV source (c) the exposed resist is developed (d) resist mould is electroplated with gold (e) unexposed resist is removed and polyimide/SU-8 is spin coated on gold electrodeposited metal wafer. (f) Stainless steel ring (black) is fixed from polyimide or SU-8 side and etched in case of SU-8 membrane mask and (g) finally the metal substrate is etched to obtain X-ray mask in right side view and on left side, thin layer of SU-8 is added for protection of gold layer.

exported in DXF format or changed to *.cif or *.gdsII. DWL 200 laser pattern generator (Heidelberg Instrument, Germany) is used to write the patterns on 1 µm thick layer of AZ 1518 photoresist coated on chrome photomask blank (Nanofilm, Wetlake Village, California, USA). The exposed resist is then developed in AZ400K developer and underlying exposed Cr layer is then etched out using Cr etchant solution containing cerium ammonium nitrate. The

UV mask for X-ray refractive lenses and general test patterns are procured from M/s Bandwidth foundry, Australia.

3.1.3.1.2 Substrate preparation

Brass substrate with 100 mm in diameter and thickness of 0.3 mm is used as a base substratefor development of X-ray masks. Brass is easily etched in nitric acid without affecting the micro patterns and membrane materials. Brass wafer is cleaned with organic solution. A protective PET layer on polished side of Brass wafer is removed. To remove any residual glue or chemical impurities, substrate is soaked in acetone for 5 minutes. It is then washed with de-ionised (DI) water and kept in iso propyl alcohol (IPA) for 5 minutes. Finally it is washed in running DI water for 5 minutes, dried using nitrogen gas and dehydrated at 100 °C. AZ4903 is spin coated (MSA100, Opticoat MIKASA, Japan) on brass wafer at 3000 RPM for 20 seconds and baked for 5 minutes at 110 °C. The 15-20 μm thick layer of positive photoresist is obtained which corresponds to the maximum possible thickness upto which Au can be electrodeposited.

3.1.3.1.3 UV Exposure and Development

Home built UV exposure system is used for carrying out UV lithography exposures. This system is economical and produces results similar to the commercial available systems. UV exposure system consists of Osram 300 W high pressure mercury UV lamp which provides a broadband wavelength from 200 to 700 nm. A collimating lens assembly consists of two borosilicate glass plano convex lens, is kept at 170 mm (focal length) from source to obtain a collimated UV light on substrates. A mask and substrate holder assembly is prepared from Perspex and routinely used to mount the UV mask and resist for their exposures.

The UV photomask with desired pattern and resist coated Brass wafer are mounted in the mask-substrate holder assembly. The AZ4903 coated wafer is exposed to UV with a dose of 100 mJ/cm^2 (value indicated in AZ 4903 datasheet) which corresponds to a 90 seconds exposure used for Osram UV lamp and considering the transmission through collimating lens. The exposed substrate is later developed in AZ 400K developer solution by mixing it with water in the ratio of 1:3. The sample is developed and dried to get clear lithography structure. The substrate is now ready for Au electrodeposition.

3.1.3.1.4 Electrodeposition (Ni/Au)

The UV lithographically patterned Brass wafer is electroplated with Ni and Au. A thin layer of Ni through electrodeposition is required on Brass for two purposes, (1). Gold grow easily on Cu or Ni layer, and (2). The non-uniformity of brass substrate is levelled by 0.5-1 μm thick layer of Ni. The electrolyte solution for Ni electrodeposition is prepared, using composition given in table 3.2.

Table 3. 2 : Composition of Ni electrolyte solution

Serial No	Name of chemicals	Weight [g/litre]
1	Nickel sulphate	200
2	Nickel chloride	5
3	Boric acid	12.5
4	Saccharin	3
5	Sodium Lauryl sulphate	1

Before Ni electrodeposition, the back side (non structured surface) of lithographically formed brass wafer is insulated with polymer tape to prevent Ni coating. The Ni electrodeposition condition is given in table 3.3. Electrodeposition is carried out only for 1-2

minutes such that a uniform thickness of 0.5-1 μm of Ni grows in the recesses of microstructure.

Table 3. 3 : Conditions for Ni electrolyte solution maintained during its electrodeposition

pH	Temperature	Current density	Anode	Anode to cathode ratio	Agitation
4	55 °C	10 mA/cm^2	Ni	1:1	High

Table 3. 4 : Conditions for Neutronex 309® maintained during Au electrodeposition

pH	Temperature	Current density	Anode	Anode to cathode ratio	Agitation
9	50 °C	2 mA/cm^2	Platinum	1:1	Moderate

The Au (10-15 μm thick) is electrodeposited over thin layer of Ni using Neutronex 309® (Enthone Inc, USA) non cyanide gold plating solution. The electroplating hull cell (YPT-01, Yamamoto, MS Co. Japan) is used for Au electrodeposition. The electrolyte solution is circulated in hull cell through 2 micron filter size using a magnetic pump. The operating condition during the Au electrodeposition of electrolyte solution is given in table 3.4. Solution is operated at pH 9.0 and solution temperature is kept at 50 °C. Normal dc mode with current density of 2.0 mA/cm^2 is provided to electrodes by pulse power supply (DuPR10, Dynatronix, USA) resulting in deposition of 8-10 μm/hr with a tensile stress in the range of 12-20 MPa.

3.1.3.1.5 Formation of mask membrane layer

X-ray transparent membrane layer of SU-8 (thickness ~ 200 μm) or polyimide (thickness ~50 μm) is used to support X-ray absorbing layer. Before applying the membrane material, polymer tape is removed and remains of AZ4903 is dissolved in Acetone and substrate is

dried. SU-8 or polyimide is spin coated over Au electrodeposited brass wafer and cured. The membrane material should form uniform thick layer on the brass substrate and its curing is important to obtain enough rigidity of the membrane layer.

SU-8 layer

SU-8 2100 is coated on the electroplated brass wafer at 1000 RPM for 30 s. During spin coating, substrate angular speed is accelerated from zero to 500 RPM with slope of 100 RPM/s. In second step, final speed is attained with acceleration speed of 300 RPM/s. The coated SU-8 is prebaked at 65 °C and 95 °C for preset time. SU-8 is exposed in X-ray beam for 25 seconds/cm for allowing its polymerisation. The detail mechanism of X-ray exposure of SU-8 is described in section 3.2.2. The post exposure bake of SU-8 is carried out at 95 °C for 30 minutes to complete the polymerisation process.

Polyimide layer

Two types of polyimide solutions are used to form the polyimide layer, “DURIMIDE 7020” from M/s Fuji Film Electronics Materials, Belgium and ABRON-S10, ABR Organics Ltd., India. The polyimide solution is spin coated at 500 RPM for 30 second with slope of 100 RPM/s to attain final spin speed. The speed is optimised to obtain polyimide membrane thickness of nearly 60-70 μm. The curing of spin coated polyimide layer is carried out on precision hot plate (~0.1 °C) providing temperature upto 500 °C. The ramping rate of the temperature is kept low (5 °C/min). The curing is carried out at 65 °C for an hour and intermediate temperatures of 100 °C, 200 °C, 300 °C for 30 minutes. Final temperature 350 °C is used for 30 minutes to complete the curing of polyimide layer.

At the end, stainless steel (SS) ring is bonded over the polyimide/SU-8 coated brass wafer using high temperature curable double side tape. This step ensures the rigid support to stand alone polyimide/SU-8 membrane which will be released in next step. The size of the used SS annular ring is 100 mm outer diameter and 92 mm inner diameter, 2 mm thickness.

3.1.3.1.6 Etching of Brass wafer

The above process is following by etching of brass wafer by keeping it in the nitric acid solution to etch the base brass wafer. The composition of nitric acid is (70ml) and DI water (50ml) at room temperature which etches the complete brass wafer in 15-20 minutes. The final fabricated X-ray mask using SU-8 and polyimide membrane is shown in figure 3.5 (a) and (b) respectively. In case of SU-8 membrane layer, a thin layer of SU-8 is coated on the gold side and cured. This additional layer of SU-8 protects the gold surface due to internal stress of SU-8/Au thick film. To the best of our knowledge, these X-ray masks are developed for the first time in the country.

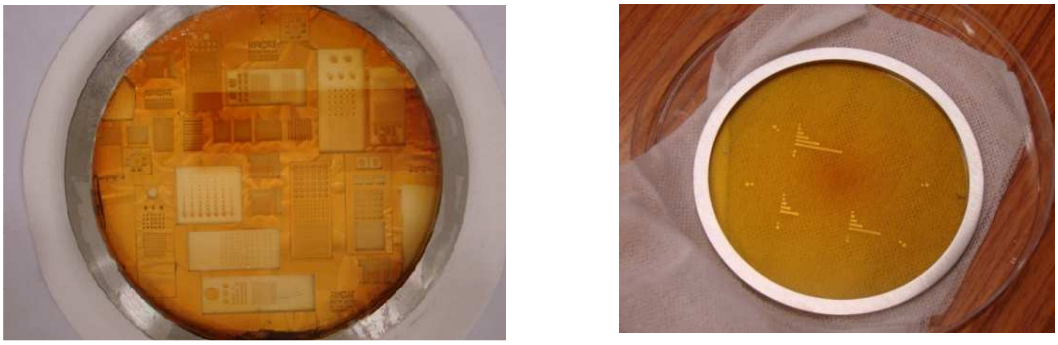

Figure 3. 5 : First series of developed x-ray masks at RRCAT (a) SU-8 membrane gold mask and (b) Polyimide membrane gold masks.

X-ray mask developed by this process have few drawbacks. In order to overcome these drawbacks, a new and improved recipe for fabrication of X-ray mask is devised during this

thesis. It is planned to obtain a patent for this new recipes of making x-ray mask. Therefore this new process is not described in this thesis.

3.1.3.2 Metal foil based X-ray mask

A low cost X-ray mask based on an etched metal foil are attractive to achieve coarse features (> 50 μm) using PCM technique. In PCM process, the mask profiles in metal substrate foil are obtained using combination of photo lithography and chemical etching. For the range of X-ray energies (2.5-9 keV), copper or stainless steel sheet of ~100 μm thickness is a suitable choice as it has high absorbance and can be etched using commonly available etching solutions. However, using PCM, it is difficult to obtain the smaller features with good dimensional accuracies, and aspect ratio is limited to 1. The use of this type of X-ray mask is limited to application requiring coarse feature like microfluidic channels with width of ~100-500 μm. The processing steps of stencil type X-ray mask is shown in figure 3.6.

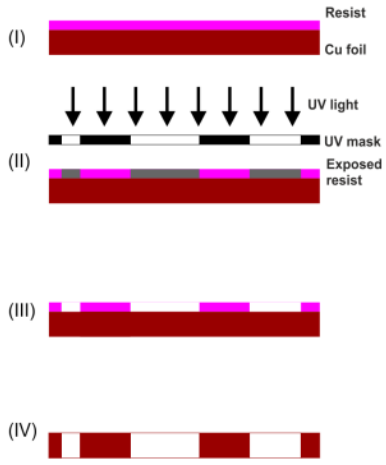

Figure 3. 6 : Schematic of X-ray mask fabrication process using photo chemical machining.

3.1.3.2.1 Cleaning of wafer

A 100 μm thick Cu foil of size 25 mm x 30 mm is taken as base substrate. Substrate is initially cleaned with tissue dipped in tetrachloroethylene and later using ultrasonic cleaned in acetone solution for 10 minutes. Cu foil is then cleaned in mixture of 10 ml H_2SO_4 and 90 ml DI water. Further, a mixture of Chromium oxide (4.5 gm), H_2SO_4 (1 ml) and 90 ml water is used to clean the surface to get shining surface of Cu substrate. Finally, the wafer is dipped in IPA for 5 minutes and washed in running DI water for 5 minutes. Cleaned substrate is then dried and hydrated at 100 °C for 10 minutes.

3.1.3.2.2 Photolithography

The substrate is coated with AZ4903 as per the recipe given in section 3.1.3.1.2. Later, the step given in section 3.1.3.1.3 for UV photolithography is followed. UV masks prepared on transparency sheet by 10000 DPI laser printing are used for photolithography. Generally this type of UV mask is used for coarse microstructures with feature dimensions more than 50 μm.

3.1.3.2.3 Etching of metal substrate

The Cu substrate with defined AZ4903 resist patterns is etched in $FeCl_3$ solution. Before dipping the substrate into etching bath, the back side of the substrate is protected with polymer tape to prevent the etching. A Cu etching solution with following composition (table 3.5) is prepared.

It takes ~ 20 minutes to completely etch 100 μm copper in the area uncovered by resist. The areas covered with resist remained un-etched. Figure 3.7 shows the fabricated X-ray mask using Cu substrate.

Table 3. 5 : Composition of Cu etching solution

Serial No	Name of the chemicals	Composition for 100 ml
1	Ferric chloride	40 g
2	Nitric acid	5 ml
3	Hydrochloric acid	15 ml
4	Water	40 ml

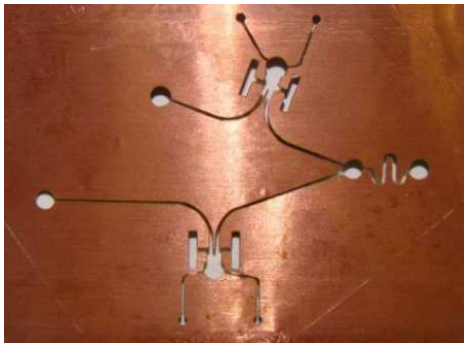

Figure 3. 7 : Fabricated metal foil based X-ray mask with coarser CD.

3.2 Development of HAR microstructures in X-ray sensitive photoresist

In this section, the role of X-ray sensitive photoresist for realisation of HAR microstructures is discussed. The X-ray exposure mechanism for PMMA and SU-8 and its utilisation for fabrication high aspect ratio are presented.

3.2.1 X-ray Exposure mechanism of PMMA

X-ray irradiation of PMMA produces physical and chemical changes in its polymeric structure. X-ray energies (0.5-10 Å) are deposited into the resist material through photoelectric and Compton effects. PMMA being low Z material, 95 % of the deposited dose is due to the photoelectric effect [110]. The molecular formula for PMMA monomer is shown

in figure 3.8. According to Miller rule, long polymeric chain scissioning is dominant and with some amount of cross linking due to alkyl group. Therefore, PMMA undergoes a decrease in molecular weight due to scissioning of main chain [111]. The most important step in X-ray degradation of PMMA is the scission of the methyl ester group which leads to the evolution of gases like CO_2, CO, H, and CH_4 [111, 112, 113] and Benzene and methyl formate are found in low concentrations [114]. The remaining polymer chain stabilizes after hydrogen abstraction by formation of a double bond or by chain scission. Approximately 80 % of the chain scissions have been reported after a preceding side chain degradation, the remaining 20 % are due to a direct decomposition of the polymer into two macromolecules [115].

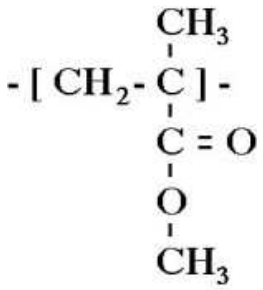

Figure 3. 8 : PMMA monomer unit

The main chain scission reduces the average molecular weight of PMMA. The number average molecular weight of the exposed polymer MW_D can be expressed as [111]:

$$\frac{1}{MW_D} = \frac{1}{MW_{D_0}} + G_{SC}.\frac{D}{100\cdot 1.6\cdot 10^{-19} N_A \rho} \qquad (3.3)$$

where, MW_{D_0} is initial number average molecular weight, N_A is the Avagadro's number, D is absorbed dose and ρ is density of the polymer. The constant value in second quantity in the denominator corresponds to the energy (in Joule). Here, G_{SC} value defines the number of scission/crosslinking events at 100 eV. Change in molecular weight as a function of exposure dose can be approximately obtained by using Gel Permeation chromatography [116, 117]. In

this thesis, a study is carried out to observe the physical/chemical changes in PMMA as a function of exposure dose using Raman, FTIR and X-ray diffraction studies. PMMA sheets are also exposed for direct correlation between the exposure studies and depth of microstructures during development.

The equation 1.2 can be written in terms of absorbed dose $D(z)$ [kJ/cm^3] attenuated within the resist material:

$$D(E,z) = D_T e^{-\mu(E)z} \qquad (3.4)$$

here, D_T is the absorbed dose on the top of the resist surface.

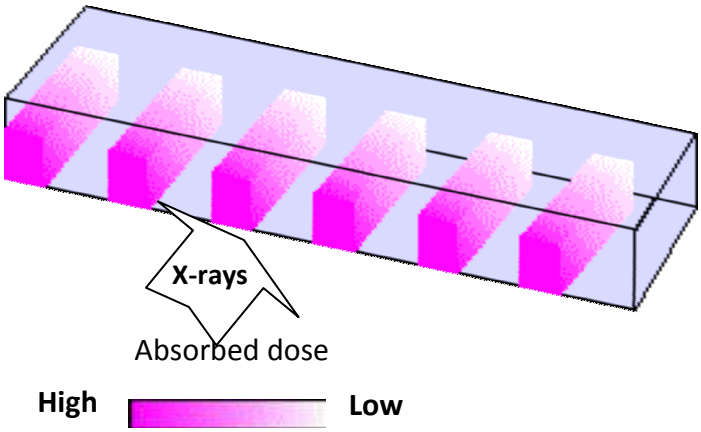

Figure 3. 9: Schematic distribution of X-ray exposure dose from top surface to bottom.

On exposure, the top layer will receive initial dose value (D_T) and it will decrease exponentially along resist depth ($D(z)$), shown using shaded area in figure 3.9. The depth of penetration increases with increasing energies and therefore higher energies are required to pattern thicker resist layers. In SR source, the stored current of electron defines the amount of photons incident on X-ray mask and resist. Hence, the absorbed dose is correlated with exposure dose in resist. The exposure dose is described in terms of storage ring current (I_R) multiplied with time (unit used are mA.sec or mA.min or A.h). Owing to X-ray irradiation effects, average molecular weight of PMMA in exposed area is reduced by two orders of

magnitude (~10k-60k g/mol) from original molecular weight 2000k g/mol for CLAREX PMMA sheet. This lower molecular weight chains are easily dissolved in appropriate organic solution. To reach such a low molecular weight a minimum dose (D_B) of 3.5 kJ/cm³ has to be absorbed in PMMA. In such conditions, the top dose (D_T) on PMMA should also be limited to 20 kJ/cm³ otherwise radiation dependant foaming will occur due to the formation of gaseous products relieved from the resist. In order to protect the resist from thermal degradation, ratio of top to bottom dose is often kept between 5 to 10. The dose under the X-ray mask, referred here as shadow dose (D_S) should be under ~100 J/cm^3, to obtain better exposure contrast (Δ_{con}) between the exposed and unexposed part of PMMA. This exposure contrast is directly dependant on the thickness of mask absorbing layer. Having said about required absorbed dose conditions at various parts of the resist, it is therefore necessary to calculate the exposure dose or absorbed dose for each spectral band of SDXRL beamline considering PMMA as a resist. This exposure dose determines the time resist must spend during exposures to obtain a particular depth of microstructure. The exposure dose can be calculated from the flux available at mask wafer plane from the beamline. Equations (2.6 to 2.9) can be used for calculation of flux at the required location along beamline. The dose rates D_{resist} in the photoresist can be calculated using [118]:

$$\mathrm{D_{resist}}(\lambda, z) = \sum_{\lambda_{min}}^{\lambda_{max}} \mathrm{D_{BL}}(\lambda)\mu_{\mathrm{resist}}(\lambda)e^{-\mu_{\mathrm{resist}}(\lambda)\cdot z} \qquad (3.5)$$

and dose rate as a function of vertical acceptance angle is

$$\mathrm{D_{resist}}(\lambda, z) = \sum_{\lambda_{min}}^{\lambda_{max}} \sum_{\psi_{min}}^{\psi_{max}} \mathrm{D_{BL}}(\lambda, \psi)\, \mu_{\mathrm{resist}}(\lambda)\, e^{-\mu_{\mathrm{resist}}(\lambda)\cdot z} \qquad (3.6)$$

Above two equations provides the exposure dose at the top of the resist and by considering the beam width as 1 cm absorbed dose is described in unit of J/cm^3 per I_R (mA). The exposure dose (A.hr or mA.min) can be obtained by dividing the required bottom dose (generally 2-4 kJ/cm^3) by the dose rate obtained above. The mass absorption coefficient values ($\mu_{resist}(\lambda)$)

is obtained from NIST website [119]. Analytical calculation is carried out for obtaining the top absorbed dose and required exposure dose for 2.5-9 keV. By considering the transmission through beamline optical elements, $D_{BL}(\lambda, \psi)$ is obtained at mask-wafer plane.

DXRL simulation software DoseSim [118, 120] and X3D [121, 122] include computation of SR spectrum from bending magnet, the effect of optical properties of materials, exposure time calculation, X-ray spectrum with and without mirrors, secondary effects, dose deposited under absorber and moving mask validation. DoseSim has been used widely as a tool to calculate absorbed and exposure dose at various SR XRL facilities. The same tool is used in this thesis for calculation of exposure dose values and validation of analytical calculations. Table 3.6 shows comparison between analytical and DoseSim calculation for power density (flux density in particular energy range at I_R = 100 mA) values, absorbed dose on top and estimated exposure dose for bottom dose D_B = 3.5 kJ/cm^3. The power measured using Cu calorimeter is also given in the same table.

Table 3. 6 : Overview of calculation of X-ray exposure dose in 2.5-9.0 keV.

Energy range [keV]	**Power density [W/cm^2]**			**D_T [kJ/cm^3]**		**Exposure dose [mA-min]**	
	Analytical	**DoseSim**	**Measured**	**Analytical**	**DoseSim**	**Analytical**	**DoseSim**
2.5-9keV	0.242	0.3[#]	0.227	9.27	10.67	1096	1275

[#]power obtained from the DoseSim is (0.003 W/cm^2/mA).

Required exposure time at scanner2 for 5 cm scanning length with average Indus-2 ring current 100 mA is found to be 55 minutes using our calculations and 64 minutes using Dosesim. The calculated power density for X-ray scanner1 is three times higher than the power densities at scanner2. Hence, the exposure time at scanner1 reduces to 1/3rd value of scanner2, with exposure dose value is 400 mA.min and total time of 20 minutes.

3.2.1.1 Impact of X-ray irradiation on (500 μm) thick PMMA

The effect of X-ray exposure dose on PMMA is well studied. The change in molecular weight with respect to exposure dose is reported using Size Exclusion Chromatography-Multi Angle Laser Light Scattering [123]. According to measurement in 50 slices of 10 μm thick PMMA film, the original molar mass of 1770k g/mole is reduced to 4.5k g/mole at top surface and 11k g/mole at bottom surface after a top exposure dose of 20 kJ/cm^3 given by ELSA synchrotron source. Henry et. al. investigated the chemical changes in PMMA during resist preparation and exposure by Gas Chromatography Mass spectrometry to observe trapped volatiles in PMMA, and Gel Permeation Chromatography and Matrix assisted laser desorption time-of-flight mass spectrometry to obtain information on polymer/oligomer characteristics [124]. X-ray irradiated PMMA also shows the various physical and chemical changes which can be correlated using FTIR spectrometry, Raman and X-ray diffraction (XRD). Recently, effect of X-ray irradiation of thin PMMA films deposited at various substrate temperatures by pulsed laser deposition is studied using FTIR, XRD, hardness and optical microscopy [125]. Our group have also characterised the effect of electron beam irradiation on surface modification of PMMA resist using FTIR, XRD and frequency dependant dielectric measurements [126]. To the best of our knowledge the impact of X-ray irradiation on thicker PMMA sheet has not been studied using FTIR, Raman and XRD techniques and its direct correlation with fabrication of microstructures. An investigation on X-ray irradiation with and without X-ray mask of 500 μm thick PMMA is carried out during this thesis. The microstructured PMMA is developed as a function of time to determine dissolution rates of PMMA.

PMMA sheets (CLAREX) of size 10 mm (width) x 10 mm (length) x 0.5 mm (thickness) are used for X-ray irradiation. The same PMMA sheets are also patterned using SS mask to correlate the effect of X-ray irradiation and obtained depth in PMMA. The details of the development of these exposed PMMA resist are given in section 3.2.3.3.

Four different series of samples are X-ray irradiated in air at scanner1 with different energy spectra shown in figure 2.6 (serial no 4, 5, 9) and white beam. The exposure doses between 83 mA·min to 1166 mA·min are given to each series of samples. For clarity of the observation, only three irradiated samples and one unexposed PMMA sample in the energy range 2.5-9 keV are compared for FTIR, Raman and XRD measurements.

3.2.1.2 Top Surface roughness

The processing method of forming acrylic sheets can be found in literature. X-ray reflectivity measurement is carried out of the top surface of CLAREX PMMA sheets which has shown the top surface roughness of 500 μm unexposed PMMA sheet ~ 7- 8 Å. The surface roughness of the same order is measured using the non contact 3D profiler Confocal Optical Microscope (COM) (Zeta20, Zeta Instruments Inc, USA) and found to be 3.8 Å. The surface roughness of standard Si wafer is also measured using X-ray reflectivity (8 Å) and COM (5.1 Å). These measurements provided benchmarking to surface roughness measurement of X-ray irradiated samples. Figure 3.10 shows top surface of three samples irradiated at different exposure dose values. The surface roughness measured data on these samples is given in table 3.7. The surface roughness values of two dose values 83 and 1166 mA.min are comparable with unexposed substrate. In each of these cases the absorbed top dose is less than the damaging dose (20 kJ/cm^3). PMMA top surface shown in figure 3.10 (c)

has absorbed dose more than the damaging dose and foaming in resist surface is observed. In this case, the value of surface roughness is more than 50 nm and cannot be measured.

Figure 3. 10 : Top surface view of X-ray irradiated samples with exposure dose (a) 0 mA.min (b) 83mA.min (c) 2834 mA.min. First two samples are used for surface roughness measurements.

Table 3. 7 : Comparison of PMMA top surface roughness with exposure dose.

Parameters	**Si wafer**	**PMMA top surface roughness**		
Exposure dose [mA.min]	--	0	83	1166
Average roughness [nm]	0.51	0.38	0.39	1.9
Roughness, peak to valley [nm]	3.8	3.0	3.5	16.4

3.2.1.3 FTIR and Raman spectroscopy

Vibrational spectroscopy provides the means of understanding of different molecular structures and changes in molecules. FTIR spectra provide insight into the intra and intermolecule interactions. PMMA FTIR spectra gives the information on various molecular modes, like change in stretching vibrational band of carbonyl ester group C=O, C-H and C-C vibrations etc. Single reflection Attenuated Total Reflection (ATR) FTIR spectra are recorded

at a spectral resolution of 4 cm^{-1} in 600-4000 cm^{-1} region using Bruker IFS 125 HR FTIR spectrometer equipped with KBr beam splitter and liquid-nitrogen-cooled MCT detector. To ensure a high signal-to-noise ratio, 200 scans are recorded. The sample and source compartments are evacuated to 0.8 Torr during each measurement. Figure 3.11 shows the FTIR ATR spectra for various PMMA sheets radiated with exposure dose of 0, 833 and 1173 mA.min in the energy range 2.5-9 keV.

The FT-Raman spectra of the exposed PMMA sheets are also recorded using Bruker MULTIRAM Raman spectrometer equipped with Nd:YAG laser source operating at 1.06 μm line with a spectral width of 4.0 cm^{-1}. The recorded Raman spectrum for PMMA sheets X-ray irradiated in 2.5-9 keV energy range for different dose values are shown in figure 3.12. The most of the peaks in Raman and FTIR spectra matches with the theoretically available data.

The C=O and the C-O bands often dominates in the IR spectrum C-C modes dominates in the Raman spectrum [127]. A strong band at peak around 1724 cm^{-1} is assigned to C=O stretching. PMMA also shows a band assigned to C=O stretching. C-O stretching frequency is variable and usually appears within 1000 – 1400 cm^{-1}. Medium bands at 1267 cm^{-1} and at 1239 cm^{-1} are also assigned to C-O stretching modes. The C=O in plane and out of plane bending is assigned to a very strong Raman band at 810 cm^{-1} (calculated value 812 cm^{-1}) and a medium strong band in IR at 750 cm^{-1} (calculated value 751 cm^{-1}) respectively. The very strong Raman band at 2953 cm^{-1} are assigned to methylene (CH_2) asymmetric stretching vibrations. The weak Raman band at 2760 cm^{-1} is also assigned to CH_2 symmetric stretching. The deformation mode of CH_3 has been observed at 1434 cm^{-1}. The above conclusion agrees well with those of Zwarich et. al. [128] and Green and Harrison [129]. The CH_2 wagging and twisting are found at 1364 and 1320 cm^{-1}.

The peak related with CO_2 is not detected; this may be due to ATR measurement where the beam penetration is not more than 5 μm. The trapping of the CO_2 could not be detected

upto this depth due to its dissipation in the atmosphere. FTIR and Raman measurement indicates the changes in polymeric as the X-ray exposures dose increases.

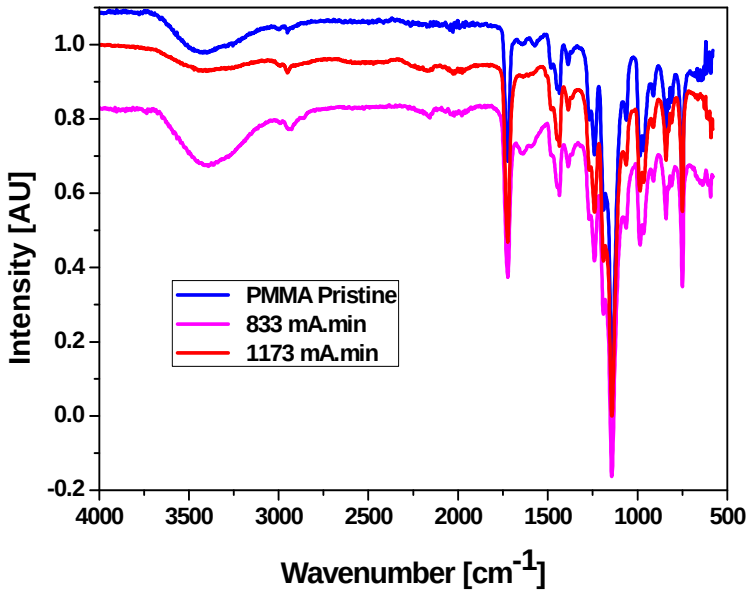

Figure 3. 11 : FTIR spectrum recorded at increasing exposed dose

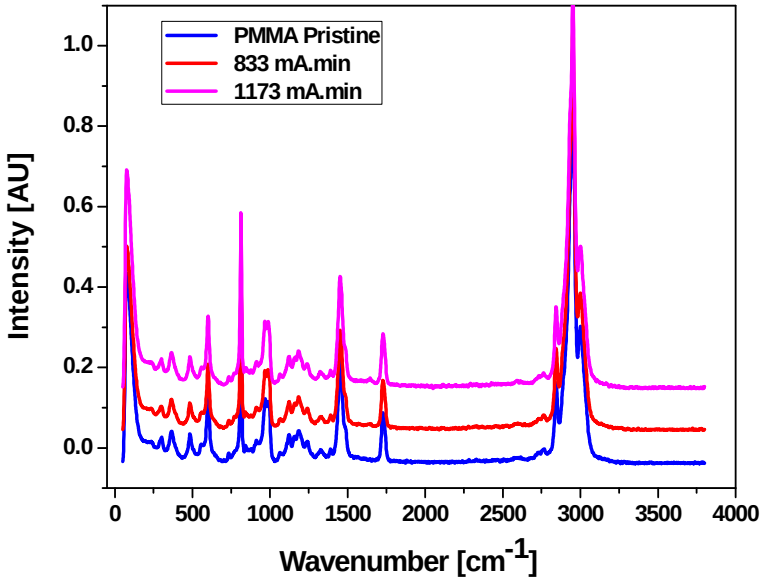

Figure 3. 12 : Raman spectrum recorded at increasing exposed dose.

3.2.1.4 X-ray Diffraction

SR XRD data of the PMMA sheets are recorded at BL-12, Indus-2. Figure 3.13 gives the recorded SR-XRD spectra of PMMA with some representative raw image plate patterns, illustrating the microstructural changes as a function of exposure dose. The sample to image plate distance was 120 mm and energy was 12 keV. The image plate data files were integrated using FIT2D, incorporating polarization correction. XRD pattern of PMMA shows a broad halo, which is a characteristic of the amorphous phase. The XRD spectra of the PMMA as a function of exposure dose can be fitted by a Lorentzian function with full width at half maximum (FWHM) of 5.25° ± 0.03°. The values of the width of first peak at different exposure dose are shown in figure 3.14 with error bars. The XRD pattern of PMMA after various dose rates show that broad halo into wider peak which is indication of PMMA becoming disordered. The increase in FWHM of exposed PMMA, as calculated from the results of XRD measurements, increases steadily with exposure dose. The increase in peak width is correlated with increase in exposure dose (and size of monomer chain scission from main polymeric chain). Generally the density of exposed polymer is lower than that of the unexposed polymer. As density is reduces with the release of gaseous molecules from PMMA, polymer structure experiences stress due to surrounding amorphous structures. Therefore, the associated microstructure results in increase in strain in the amorphous structure as a function of exposure dose. This increase in strain due to increase in exposure dose (time), will create cracks or dislocation lines which acts as easy centres for attacking the OH^- ions of PMMA developer solution resulting in faster rate of development.

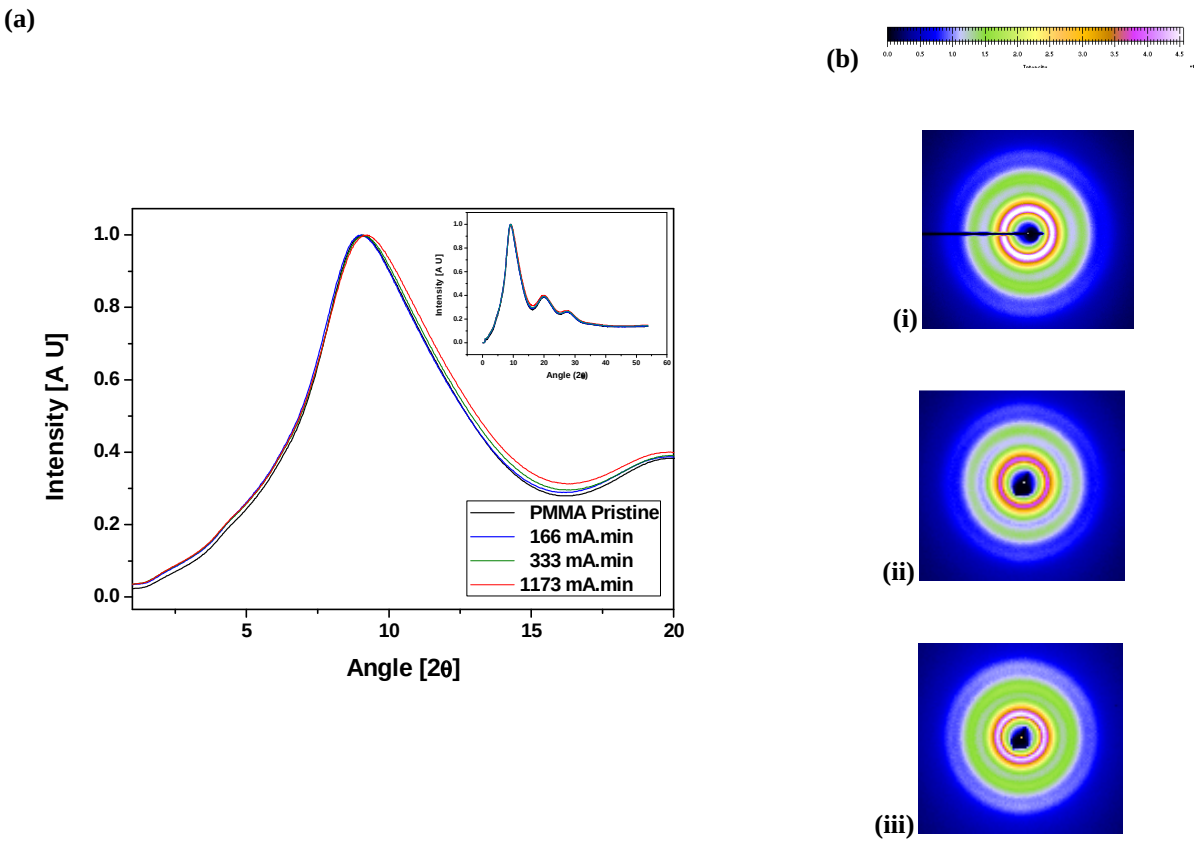

Figure 3. 13 : (a) XRD patterns of the PMMA after X-ray exposure(in inset) and the enlarged first diffraction maximum (b) Raw image plate XRD data (i) for PMMA Pristine (ii) exposed at 333mA.min and (iii) exposed at 1173 mA.min.

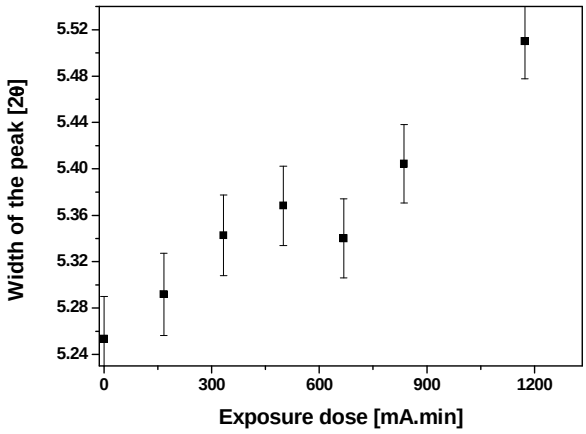

Figure 3. 14 : Variation of width of first diffraction peak with increasing exposure dose.

3.2.2 X-ray Exposure mechanism of SU-8

Like chemically amplified photo-resists, SU-8 contains three main components, base resin, solvent and photo acid generator (PAG). The base resin is SU-8 polymeric epoxy resin consist of Bisphenol A Novolak epoxy oligomer (EPON® SU-8 resin, Shell Chemical) which is highly cross-linkable in an acidic environment. This SU-8 epoxy resin is dissolved in Gamma-Butyrolactone (GBL) or cyclopentanone (CP). PAG is made of a combination of triaryl sulfonium salt and sulfonium hexaflorate [130]. PAG is added upto few mass percentage based on the weight of epoxy resin. The structure of SU-8 polymer is shown in figure 3.15. The resist used during various studies in this thesis is brought from Microchem Corporation, USA. SU-8 is available in various grades with various percentages of solid content or viscosities. In this thesis, variant SU-8(2000.5), SU-8(25), SU-8(2100), and SU-8(2150) are used.

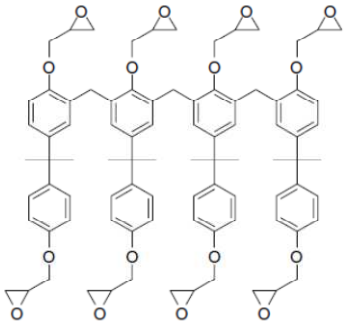

Figure 3. 15 : Chemical structure of Bisphenol A Novolak epoxy oligomer contained in SU-8. Eight reactive epoxy molecules and therefore 8 in SU-8.

SU-8 is sensitive to UV and X-ray photons, e-beam and high energy proton beam. In illuminated regions, low concentration of acid will be generated by PAG. This produced acid act as catalyst in the subsequent cross linking reaction that takes place during post exposure

bake. The catalyst is present only in the X-ray irradiated area and therefore the resist cross links only in the exposed region. Each monomer molecule contains eight reactive epoxy sites and therefore high degree of cross linking is obtained after photothermal activation giving negative tone [131]. The exposed, cross linked resist is insoluble in organic developers, while the unexposed uncrosslinked resist dissolves in SU-8 developer, thus creating the contrast between the exposed and unexposed part. The sensitivity of SU-8 is very high in comparison to PMMA. The discussion is given in next section where comparison between PMMA and SU-8 is carried out.

SU-8 is good structural material for MEMS applications, and also it is used directly in the microfluidic network due to its adaptability for biological species. Various physical properties of SU-8 are summarised in the table 3.8 [132].

Comparison between SU-8 and PMMA for LIGA

PMMA allows the replicating of microstructure with best quality in terms of accuracy and sidewall roughness. It requires high value of exposure dose for proper development upto required depth. Therefore, it is very insensitive to X-rays. SU-8 has higher sensitivity than the PMMA and it is good construction material for faster prototyping.

Comparison between few properties and exposure dose requirement in case PMMA and SU-8 is illustrated in table 3.9. The main advantage of choosing SU-8 over PMMA is its sensitivity. The minimum dose required for cross-linking is ~20 J/cm^3. Similarly, the minimum dose require in case of PMMA for complete removal from depth is 3500 J/cm^3. SU-8 requires around two orders less exposure time in comparison to PMMA. Second advantage using SU-8 is due to its higher damaging dose because of which there is no limiting top exposure dose like in case of PMMA. However, the disadvantage using SU-8 that it is required to reduce the shadow dose under X-ray mask lesser than 0.05 J/cm^3

otherwise suitable exposure contrast will not be obtained. Therefore, this value should be considered while designing and fabrication of X-ray mask. The mask contrast of more than 1000 is preferred in SU-8. The second disadvantage is removal of cross linked SU-8 once the fabrication process is over. PMMA can be easily removed either by dipping in acetone for prolonged time or flood exposure of X-rays and development. Removing crosslinked SU-8 of thickness greater than > 500 μm is tedious process. It can be removed under oxygen plasma or by heating at temperature above 500 °C for an hour.

Table 3. 8 : Few physical characteristics of SU-8 resist layer

Property	**Value**
Young's modulus (post-bake at 95 °C)	4.02 GPa
Young's modulus (hard bake at 200 °C)	4.95 ± 0.42 GPa
Biaxial modulus of elasticity, $E/(1-\nu)$	5.18 ± 0.89 GPa
Film stress (post-bake at 95 °C)	16–19 MPa
Maximum stress (hard bake at 200 °C)	34 MPa
Friction coefficient (post bake at 95 °C)	0.19
Glass temperature, T_g (unexposed)	~50 °C
Glass temperature, T_g (fully cross-linked)	>200 °C
Degradation temperature (fully cross-linked)	~380 °C
Thermal expansion coefficient (post-bake at 95 °C)	52 ± 5.1 ppm K^{-1}
Polymer shrinkage upon cross-linking	7.5%

Table 3. 9 : Comparison of characteristic dose values of SU-8 and PMMA resist

Resist	**PMMA**	**SU-8**
Tone (exposure mechanism)	Positive (Scission)	Negative (crosslinking)
Molecular formula	$C_5H_8O_2$	$C_{87}H_{98}O_{16}$
Density [g/cm^3]	1.19	1.2
Damage/Top dose (D_T) [J/cm^3]	20,000	>10,000
Development dose (D_B) [J/cm^3]	3,500	20
Threshold dose (D_S) [J/cm^3]under shadow	100	0.05
Removal	Easy removal through wet etch	Difficult removal, dry etching

3.2.3 Fabrication of microstructure in PMMA

3.2.3.1 Sample preparation

PMMA substrates required in X-ray lithography are prepared in different ways depending upon their required thickness. Relatively thin layers (< 25 μm) of PMMA are prepared by multiple spin coating of a PMMA solution made from high molecular weight PMMA mixed in a solvent (Anisole/Chlorobenzene) and subsequent baking to remove the solvent [133] or use of commercially available PMMA solution and its copolymer from Microchem Corp, USA [134]. PMMA substrates of thickness upto 100 μm are prepared by polymerising methylmethacrylate (MMA) on the surface of the substrates [135]. DXRL substrates are prepared by bonding pre casted thicker sheet (200 - 3000 μm) of high molecular weight to metal or Si substrate by use of a solvent or PMMA bonding solution and desired thickness can be obtained by using flywheel cut [136]. In this thesis, the characterisation and fabrication are carried on pre casted PMMA sheets (make CLAREX) of varying thickness 200-6000 μm. The PMMA sheet is pre baked at 75-80 °C for an hour in oven and cooled to room temperatures before exposures. This prebake exposure annealing of commercial PMMA sheet reduces the swelling behaviour of PMMA during and after exposure [137].

3.2.3.2 X-ray exposure of PMMA

The various exposure conditions for PMMA to obtain the desired depth keeping the resist integrity intact is described in section 3.2.1 (and also table 3.9). The X-ray exposures are carried out at SDXRL beamline and at the different energy band.

Figure 3.16 illustrates the typical tuned energy-flux spectrum (after polyimide mask membrane) between 2.5-9 keV at SDXRL beamline for carrying out X-ray exposure in resist. This figure shows the contribution of various beamline components (source, entrance Be window, two mirrors, exit Be window and thin polyimide based X-ray mask membrane).

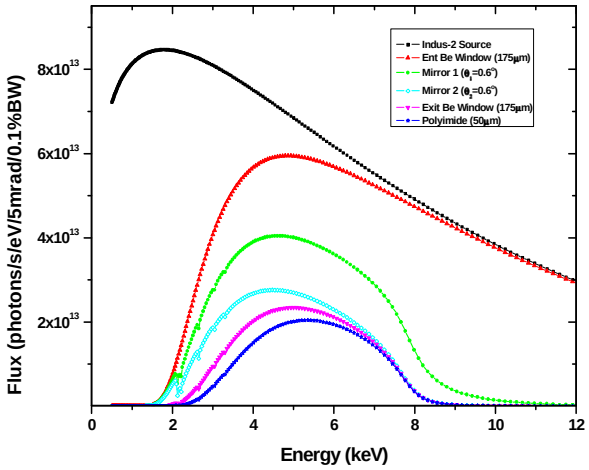

Figure 3. 16 : Typical X-ray energy-flux spectrum available for exposures at SDXRL beamline.

The sensitivity of CLAREX PMMA sheet in our case is found to be 2.5-3.5 kJ/cm^3 (i.e. ~166 mA.min) on top surface. However, a bottom absorbed dose of at least 2.5 kJ/cm^3 is needed to develop PMMA cleanly. For example, at SDXRL beamline, a 50 x 50 mm^2 square sample with a PMMA thickness of 500 μm (Dose 2,477 mA.min) would require a total exposure time of at least ~115 min at scanner2 when average stored current in Indus-2 is 100 mA. Table 3.10 gives the time required per cm for PMMA sheet of various thicknesses at 2.5-6 keV, 2.5-9 keV, 2.5-24 keV energy spectra at scanner1 and scanner2.

From table 3.10, it is concluded that the exposure dose required at scanner2 is higher than at scanner1. It is mainly due to the higher photon density available at scanner1. The role of different energy spectrum for various PMMA exposures is distinctly observed. In case of low energy spectrum (2.5-6 keV), X-ray has less penetration power and exposure time is very high for thick resist layers. Also, the calculated top dose is very high due to high soft X-rays absorption at top surface. The through development of 500/1000 μm thick PMMA requires much higher exposure dose which leads to top dose beyond the threshold level which is

impractical. Similarly in case of 2.5-9 keV, exposure of 1000-2000 μm requires high exposure time. To keep the total top absorbed dose below threshold value, Al filter of 18 μm thickness is used. This ensures the top dose does not exceed the damage threshold. As energy increases the exposure time is decreasing. Therefore, it is preferable to have high energy beam to obtain ultra deep microstructures (500-2000 μm). However, the increase in energy creates different complexities in terms of smallest features and requirement of high thickness of gold absorbing layer on X-ray mask. Table 3.10 also provide the possible overall exposure dose delivery by SDXRL beamline and it gives the bird eye view why the beamline is designed to provide various energy spectrum to carry out X-ray exposures.

Table 3. 10 : Time required for various PMMA sheet of various thickness in various energy spectrum keeping bottom dose constant D_B = 2500 kJ/cm^3 (at scanner1).

Serial No	PMMA Thickness [μm]	Exposure time [mA.min] for various energy spectrum			
		2.5-6keV	2.5-9keV	2.5-24keV	White beam
At Scanner1					
1	100	2313	445	441	150
2	200	5061	701	605	214
3	500	#29945	1784	1086	407
4	1000	#269570	#@8563	1912	741
5	2000	#606571	#23231	#@4412	#@1713
At Scanner2					
1	100	3238	579	555	202
2	200	7041	910	763	285
3	500	41228	2300	1377	532
4	1000	367470	#@10968	2439	954
5	2000	813890	#29671	#@5690	#@2171

Where the top dose is greater than 20 kJ/cm^3, @ Calculated when 18 μm Al filter is used to reduced the top dose below 20 kJ/cm^3.

3.2.3.3 Development of PMMA

PMMA after exposure is developed in the suitable organic developer. Few combinations of organic constituents eg. MIBK, IPA and water are used for development of exposed PMMA. The GG developer name given after their inventors Ghica and Glashauer is the most sensitive developer for PMMA HAR microstructures irradiated with X-rays. It is composed of four solvents, Diethylglycolmonobutylether, Morpholine, Ehanolamine and deionized water [138]. The table 3.11 gives the compositions of GG developer and rinser solution. GG developer allows developing of PMMA with molecular weight having values 10k g/mol. Mechanical agitation given by Megasonic instrument during the development increase the rate of the development but is found less effective for deep recesses (HAR > 10).

Table 3. 11 : Composition of GG developer and GG rinser solutions

Chemical name	**Developer**	**Rinse**
Di-ethyleneglycol monobutyl ether	60%	80%
2-Ethanolamine	20%	Not required
Morpholine	5%	Not required
DI water	15%	20%

The development of HAR microstructure requires not only the understanding of the X-ray irradiation condition but also an understanding of the reaction of developer solution with irradiated samples. In general, the development of PMMA in organic solvent such as GG developer is complex and many aspects are not known. However, many studies directly attributes the dissolution of PMMA to reduction in molar mass in the exposed area. This gives rise to a molar mass-dependant solubility which can be described by applying the model of Hildebrandts solubility parameter or Hansens solubility sphere [139]. Also each X-ray lithography facility use different PMMA sheet formulated with different processing

conditions. It is essential to establish relationship between X-ray exposure dose and corresponding realised structural depths for a particular beamline setup/X-ray lithography facility. It is therefore required to estimate the relationship between the delivered dose and obtained depth for test structures fabricated in PMMA at SDXRL beamline

Dissolution of PMMA in GG developer

The dissolution of a polymer into a solvent involves two transport processes: (i) solvent diffusion (ii) chain disentanglement [140]. When un-crosslinked polymer is in contact with a thermodynamically compatible solvent, the solvent will diffuse into the polymer. As a result of plasticisation of the polymer by the solvent, a gel-like swollen layer is formed along with two separate interfaces, one between the glassy polymer and gel layer and the other between the gel layer and the solvent. Stress in the gel layer relaxes by disentanglement of the polymer chains. The released and now independent polymer chains diffuse through the developer away from the developing resist surface. Each stage in the dissolution process is accompanied by a large reduction in viscosity of the polymer solvent mixture as the solvent fraction in the polymer increases.

Pure polymer	Infiltration layer	Solid swollen layer	Gel layer	Liquid layer	Pure solvent

Figure 3. 17 : **Schematic representation of the composition of the surface layer during polymer/solvent dissolution**

The structure of the surface layers of glassy polymers during dissolution from the pure polymer to the pure solvent is given in the figure 3.17**.** A polymer contains free volume in the form of number of channels and holes of molecular dimensions. The first penetrating solvent molecules fill these empty spaces and diffusion process starts. The dissolution process containing all the above layers is called ‘normal dissolution’ and PMMA showed normal

dissolution process beginning at the glass transition temperature. By decreasing the experimental temperature a steady decrease in the gel layer thickness was observed and finally no gel layer was visible at the gel temperature (temperature at which transition from normal dissolution to cracking occurs) [140].

In a study by Parsonage et. al. [141] it was shown that the dissolution is controlled by *chain disentanglement*, which is a function of polymer molecular weight. Larger molecular weights results in higher levels of disentanglement. Besides the molecular weight of the polymer, the dissolution process can also be affected by the chain chemistry, composition and stereochemistry of the polymer as well as the type of penetrating solvent [142]. External parameters such as agitation, temperature and radiation exposure influences the dissolution process. The ultrasonic agitation causes the solvent molecules to penetrate inside PMMA into greater depths and as such the velocity of dissolution increases. When agitation is present, no gel layer is formed because it is stripped off rapidly by the stirring process. The effect of temperature on the dissolution of polymer is given by the polymer-solvent interaction parameter. The Flory-Huggins solution theory uses ξ to determine whether two polymers A and B will be miscible by the equation:

$$\chi_{AB}=[V_{ref}\,(\xi_A-\xi_B)^2]/R_GT \qquad (3.7)$$

where V_{ref} is an appropriately chosen reference volume, often taken to be 100 cm^3/mol, R_G is gas constant. Liquids with small χ are usually best solvent for a polymer and with increase of temperature χ decreases. This enhances the process of dissolution as compared to that taking place at lower temperatures. Dissolution of a polymer in a solvent is governed by the free energy of mixing governed by the equation:

$$\Delta G_m=\Delta H_m - T\Delta S_m \qquad (3.8)$$

where ΔG_m is the Gibb's free energy change on mixing, ΔH_m is the enthalpy change on mixing, T is the absolute temperature and ΔS_m is the entropy change on mixing. A negative value of the free energy change on mixing means that the mixing process will occur spontaneously. Hence when the temperature is increased, a negative value of free energy will indicate a spontaneous dissolution process.

Huggins coefficients have been estimated and knowledge about the dissolution of PMMA in tetrahydrofuran (THF), MIBK, methyl acetate has been investigated [142]. But behaviour of exposed PMMA in GG developer has more interest and has been studied by Schmalz et. al. [143]. It was shown that removal of the irradiated parts of PMMA is not a pure physical dissolving, but that there is a chemical reaction proceeding, the products of which are well soluble in polar solvents. They investigated the effect of GG developer on various types of PMMA samples with different tacticity, including atactic, syndio-tactic and isotactic. GG-developer is an alkaline liquid (pH 11.5-12) containing two long-chain alcohols which not only cause physical dissolution but also saponification and other side reactions. The reactions obey a two step mechanism. However, the primary nucleophilic attack of the carbonyl carbon by an OH^- ion is hindered in PMMA at pH < 12.5 because of the steric shielding by the neighbouring side chains. Only after some of the shielding side chains have been split off, may be due to X-ray irradiation, the reaction can take place on the neighbouring side chains. After the formation of the first carboxylic groups on this way, the saponification can continue in an intramolecular, autocatalytic process along the main chain. The active centers which facilitate the primary attack of OH^- can be methacrylic acid units as they exist in PMMA-MAA copolymers. These copolymers start the autocatalytic reaction by themselves. Another type of active centers are irregularities, defects in the shield which is result of exposure to high energy X-ray radiation causes the splitting of $-COOCH_3$ group in PMMA. This explains

the fact that an irradiated PMMA where these defects are randomly distributed along the polymer chain hydrolyzes much faster than unirradiated PMMA.

Isotactic PMMA shows a series of advantage over syndio-atactic PMMA. In an unirradiated state it is much less sensitive against the GG-developer and can tolerate longer exposure to GG developer solution. Therefore, the higher resist layer lithographically patterned isotactic PMMA can be kept in GG for longer time to obtain thicker microstructures without dissolving the unexposed part. The intra molecular, autocatalytic process requires intermediate unhydride ring structures which are more easily formed in isotactic PMMA. This is the reason why the autocatalytic saponification, after it has been started, is faster in isotactic PMMA than in syndio-tactic resulting faster development rate [143].

Previous studies have been reported for establishment of relationship between the exposure dose and developed depth in PMMA for few LIGA beamlines. These studies are carried out by groups at IMT, Karlsruhe at 2.3 GeV ELSA Bonn source, KIT at 2.5 GeV ANKA source, BESSY-II at 1.7 GeV machine with 4 T wavelength shifter and Taiwan light source. In such studies, the development of PMMA in GG developer at temperature (room, high and reduced), and with mechanical agitation were investigated. Pantenburg et. al. have shown that, at room temperature, crosslinked material has a higher contrast and a higher development dose compared to noncrosslinked material, while at 37 °C they observed no significant difference in contrast and minimum dose. It suggests that at high temperature, the GG developer has dissolubility of lower molecular weight PMMA. The developing rates at 21 °C are approximately ten times slower than at 37 °C for dose values at 3 kJ/cm^3, which is a typical dose value at the bottom of irradiated PMMA areas. Further, the difference in developing rates becomes less for higher dose values [144, 145]. The mechanical agitation using megasonic agitation increases the development rate without producing any negative

effect on low feature PMMA structures [146, 147]. The dissolution rates using micro structured PMMA and bare PMMA sheet, is given by Meyer et. al. [148]. It was pointed out that dose deposition at the depth may vary, leading to different dissolution rate and thus proposed to use bare PMMA sheet. It will be always better to obtain the dissolution rates inside the microstructures and higher resist thickness to estimate actual development rates of the microstructures. Very small features of the microstructures should be avoided to reduce the error in estimation; preferred features are 100-500 μm. In summary, these studies shows involvement of many parameters to account the development of PMMA including type of PMMA used (crosslinked, non-crosslinked, Molecular weight), the developer temperature, the developer type, synchrotron source used (dose rate, mean photon energy), the time between the exposure and the development, the aspect ratio of the microstructures, the dose deposited.

Processing depths of resist (PMMA) as function of exposure dose is investigated at two X-ray energy spectral band. The first energy range 2.5-9 keV and second energy spectral band of 2.5-24 keV are used. During exposures at both spectral energy range, Indus-2 is under 2.5 GeV operation and average ring current is between 60-80 mA. Exposures of PMMA are carried out using polyimide (50 μm) gold (15 μm) X-ray mask containing curved structures. Figure 3.18 (a) shows the established relationship between the processing depth of PMMA resist after 24 hours of development and various X-ray doses given at SDXRL beamline. Initially, a steep upward trend in development rate is observed and is due to faster dissolution of PMMA at top surface, where maximum dose have been deposited and dose scales with depth. As the developing time increases, dissolution rate is low due to lower dose deposited at higher depths.

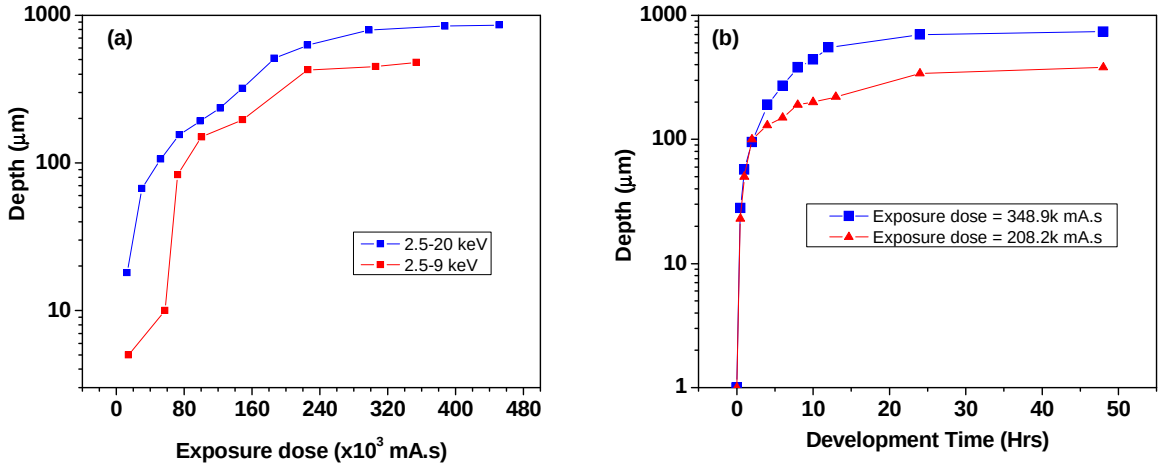

Figure 3. 18 : (a) Processing characteristics of SDXRL beamline at various exposure dose with constant development time, and (b) processing depth at two exposure dose as function of development time.

For a dose value of (1483 mA.min), the obtained depth is 130 µm for 24 hrs of development which is close to estimated values of 200 µm given in table 3.10 at scanner2. The obtained depth shown in figure 3.18(a) is for 24 hours. However, if the same sample is kept for longer time in the developer solution, the depth will be more than 200 µm. Two different exposure doses in 2.5-9 keV spectral range are given to PMMA sheet. Samples are separately developed upto 48 hours and measured depth as a function of development time is shown in figure 3.18 (b). Upto a depth of 100 µm, the two curves follow identical path. Owing to different exposure dose values, the depth achieved in both the cases are different which is in accordance with the bottom dose value delivered at that depth.

3.2.3.3.1 Estimation of dissolution rate of PMMA in GG Developer

The dissolution studies for PMMA are carried out at SDXRL beamline to determine the effect of exposure dose rate and exposure energy. Dissolution of PMMA microstructures is

estimated by maintaining the developer in three different conditions (different temperatures and mechanical agitation).

The dissolution rate is a function of polymer molecular weight and is related to the initial molecular weight of PMMA, the dose given and the main chain scission yield. The dissolution rate $R(D)$ is estimated based on the similar studies carried out by Meyer et. al. [148]. The dissolution rate $R(D)$ is given by the following formula [149, 150]:

$$R(D) = R_0 + C\left(MW_D\right)^{\varphi} \tag{3.9}$$

Using equation (3.3).

$$R(D) = C \times \left(\frac{1+\frac{G_{SC} \times MW_{D_0} \times D}{100 \times 1.6E-19 \times N_A \times \rho}}{MW_{D_0}}\right)^{\varphi} \approx C \times \left(\frac{G_{SC}}{100 \times 1.6E-19 \times N_A \times \rho}\right)^{\varphi} \times D^{\varphi} \tag{3.10}$$

Finally the above equation can be approximated by empirical relation [151]:

$$R(D) = KD^{\varphi} \tag{3.11}$$

with $K = c \times \left(\frac{G_{SC}}{100 \times 1.6E-19 \times N_A \times \rho}\right)^{\varphi}$ and K is function of particular beamline configuration and type of resist. φ is dependent on solvent, temperature and agitation of solvent, type of resist.

The dissolution rate can be estimated by measuring the etched depth of PMMA once the development is done, using suitable microscope/CMM/stylus probe as a function of time. The calculation of the rate, using the experimental data, depth h versus dose (D), is based on the following equation [148]:

$$h_i = \int_0^{t_i} R\left(D_{h(t)}\right) dt \text{ and } D_{(h)} \approx D_T e^{-\mu h} \tag{3.12}$$

where D_T is absorbed dose at the top surface of PMMA, h the distance measured from the top surface to bottom, $h(t)$ is the distance from the surface at time t. Using (3.11) and (3.12),

$$h = \frac{1}{\mu\varphi}\ln\left(1 + KD_T^{\varphi}\mu\varphi t\right) = a\ln(1 + bt) \tag{3.13}$$

where $a = (\mu\varphi)^{-1}$ and $b = KD_T^{\varphi}\mu\varphi$

and dissolution rate $R(t) = \frac{dh}{dt} = \frac{ab}{1+bt}$ (3.14)

In order to estimate the value of dissolution rate, using (3.13), the experimental data of depth verses time for various dose profiles are fitted. The various values of *a* and *b* are calculated from fitting done for respective absorbed dose. These values are used to calculate the various *R*(*t*) values corresponding to dose profiles at specific time. Finally, a curve of dissolution and dose is obtained which is fitted using equation (3.11) to obtain the value of *K* and φ parameters.

PMMA sheets of dimensions 10 mm (width) x 10 mm (length) of 1 mm and 2 mm (thickness) are patterned at the same exposure dose values as given during X-ray exposure studies and also higher exposure dose values. Stencil cut SS mask containing squares and hexagonal patterns are used to replicate the patterns on PMMA at same exposure dose 166-833 at Scanner1 and 385-4000 mA.min at Scanner2 in vacuum condition. Polyimide membrane mask containing curvature profiles (as shown in figure 3.5(b)) are used to transfer its pattern by providing exposure dose of 166-833 mA.min. The care is taken that scattered dose from resist mounting plate does not absorb at bottom side of PMMA by introducing a 200 μm PMMA sheet. The effect of mechanical agitation of developer solution on PMMA developed is explored in case of one sample. For this, ultrasonic system operating at 25-30 kHz frequency is used. The measurements of processed depths are carried out using COM. The minimum step resolution of this microscope is 7 nm with repeatability of 13 nm along depth direction. The depth measurement are done after each development time is done by focusing the top/bottom surface in the eyepiece and recording their position difference.

For simplicity and accuracy of measurements, 100 and 200 μm wide features are used to determine the depth of the structures. Figure 3.19 (a) shows time dependant measured depth

for respective exposure dose profiles. The measured points are fitted using 3.13 to obtain the values of a and b from fitting. Dissolution rate $R(t)$ for each exposure values is calculated using 3.14. Calculated value of $R(t)$ for different exposure dose is shown in figure 3.19 (b) is then used to derive the values for K and φ. Similarly, the same depth and dissolution rates are estimated for polyimide membrane based mask. The obtained depth-development time curve and dissolution rate are shown in figure 3.20 (a) and (b) respectively. In order to quantify the performance of beamline at scanner2, a higher exposure dose is given to PMMA and keeping the top dose below the damaging dose. Figure 3.21 shows the depths obtained in PMMA for preset development time. In this case, for each exposure dose, the absorbed dose profile is obtained using DoseSim and shown in figure 3.21 (b) with the measured value of $R(t)$. The values of K and φ for these three exposure conditions are estimated. Therefore equation 3.11 in dip development of PMMA resist for SDXRL beamline in the energy range 2.5-9 keV for different X-ray mask type and exposure dose values is given in table 3.12. These values are calculated for /s exposure time and not normalised for /cm exposure scanning length.

Table 3. 12 : Estimated value of K and φ in different exposure conditions.

Type of X-ray mask	**Equation 3.11 can be written as:**
For SS mask, scanner1	$R(D) = 0.0001 \pm 0.000031 D^{1.281 \pm 0.23}$
For polyimide mask, scanner1	$R(D) = 0.00013 \pm 0.00006 D^{1.21 \pm 0.24}$
For SS mask and high exposure dose, scanner2	$R(D) = 0.0046 \pm 0.00074\, D^{0.51 \pm 0.1}$

The value of K matches with the reported results in the literature. However, the value of φ is 20-30 % lower. This difference is may be due the different PMMA sheet used in present work and change in exposure dose. The molecular weight is 2000k mol/g and it is likely to dissolve slower in comparison to 450k or 950k PMMA resist. Change in exposure dose

profile may be due to source oscillation or beamline optics and it may also due to the variation in dose deposition along the depth due to ± 7 % variation in horizontal intensity.

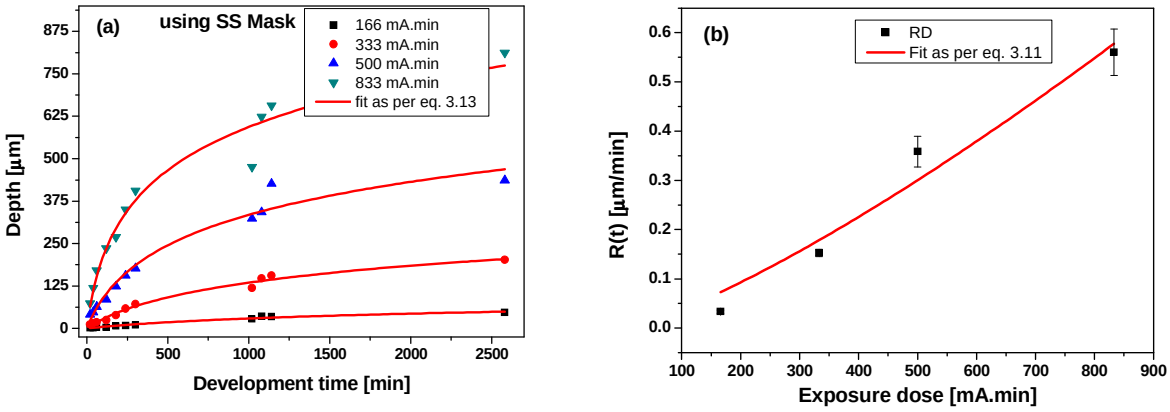

Figure 3. 19 : Depth (symbol) Vs the development time for different exposure dose and solid line shows fit for estimating the value of *a* and *b* when SS mask is used, and (b) Dissolution rate obtained from various *a* and *b* values for different exposure dose and fitted to obtain the value of *K* and *φ*.

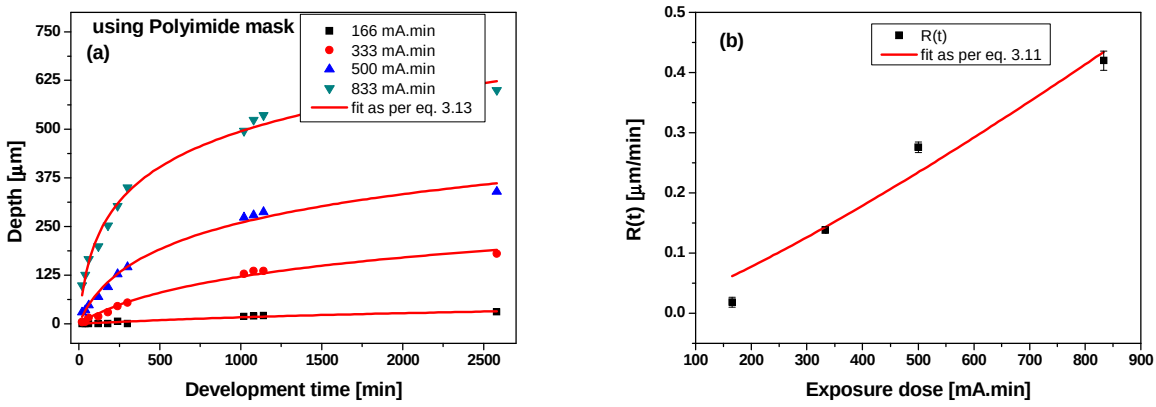

Figure 3. 20 : Depth (symbol) Vs the development time for different exposure dose and solid line shows fit for estimating the value of *a* and *b* when polyimide mask is used, and (b) Dissolution rate obtained from various *a* and *b* values for different exposure dose and fitted to obtain the value of *K* and *φ*.

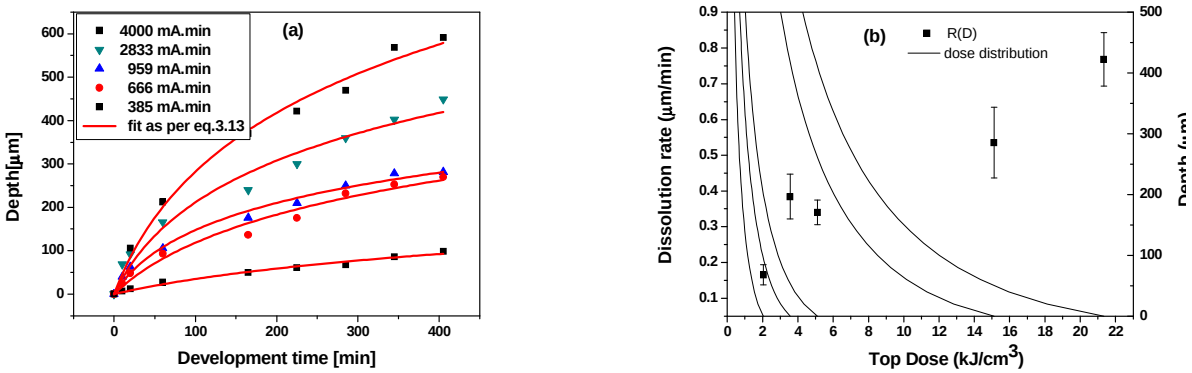

Figure 3. 21 : (a) The development depth when high exposure dose are used. (b) Dissolution rate as a function of top and bottom dose.

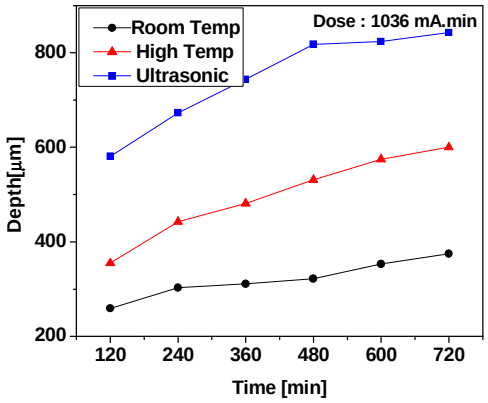

Figure 3. 22: Development of PMMA in three different conditions.

Figure 3.22 shows obtained depth of microstructures in three development conditions, room temperature, 37 °C and ultrasonic agitation condition for X-ray exposure value of 1036 mA.min in the same energy range. The obtained depth from ultrasonic development is almost three times higher compared to the room temperature development. This is understood that mechanical agitated development quickly removes the gel layer and thus allowing the high rate of pure solvent availability into pure polymer layer to achieve higher depth. The χ parameter is temperature dependant. At higher temperatures, χ reduces and enhances the miscibility of two solutions giving more depth compare to room temperature.

Taking into account the understanding of the dissolution rate of PMMA and the required absorbed dose for obtaining high depth, HAR microstructure are developed. One such typical structure is fabricated using stainless steel X-ray mask in PMMA resist is shown in figure 3.23. The exposure is carried out in vacuum (10^{-2} mbar) using scanner2 and given exposure dose is ~ 5500 mA.min and development time of 3000 min. The shown honeycomb patterns are in HAR of 25. This hexagonal structure with minimum feature size 30 μm may be used as IR filter or if moulded in PDMS, can be used as microsieve for filtration of liquid flowing from top to bottom.

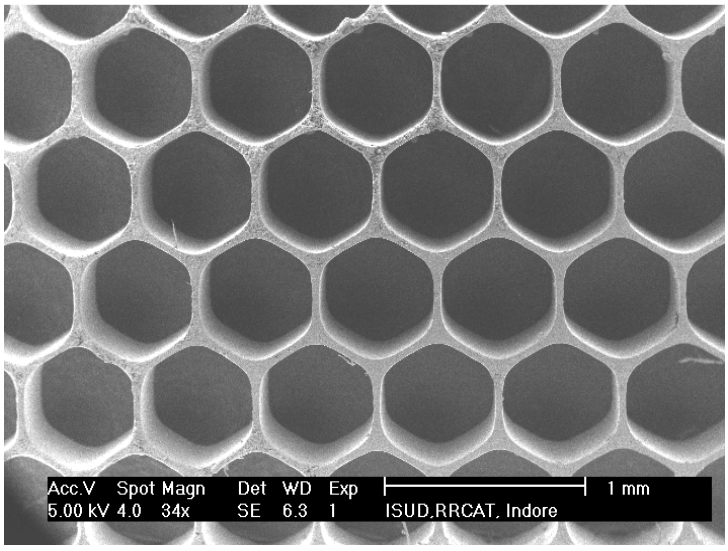

Figure 3. 23 : HAR microstructure of hexagonal pattern with 30 μm wall thickness and 1000 μm in deep fabricated in PMMA.

3.2.4. Fabrication of microstructures in SU-8

3.2.4.1 Sample preparation

SU-8 with various viscosities are spin coated over ϕ 100 mm Si wafer for obtaining thickness of 1-600 μm in single steps. Higher thickness (>1 mm) are obtained through casting process.

SU-8 is required to be prebaked on hot plate for solvent removal. Solvent removal during soft baking is accompanied by volume shrinkage and mechanical stress. Accumulated stress in the resist layer increases with increasing film thickness. A study highlights that major (upto 50 %) contribution to film internal stress is due to soft baking and remaining come from exposure, post exposure and development conditions [152]. Insufficient prebaking leads to the non removal of solvent which results in (1) formation of bubbles during post-exposure baking, (2) collapse of features due to lower mechanical stability at the bottom because of the higher solvent content and (3) increased lateral diffusion rates of the acid generator molecules outside of the masked areas during post exposure baking and therefore lower contrast between crosslinked and un-cross-linked areas [153]. If the resist is too hard, cross-linking in the irradiated areas will be hindered. Therefore, soft baking time is optimised for each particular thickness during fabrication. Table 3.13 illustrates the processing parameters for various SU-8 variants optimised for fabrication of HAR microstructures. The shown values are based on the SU-8 datasheet and our optimised processed values. In a typical soft baking cycle, SU-8 is soft baked for few minutes at 65 °C (above glass transition temperature T_g = 55 °C) where organic molecules can freely migrate. A slow ramping from 65 °C to 95 °C is done in order to reduce the internal stress of thicker films. The sudden changes in soft baking temperature provide thermal shock to resist layer and this may leads to cracks or rippled structure on top layer. The soft baking temperature higher than 95 °C can be increased upto 120-130 °C to reduce the soft baking time but less than 135 °C to prevent SU-8 from polymerisation due to activation of photoactive compound [154]. At the end of soft baking cycle for each substrate, SU-8 coated substrate is removed from the hot plate only when temperature is below 50 °C which ensures re-crystallisation of SU-8 film around its T_g and reduce its internal stress. SU-8 can also be coated to a thickness greater than > 1 mm using

multiple spin coating. However, multi coating is a time consuming process and surface flatness is a critical issue. The solvent content in subsequent coating layers may be different, resulting in a complex and complicated lithography process. In the present case, multi-spin coating is not carried out for formation of thick resist layer. The thick layer of SU-8 is instead obtained by introducing the fixed volume of SU-8 25/2100 solution on the substrate and soft baking is carried out. In order to obtain 600-700 μm thick layer, SU-8 25 is dispensed on the substrate to an approximate diameter of 50 mm. The solution is spread on the wafer by slowly tilting and rotating. The thickness of the SU-8 resist layer is dependent on the diameter of the dispensed liquid on the surface and error of ± 50 μm is observed. Thickness of 600-1000 μm having smooth flat SU-8 layer is obtained using this technique in comparison to casting process and also reduces mechanical machining step for removing the casting jig. Same method has been followed to obtained the higher thickness (>1mm) using SU-8 2150.

Table 3. 13: SU-8 characteristic processing times (in minutes) for different variants and film thickness used in this thesis [55, 56].

SU-8 type	**Viscosity [cSt]**	**Thickness [μm]**	**Soft bake [min]**		**Post-exposure bake[min]**		**Development [min]**
			at 65 °C	**at 95 °C**	**at 65 °C**	**at 95 °C**	
Spin coating technique							
SU-8 2002	7.5	2–5	1	2	1	1	1
SU-8 25	2500	15–100	3–5	5–30	1-5	2–20	3–6
SU-8 2100	45000	100–400	5–7	20–240	1-5	10–30	10–40
SU-8 2150	45000	300–600	5–7	60–300	5-7	15–40	20–50
Constant volume technique							
SU-8 25	2500	600-1000	90	720-900	10	50	45-50
SU-8 2100	45000	1000-1500	120	1200	10	60	60-90

3.2.4.2 Exposure at X-ray lithography beamline

The exposure dose criterion for SU-8 is discussed in table 3.9. The sensitivity of SU-8 to X-ray is dependent on the concentration of PAG present in its formulations. The Microchem datasheet suggests that for 1% (5%) PAG concentration in SU-8 formulation, X-ray absorbed dose of 20 (10) J/cm^3 is required. During each exposure at beamline, care is taken to keep the temperature of SU-8 due to SR heat load below its glass transition temperature otherwise the flow of SU-8 is observed which distorts or collapses the microstructures. The exposed SU-8 area has different glass transition temperature. X-ray exposure time for SU-8 samples at SDXRL beamline is reasonably smaller in comparison to PMMA. Table 3.14 gives the various exposure times for absorbed dose of $D_B \sim 20$ J/cm^3 and required mask contrast. The X-ray lithography experiments are carried and optimised for X-ray energy range 2.5-9 keV considering the designing of X-ray mask, dose under shadow region, pre and post exposure bake and development. Thicker SU-8 resist layer and higher photon energies require very high mask contrast leading to complexities in fabrication of higher absorber thickness with high quality X-ray mask.

Table 3. 14 : Exposure parameters for SU-8 at SDXRL beamline

Serial no	Thickness of substrate [μm]	Mask Absorber thickness [μm]	Dose under mask [J/cm^3]	Dose top [J/cm^3]	Mask contrast	Exposure time /cm scan length [min]
1	200	9.7	0.050	41.5	830	12
2	500	11.4	0.049	90.5	1846	26
3	1000	13.5	0.052	237.8	4756	67
4	2000	17.0	0.053	1010.8	19056	285

3.2.4.3 Development of microstructure

Before development, post exposure bake (PEB) is necessary to complete polymerisation of SU-8. PEB is equally important steps like soft bake. During this process, additional thermal energy is supplied to resist layer to amplify the concentration of acid to complete the crosslinking reaction quickly. In this thesis, PEB temperature is used above 65 °C, which is again higher than T_g of unexposed SU-8 layer. The optimised PEB time is given table 3.13. PEB will re-softened the unexposed resist at > 65 °C and the stress formed at exposed/unexposed interface layer of SU-8 will be released. The SU-8 substrate is again allowed to reach to the temperature below 50 °C before its removal from hotplate. Faster cooling creates stress at exposed/unexposed interface which may leads to the cracks of fine features. Cross-linked SU-8 is highly resistant to chemical attack, sustain at higher temperature and it also used as a structural material for many device applications.

Finally, SU-8 is developed in propylene glycol monoether acetate (PGMEA) (Microchem Corporation, USA). Figure 3.24 shows the first X-ray lithography structure fabricated at SDXRL beamline on early dawn of February 19, 2011. Si wafer (ϕ 50 mm diameter) coated with SU-8 2100 is used to form the lithographic structure at air based scanner. A micropillar of 200 μm diameter with depth of 170 μm is shown.

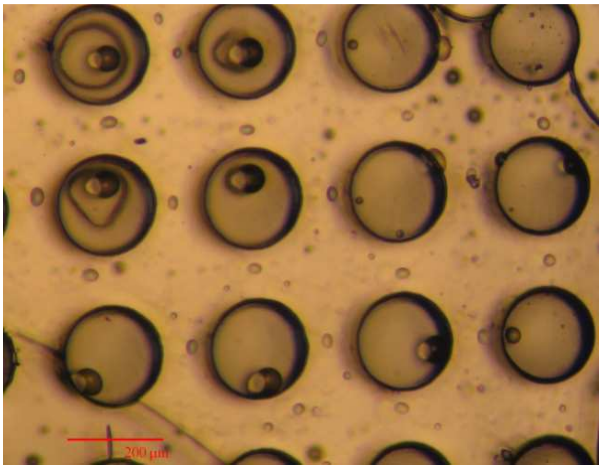

Figure 3. 24 : Micro-pillars fabricated in SU-8, 200 µm in diameter, 170 µm deep and 300 µm pitch. The bubbles observed on the substrate are due incomplete washing and drying of substrate.

3.2.5. A few studies on the micro fabricated structures

In this section, few analyses of structural accuracies of fabricated microstructure are presented. The microstructures produced in two different X-ray energies are compared as well as their dimensions in the exposed side and back side are measured.

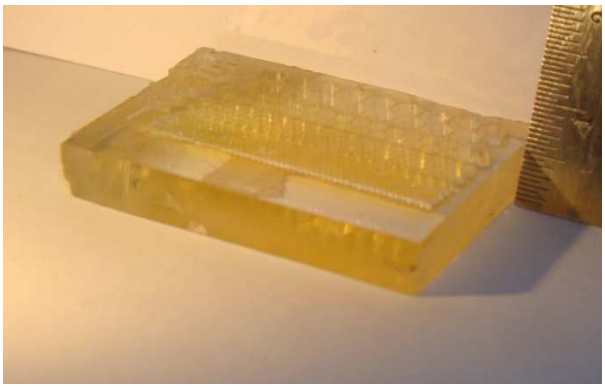

Figure 3. 25 : Photograph of 6mm thick PMMA sheet showing the developed Honeycomb structure using DXRL process.

3.2.5.1 HAR fabricated at SDXRL beamline

The smallest dimension that can be obtained in case of PMMA depends on the X-ray energy spectrum, dose profile and molecular weight of the PMMA. The smallest feature and also the taperdness in the structure is also dependant on the quality of the collimation of the X-ray beam from synchrotron after conditioning it using mirror. The smallest dimension produced with Indus-2 X-ray lithography system is down to 5 μm. The MFSs are limited by the availability of technology for producing submicron features X-ray mask. The maximum depth of ~ 3200 μm is achieved in 6 mm thick PMMA resist layer. Photograph of 6 mm thick PMMA substrate with hexagonal structures is shown in figure 3.25 and corresponding top view of microstructure obtained from SEM is shown earlier in figure 3.23. The MFS of 30 μm and HAR ~ 100 are obtained.

Similarly, the SU-8 resist layer of 1200 μm is prepared using constant volume technique over OmniCoat layer on Si wafer. A microgear pattern is formed on SU-8 layer using sacrificial process in SU-8 is shown in figure 3.26. In this case a variation at the teeth profiles is due to error/distortion in UV mask which is used to produce X-ray mask. The measured dimensions are in concurrence with the dimensions of X-ray mask.

The effect of horizontal and vertical divergence with one to one dimension correlation of UV mask, X-ray mask and actual produced structure is carried out and is discussed in next Chapter, section 4.4.2.

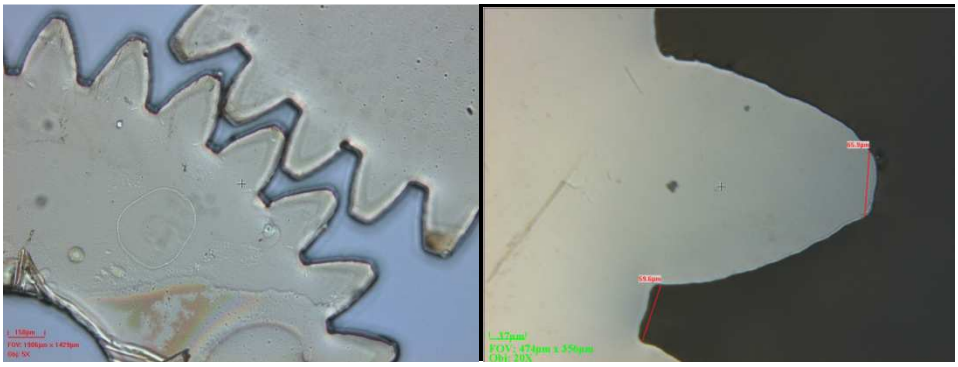

Figure 3. 26 : SU-8 microgears with involute profile.

3.2.5.3 Effect of horizontal intensity uniformity

Though the horizontal intensity uniformity is within acceptable limit, the dose deposition inside resist along depth would be non uniform. Therefore it is not straight forward to estimate the depth according to horizontal uniform intensity. PMMA 2 mm thick sheet is used to copy the X-ray mask patterns (40 μm-500 μm features) using X-ray lithography 2.5-9 keV X-ray spectral range. The lateral size of the sheet is 80 mm x 30 mm. After each development step, the depth of the microstructure is measured using COM. Total 14 measurement points on resist, each separated at 5 mm distance along the width of beam (70mm) at scanner1, are used to measure the depth. There are five points at which the measurements are not performed; two of them are extreme ends where the beam intensity falls rapidly and three points at the middle where no microstructure patterns are available from X-ray mask. No systematic influence of the feature sizes or geometry of the microstructure on the development is observed. Figure 3.27 shows the depth measurement carried out for resist exposed for 2167 mA.min in the energy range 2.5-9 keV. The solid line shows the average depth along horizontal line of the resist and each symbol represents the measurement carried out at points mentioned earlier. The values given near the right hand

axis are for development time. For a measured average depth upto 820 μm and total development time of 660 minutes, variation in depth is within ± 5% from average value. As development time increases (24-48 hrs), the measured depth values on right side of figure matches well with average depth values as the width of recesses is 800 μm wider. Left side measured depth values shows larger difference, 73 μm less than the calculated average value 1104 μm. This difference in the measurement corresponds to an error of 6.6 % which is below the measured intensity uncertainity of ± 7 % in horizontal line. For 2880 minutes development measurement, the clean focused bottom surface could not be detected in left side structures (see figure 3.27) and this may be due to non-reflection of light from higher depths.

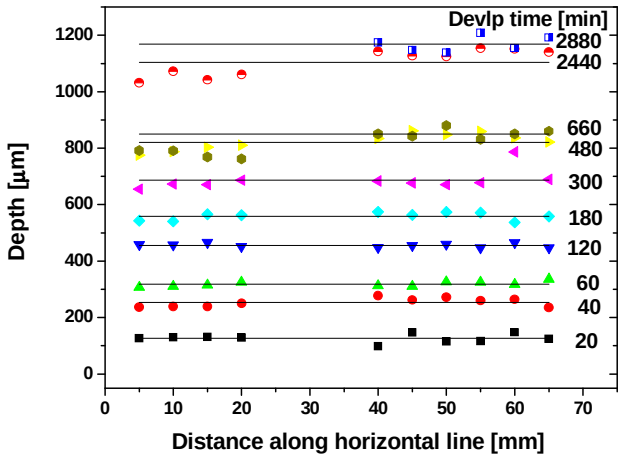

Figure 3. 27: Measured depth profile along 80 mm wide PMMA sheet.

3.2.5.5 Surface roughness measurements, SU-8 and PMMA.

X-ray lithography provides the vertical sidewall roughness in the range of 10-20 nm. The surface roughness is a quality factor for microstructure produced using X-ray lithography,

particular useful for the devices used in optics. The surface roughness measurements of sidewall of produced structures are carried on suitable microstructures detached from PMMA/SU-8 resist layer. The structure is fixed on the COM stage using clay, such that the vertical sidewall of microstructure faces up under microscope. The COM is calibrated using polished Si wafer (roughness 0.5-0.7 nm). The samples are aligned normal to microscope optics and area used for surface roughness measurements is 474 μm x 356 μm with 20X magnification objective. The measured sidewall roughness results of PMMA and SU-8 microstructures are given in table 3.15. Both the samples show average roughness in the range reported in the literature. If any deviations in the X-ray mask are easily replicated in higher sensitive SU-8 material. The surface height variation is found to be 32 nm. The average roughness of this sample is 4.9 nm with peak to valley roughness value is 32 nm. PMMA has shown comparatively better value.

Table 3. 15 : Roughness measurement of vertical sidewall in PMMA and SU-8

	Top Surface	**Sidewall Roughness**	
Materials	**Si wafer**	**PMMA**	**SU-8**
Average roughness [nm]	0.55	1.6	4.9
Roughness, peak to valley [nm]	4	12.6	32

3.2.5.7 Fabrication of 3-D structures

At SDXRL beamline, variation in X-ray exposure dose is possible by either using grey scale mask or independent movement of varying profile of mask and a resist. The grey scale mask is not yet fabricated at SDXRL facility. Independent motion of resist and mask are possible using the home made linear and rotary stages at air based scanner1. Resist or mask can be displaced with respect to each other by keeping reasonable gap (10-30 mm) between them. In this, two exposures on front and back side using tilted line mask is carried out. In

second exposure, the mask is translated by pitch length of coil and resist is rotated by 180°. The fabricated microcoil structure in PMMA coated over cylindrical substrate is shown in figure 3.28. Due to poorer resolution and back lash error in the stages, two step exposed structure did not match well and error is seen in the produced structure.

One more type of 3-D structure is fabricated where two exposures are carried out with and without X-ray mask. In a typical exposure condition, X-ray mask with 100 μm diameter holes is used for first exposure in PMMA. The exposure dose of 1333 mA.min is given. In second exposure, mask is removed and PMMA sheet is only exposed to X-ray beam with delivered exposure dose of 666 mA.min. A curved neck structure is generated with topmost diameter of ~150 μm and bottom diameter ~100 μm. The developed curved neck holes in PMMA are shown in figure 3.29. X-ray exposure of same hole dimension is given to PMMA at 45° tilt and both resist and mask is rotated at 0°, 90°, 180°, 270°. In this way of exposure, an interwoven crossed microcavity structures are fabricated in PMMA which can be used for photonic crystal.

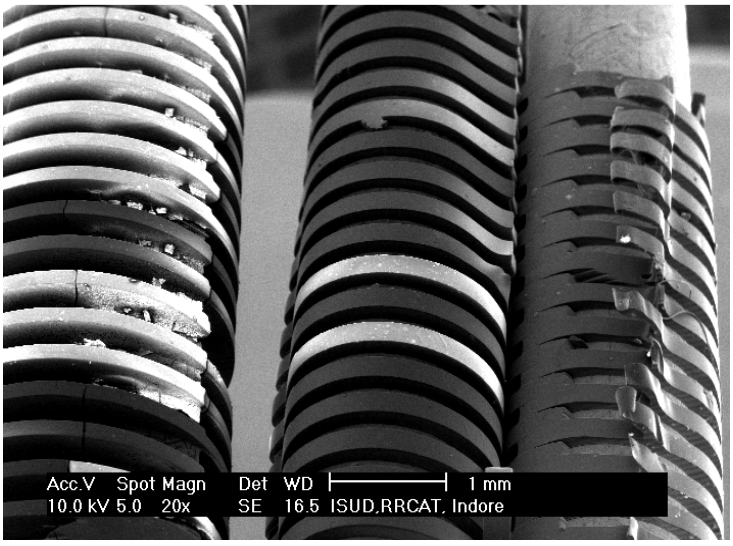

Figure 3. 28: SEM micrograph of fabricated microcoil on cylindrical substrate.

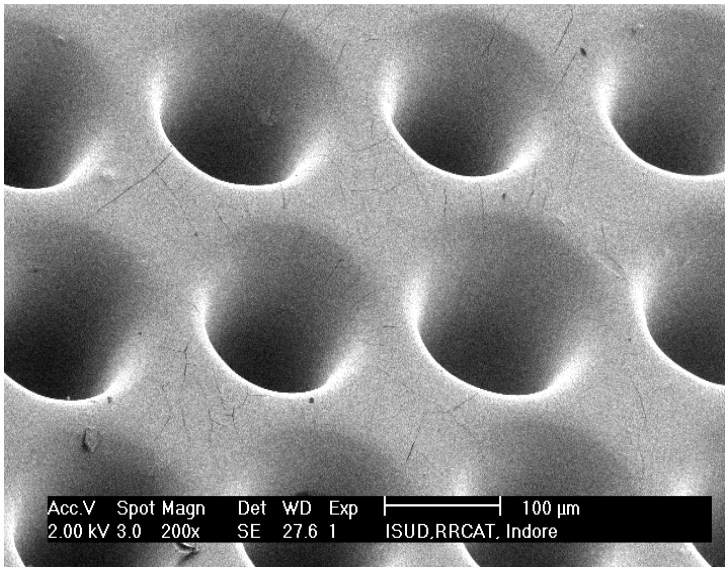

Figure 3. 29 : Curved neck tapered structures fabricated in PMMA. The diameter of top circular hole is 150 μm and bottom circular hole is 100 μm.

In conclusion, a technology for the fabrication of two membranes (SU-8 and Polyimide) based X-ray masks has been achieved. The X-ray mask based on Cu metal foil was also developed. In order to qualify the developed X-ray lithography facility, a few test structures in PMMA and SU-8 were patterned. In series of experiments carried out where different thickness of resist are used. also In this case, exposure time, processing conditions are optimized for obtaining a depth ~3200 μm in PMMA and 1200 μm in SU-8. The effect of X-ray exposure dose on PMMA is evaluated using FTIR, Raman, optical microscope and XRD measurements. The analysis on structural accuracy of produced microstructure is carried out and the results compare well with theoretical estimated results and are also comparable with DXRL results available in the literature.

Chapter 4

Design and development of X-ray refractive lens and its characterisation

Almost two decades back, refractive optics for focusing X-ray was considered impractical, as in this region refractive index is slightly less than unity and absorption is high [155]. With the surge in microfabrication technologies, the possibility of developing X-ray refractive lenses became viable. The first design concept for the fabrication of X-ray refractive lens was proposed by Tomie [156]; pointing out the advantages of such optics compared with reflecting and diffracting X-ray optics. To compensate for weak refraction, many lenses were stacked together. The first refractive lenses for focusing hard X-rays were fabricated and tested by Snigirev et al [157]. A series of cylindrical holes drilled by them in Aluminum with radius of curvature of 300 μm, focused 14 keV X-rays to 8 μm focal spot. The focal spot depends on source size, demagnification and aberrations. Cylindrical surface has spherical aberrations leading to the blur in the focus spot. The spherical aberrations can be removed using parabolic profiles and focal spot below 100 nm are achievable [158]. The developmental efforts towards refractive X-ray lens are focused towards smallest focal spot and operation at high energy with greater collection efficiency. X-ray refractive optics has been used for full field imaging [159], scanning imaging [160], SR beam collimation [161],

momentum resolved spectroscopy [162], reflectivity [163], diagnostics [164], XFEL pulse focusing [165] etc.

At Indus-2, X-ray beamlines are operational for X-ray diffraction, EXAFS, fluorescence and protein crystallography in 5-25 keV energy range. Using SDXRL beamline, the development of HAR X-ray refractive lens is initiated with an aim to deploy these X-ray lenses on synchrotron beamlines. Such developments were also initiated at ALS, ANKA, PLS SR sources. Presently, only ANKA has an active program for X-ray lenses development using XRL. The capabilities of SDXRL beamline and optimization studies carried out for microfabrication of HAR microstructures has played a pivotal role for developing the technology reported in this chapter. The present work is aimed towards the development of planar parabolic refractive lenses. The performances of these lenses are evaluated at Indus-2 (moderate emittance) and DLS (low emittance). The design, fabrication and microfocusing characterization results of X-ray lenses are presented in this chapter.

4.1 Choice of lens materials

All materials in the X-ray region have very small refractive index decrement and strong absorption. The refractive index decrement δ describes the strength of refraction with respect to vacuum. The imaginary part β is related to the absorption of X-rays in the medium. Owing to small refraction effects in the medium at X-ray wavelengths, the converging power of the lens is very small. δ / β is the figure of merit, that can be used as a criterion to choose the lens material for a given photon energy. Higher the ratio, higher the numerical aperture and better will be the resolution. Figure 4.1 shows δ / β for various materials of interest for refractive lens.

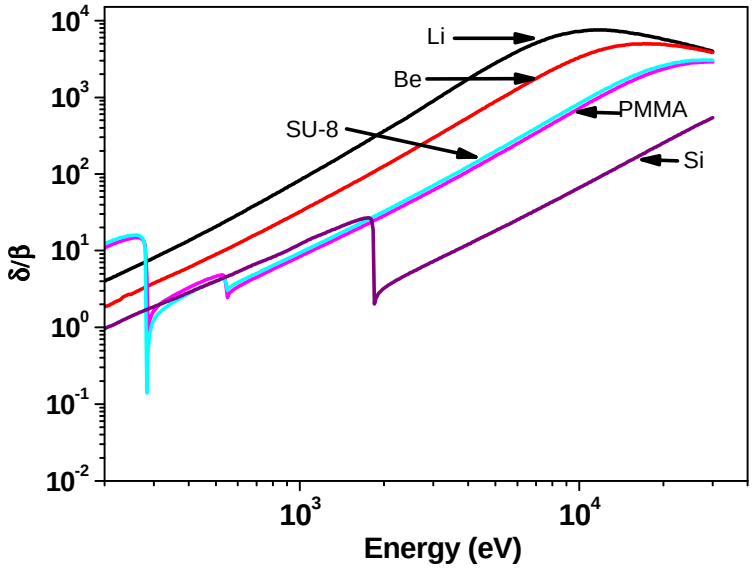

Figure 4. 1 : Figure of merit δ / β for various X-ray lens materials.

Lithium has best figure of merit. However, due to difficulty in handling, it is not suitable choice. Be is an interesting material but is hazardous due to toxicity of beryllium oxide. Be is used to make X-ray lens by mechanical punching process. Radius of curvature less than 50 μm is difficult to produce by punching method. The next suitable element is Carbon and its diamond form is presently being explored for the fabrication of CRL. The carbon based polymers are available as X-ray sensitive resist; PMMA and SU-8. The densities of these materials are 1.19 and 1.2 g/cm^3 respectively and provide reasonable good refractive power through lens surface. DXRL can produce X-ray lenses with high profile accuracy, HAR and low sidewall roughness in PMMA and SU-8. PMMA microstructure produced from DXRL has excellent side wall roughness (10 nm) but has low radiation resistance. SU-8 has comparable transmission and higher radiation stability > 2 MJ/cm^3 [166]. X-ray lenses made from PMMA are useful for microfocusing low intensity monochromatic X-rays. SU-8 can be used at high intensity and high energy in third generation SR source. Si has one order higher

absorption and therefore perform less efficiently. However, the microfabrication technology of Si is well established in micro electronics industry and used for X-ray fabrication.

In most of these materials, X-ray absorption is primarily due to photoelectric absorption. Therefore low Z materials are always preferred. At higher energy, Compton scattering dominates and small angle scattering causes the blur in the focal spot [167]. In photon energies 12-20 keV, materials like PMMA and SU-8 are good choice. Table 4.1 gives the summary of X-ray refractive lenses fabricated in various materials and their performances.

The most popular X-ray lenses are Be lenses which have been used at many SR sources for focusing and collimation. SU-8 X-ray lenses are now being used at few SR sources. The focused spot is dependent on the radius of curvature, source size and the source demagnification. If the lenses can be fabricated with higher accuracies and profile then ideally diffraction limited focused size is achievable.

4.2 Design of parabolic refractive X-ray lenses

In visible light optics, a focusing lens needs a convex profile because the index of refraction is larger than unity (n_{quartz} = 1.5). As discussed in Chapter 1, the real part of the refractive index (1-δ) for X-rays is slightly less than unity. Thus, focusing X-ray lens requires a concave shape. X-ray lenses can be fabricated in cylindrical, spherical, elliptical and parabolic profiles. X-ray lenses with spherical and cylindrical shape show strong spherical aberrations [168]. X-ray lenses are fabricated by punching, drilling and lithographic techniques. A trail of cylindrically parabolic shape is fabricated by lithography techniques

Table 4. 1 : Overview of refractive X-ray lenses developed worldwide using different techniques.

Lens Material	Energy range [keV]	Methods of fabrication	Focussed spot size [μm]	Profile /radius of curvature [μm]	Group/ Developer
Al	5-40	Drilling	8 @ f = 1.8m, 10 keV	Cylindrical/ 300	Snigirev 1996 [157]
Al	19.5-25	Mechanical punching	2-D: 0.55 x 5.4 @ f = 0.57m, 19.5 keV	Parabolic/200	Lengeler 2001[169]
Be	2-30, upto 120	Mechanical punching	1.14 @ f = 0.49 m, 12 keV	Parabolic/ 200	Schroer 2002 [170] , Lengeler 2004 [171]
Diamond	12.4-17.5	e-beam and DRIE	3.2 @ f = 1 m, 17.5 keV	Parabolic	Nöhammer 2003 [172]
Diamond	5-20	DRIE and deposition	1.6 @ f = 0.56 m,	Parabolic/ 50-60	Alianelli 2010 [173]
Glassy Carbon	12.2-25	Laser evaporation and copper vapor laser	1.4 @ f = 2.8 m, 25 keV	Parabolic/ 5-200	Artemiev 2005 [174]
Li	10.87	Mechanical punching	2-D: 17 x 33 @ f = 2.13 m	Parabolic/ 263	Pereira 2004 [175]
Ni	174	Punching	5 @ f = 3.1 m, 174keV	Parabolic/ 100	Andrejczuk 2014 [176]
Ni	100-1000	X-ray LIGA	1-D: 6 @ f = 4.6 m, 212 keV, 2-D: 7 x12 @ f = 2.3 m, 212 keV	Parabolic/20	Nazmov 2005 [177]
PMMA	8-16	X-ray lithography	16 @ 11.5 keV	Parabolic/1000	Mancini 2002 [178]
PMMA	10	X-ray lithography	0.7 @ , f = 0.75m, 10 keV	Parabolic/ 4	Zhang 2001 [179]
PMMA	10	X-ray lithography	2 @ f = 1 m	Parabolic/ 200	Dhamgaye 2014 [180]
PTFE	10	X-ray lithography	0.6 @ , f = 0.75, 10 keV	Parabolic/ 4	Zhang 2001 [179]
Si	8-25	photolithography and DRIE	1.8 @ f = 0.8 m 15.6 keV.	Parabolic with low absorption	Aristov 2000 [181]
Si NFL	21	e-beam and DRIE	2-D: 0.047 x 0.055 @ f = 0.011 m and 0.019 m.	Parabolic/ 2.0 and 2.86	Schorer 2005 [182]
SU-8	17.45	X-ray lithography	2.1 @ f = 0.57 m 17.45 keV	Parabolic/ 320 and 350	Nazmov 2004 [183]
SU-8	5-40	X-ray lithography	2-D: 0.3 x 0.7	Parabolic/5-20	Nazmov 2011 [184]
SU-8	8-100	X-ray lithography	0.8 @ f = 0.3 m, 14.9 keV	Parabolic/ 25, 50 and 100.	This work 2014 and [185]
SUEX	8-20	X-ray lithography	4-8 @ f = 0.3 m	Parabolic/ 25, 50 and 100	This work 2014.

and they focus the beam only in one dimension. To create a point focus, a cross geometry of two planar lenses are required. Concave X-ray lens profile (in 2-D and 3-D) with relevant terminology of cylindrically parabolic X-ray lens profile ($y^2 = \pm 2R\,x$) is shown in figure 4.2. X-rays are incident from left side and transmitted through lens to the right side. Along the bi-concave edges, incident X-rays undergoes refraction and converge at a focal plane due to the variation of refractive index between material and air.

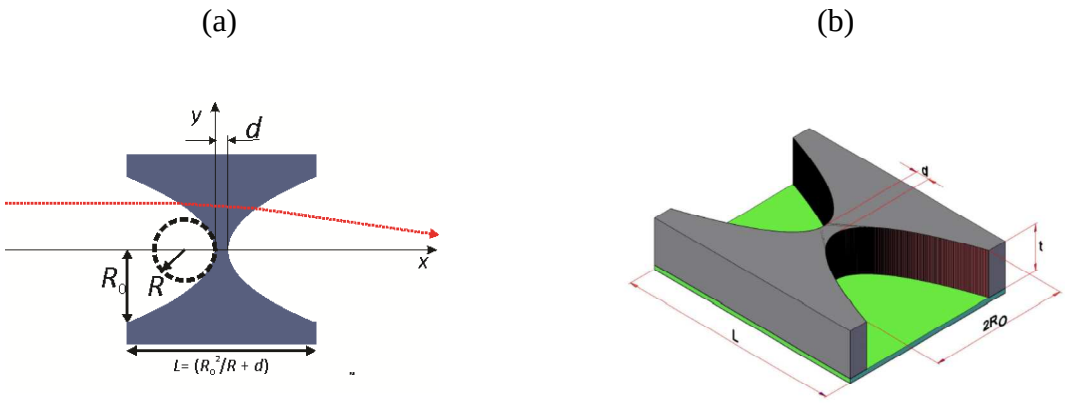

Figure 4. 2: Single parabolic lens consisting of bi-concave lens (a) 2-D view (b) 3-D view, where *R* is the radius of curvature at the apex and $2R_0$ defines the geometrical aperture. The thickness of the lens at the apex is *d* and total length of the single lens is given by ($R_0^2/R + d$) and lithographically developed depth *t*.

4.2.1 Focal length

When length of lens is very small compared to focal length, thin lens approximation can be used, where focal length of single cylindrically symmetrical parabolic lens is given by:

$$f = \frac{R}{2\delta} \qquad (4.1)$$

where R is radius of curvature of lens at the apex. For PMMA, at 10 keV, δ = 2.5 x 10^{-6} and R = 500 μm, the focal length for a single lens will be ~100 m. The radius of curvature has to be as small as possible to reduce the focal length which is limited by the manufacturing technology. Focal length can be reduced by increasing the number of individual lenses (N) with focal length $f_N = \frac{f}{N}$ and such lens combination is referred as compound refractive lens (CRL). With number of lenses (N), the focusing power of the lens increases due to 2N refraction by biconcave surface. However, this increases total length (L) of CRL and decreases the transmission due to absorption in the lens material.

4.2.2 Transmission

The transmission can be derived by integrating Lambert-Beer's law about the shape of the lens. The transmission T_{crl} for cylindrically symmetric parabolic shape is given by [186, 187]:

$$T_{crl} = \frac{\exp(-\mu N d)\left[1-\exp(-2a_p)\right]}{2a_p} \qquad (4.2)$$

where $a_p = \frac{\mu N R_0^2}{2R} + \frac{N\delta^2 R_0^2 k^2 \sigma^2}{R^2}$ accounts the attenuation inside the lens (first term) and effect of rms roughness (σ) of the lens, k is the wave number of the incident radiation. The second term of a_p can be neglected as roughness produced from DXRL is much smaller than attenuation length.

4.2.3 Effective aperture

The effective aperture of the lens is less than the geometrical aperture of the lens due to absorption of the incident beam in thickness of lens material through which rays are passing

and increases rapidly due to the parabola's radius of curvature. The effective aperture for a refractive lens is

$$A_{eff} = 2R_0\sqrt{\frac{1-e^{-a_p}}{a_p}} \tag{4.3}$$

Again surface roughness can be ignored here and for smaller value of a_p, effective aperture can be written as:

$$A_{eff} = 2\sqrt{\frac{2R}{\mu N}} \tag{4.4}$$

Effective aperture is related with the numerical aperture (NA) of the lens. Larger the effective aperture, larger the NA and better is the resolving power of the lens $\left(\text{NA} = \frac{A_{eff}}{2q}\right)$, where q is the distance between the image and lens.

4.2.4 Spot size

The microfocus beam sizes in lateral and transverse direction is an important property to define the performance of the microfabricated lens. The geometrical spot size is determined by the geometry of the lens setup and is given by:

$$F_{geo}^{x,y} = \frac{q}{p} S_{source}^{x,y} = m_{dem} S_{source}^{x,y} \tag{4.5}$$

where $S_{source}^{x,y}$ is the size of the source in lateral and transverse direction, p is the distance between the source and lens, q is the distance between the lens and image, m_{dem} is the demagnification factor. However, focus spot size is related to beam size due to geometrical setup and broadening by diffraction at the aperture. Therefore total lateral spot size is

$$F_{total} = \sqrt{F_{diff}^2 + F_{geo}^2} \tag{4.6}$$

and diffraction limited spot size is given by

$$F_{diff} = 0.75\frac{\lambda}{\mathrm{NA}} \tag{4.7}$$

which corresponds to FWHM of airy disc due to diffraction at the lens aperture.

4.2.5 Gain

Another important property which defines the performance of the X-ray lenses is gain. It depends on the beam size at focus, aperture of the lens contributing to the focus size and transmission of the lens.

For a cylindrically symmetric parabolic CRL, the gain is

$$G = \frac{2T_{crl}R_0^2}{F_{total}}\left(\frac{p-f}{f}\right) \tag{4.8}$$

4.3 Design of X-ray lenses

X-ray lenses are designed by considering the requirement of hard X-ray (8-20 keV) focusing experiments at Indus-2. The design specifications of the X-ray lenses are worked out for cylindrically symmetric parabolic shape lenses. Three different radii of curvatures are selected for design and development of lenses and some relevant parameters are given in table 4.2. The X-ray lenses with different radius of curvature are assigned as series name like, R = 100 μm is called here as Series A, Series B for R = 50 μm and Series C for R = 25 μm. The design of the lenses on a single chip (100 mm diameter Si wafer) ensures the constant focal length for desired energy range. Series A, B, C lenses are available on same chip and any trail of lenses can be brought in X-ray beam by traversing a distance ~45 mm in lateral or transverse direction depending upon the focusing geometry. Therefore, a designed lens chip provides versatility by microfocusing at different X-ray energy range and different focal

lengths. X-ray mask is engineered in such a way that 100 mm diameter Si wafer will have at least two sets of X-ray lenses pertaining to Series A, B and C.

Table 4. 2: List of few lens parameters chosen for design and development in this thesis.

	***R*[μm]**	**$2R_0$ [μm]**	***d* [μm]**	**Designed energy range [keV]**	**Total lenses (*N*)**
Series A	100	400	15-20	8-20	14-90
Series B	50	300	15-20	8-20	24-150
Series C	25	250	15-20	8-20	12-75

Table 4. 3: Various parameters calculated for series B lenses (01-13), *f* = 300mm, Source to lens distance (*p*) = 23 m, Indus-2 vertical source size 0.2 mm and estimated focus spot of 2.6 μm.

Lens nomenclature	**No of lenses**	**Energy [keV]**	**Transmission [%]**	**Gain**	**Effective Aperture [μm]**
#*B01	24	8.6	27.3	12	164
#B02	30	9.7	30.4	14	182
#B03	37	10.7	33.2	15	199
#B04	45	11.8	35.5	16	213
#B05	54	13.0	37.4	17	224
#B06	63	14.0	38.85	18	230
#B07	74	15.1	39.9	19	239
#B08	84	16.	40.6	19	243
#B09	96	17.3	41.1	19.6	246
#B10	108	18.3	41.2	19.9	247
#B11	122	19.4	41.31	20	247
#B12	135	20.4	41.3	20	247
#B13	150	21.5	41	20	245

* # indicates the number of chip

The performance of X-ray refractive lens depends on figure of merit of lens material, lens configuration and fabrication accuracies. Looking into X-ray sensitivity and route of fabrication, the choice of lens materials are PMMA and SU-8. These materials provide high throughput in comparison to the structure fabricated using other techniques on 100 mm diameter wafer and etched developed depth profile of 500-1000 μm. A new resist material which has similar properties like SU-8 is also considered as a choice of lens material. To the best of our knowledge, this material has not been used for fabrication of X-ray LIGA lenses. The details of the material are described in section 4.4.3. Table 4.3 provides typical calculated values for Series B SU-8 X-ray lenses, in the designed energy range 8-20 keV.

4.4 Fabrication of X-ray lenses

X-ray lenses in three different materials are fabricated using SDXRL beamline. X-ray mask for fabrication of PMMA and SU-8 X-ray lenses are developed with polyimide as a membrane and gold of thickness ranging 10-15 μm as a absorbing layer. Figure 4.3 shows the developed X-ray masks for SU-8 X-ray lenses. The X-ray mask shown in figure 3.5(b) is used for PMMA X-ray lens fabrication. These produced X-ray masks have enough thickness of Au to provide dose contrast for PMMA and SU-8.

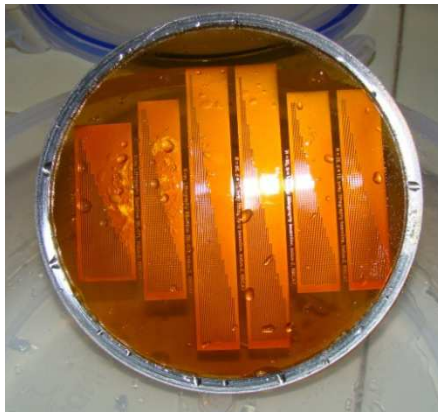

Figure 4. 3: Developed X-ray masks for SU-8 X-ray refractive lenses

4.4.1 Fabrication of PMMA lenses

X-ray lenses are first fabricated in PMMA to evaluate the X-ray lithography process for lens fabrication. The knowledge gain from the processing of CLAREX PMMA sheet, including exposure dose, development time has been helpful here to obtain parabolic lens profile in 500-800 μm thick resist layer. X-ray exposures are carried out in 2.5-9 keV energy range. Number of lenses N = 1, 2, 5, 10, 20 and 50 are produced in PMMA with radius of curvature R = 200 μm, geometrical aperture $2R_0$ = 400 μm and focal length of ~1 m. The thickness d of the lenses at apex is 20 μm. Figure 4.4 shows the SEM micrograph of produced PMMA X-ray lenses with parabolic profile. The microfocusing characterisation of PMMA lens is discussed in section 4.6.1.

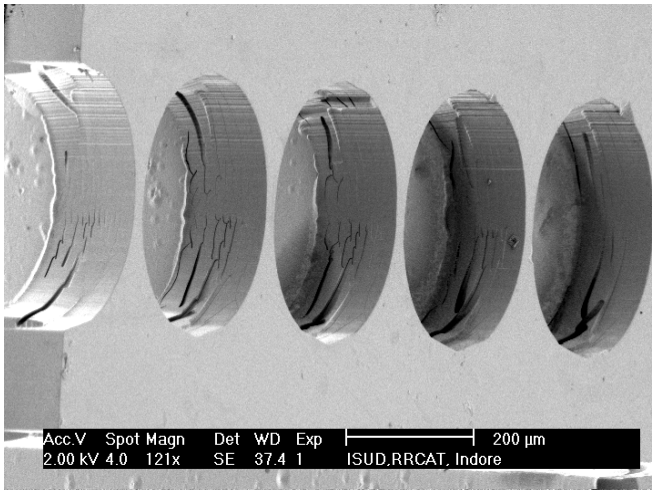

Figure 4. 4 : SEM micrograph of PMMA X-ray lenses fabricated at SDXRL beamline

4.4.2 Fabrication of SU-8 lenses

The designed X-ray mask is used for fabrication of SU-8 X-ray lenses included three series A, B, C of lenses. The chip contains total ~ 4000 parabolic X-ray lenses. Processing parameters of SU-8 resist on Si wafer is discussed in Chapter 3. The total processing time of these lenses are 8-9 hours for 500 μm thick resist layer (preparing substrate : 5 hours,

exposure: 15 minutes (45 minutes for evacuation, venting scanner2), and PEB/development : 2 hours) which shows sufficiently high throughput for obtaining X-ray lenses. The actual fabricated X-ray lenses on 100 mm Si wafer is shown in figure 4.5(a). Enlarged view of X-ray lenses by SEM micrograph is shown in figure 4.5(b). Minimum feature size of 15-17 μm (*d*) with developed depth of 300-1200 μm is obtained on different chips.

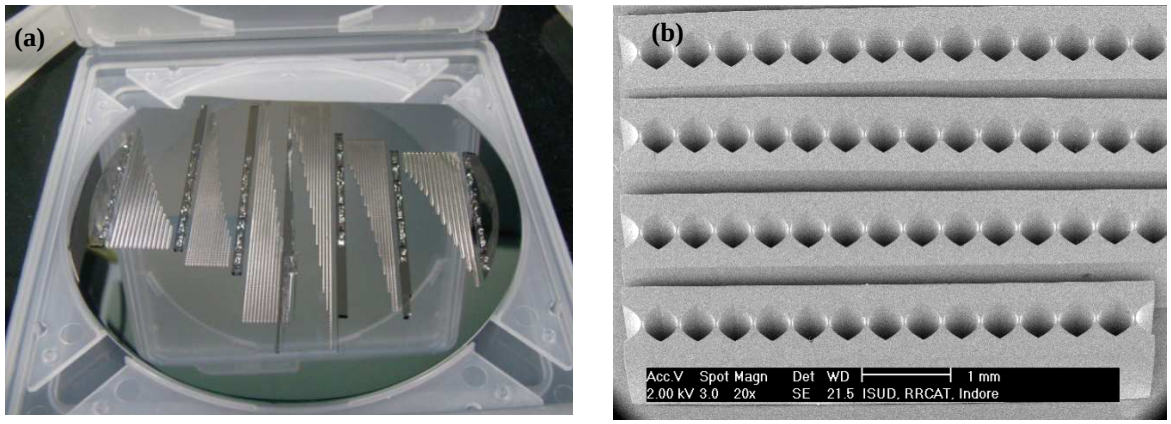

Figure 4. 5 : Fabricated SU-8 X-ray lenses (a) actual photograph of 100 mm wafer (b) SEM of series A X-ray lens.

A study is carried out for correlating the various dimensions of X-ray lens profiles during each stage of fabrication from design, X-ray mask fabrication to actual structure in SU-8.

Analysis of radius of curvature and depth of lenses

Curvature and depth of fabricated SU-8 X-ray lenses are measured using COM. There are two critical points at which X-ray lenses are evaluated or crosschecked during manufacturing. First is the steep sidewalls including depth and second is the error in the parabolic profile.

The 3-D image obtained from COM of X-ray lenses R = 100 μm and 25 μm is shown in figure 4.6 (a, b). The depth of the structure is ~ 470 ± 5 μm for both the lenses. The variation of microstructure dimensions during each stages of fabrication is compared with the dimensions of UV mask, X-ray mask and actual SU-8 structure. The comparison of measured

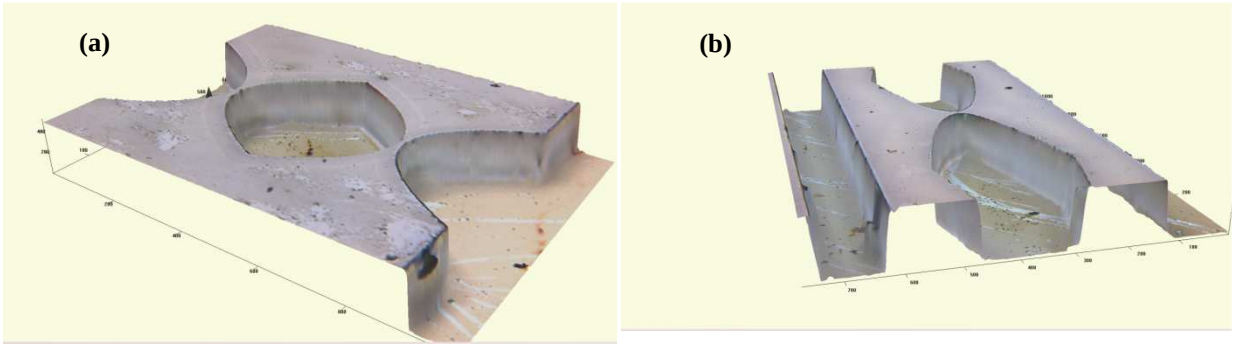

Figure 4. 6 : 3D surface profilometry of X-ray lenses with radius of curvature (a) 100 µm and (b) 25µm

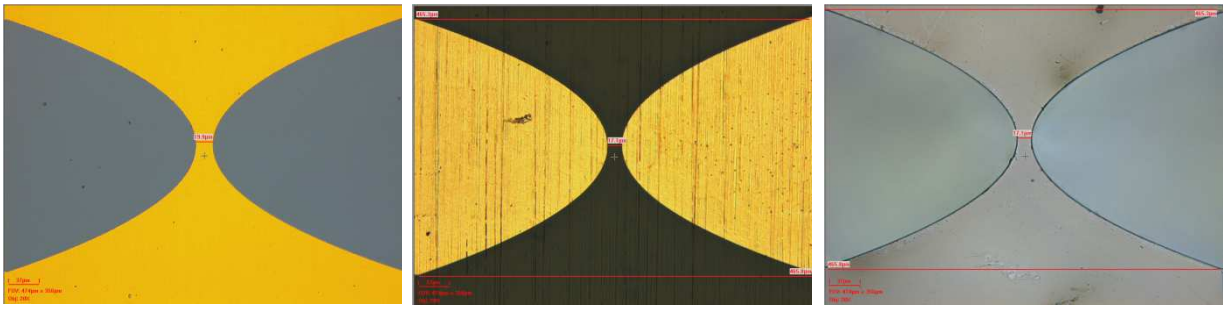

Figure 4. 7: Comparison of measured *d* value for X-ray lens in (a) UV mask (b) X-ray mask (c) SU-8 X-ray lens.

microstructures dimensions in case of (a) UV mask (b) X-ray mask and (c) actual SU-8 structure are shown in figure 4.7 and obtain values are given in table 4.4. An error of 1-2 µm in all dimensions are observed for UV mask transformation to X-ray masks. This error is due to the divergence of the UV lamp. In order to produce the actual *d* value of the X-ray lenses of 20 µm, a positive biasing value of 1.5 µm is required in the lateral dimensions. In transforming structures from the polyimide-Au mask to SU-8, the dimensions matches well. However, in some case, the deviations in the microstructure are observed within 0.1 %. It is difficult to measure the vertical sidewall steepness of more than 85° using the existing COM.

In order to estimate the steepness in the sidewall, new sets of SU-8 X-ray lenses are fabricated which can be removed from wafers. SU-8 CRLs are fabricated over a thin layer of OmniCoat which acts as sacrificial layer to remove the single strand containing multiple lenses. Using front and back 2-D profile of the same lens, parameters such as d, $2R_0$ and L are measured.

Table 4. 4: Comparison of microstructure dimensions of X-ray lenses profiles between (1) UV mask, (2) X-ray mask and (3) actual fabricated X-ray lens (for nomenclature of variables, please see figure 4.2)

	R[μm]	$2R_0$ [μm]	d [μm]	L [μm]	Depth t [μm]
UV Mask	100	300	19.9	465	-
X-ray mask	100	301.0	17.1	468	12
SU-8 on ϕ 100 mm wafer	100	300.6	17.1	469	480
UV Mask	50	300	19.9	539	-
X-ray mask	50	301.0	17.1	540.1	12
SU-8 on ϕ 100 mm wafer	50	302.1	17.3	541.9	485
UV Mask	25	250	19.9	650	-
X-ray mask	25	250.3	17.1	649.6	12
SU-8 on ϕ 100 mm wafer	25	251.2	17.2	651.5	483

If the vertical sidewall has tapering of about 17.5 mrad for 500 μm thick SU-8 resist layer, then the error introduced is ~ 8.75 μm from front to back side of x-ray lens. However, the estimated vertical and horizontal divergence offered by beamline at Scanner2 in 2.5-9 keV energy range is 1 mrad which leads to an error of 0.5 μm in feature size. The observed dimensions are in similar range and indicated in table 4.5. These measured values in the front and back side of X-ray lenses matches well. This also confirms the performance of the

beamline (in terms of runout error) in the required energy range for obtaining better microstructure fidelity.

Table 4. 5 : Measured profile of SU-8 X-ray lenses from front and back side which correlates with divergence of X-ray beam.

	$2R_0$ [μm]	d [μm]	L [μm]
Front side, Lens 1, R = 25 μm	250.3	17.2	649.5
Back side, Lens 1, R = 25 μm	252.2	17.5	650.9
Front side, Lens 1, R = 50 μm	300.2	17.1	535
Back side, Lens 1, R = 50 μm	302.1	17.4	536.9
Front side, Lens 2, R = 50 μm	300.4	17.2	535.6
Back side, Lens 2, R = 50 μm	302.5	17.4	537.1

The fidelity in parabolic profile is determined using the following method. The measured 2-D shape of X-ray lens obtained from microscope is shown in figure 4.8 with a fitted parabolic profile. This picture is prepared in CAD software and the profile of parabola (R =100 μm, $2R_0$ = 400 μm) is scaled to the size of image. The scaling of (x1130) designed parabola matches with the 2-D picture parabola profile. Deviation between the measured and final shape of the lens is observed within ~1 μm. The fitted radius of curvature at apex is found to be 100 μm. The fitted profile of $2R_0$ = 452 mm is obtained from CAD software, when scaled down by 1130, it gives value of $2R_0$ = 400 μm which matches with the design value.

4.4.3 Fabrication of SUEX lenses

A new material, negative tone, called SUEX is used for development of X-ray lenses in this thesis. SUEX epoxy thick dry film sheets (TDFS) laminates is developed by DJ DevCorp, USA. SUEX contains a cationically cured modified epoxy formulations utilizing

an antimony free PAG. A highly controlled solvent less process provides uniform coatings of resist layer thickness from 100-1000 µm and more. SUEX TDFS are sensitive to UV and X-ray photon. X-ray absorbed bottom doses are in the range of 100-400 J/cm^3 and top/bottom surface dose ratio equal to 3-4. SUEX enables the fabrication of multi-level, complex designs as well as HAR MEMS components [188, 189].

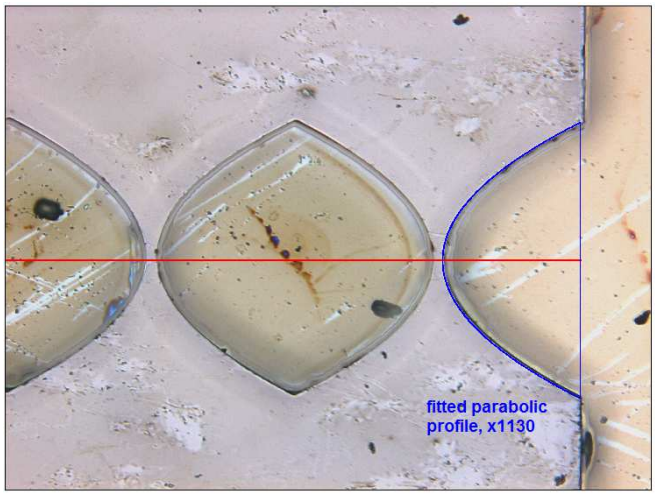

Figure 4. 8 : The fidelity in parabolic profile, measured 2-D optical image is fitted with original designed parabolic curve and enlarged 1130 times.

Table 4. 6: Chemical composition and weight percentage of SUEX and SU-8

Material	Chemical composition	Weight percentage (%)						
		C	H	O	Sb	F	S	Si
SUEX	$C_{66.1}H_{71.4}O_{14.6}F_{0.036}S_{0.028}Si_{0.020}$	72.6	6.75	20.3	0	0.06	0.08	0.27
SU-8	$C_{87}H_{98}O_{16}Sb_{0.16}F_{0.45}S_{0.088}$	72.7	6.9	18.2	1.4	0.6	0.2	0

SUEX TDFS is developed for LIGA community to replace in-sensitive and time consuming PMMA sheet and struggle associated with epoxy liquid formulations and achieving repeatable and reliable results. The properties of SUEX TDFS are similar to SU-8 but absence of Antimony (Sb) which has very significant advantage in X-ray optics. The

weight percentage and elemental composition of SUEX is compared with SU-8 composition and is given in table 4.6. The calculated molecular formula is with a blended MW 1101.5 for SUEX and MW of 1388 for SU-8. Elemental composition of SUEX is verified by X-ray fluorescence (XRF) spectrum recorded at BL-16, Indus-2. Figure 4.9 shows the XRF spectrum obtained from SUEX and SU-8 photoresist taken at the same incident X-ray

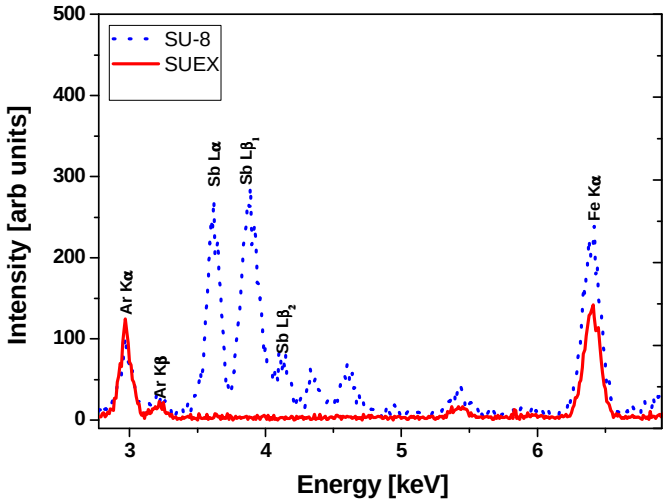

Figure 4. 9 : X-ray fluorescence data for SUEX and SU-8 resist layers

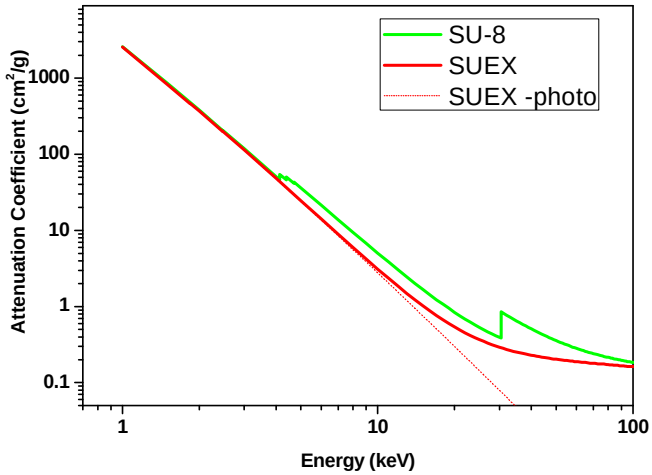

Figure 4. 10: Calculated attenuation coefficients for SUEX and SU-8 for E upto 100keV.

energies for total integration time of 300 s. In SU-8, a peak at 3.6 and 4.3 keV corresponds to Sb L_α and L_β emission lines. The Sb peak at this corresponding energies are absent for SUEX

recorded spectrum. Fe K_α line is due to scattering from the adjacent stainless steel beamline components. The value of attenuation coefficients for SUEX and SU-8 are calculated from NIST website and plotted in figure 4.10. SUEX is preferred choice of X-ray lens materials over SU-8 due to absorption of X-ray is half order less above Sb K edge. If micro patterned SUEX resist sustain similarly like SU-8 at a high exposure dose and consistently at temperature above 100 °C, introduces a better proposition to use it as a lens material.

4.4.3.1 Optimization studies for fabrication of SUEX X-ray lenses

Substrate preparations

Resist application of SUEX TDFS is simple process over solution based resist. A thoroughly cleaned Si wafer is used as a base substrate. SUEX sheets are laminated on Si wafer using a hot roll laminator. A simple office laminator with a provision of temperature stability and accepting at least 1 mm thick sheet is used for SUEX lamination procedure. Sample for X-ray exposure is prepared by first placing the substrate (Si) face up on Aluminum carrier and in next step place the SUEX TDFS on Si. For lamination the stack consisting Al carrier, Si wafer and SUEX TDFS is moved through the heated rollers at a speed of 300 mm/min at 65-75°C depending on the thickness and thermal conductivity of the carrier, the resist, and the substrate. In our case, Si wafer is fixed to a projection transparency (PET) sheet by adhesive tape. The protective layer on SUEX is removed and same side is placed carefully on Si wafer. Now, another transparency sheet is placed over it. This stack is moved in the hot roll laminator at desired speed. SUEX TDFS are prepared through solvent free processing and removal of solvent by soft baking like in case of SU-8 is not required. However, soft bake before exposure is must to remove various coating defects from the laminated film. Soft baking is carried out in oven at 80 °C for 30 minutes by placing the laminated substrate on Cu plate. In this case, there is no role of solvent removal during soft

baking and therefore no volume shrinkage or mechanical stress is observed. Substrate is kept in oven till the temperature of oven reaches to room temperature during cooling. Finally, the laminated substrate is stored in dry cabinet for X-ray exposure.

X-ray exposure

SU-8 X-ray lens design methodology is also used for SUEX lens fabrication. X-ray exposure of SUEX samples is carried out at SDXRL beamline in the energy range 2.5-9 keV. Bottom dose of (D_B) ~ 300 J/cm^3 is decided to impart to SUEX for its complete polymerization with top to bottom dose ratio in the range of 3-4. The calculated exposure time for different thickness of SUEX resist is given in table 4.7. For scanning length of 9 cm, an exposure cycle is run for 90 minutes at average ring current of 100 mA for obtaining a suitable bottom dose for 500 μm thick resist.

Table 4. 7 : Exposure parameters for SUEX at SDXRL beamline

Sr no	**Thickness of substrate [μm]**	**Mask Au thickness [μm]**	**Dose under mask [J/cm^3]**	**Dose top [J/cm^3]**	**Mask contrast**	**Exposure time /cm scan length [mA.min]**
1	200	5.7	10	436	44	660
2	500	6.6	10	710	71	1075
3	1000	8.0	10	1420	142	2148

Post exposure baking at 80 °C for 60 minutes is carried out in oven. Development is done at room temperature by keeping the wafers face-down in the PGMEA developer with gentle agitation. 500 μm thick SUEX is developed for 50-60 minutes. The substrates are rinsed in second bath of PGMEA and finally rinsed with IPA. Figure 4.11 shows the SEM micrograph of developed SUEX lenses with R = 50 μm.

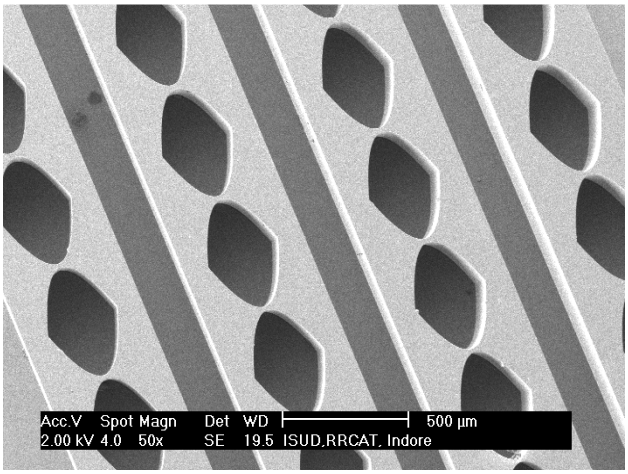

Figure 4. 11 : Fabricated SUEX X-ray lens on Si wafer at SDXRL beamline

4.5 Performances of X-ray lenses

The performance of CRL is carried out by evaluating their focusing and transmission efficiency. This depends on structural and material properties like lens profile, radius of curvature at the apex, thickness of the lens profile at the apex, number of lenses, surface roughness, density and optical constants.

4.5.1 Experimental test setup at Indus-2

Microfocusing characterization of X-ray lenses is carried out at BL-16, Indus-2. The details of the beamline configuration are available elsewhere [190]. Schematic of the experimental set-up used for lens characterization at BL-16 is shown in figure 4.12. It comprises of Si (111) double crystal monochromator (DCM) with energies tunable between 4-20 keV with resolution $E/\Delta E=10^{-4}$, precision slits, mounting tower containing multiple stages for maneuvering CRL containing chip, edge scan setup with AXUV 100 photodiode and X-ray CCD camera (Photonic Science). The distance (p) between the source and the centre of lenses is 23 m. The incident beam for refractive lenses is shaped using four jaw slit. The tower for mounting CRL chip and diagnostic set up is developed as part of this thesis. This setup is upgraded time to time as per the requirement during various measurements. The

alignment of CRLs is very important and critical to obtain final focused spot. The developed tower has 5 degrees of freedom (pitch, roll, yaw, lateral and transverse movements) for placing and alignment of CRL. The lenses can be adjusted in angles and in coordinates with the help of rotation and translation stages with an accuracy of 0.01° and 10 μm respectively.

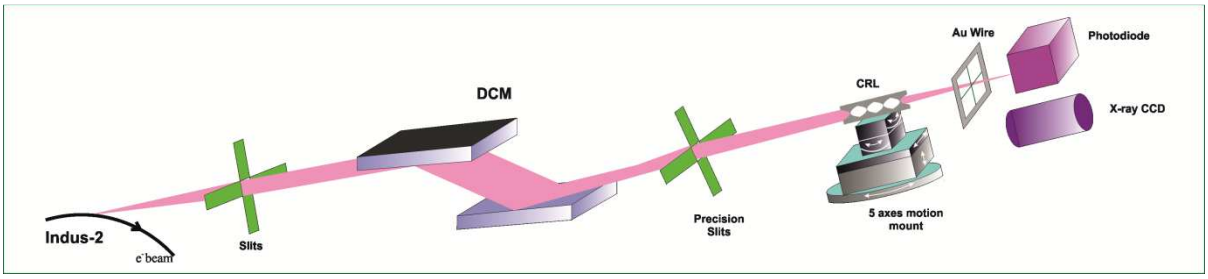

Figure 4. 12 : Schematic setup adopted for X-ray lens characterization at BL-16, Indus-2

Alignment of the X-ray lenses is carried out by placing the X-ray CCD (Photonic Science) behind the lens. In some cases, self developing radio chromic film is also used to check the focusing effect. The intensity distribution in the lens focal plane is measured by wire edge scan method and recording the current from photodiode as function of position of the wire. In present case, cross Au wire of 100 μm diameter is used to determine the focus spot size in both the directions. An actual view of the experimental setup developed at BL-16 is shown in figure 4.13.

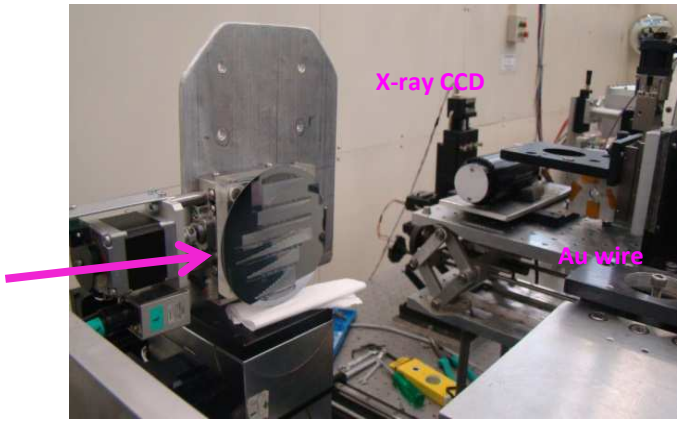

Figure 4. 13 : View of experimental setup developed at BL-16, Indus-2 for X-ray lens chracterisation

4.5.2 Experimental test set up at Diamond

Diamond is a third generation, high brightness SR facility with low electron-beam emittance (~ 2.74 nm rad). For a given demagnification, the source contribution to focal spot dimension is lower for Diamond compared to Indus-2. With higher source stability and smaller source size, the evaluation of lenses at Diamond helps in estimating the profile accuracies, and would be important towards improving the fabrication tolerances for obtaining source limited focal spot. The evaluation of the X-ray LIGA lens developed at SDRXL beamline, are done at Diamond, through a collaborative program.

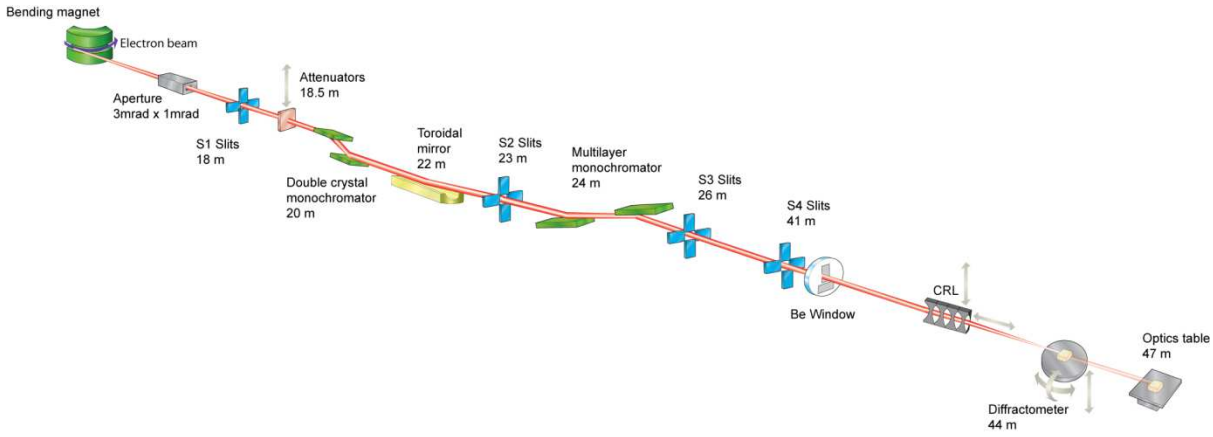

Figure 4. 14 : Schematic of B-16 beamline, Diamond used for PMMA and SU-8 lens characterisation.

The details of Diamond's B16 Test beamline are given by Sawhney et. al. [191]. This is a flexible and versatile beamline for characterisation of optics, detectors and other instrumentation, and for the development of novel techniques and technologies. The schematic layout of B16, Diamond is shown in figure 4.14. The beamline provides both white and monochromatic X-ray beams in the 4-25 keV energy range by a Si (111) DCM. B16 has dedicated micro optics test bench facility for characterization of X-ray optics. This optics test bench has three multi-axis motorised tables (1, 2 and 3) for installing the optics, the

diagnostics and the detectors. The lenses can be adjusted in X-ray beam in angles and in coordinates with the help of dedicated stations consisting six degrees of freedom, with an accuracy of < 0.01° in angular and ~ 1 μm in linear translation. For precise measurement of the microfocused beam size, knife-edge scans using a 200 μm diameter gold wire attached to a piezo translation stage with minimum step size of 0.1 μm and a photodiode downstream to record the X-ray intensity, is used. The focal point images are recorded using X-ray CCD with 6.5 μm pixel size for coarse beam size observation (Photonic Science) and high resolution X-ray CCD (PCO 2000 coupled with microscope and scintillators) with pixel size 0.45 μm. The intensity (flux) is recorded using PIPS photodiode.

4.6 Microfocussing using X-ray lenses

4.6.1 PMMA X-ray lenses

PMMA plane parabolic CRLs with total lenses (N) equal to 50 on chip are characterised at Indus-2 and Diamond. The radius of concave surface at apex is R = 200 μm, d = 20 μm and geometrical aperture $2R_0$ = 400 μm for a focal length of ~1 m. The studies in PMMA are carried out during the beginning stage of the CRLs development and therefore the characterisation at Indus-2 is carried out only with radiochromic film and CCD.

4.6.1.1 Results of experiment at BL-16, Indus-2

The PMMA CRL chip is mounted in vertical focusing geometry on a precision platform with 5 degrees of motion). The alignment of CRL in pitch, yaw and roll movements are carried out with the help of self developing X-ray film. In every measurement, film is exposed for 10 sec in the beam to avoid the saturation of the developed spot. The film is kept

at 1 m away from the lens to determine microfocus line image. The incident and vertically focused beam are shown in figure 4.15 (a) and (b) respectively. The incident beam size is 300 x 400 μm^2 which is focused by CRL to 300 x 20 μm^2. In this measurement, demagnification of 20 is obtained. X-ray CCD is used to observe the micro focus line from PMMA CRL. The CCD image of the focus spot is shown in figure 4.15 (c). The measured focus spot size is found to be ~20 μm.

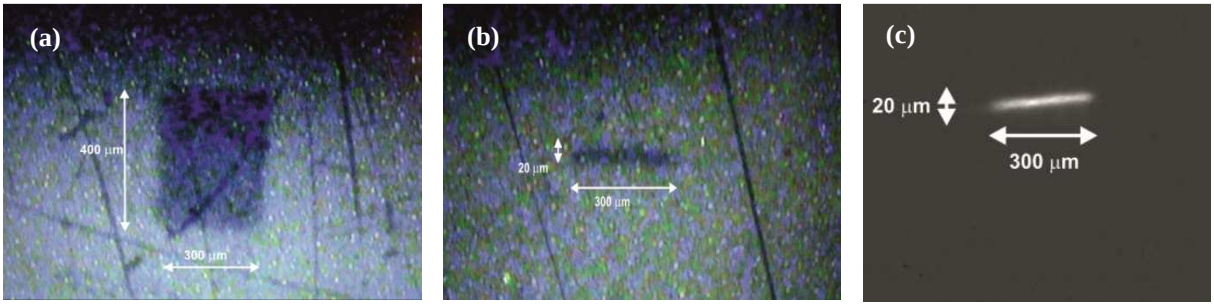

Figure 4. 15 : Microfocusing of PMMA X-ray lenses (a) Incident beam impinging on X-ray lens (b) line focus measured using self developing film and (c) line focus measured using X-ray CCD.

4.6.1.2 Results of experiment at B16, Diamond

The testing at Diamond is carried out for same PMMA X-ray lens profile with N = 50 with etch depth of ~500 μm. The lens stack is mounted on the table1 of optics test bench in a vertical focussing geometry. An X-ray CCD detector that had an effective pixel size of 6.5 μm is used for initial alignment of the lens. Multiple wire scans are performed to optimise the focal length and for fine adjustment of the lens. The focal length of the lens is greater than expected at 10 keV (920 mm against 755 mm). This is perhaps due to the difference in bulk density of PMMA and the density of as-deposited lenses. The derivatives of the wire scans gave the beam size. The raw data and the derivative for the best achieved focus size are

shown in figure 4.16. The measured FWHM size of the microfocused beam is 2 μm, using a Lorentzian fit. Ideally the derivative profile of the measured data point must be fitted by Gaussian distribution representing the source profile. The Lorentzian profile suggests that the more X-rays are scattering from the lens profile due to profile errors/ material inhomogeneity. For a comparison, when using a lens with a 920 mm focal length, to image a 70 μm source at 47 m, the de-magnified image would be expected to be 1.4 μm. Consequently, an extra contribution of about 1.5 μm exists, which can be attributed to the shape and in-homogeneity of the lens.

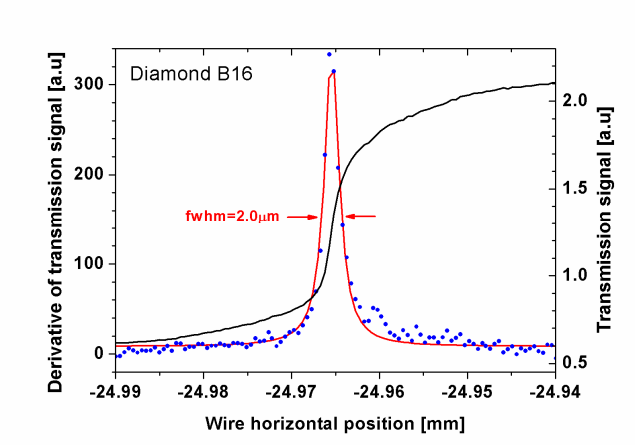

Figure 4. 16 : Transmission signal from a gold wire scan (black line) in the focal plane of the planar PMMA refractive micro-focusing lens, measured at 10 keV energy. The derivative of the raw data (blue dots) and a Lorentzian fit (red line) are also shown, indicating that the beam has an FWHM of 2.0 μm.

Table 4. 8 : Comparative performance of X-ray lenses on two synchrotron radiation sources, Diamond and Indus-2 [180].

SR Source	$\delta[10^{-6}]$ at10keV	$\beta[10^{-9}]$ at 10keV	Distance between source and lens [m]	Source size [μm]	Vertical Focal Spot [μm]	
					Calculated	Measured
Diamond	2.67	3.54	47	70	1.4	2.0
Indus-2	2.67	3.54	20	232	13.5	20.0

Table 4.8 gives the comparison of microfocusing characterisation of PMMA CRL carried out at two SR sources. It is apparent that for same set of lenses, the performance at low emittance storage ring Diamond is found to be better. X-ray lens characterization at low emittance machine has given valuable inputs to improve further on the design aspects.

4.6.2 Characterisation of SU-8 lenses

4.6.2.1 Results of experiment at BL-16, Indus-2

Investigation of SR beam microfocusing with SU-8 CRL is carried on the earlier described dedicated setup at the Indus-2 BL-16 beamline. The 100 mm diameter chip containing X-ray lenses (as described in table 4.2) is mounted on a platform having five degrees of freedom to obtain vertical focusing. The chip contains all three series of X-ray lenses with radius of curvature 25-100 μm and focal length lie in the range of 0.3 -1m. The focal length smaller than 0.3 m is possible for B and C series lenses using higher number of lenses at lower energies compared to their design energy. Alignment of X-ray lenses is performed by observing the focused X-ray beam in X-ray CCD. The lenses fabricated through XRL process have tighter spatial tolerance and hence the alignment of one of the lenses trail in the chip ensured the alignment of all other lenses trails in the chip. In each measurement, the profiles of intensity distribution at focal plane of lens are measured using edge scan method. The CRLs are placed at 23 m from the source and spot size is determined at 0.3 m or 1 m. The present test bench does not have the possibility of moving the X-ray lenses/detector along the direction of propagation of the beam. Therefore, the energies from DCM are varied to determine the best focal spot sizes for respective X-ray lenses.

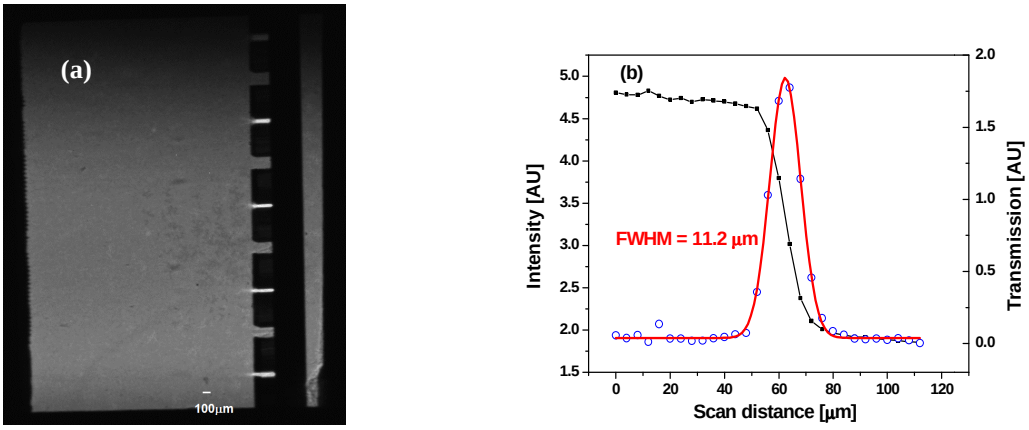

Figure 4. 17 : (a) X-ray CCD Image of CRL numbers 8 to 11 at 15.9 keV, (b) Intensity profile of beam in lens focal plane measured using gold knife edge scan method. X-ray energy of 15.9 keV was focussed at focal distance of 1.07 m with *N* = 58 lenses. The derived derivative of the knife edge scan is also shown with FWHM = 11.2µm

Figure 4.17(a) shows the focus of lens number 2A09 with *N* =58 (here 2 stands for chip number, A stands for lens series and 09 for lens number) on chip at 16 keV at a distance of ~1.0 m from the centre of lens. CCD image also shows lens number 2A07, 2A08, 2A10, 2A11 which gives the quick comparisons of focusing performance of the lenses at fixed energy and fixed distance. The spatial resolution of CCD is 6.5 µm and is not sufficient to obtain the FWHM values of focal spot. The FWHM of focal spot at focal distance is measured using knife edge scan method. A gold wire of 100 µm diameter is scanned in front of photodiode operated in current mode. The light intensity profile of the vertical focused beam for lens 2A09 at 15.9 keV and its derivative function are shown in figure 4.17(b). The current in photodiode is 500 pA with focused beam impinging on photodiode while a current of 220 pA is recorded when gold wire occluded the focused beam. To locate the best focus position for a particular lens, focal spot as a function of energy is measured. The best focal spot at focal distance of 1.07 m for various lenses are obtained. The minor difference between the measured and expected focal distances is likely due to lower density of SU-8 compared

to the tabulated density (ρ = 1.2 g/cm^3) used for calculation. The focal spot for lens 2A09 is 12 ± 1 μm at 15.9 keV. This size is larger than the estimated 9.4 μm which can be attributed to the broadening of the focused beam due to imperfections in fabricated parabolic lens profile, edge roughness, small angle scattering due to impurity atoms/inhomegeinity in SU-8, beam instability and the fluctuations in Indus-2 emittance. The measured profiles of focal spot size of these fabricated lenses are fitted using Lorentzian distribution. It is due to the roughness in the X-ray lens profile which scatters of the beam. The origin of roughness in the lens profile is due to errors in X-ray masks fabricated using low cost route. In first phase of studies, the process parameters for SU-8 are optimized to obtain the better features and fidelity of microstructures.

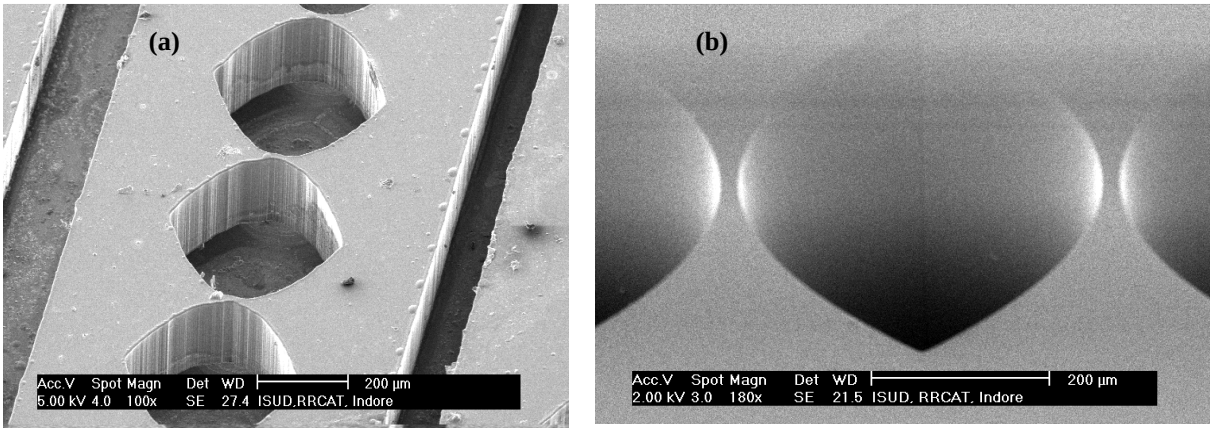

Figure 4. 18 : SEM micrograph showing the distinct qualitative difference X-ray lenses (a) old sets (b) new sets.

New X-ray masks are developed using UV mask prepared from laser pattern generator with minimum writing step size of 25 nm where the errors at the edges of parabolic profiles are minimised. In new sets of X-ray lenses, the conditions of baking, exposure and development is further optimized to obtain the process repeatability of the microstructures.

The difference between the two series of X-ray lenses are shown in figure 4.18. Here, the effects of the better quality of X-ray mask on vertical sidewalls of X-ray lenses are observed.

The new sets of X-ray lenses are characterised at BL-16. In this case the lenses with reduced radius of curvatures 50 µm and 25 µm are characterized at focal length ~ 0.3 m Figure 4.19 (a) shows the aligned X-ray lens number 4B06 along with adjacent lenses as observed in X-ray CCD at incident energy of 14keV. The precision slits in front of the X-ray lens is then closed to choose only one lens at a time. The slit size (incident beam size on X-ray lens) is kept ~ 300 µm (V) x 460 µm (H). The intensity profile is measured using edge scan method by varying the energy and keeping the distance between the lens and diagnostic setup fixed. The best focused size (FWHM) of 8.4 µm is obtained when lens 4B06 (~ 480 µm etched depth and R = 50 µm, N = 63) is illuminated at 14 keV. The differential curve of focused beam profile is fitted with Gaussian profile with reasonable goodness of fit. The focusing performance between old and new sets of X-ray lenses is clearly seen with the observed focus profile and fitting of differential curve (Gaussian or Lorentzian).

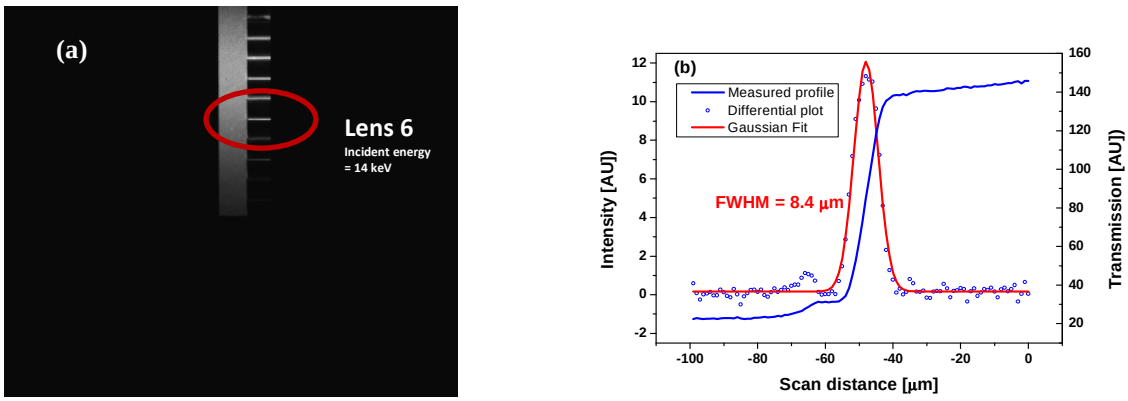

Figure 4. 19 : (a) X-ray CCD image of lens 4B06 and (b) the focus spot obtained using this lens at 14 keV.

The measured FWHM of focus beam from 4B06 is three times higher than the estimated focus beam. Large deviation between observed and estimated focus spot is further investigated by moving the X-ray lens in horizontal beam. This error can be due to the error in lens profile or instrumentation error. Lens is moved at various parts (vertical and horizontal) of the incident X-ray beam to check the effect of divergence of diffracted beam from DCM. The FWHMs of the focus spot is found within range of 8.4-9.5 μm. This indicates that there is no role of divergence of diffracted beam in broadening the focus beam. On further investigation and from literature, it is found that knife edge scans do not show the expected theoretical performance of the lens. These scans are probably influenced by beam widening effects, eg. knife edge artifacts, vibration of the setup etc. Knife edge scan show a combined effect of the focus spot size generated by the X-ray lens and the broadening due to the environment. Apart from this, many other reasons which can lead to the broadening of focused beam including imperfection of the used crystals of the monochromator, parasitic ground vibration of the experimental hall, any scatter in beam path (may be Be foil used as transmission window), etc.

The knife edge scans are mounted on the rigid platform and the measurements are carried few minutes after moving the setup in beam path to allow the diagnostic setup to stabilise One dimensional focusing of the X-ray lenses in vertical direction has provided the horizontal line width of 480 μm and any tilt error in wire can also broaden the beam. The lens performance is checked by reducing the horizontal illumination of lens to a smaller size (~ 100 μm) by using horizontal aperture. In this case, FWHM of the vertical profile of intensity distribution with reduced aperture is found 3.4 μm which is very close to the geometrically estimated value of 2.7 μm. The measured intensity distribution and its derived profile (with fit) of the focus beam are shown in figure 4.20 (a). The deviation from the. estimation can

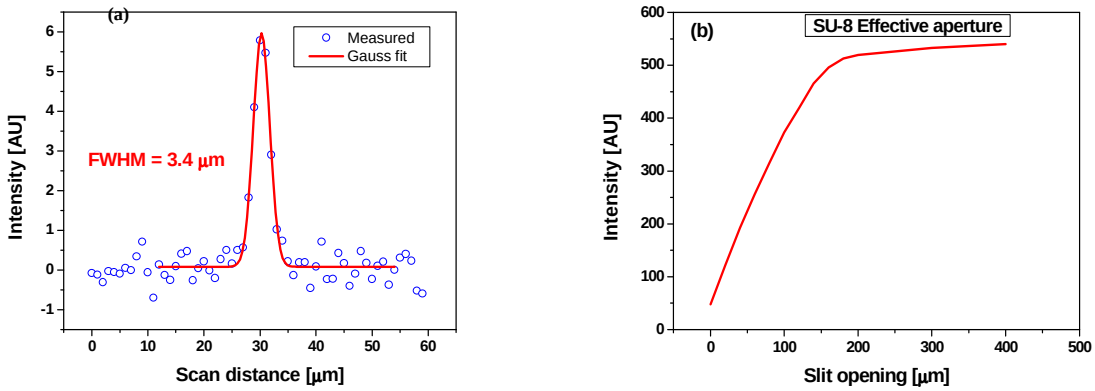

Figure 4. 20 : (a) Measured focus spot when X-ray lens 4B06 is illuminated only with 100 µm beam (b) measured effective aperture of X-ray lens at the same energy with 460 µm horizontal aperture.

be attributed to the density variation in as coated, cured sample and tabulated optical constants. Also, diffuse scattering from lens material, contribute to increase in spot size. The effective aperture and gain for this lens is measured. The slit upstream to X-ray lenses is closed in equal steps of 20 µm and intensity with and without lens is measured using photo diode to determine the effective aperture and transmission of the lens. Figure 4.20 (b) shows the intensity of X-ray lens as function of slit opening. The value of effective aperture in this case is 160 µm which close to its estimated value, 159 µm. The gain of the lens is estimated and found ~ 12 which is of the order of estimated gain (18). The gain from the lenses can be increased either by lowering the Indus-2 source size or increasing the demagnification factor by means of lowering the value of *R*. The measurement using 100 µm slit size with translation step size of 50 µm along lateral direction of focussed line is carried out to investigate the fabrication errors along depth of X-ray lenses. Figure 4.21 shows the positions of slit centres at different locations along the X-ray lens starting from position number 1 to 9. The position 5 correspond to the centre of the lens in horizontal direction, for which the focus

spot profile is shown above (figure 4.20 (a)). Table 4.9 shows the position number and slit centre in accordance with figure 4.21 from the top surface of X-ray lens and obtained focussed spot (FWHMs) in each case. The variation of the focused spot along the depth of the lens at different positions is found to be 3.94 ± 0.5 μm. The result for last position; 9 cannot be recorded due to less signal strength from 50 μm X-ray lens aperture. The deviation of ~ 1-1.5 μm may be attributed to the diffuse scattering from lens material or inline beamline components.

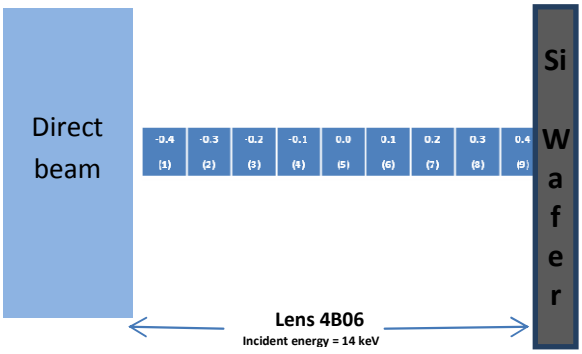

Figure 4. 21 : Schematic of measurement strategy for determining the performance of the X-ray lens along its depth.

In same characterisation setup, other lenses on the chip are also characterized. Table 4.10 shows the focusing parameters obtained for various other X-ray lenses. The value of focus spot (FWHM) given in parenthesis is obtained when only part of X-ray lens (100 μm) is illuminated with incident beam. The main objective of lens characterisation was to evaluate the focusing characteristics of X-ray lenses. In order to optimise the available beam time, the effective aperture and transmission are measured for a few representative lenses and measured values matches with the estimated values. Therefore, in the table, the gain, effective aperture and transmission values are given only for estimated values.

Table 4. 9: Measured FWHM of focus beam as a function of lens depth

Position	1	2	3	4	5	6	7	8	9
Slit centre [mm]	-0.4	-0.3	-0.2	-0.1	0.0	0.1	0.2	0.3	0.4
FWHM [μm]	4.2	4.0	3.48	4.27	3.40	3.84	4.51	3.80	NA

Table 4. 10: Overview of SU-8 lens characterisation at BL-16, Indus-2

Lens	E [keV]	R [μm]	N	f [m]		F_v [μm]		A_{eff} [μm]	T_{crl} [%]	Gain
				Exp.	Calc.	Exp.	Calc.	Calc.	Calc.	Calc.
3A10	18.88	100	65	1.083	1.074	17.9	9.4	288	43.6	19.8
3A11	20.0	100	73	1.085	1.074	14.6	9.4	289	44	18
4B04	11.8	50	45	0.300	0.291	3.2(7.6)	2.57	151	21.9	17.2
4B06	14.8	50	63	0.305	0.291	3.4(8.4)	2.59	159	25	19.4
4C07	15.3	25	37	0.322	0.294	6.28	2.59	156	35	18
4C05	15.2	25	27	0.263	0.403	5.3	3.0	174	42	18
5C07	15.2	25	32	0.339	0.340	9.3	211	164	38	389

2-D focusing

Series C X-ray lenses 4C05 (N = 27) is oriented in vertical dispersion plane and X-ray lens 5C07 (N = 32) is placed in horizontal dispersion geometry to obtain 2-D focusing. Both these X-ray lenses are mounted on single tower having five degree of motorised movement. To enhance the flexibility during alignment, two chips are mounted on a two different manual stages for bringing different lens stack in beam path. These chips can be individually rotated in the beam path. The actual view of two chips mounted in 2-D focusing geometry is shown in figure 4.22. The X-ray lenses are first positioned using motorized stages to the closest focusing, the fine adjustment are then carried out using manual stage. The two dimensional focusing has many permutation and combinations of final alignment. The process was tedious, but could not be avoided due to non availability of second motorised tower. The

distance between both the lens chips was 78 mm and distance of vertical and horizontal focusing lens was 340 mm and 263 mm from centre of edge scan setup and energy 15.2 keV.

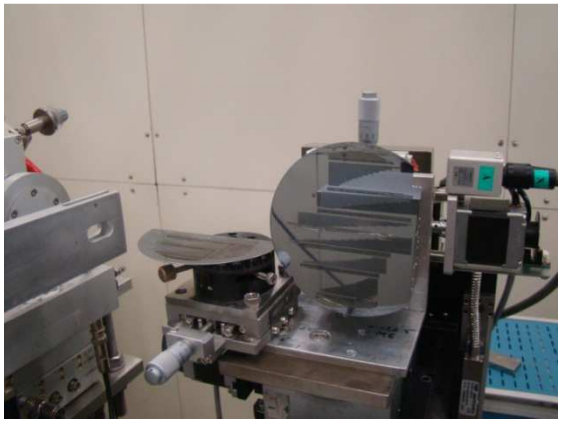

Figure 4. 22 : X-ray lenses mounted in 2-D focussing arrangement.

Figure 4.23 shows 2-D focused spot obtained after alignment procedure. In vertical dispersion geometry the lens chip with developed depth of 500 μm and in horizontal dispersion geometry the lens chip with maximum 1200 μm developed depth are used. The figure 4.23 (b) shows enlarge view of 2-D spot, which shows uniform spot size in both the dimensions.

Figure 4. 23 : SU-8 X-ray lens 2D focussing at Indus-2 (a) the crossed geometry of two lenses, tallest fabricated lense is used in horizontal dispersion geometry, (b) enlarged view 2-D focussed spot size showing uniform normal distribution.

A gold wire cross is first scanned horizontally and then vertically through the focused beam. The edge scan data shows the 2-D focus spot size is 5.3 μm (V) and 9.3 μm (H) (Figure 4.24(a), (b) respectively). Transmission and effective aperture are also measured and their profiles are shown in figure 4.24 (c) and (d) for vertical and horizontal focusing lens respectively. All measured parameters for X-ray lenses in 2-D focusing are compared with theoretical values (table 4.10). Due to the limited constraints of motions, fixed distance between two lens chips and fixed number of X-ray lenses on the chip, 2-D focus of the same FWHM sizes in vertical and horizontal direction could not be obtained.

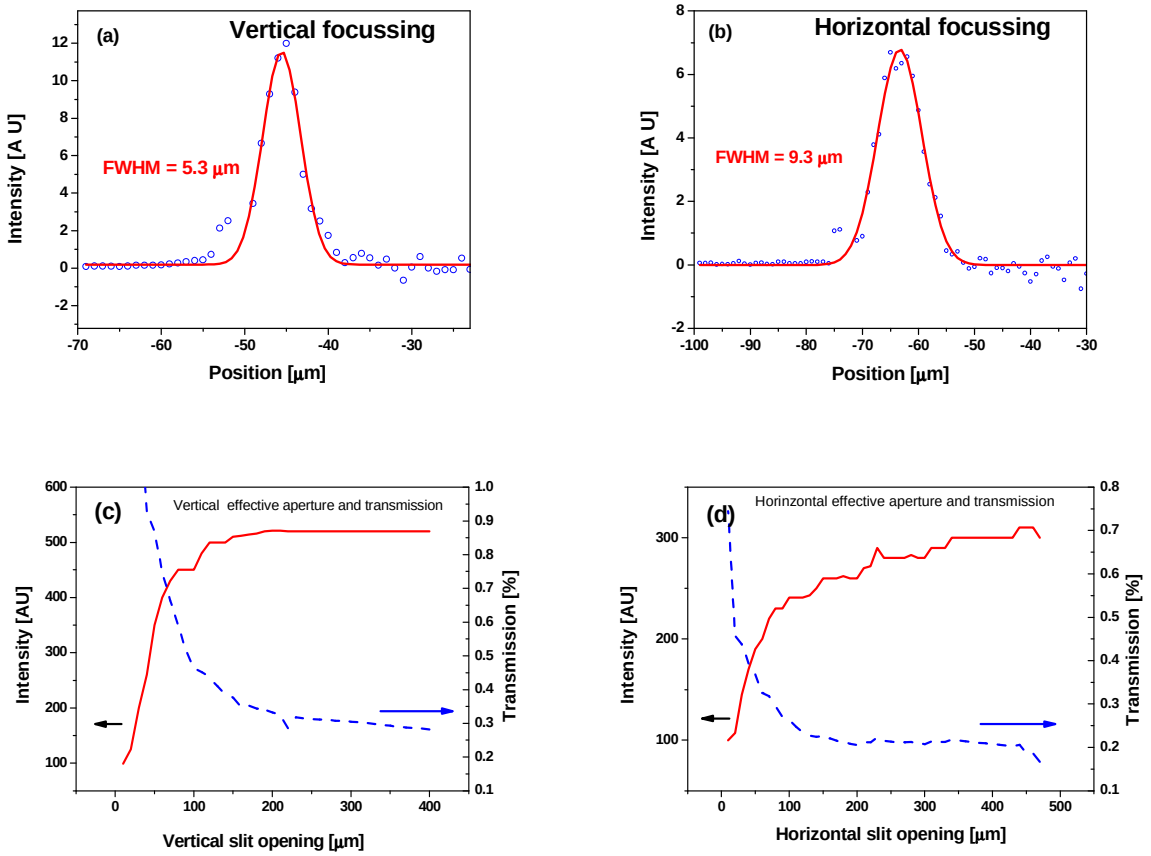

Figure 4. 24 : SU-8 X-ray lenses 2D focusing characterstics (a) FWHM in vertical direction (b) FWHM in horizontal direction (c) effective aperture and transmission of vertical lens (d) effective aperture and transmission of horizontal lens

The 2-D focused beam is later used for performing absorption imaging experiments and described in section 4.7.1.

4.6.2.2 Results of experiment at B16, Diamond

The X-ray lens with all series R = 100 μm, 50 μm and 25 μm are characterised at Diamond. Si chip containing X-ray lenses are mounted on table1 of the micro optics test bench. On table3, X-ray CCDs and Au wire edge scan setup are mounted. The distance between the table1 (centre of the lenses) and table3 (centre of the Au wire) is fixed to 0.8 m. The required energy is tuned by DCM Si (111) to 13.4 keV for focusing X-ray lens 5A08. The X-ray lens chip is aligned in beam path by observing the focused beam shape in high resolution X-ray CCD. Once the alignment of the X-ray lens is completed, the focus spot is measured using edge scan method. The measured FWHM of focus spot is ~1.1 μm which matches well with estimated focal spot of 1.07 μm (shown in figure 4.25 (a)). However, the estimated focal distance of 0.698 m deviates from measured distance 0.8 m. This is likely due to the density variations of as coated and after curing SU-8 resist (ρ = 1.2 g/cm^3). If change in density is accounted then SU-8 may have ρ = 1.01 g/cm^3 in order to provide the focal length of 0.8 m. The other probability is likely in the parabolic profile and radius of curvature. If the value of density is fixed to 1.2 g/cm^3, then error in R by +19μm will correspond to 0.8 m focal length. However, the error in radius of curvature to this level is ruled out (section 4.4.2). X-ray lens properties; effective apertures (251 μm) and focus spot sizes (1.2 μm) are same if the lower side of density value and higher side of profile error are considered for this lens. For these errors, the change in transmission value is only 1.3 % with same gain. It is therefore difficult to detect the contribution from density/error in profile. The error in focal length may be considered as convoluted contribution from profile error and density of lens material. It is

interesting to note here that while characterising at Indus-2, the measured focal length closely matches with estimated focal length but due to high errors in focal spot (2-3 times higher) this error could not be detected. Therefore, the testing of X-ray lenses at low emittance source, Diamond has provided the route to better understanding about errors in the manufacturing process or material properties.

X-ray lenses with same radius but N = 73 is characterize at focal length of 0.6 m by varying the photon energies from DCM. At 15 keV, a focal spot size of 1.3 μm is measured, compared to the estimated value of 0.96 μm. The estimated focal length 0.591 m also matches with measured value. The values are given in table 4.11.

In order to investigate this further, X-ray lens 5B03 with N = 37 is characterized at fixed focal length of 0.6 m. The figure 4.25 (b) shows the FWHM value obtained at best focusing energy. The focal spot size of 0.8 μm is measured in comparison to its estimated value of 0.88 at incident photon energy of 14.9 keV. The measured focal length at this energy is 25 mm higher than estimated value. The error in radius of curvature by 2 μm or lowered density by 0.05 g/cm^3 can compensate this difference without much change in the focal spot size. Though X-ray lenses are fabricated using X-ray lithography have tight tolerance and validated by measured profile (presented earlier), the error along the depth and lens to lens can be in the range of 1 μm. The focal length error observed in lens 5A08 may largely due to fabrication error in some of the produced X-ray lenses.

The lenses fabricated without error has produced the results comparable to estimated values. X-ray lens 5C03 on same chip has given FWHM of focal spot 0.9 μm which is in close approximation with estimated size 0.92 μm. Similarly, measured focal length 0.6 m matches with estimated focal length (0.598 m) of the same lens. The transmission and effective aperture of this lens is determined at 15.4 keV. Figure 4.26 shows the measured

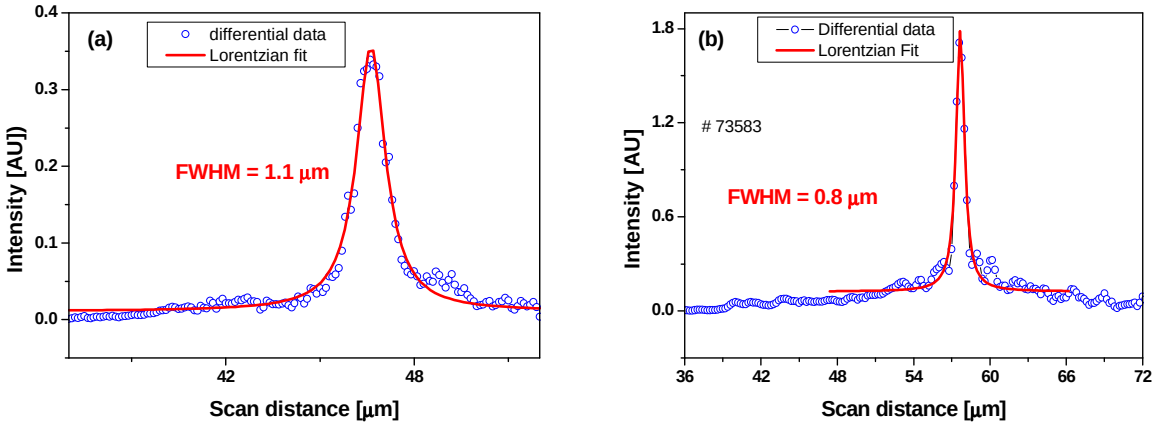

Figure 4. 25 : Focused beam obtained from (a) 5A08 lens at 13.4 keV, *f* ~ 800 mm and (b) 5B03 lens at 14.9 keV, *f* ~ 600 mm with 0.1 µm scan step size.

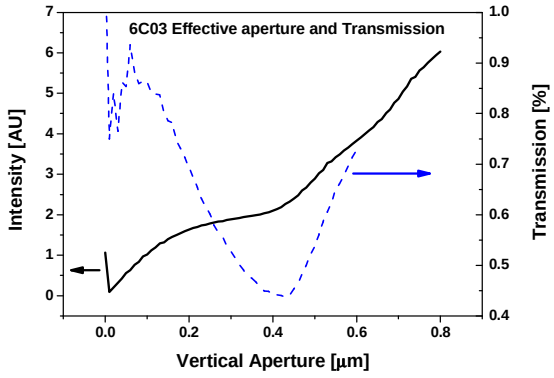

Figure 4. 26 : Measured transmission and effective aperture for X-ray lens (56C03) *R* = 25 µm, *N* = 19 at 15.4 keV.

intensity profile from lens as a function of vertical slit opening from which transmission and effective aperture are determined. At experimentally measured effective aperture (190 µm), the transmission efficiency of 71 % is obtained which is significantly high compared to its theoretical value 51.6 %. If one considers transmission of 51.6 %, then corresponding effective aperture is 310 µm, which significantly deviates from designed geometrical aperture

of 250 μm. The higher transmitted intensity from the X-ray lens is attributed to the diffuse scattering from the lens material. In order to reduce this scattering it is recommended to place a pinhole behind the X-ray lenses during their characterisation.

Table 4. 11 : Overview of SU-8 lens characterisation at B16, Diamond

Lens	E [keV]	R [μm]	N	f [m]		F_v [μm]		A_{eff} [μm]	T_{crl} [%]	Gain
				Exp.	Calc.	Exp.	Calc.	Calc.	Calc.	Calc.
5A08	13.4	100	51	0.8	0.698	1.1	1.07	238	29.3	42
5A11	15	100	73	0.6	0.591	1.3	0.9	229	27.9	45
5B03	14.9	50	30	0.6	0.575	0.8	0.88	208	40	45
5C03	15.4	25	19	0.6	0.598	0.9	0.92	193	51.6	46
2D focusing										
5C03	16.4	25(V)	37	0.361	0.300	6	0.5	170	41	109
6B08	16.4	50(H)	84	0.318	0.615	3	2.7	171	29	9627

From the above observation, it is desirable to have stable, precision micro optics bench and highly stable source. Thus, the measurements carried out at Diamond are reliable for X-ray lens characterisation. The same measurements can also be carried out at Indus-2 with availability of sophisticated instrumentation with stable beam.

2D Focusing

SU-8 X-ray lenses are also characterized in 2-D focussing geometry at Diamond. Two separate X-ray lens chips are mounted in vertical and horizontal dispersion geometry. The distances between the chip1 and chip2 from wire scan set up are 670 mm and 300 mm respectively. The detail of X-ray lenses used for two dimensional focussing is given in Table 4.11. Figure 4.27 shows the X-ray CCD images taken from high resolution camera during 2-D focussing. The focus spot of 6 μm (V) x 3 μm (H) is obtained when lenses illuminated with photon energy of 16.4 keV. The transmission and gain is determined by directly measuring

the beam intensity using PIPS diode. By taking into account the dark current of the diode, measured 2-D transmission is 28%. The total gain of the X-ray lenses is 625 which is 2-4 times smaller. The X-ray lenses used in vertical geometry has earlier produced the focussed spot of 0.8 μm in same setup. More precise measurements for 2-D focusing are required.

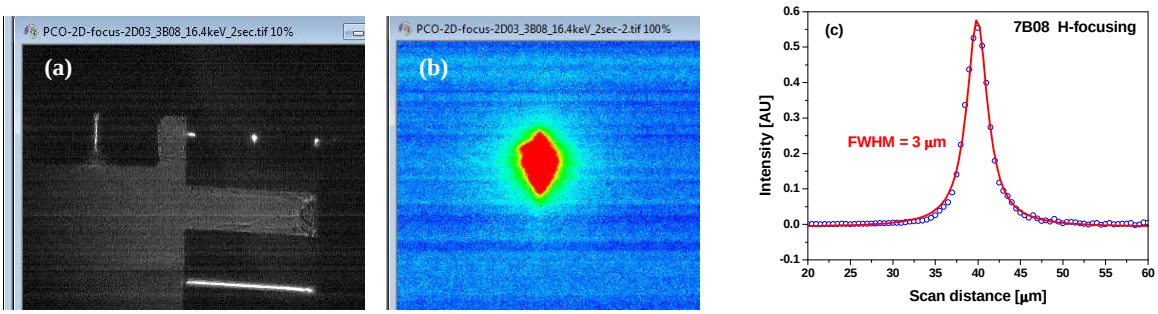

Figure 4. 27 : SU-8 X-ray lens 2D focusing at Diamond (a) High resolution X-ray CCD image (b) Enlarged view of 2D focused spot with measured gain of 624 (c) Focused beam profile in horizontal direction.

4.6.2.3 Results of experiment at I12, Diamond

Diamond's super conducting multi-pole wiggler provides energies upto 150 keV. SU-8 X-ray lenses are used for microfocusing at a high energy 60-100 keV at I12 Joint Engineering Environmental Processing (JEEP) beamline [192]. The main research technique performed at JEEP beamline are imaging, tomography, XRD and small angle X-ray scattering. The SU-8 X-ray lenses are placed at 50 m from the source and the focused beam is observed at 30 m from the lens. In energy range 60-100 keV, SU-8 X-ray lenses with R = 100 μm has almost 90% transmission. Figure 4.28 shows the focusing of 7A13 X-ray lenses (N = 90), lens depth (t) = 500 μm at 94 keV. The focused spot of 69 μm with a gain of 5.4 is recorded. Table 4.12 gives the overview of the microfocusing results up to 100 keV.

The earlier reports of microfocusing characterisation of SU-8 X-ray lenses are limited upto 55 keV by Nazmov et. al. [193]. In this thesis, we have shown the performance of the X-ray lenses from 8-100 keV.

Table 4. 12 : Microfocusing using SU-8 X-ray lenses at 60-100 keV.

Lens number	*N*	*E* [keV]	FWHM [µm]	Gain
7A06	38	64	99	~ 4.9
7A10	65	94	92.4	~ 4.4
7A13	90	94	69	~ 5.4
7A13	90	97	56	~ 6.5
7A13	90	100	66	~ 5.0

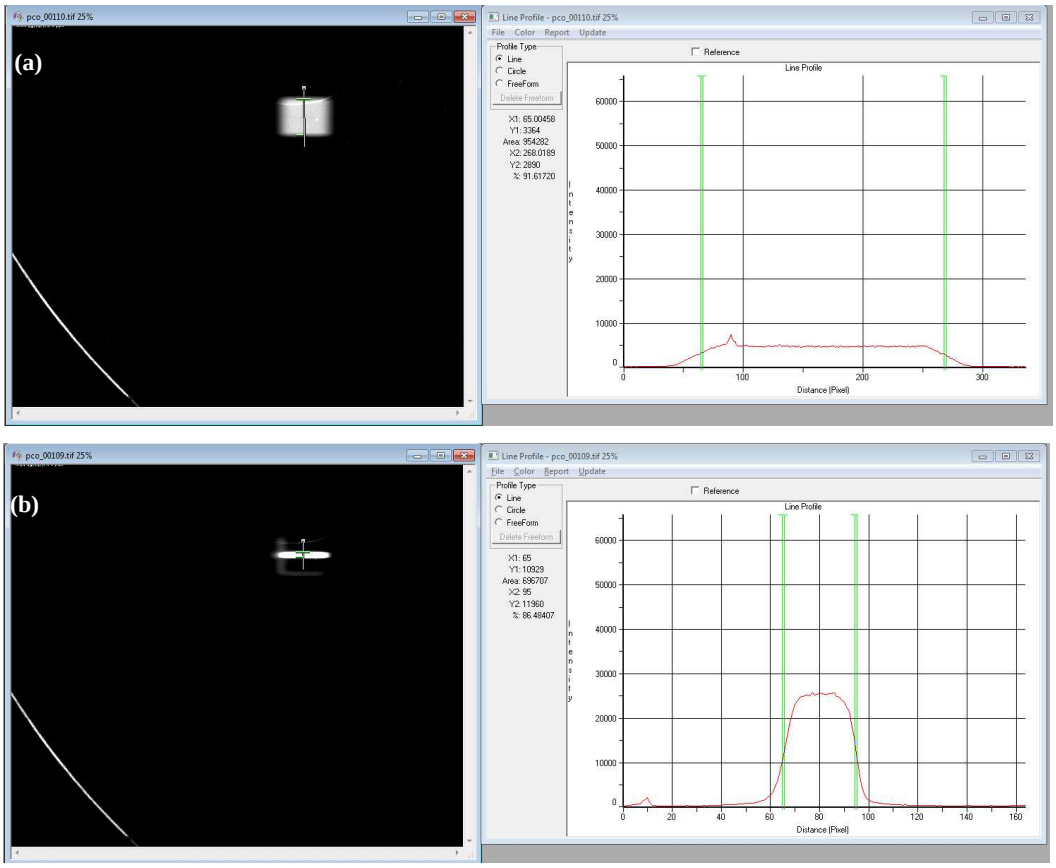

Figure 4. 28 : High energy focussing using SU-8 CRL (a) incident beam (b) focused beam observed on X-ray CCD

4.6.3 Characterization of SUEX lenses

Results of experiment at BL-16, Indus-2

SUEX lens chip containing Series A, B and C X-ray lenses are used for microfocus characterisation at BL-16, Indus-2. The major goal of this study is to evaluate the performance of the SUEX X-ray lenses in terms of focusing and transmission with respect to SU-8. It has been pointed out earlier that the performance of the SUEX X-ray lenses is likely to be better than SU-8 X-ray lenses due to absence of Sb impurity atom.

The measurement of SUEX X-ray lenses are carried out as per described in case of SU-8 lenses. The distance from end of the lenses to edge scan system is initially fixed to ~ 291 mm for Series C lens, ~ 280 mm for Series B lens and ~ 1060 mm for Series A lens. The exact distance from the centre of the lens is calculated by adding the half length of CRL lenses in the above values. Table 4.13 gives the various values pertaining to X-ray lens characterisation at Indus-2.

Table 4. 13 : Overview of the SUEX X-ray lenses measurements at Indus-2

Lens	E [keV]	R [μm]	N	f [m]		F_v [μm]		A_{eff} [μm]	T_{crl} [%]	Gain
				Exp.	Calc.	Exp.	Calc.	Calc.	Calc.	Calc.
8A06	14.45	100	38	1.065	1.076	13.69	9.8	319	53.5	18.5
8A10	18.88	100	65	1.070	1.074	16.36	9.8	324	56.7	20
8A11	20.0	100	73	1.072	1.074	16.52	9.8	324	56.8	20
8B04	11.75	50	45	0.291	0.300	5.8(11.4)	2.65	187	33	16.6
8B06	13.9	50	63	0.295	0.301	4.2 (7.2)	2.65	195	36.5	18.2
8B08	16.15	50	84	0.300	0.305	5.7 (8.5)	2.69	201	39	19.2
8B10	18.3	50	108	0.305	0.305	4.8 (7.3)	2.69	203	40	19.9
8C04	11.95	25	23	0.298	0.304	3.7 (8.4)	2.68	176	43	16.8
8C07	15.2	25	37	0.303	0.306	4.7(10.3)	2.7	184	48	18.8

Table 4. 14: Measured FWHM of focus beam as a function of lens depth at three points

Position	1 (top)	2 (centre)	3 (bottom)
Slit centre [mm]	0.15	0.0	-0.15
FWHM [μm]	4.0	4.27	3.84

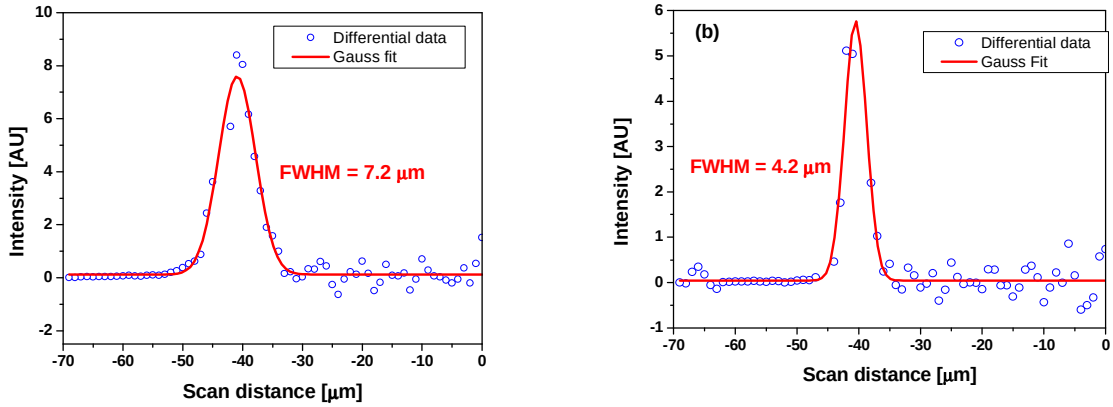

Figure 4. 29: Focused beam obtained from lens 8B06 when x-ray lens is illuminated with (a) 450 μm and (b) 100 μm horizontal slit width.

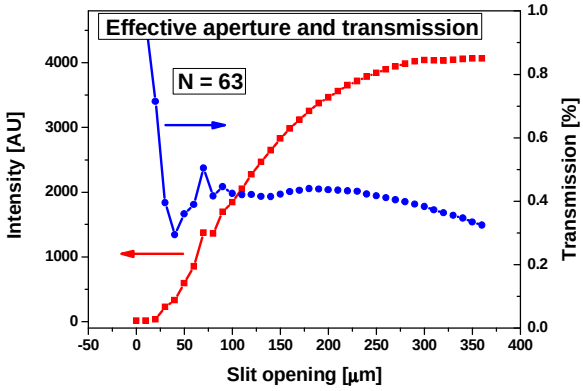

Figure 4. 30 : Measured effective aperture and transmission for SUEX lens 8B08.

The best focal spot size of ~7.24 μm for lens 8B06 at ~ 13.7 keV is shown in figure 4.29 (a). Similarly, the performance of the lens is checked along the etched depth, when a slit

width of 100 μm used to illuminate the lens surface. The profiles are recorded only at three points, first at centre, second and third profiles are obtained at ± 150 μm around the centre position. The FWHM value at lens centre is found 4.2 μm and is shown in figure 4.29 (b). The variation in spot size along the depth is 4.0 ± 0.3 μm and values are tabulated in table 4.14.

Figure 4.30 shows the intensity and transmission values as a function of vertical slit opening for lens 8B08 at 16.15 keV (the focussed spot size ~ 8.47 μm). Transmission of ~ 39 % is expected for lens 8B08 at 250 μm effective aperture. There is significant deviation from the theoretical estimate of ~200 μm. It seems the contribution coming from small angle X-ray scattering in the lens material to focus spot. The effective aperture for this X-ray lens is found to be 25% more than estimated values. The reason of increased effective aperture needs to be quantified further by using a small pin hole in the focused beam.

SUEX radiation stability test

The radiation stability test of X-ray lens material is performed by irradiating SUEX X-ray lens chip at BL-07 and later it is characterised at BL-16. The similar type of test is earlier reported by Snigirev et. al. where they have used two methods (1) focusing undulator beam by Be lens on SU-8 X-ray lens under study [194] and (2) mounting the SU-8 X-ray lens chip perpendicular to beam path and delivering the dose of 2 MJ/cm^3 [195]. Here, second method is adopted for investigating the heavy radiation dose effect. Chip containing SUEX X-ray lens is exposed to white X-ray beam at BL-07 in vacuum chamber with ambient pressure of 5.0 x 10^{-02} mbar and exposure dose of 11184 mA.min is given to X-ray lenses. Two more substrates, a bare 2 mm thick PMMA sheet and SU-8 X-ray lenses on Si wafer is also mounted in the same setup and identical exposure dose is given. The deposited top dose in these substrates is calculated. The table 4.15 shows the deposited dose rate at the top of PMMA, SU-8 and SUEX and absorbed dose at an approximate depth of 500 μm (depth of SUEX lenses). Due to heavy X-ray exposure dose, the PMMA foamed and swelled to 8 mm from its original thickness (2 mm). There is no significant change is observed in SU-8 and

SUEX substrate except colour change. Colour of SU-8 and SUEX changes from transparent white to black and dark brown respectively. Further, no structural deviations in SU-8 and SUEX X-ray lens profiles are observed. Unexposed and exposed SUEX X-ray lenses are also characterised at BL-16, Indus-2. No major changes in focus beam spots and its profile are observed. Presently, it can be concluded that the 0.26 MJ/cm^3 exposure dose not produced any significant damage in SUEX microstructures. In future, the effect of higher exposure dose on SUEX X-ray lenses will be studied.

Table 4. 15: Calculated top and bottom absorbed dose for SU-8, SUEX and PMMA in white beam.

Total exposure dose [mA.min]	11184	
Resist material	**Absorbed dose in the resist material [MJ/cm^3]**	
	Top	**Bottom**
SU-8	0.285	0.058
SUEX	0.263	0.055
PMMA	0.289	0.056

4.6.4 Comparison between SU-8 and SUEX X-ray lenses

Figure 4.31 shows the calculated effective aperture and transmission for SUEX and SU-8 X-ray lens materials in energy range of 8-100 keV for B series X-ray lenses with fixed focal length ~ 0.32 m. The measured values for both the materials with their estimated values are given in table 4.16. At higher energies (particularly above Sb K edge) the performance of SUEX lenses exceeds the performance of SU-8 lenses in terms of effective aperture and transmission. In this thesis, X-ray lenses measurement at above Sb K edge are not carried out due to non-availability of monochromatic beam at BL-16. The performance of SUEX and SU-8 X-ray lens is carried at 13.9 keV for lens #B06. The transmission curves and curves to

determine effective aperture is shown in figure 4.32 (a, b). SU-8 with effective aperture 160 μm, a value of transmission ~ 41% is obtained which is higher and may be attributed to the diffuse scattering. The corresponding transmission value for SUEX lens material is higher. As per our calculations, it should be higher by 11% than of SU-8. The transmitted intensity of SUEX X-ray lenses is 53% at effective aperture 190 μm. This corresponding value shows clear indication of better performance of SUEX X-ray lenses over SU-8. It is also likely that the effective aperture of 8B06 is more than that of theoretical estimate much similarly like reported for 8B08 lens.

Table 4. 16: Comparison between the effective aperture and transmission data of SUEX and SU-8 X-ray lenses

Lens	***E*** **[keV]**	***R*** **[μm]**	***N***	***f*** **[m]**		***F*****$_v$** **[μm]**		***A*****$_{eff}$** **[μm]**		***T*****$_{crl}$** **[%]**	
				Exp.	**Calc.**	**Exp.**	**Calc.**	**Exp.**	**Calc.**	**Exp.**	**Calc.**
SU-8 4B06	14	50	63	0.304	0.292	3.5	2.59	160	159	41	25
SUEX 8B06	14	50	63	0.294	0.301	4.2	2.65	190	195	53	36

The measurements of SUEX lenses are planned at Diamond. The measurement at above Sb edge is also expected to show the better performance in comparison to SU-8 lenses. At around 32 keV, the expected transmission of SUEX X-ray lenses is 34 % (A_{eff} = 186 μm) compare to corresponding transmission of SU-8 X-ray lenses which is 15.2 % (A_{eff} = 118 μm) for f = 0.32 m, R = 50 μm and N = ~ 330.

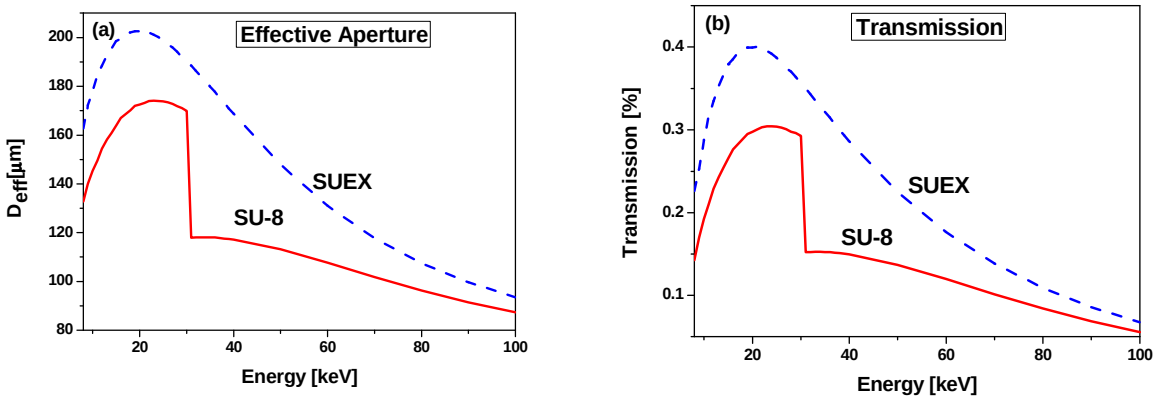

Figure 4. 31 : Estimated performance between SUEX and SU-8 on the basis of their effective aperture and transmission.

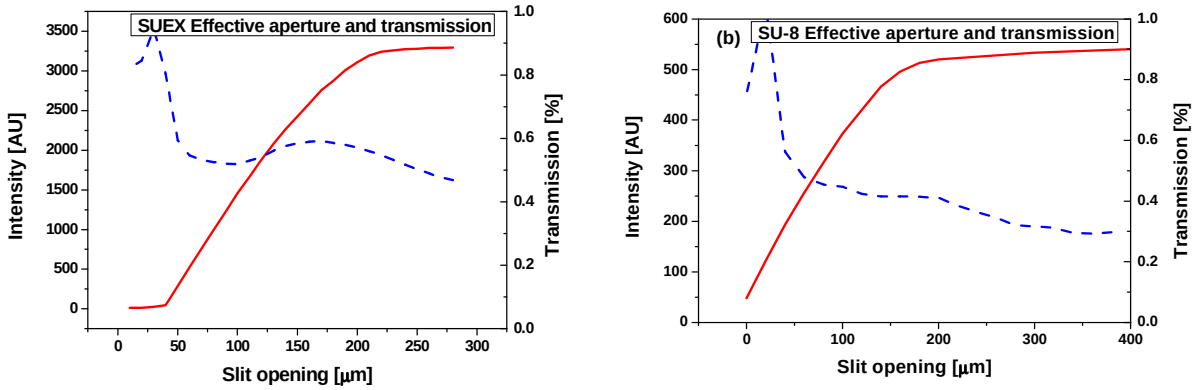

Figure 4. 32 : Effective transmission of SU-8 and SUEX X-ray lenses measured at BL-16, Indus-2

4.7 Experiments using SU-8 CRLs

Micro- and nanofocused spot size obtained using CRLs can be used in many X-ray techniques. They can be used in full field or scanning field microscopy. In scanning field microscopy, various X-ray analytical techniques, such as microfluroscence, microdiffraction and microabsorption spectroscopy can be performed. In this section, the details of two experiments are described which demonstrates the potential of developed SU-8 CRLs.

The first experiment is full field imaging of Cu grid, where the magnification of Cu grid image is presented. This experiment is carried out at BL-16, XRF beamline on Indus-2. In this experiment we have studied the projection of the object by CRL. The second experiment is a recording of high pressure X-ray diffraction of CeO_2 sample using CRLs. This experiment is performed at BL-11, Energy and angle dispersive X-ray diffraction beamline on Indus-2.

Table 4. 17: Details of the X-ray lenses used for imaging experiment.

Lens	***N***	***R* [μm]**	**Calculated spot size (FWHM) [μm]**	**Measured spot size (FWHM) [μm]**
Vertical	54	50	4	5.3
Horizontal	68	50	8	9.3

4.7.1. X-ray imaging experiment

The experimental setup used earlier for 2-D focusing is used for this experiment. In this experimental setup, edge scan setup and CCD camera is removed from previous setup. A Cu grid sample of 23 μm wide pattern width is used. This grid sample is generally used in sample preparation for transmission electron microscope. Cu grid sample is mounted on a stage at a distance of 480 mm away from the X-ray lenses. Two X-ray lenses are mounted in crossed geometry at a distance of 23 m from the source with combined focal length 300 mm. The beam is horizontally and vertically focused by SU-8 lenses to 5.3 μm (V) and 9. 3 μm (H). The radii of curvature *R*, the fixed *N* for lens trail and obtained FWHM of point focus are given in table 4.17.

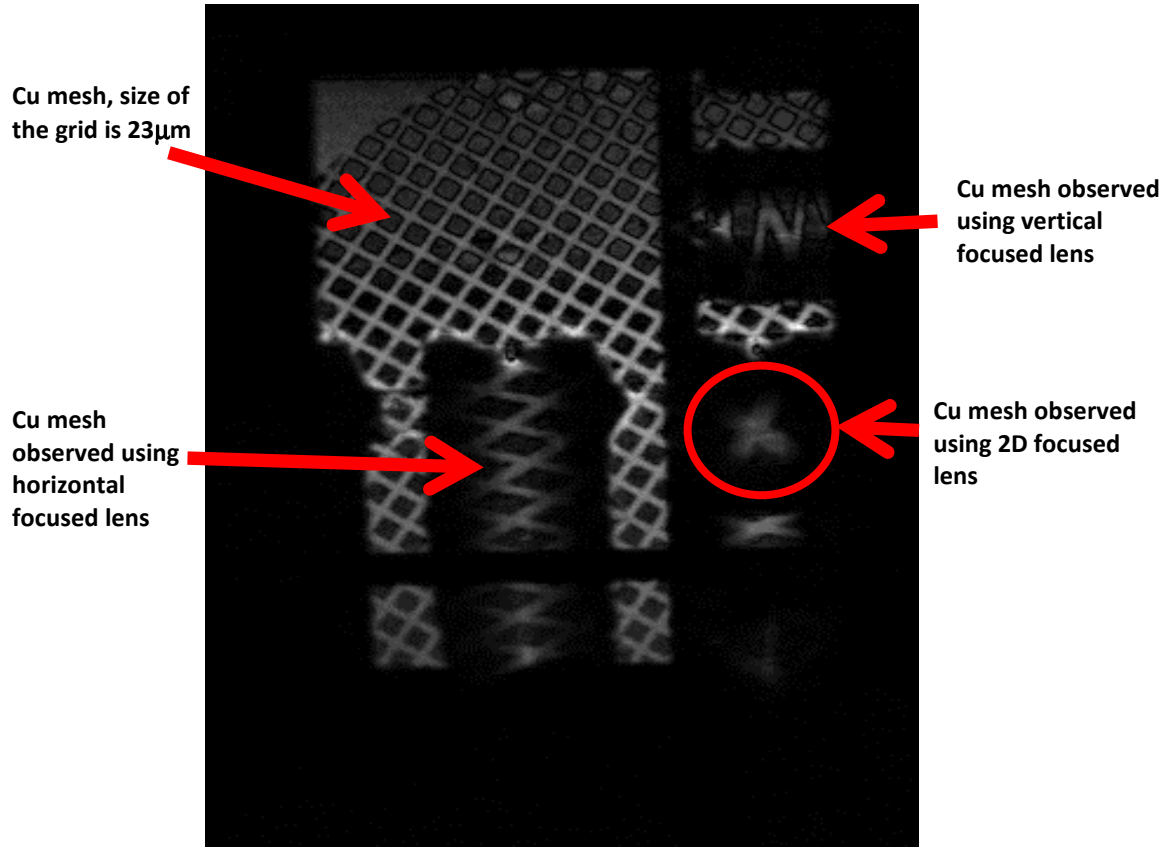

Figure 4. 33 : Full field imaging of Cu TEM sample grid using X-ray refractive lenses.

If the x-ray imaging of Cu grid is recorded in X-ray CCD with pixel resolution of 6.5 µm with no projection lens system, then the resolution of this absorption imaging spectrum would not be less than 10 µm. However, if lenses are used to project the image of sample in magnified way on CCD chip then obtained resolution will be better. A magnified image of the Cu grid with original 23 µm is observed in X-ray CCD kept at 600 mm downstream to sample position is shown in figure 4.33. The broader area of incident beam (5 mm x 5 mm) coming through Cu grid and beam through horizontal focusing lens, vertical focusing lens and 2D focusing lens are also shown. The image shows the original size of Cu grid at X-ray CCD due to natural divergence of the incident beam and magnified image of Cu grid due to projection of CRLs. The crosswire of gold wire 100 µm diameter is also observed and is used

here as reference for scaling. The vertical structures are horizontal focusing lens where the size of the grid is magnified only in horizontal direction. Similarly, for X-ray lenses focusing in vertical direction (right side of the figure), the Cu grid is projected in vertical direction. The right middle image corresponds to the beam coming from 2-D focusing lens through Cu grid sample. The Cu grid is magnified in both the direction as the combining effect of 2-D focusing CRLs. Further on investigating with the Cu grid patterns, it is found that the original size of the Cu is magnified 3 times when using 2-D CRLs. The 2-D focused image is therefore useful in projecting the image at X-ray CCD. The smaller details of the sample which was not recorded by normal 6.5 μm pixel resolution CCD can now be recorded with sample details magnified by X-ray lenses. X-ray lenses are, therefore, useful in projecting the sample and recording better spatial resolution.

4.7.2. High pressure X-ray diffraction

The motivation behind this study is to evaluate the use of CRL for improving the signal to noise ratio in high pressure X-ray diffraction spectrum of a standard sample. X-ray lenses with 2-D microfocusing is tested for recording high pressure X-ray diffraction pattern in angle dispersive mode at BL-11 dedicated for energy and angle dispersive X-ray diffraction [196].

In this experiment, the two lens chips of 2 inch diameter are mounted on two manual stage, in vertical and horizontal direction (figure 4.34 (a)). One of the lens chips, focussing in horizontal direction is aligned along CRL optics axis within 0.2° using optical microscope. These two manual stages carrying two lens chips are further mounted on a motorized tower with 5 degrees of motions. The motorized pitch angle set for one chip (vertically focusing) will disturb the roll angle of other chip (horizontally focusing) or vice versa. Therefore, two

manual stages are mounted with rotational stages between the lens chip and manual stages. However, the error in alignment cannot be ruled out.

Table 4. 18 : Details of the X-ray lenses used for X-ray diffraction experiment.

Lens	***N***	***R* [μm]**	**Theoretical spot size (FWHM) [μm]**	**Measured spot size (FWHM) [μm]**
Vertical	54	100	13	33
Horizontal	68	100	40	45

A 20 keV X-ray beam monochromatised by channel cut crystal monotchormator is used to obtain the point focus dimensions from X-ray lenses. Two X-ray lenses are aligned using X-ray CCD and 2-D focus spot is obtained. Figure 4.34 shows the obtained 2-D focus spot FWHM values 33 μm (V) and 45 μm (H) and compared with theoretical calculated values in table 4.18. The significant deviation in theoretical and obtained spot size is mainly due to alignment error.

The schematic of Diamond Anvil Cell (DAC) used for loading the sample at BL-11 is shown in figure 4.35. Here, Tungsten material with 100 μm pin hole is used as gasket material. The XRD spectrum of CeO_2 sample placed inside DAC is recorded with and without X-ray lens. Figure 4.36 shows the recorded spectrum of CeO_2 sample at 20 keV. The XRD spectrum obtained from unfocused beam shows many peaks from W gasket of DAC. However, the spectrum recorded using X-ray lens has shown no peaks from W gasket.

Utilisation of X-ray lenses in recording high pressure experiments has shown the XRD spectrum free from gasket peaks. Use of X-ray lenses has provided the qualitatively better data which otherwise can be obtained from using pinhole with reduced flux. The intensity rise with use of CRL as shown in figure 4.36 is 1.5 times. However, the intensity obtained from CRLS is around 7.5 times more from the intensity obtained from pinhole aperture of 40

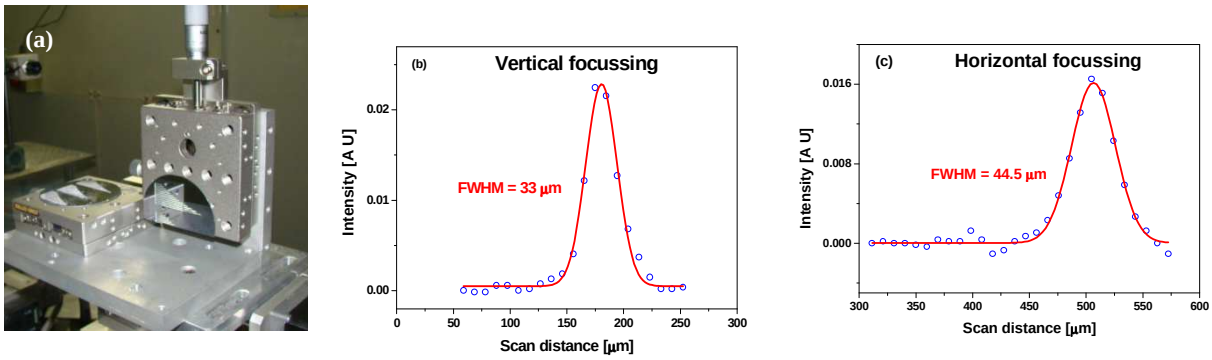

Figure 4. 34 : (a) Cross geometry of CRLs used for XRD experiments and obtained FWHM of focused beam (b) in vertical and (c) horizontal direction.

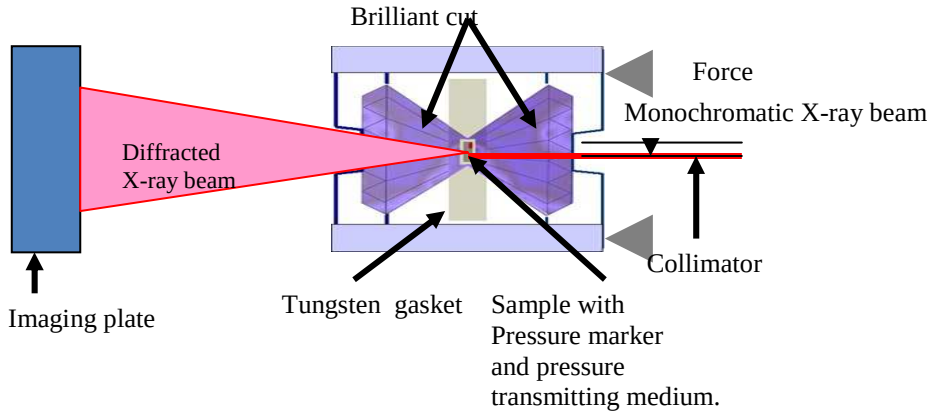

Figure 4. 35 : Schematic of High Pressure XRD measurements with DAC.

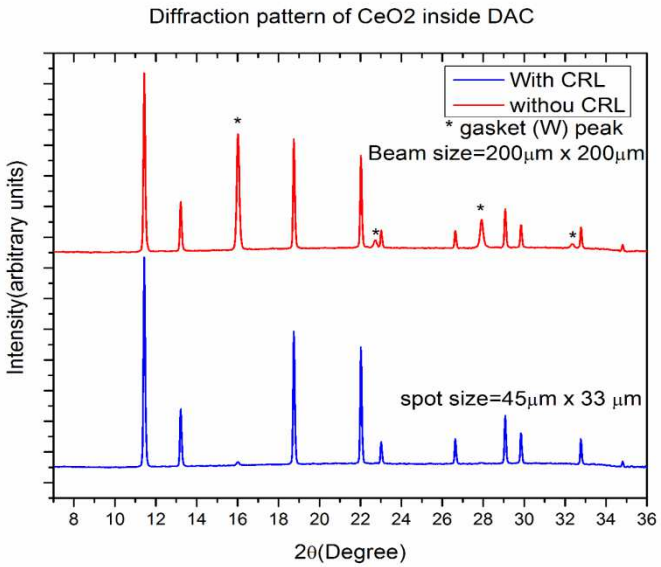

Figure 4. 36 : Comparison of CeO_2 XRD data obtained using 2D focused CRL and without CRL.

μm diameter for recording same spectrum. This gain in the flux is close to the calculated value. There is scope of improvement in the gain by using motorised alignment scheme to obtain 2-D focusing.

During the utilisation of these lenses at BL-16 and BL-11 beamlines, it is realised that high numerical aperture lenses are required to collect more flux such that data is collected in short time. It is concluded that lenses for particularly high pressure experiments, higher geometrical and effective aperture of the lenses are required with two-three order higher gain than usual normal experiment conditions. Two experiments carried out using SU-8 X-ray lenses have shown the quality of the data that can be recorded using X-ray lenses. This type of studies is first of its kind on Indus-2 which have opened up a new opportunities for various new types of experiments at other Indus-2 beamlines.

In summary, three different materials are used for fabrication of X-ray lenses. These lenses are characterised by demonstrating their microfocusing abilities at Indus-2 and Diamond. Their merits and demerits in terms of X-ray lens fabrication and performance characteristics are summarised in table 4.19. PMMA is the best material to choose for obtaining the X-ray lens microstructure. However, it suffers the high radiation damage and extensive use of these lenses is not possible. PMMA lenses can be good choice at the instruments where low monochromatic flux from SR beamlines or lab based X-ray generator is available. Very HAR PMMA X-ray lenses are also not possible as smaller *d* values may collapse the PMMA microstructures.

SU-8 is proven material to sustain at very high exposure dose values. However, the presence of impurity atom limits its use in wide energy ranges. Being chemically amplified resist, the small errors of X-ray mask is transferred to the lens profile creating high sidewall

surface roughness. Therefore, it requires high quality X-ray mask such as fabricated from electron beam pattern generator.

Table 4. 19 : Comparison between three X-ray lens materials used for X-ray lens fabrication in this thesis.

Physical parameters	**PMMA**	**SU-8**	**SUEX**
HAR microstructures	++	+++	+++
Surface roughness	+++	+	++
Effective aperture	++	+	+++
Radiation damage	– –	+++	++

+++ best , ++ better, + good and – – poor

SUEX is better in comparison to both PMMA and SU-8. It offers higher efficiency and transmission compare to SU-8 and higher radiation resistance compare to PMMA. The sidewall surface roughness (average) of SUEX resist layer is measured and found in the range of 5-12 nm (peak to peak 10-38 nm).

Table 4. 20 : SU-8 X-ray lens performance at Indus-2 and Diamond.

Lens (SR Source)	***E* [keV]**	***R* [μm]**	***N***	***f* [m]**		**F_v [μm]**		**A_{eff} [μm]**		**T_{crl} [%]**	
				Exp.	**Calc.**	**Exp.**	**Calc.**	**Exp.**	**Calc.**	**Exp.**	**Calc.**
4B06 (Indus-2)	14	50	63	0.304	0.292	3.5	2.59	160	159	41	25
8B06 (Diamond)	20	50	63	0.600	0.599	1.0	0.913	219	218	50	45

Comparing Diamond with Indus-2, it is possible to obtain 1/3rd or better spot size in vertical and horizontal direction for constant de-magnification due to smaller source size. It means that the more photon can be concentrated in the focus spot. Due to higher flux density,

the setup can also be installed at longer distances from source to obtain higher demagnification and in this case diffraction limited spot is feasible. The limitation at Indus-2 are due to smaller beamline length and higher source size restrict focusing to size of a few μm and makes difficult to reach diffraction limited spots. It is therefore beneficial to use third generation machine with sub nmrad beam emittance in vertical direction to investigate the performance of X-ray lenses developed at SDXRL beamline. A comparison of simillar lenses characterised at Indus-2 and Diamond is given in table 4.20 which clearly validates the argument given above. Diamond is equipped with wiggler where these X-ray lenses are characterised at high energies upto 100 keV which was not possible at Indus-2. In near future, wiggles are going to installed on Indus-2. These characterised lenses at high energy and knowledge generated from these developments will be very useful for deploying X-ray lenses on Indus-2 wiggler source.

Chapter 5

Design and development of Bio sensor

5.1 Introduction to biosensors

With the improvement in microfabrication technology and development of enzyme and DNA detection based techniques, there is a growing interest towards the development of biosensing chips. The miniaturized biochip based on MEMS are used for fast steady state signal, high sensitivity, low sample volume, cost efficiency and portability [197, 198, 199, 200]. Sensing techniques are based on optical, fluorescence or conductivity measurements. Electrochemical sensing is extensively employed for clinical diagnosis and environmental monitoring [201, 202]. Cyclic voltametry, amperometric and impedance measurement techniques are used for electrochemical sensing. Electrochemical impedance spectroscopy (EIS) is useful for studying bulk and interfacial electrical properties [203, 204]. Electrodes are core component of electrochemical sensors. Microelectrodes have better performance in terms of sensitivity, signal stability, diffusion rate of substances, signal to noise ratio and rate of electron transfer [205, 206]. Microelectrodes in disk shape [207], ring shape [208] and comb type interdigitated electrode [209] geometries have been reported.

For reliable and fast clinical diagnostics and better quality control in food industry, glucose sensors with high sensitivity, fast response, excellent selectivity and low cost are

required [210, 211]. Optical [212], calorimetric [213] and electrochemical [214] techniques have been used for the detection of glucose. Glucose sensors based on Glucose oxidase (GOD) enzyme are reported [215, 216]. Several technological approaches have been used towards integrating electrochemical glucose biosensors into small easy-to-use assay formats [217].

Microfluidic system based on Copper laminated printed circuit board (PCB) was introduced in 1999 as low cost alternative to Si fabrication technology [218]. Cu is used as electrode material as replacement of noble metals due to integration compatibility with electronics on the same chip and good electro migration resistance. Copper based electrode materials are used for the analysis of carbohydrates [219, 220].

Cu needs passivation layers to protect the surfaces and interfaces to inhibit oxidation and electrochemical transport of the Cu ions into adjacent dielectric materials, while maintaining good interfacial adhesion [221]. Self-assembled monolayers (SAMs) formed by chemisorptions of thiols on copper protect the underlying metal surface from corrosion. The strong chemical interaction between sulphur atoms and the copper surface leads to stable and easy to prepare chemisorbed organic films [222].

In this chapter, the development of biosensing chip using UV and X-ray lithography is discussed. The Biochip is fabricated using SDXRL beamline and the characterisation is carried out at BITS, Goa by Professor S Bhand's group. Our role was to design and fabricate Biochip. Few performance evaluation results are also included in this chapter to demonstrate usability of the device.

5.2 Materials and methods

5.2.1 Microfabrication of device

The processing steps involved in the fabrication of monolithic biosensor is shown figure 5.1.

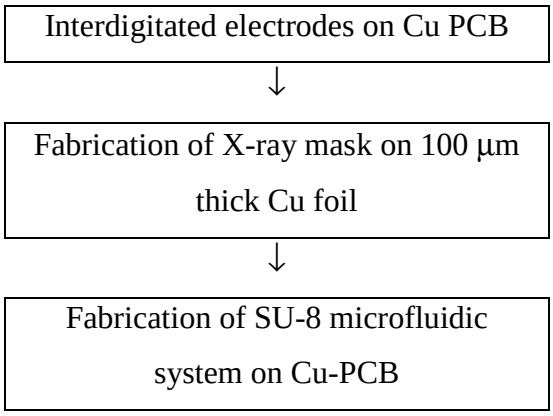

Figure 5. 1 : Processing steps involved in the biosensor fabrication

The circular interdigitated electrode array is fabricated on Cu PCB by following the simillar route used for metal based X-ray mask fabrication. The entire process of fabrication for monolithic bio sensing chip is schematically shown in figure 5.2.

The cleaning process described in Chapter 3 is used for cleaning 25 mm x 40 mm PCB with 35 μm thick Cu laminate. Photolithography is carried out using AZ4903 resist and Cu is wet etched. The prepared substrate with multiple array of Cu-CMEA is shown in figure 5.2 (a) at bottom side. Cu-CMEA with diameter of ~1000 μm, consists of circular cavity type interdigitated micro electrode array. The width of microelectrode is 70 μm with inter-electrode spacing of 110 μm.

The fabrication route of metal type X-ray mask required for this device is discussed in Chapter 3. The same method has been followed to fabricate the X-ray mask. Figure 5.2(b) shows scheme of fabrication and photograph of the actual X-ray mask.

SU-8 2150 is spin coated to obtain 300-1000 μm thick layer on PCB containing Cu-CMEA. Soft baking and post exposure bake timings of SU-8 2150 are given in table 3.13. For obtaining a microwell over CMEA pattern, alignment of mask pattern with Cu-CMEA is carried out. X-ray exposure dose 16-100 mA.min are given to SU-8 through developed X-ray mask at SDXRL beamline. After post exposure bake, SU-8 is developed in PGMEA solution for 20-60 minutes, rinsed in IPA and dried. The involved fabrication steps of the device using X-ray lithography is shown in figure 5.2 (c).

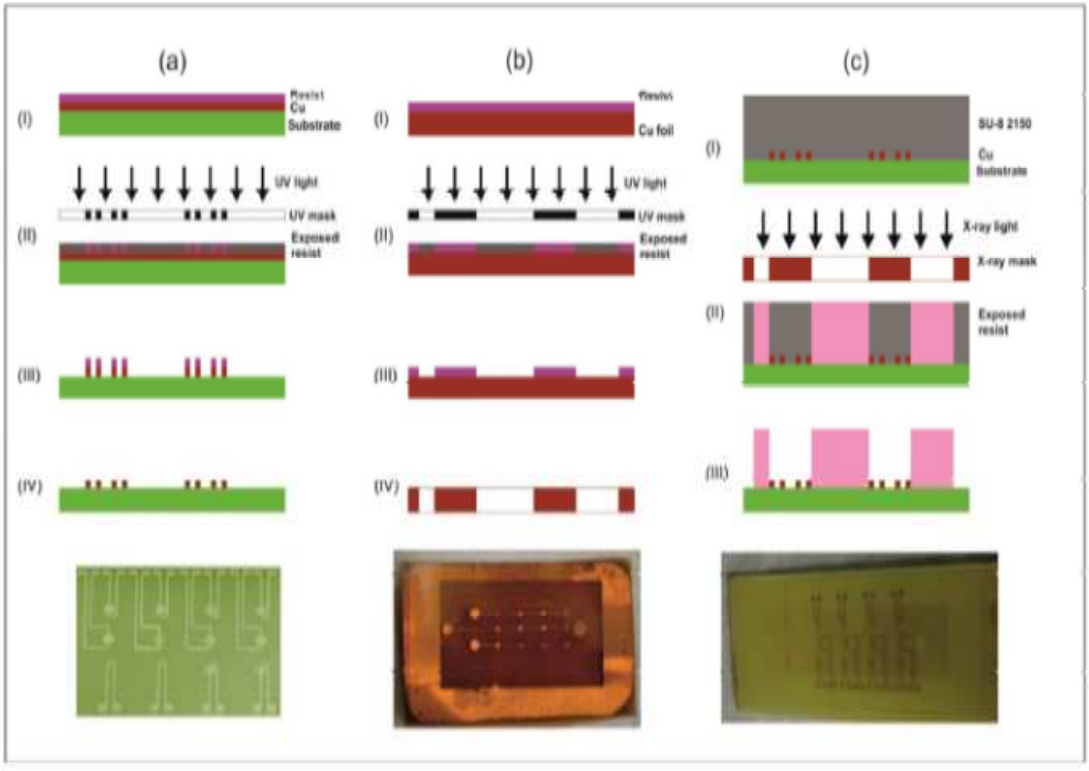

Figure 5. 2 : Schematic of entire fabrication process for developing biochip (a) CMEA on Cu-PCB (b) X-ray mask on Cu foil (c) SU-8 microwell and microfluidic channel over Cu-PCB using SDXRL beamline.

The fabricated device is optically characterized by using COM. Measured diameter of microwell is 962 µm (please refer to figure 5.3). Microwell can be filled with 0.22-0.7 µl equivalent water solution. The width of microelectrode is ~65 µm and spacing between the electrodes is 110 µm. The total area occupied by Cu-CMEA in microwell is 0.19 mm^2 and total length of electrode is ~2.9 mm in the microwell area.

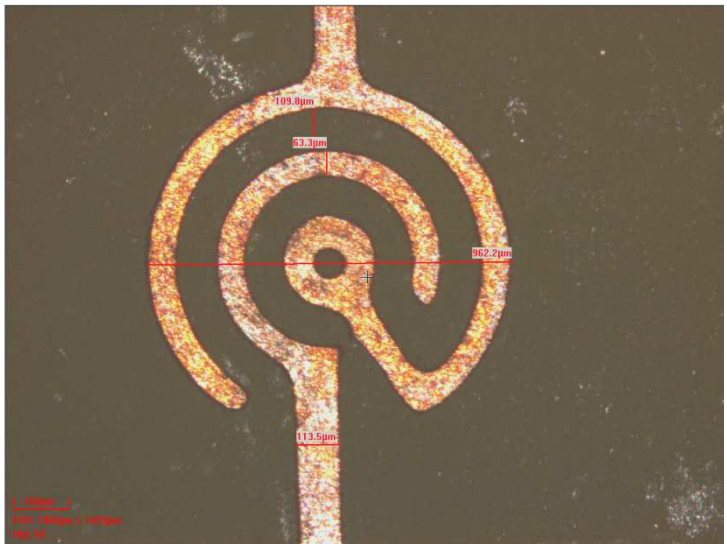

Figure 5. 3 : Cu-CMEA pattern on Cu laminate PCB. The dimensions are measured using COM and shown above.

5.2.2 Materials and instrumentation

Solution preparation

Phosphate buffer (PB) 100 mM, pH 7.4 is prepared by mixing 100 mM of Na_2HPO_4 and 100 mM of NaH_2PO_4 in double distilled water (dd-H_2O). 100 mM Phosphate buffered saline (PBS) is prepared by dissolving appropriate amount of Na_2HPO_4, NaH_2PO_4 and NaCl and is used for incubation and washing purpose. KCl (100 mM) is prepared by dissolving 74.55 mg in 100 mL in dd-H_2O. A stock solution of glucose (100 mM) is prepared by dissolving 0.180

g in 10 mL of PBS (100 mM, pH 7.4). Working solution of KCl and glucose is prepared freshly. Enzyme stock solutions are prepared in PB (100 mM, pH 7.4).

EIS measurements

Impedance measurements are carried out using IVIUM™ CompactStat impedance analyzer, Netherland in two electrode setup configuration. All the measurements are carried out in a grounded Faraday cage, to avoid the interference of the external field strength with the measured impedance signal. Experiments are designed for the development of a glucose biosensor using (a) physically absorbed GOD, *(b*) covalently immobilized GOD.

Development of glucose biosensor chip

Cu-CMEA is functionalized by immobilization of enzyme GOD through self assembled monolayers (SAMs). The glass containers used for monolayer preparation is cleaned with Piranha solution (a mixture of 98% H_2SO_4 and 30% H_2O_2, 7:3, v/v; **caution**: piranha solution reacts exothermally and strongly reacts with organics) for 1 h and rinsed with dd-H_2O and ethanol. The device is washed with ethanol, and dried using high purity nitrogen before use. In second case, the enzymes are covalently coupled on Cu electrode of CMEA through SAMs as described elsewhere [223] with few alteration. These samples are immersed into 4 mM ethanolic solution of 11-*Mercaptoundecanoic acid (11-MUA)* for 12 h (assembly time). After the assembly time, the SAMs functionalized Cu electrode of CMEA are rinsed in ethanol followed by dd-H_2O and dried using dry nitrogen. For enzyme immobilization, the carboxylic acid-terminated SAMs are modified using an aqueous equimolar solution (100 mM) of carbodiimide hydrochloride (EDC) /N-hydroxysuccinimide (NHS) for 1 hr at room temperature. The resultant NHS ester monolayers are reacted for 4 h in a solution of GOD (0.0625 IU/µL) in PB. The enzyme (GOD) coupled Cu electrode of CMEAs is washed thoroughly with PB to remove non-specifically bound enzymes. An optimized enzyme i.e.,

0.0625 IU/µL is physically adsorbed on the surface of Cu electrode of CMEA to compare with covalently attached enzyme. For glucose measurement different concentration of glucose ranges from 10 nM to 20 mM are prepared. Total volume of 0.4 µL of glucose, prepared in PBS is injected on the device. All impedance measurements are performed in the frequency range 10 Hz to 10 kHz using 5 mV ac voltage.

5.3 Results and discussions

5.3.1 Optimization for Glucose sensor

The response of the glucose sensor depends on the activity of GOD, and is related to concentration of GOD, applied potential, applied frequency and sample volume on Cu-CMEA. The reaction between glucose and GOD directly affects the sensitivity of the glucose sensor. The concentration of GOD plays an important role in the reaction. Various concentrations of GOD solutions are tested with Cu electrode of CMEA. The electrochemical signal depends upon Glucose-GOD interaction and reaction time. Hence, the effect of the concentration of GOD and reaction time are investigated. Various GOD concentrations such as 0.0625 IU/µL, 0.13 IU/µL and 0.26 IU/µL are studed using 1 mM glucose. It is found that GOD concentration 0.0625 IU/µL is optimum. Respect to other concentrations of GOD, concentration of 0.0625 IU/µL is showing enhanced impedance response. Further, the reaction time of GOD biosensor is optimized. The impedance response of the biosensor gives a stable response upto 2 min. The result confirmed that the catalyzed oxidation process of glucose is finished in 2 min. Thus, 2 min is adopted for further impedance measurements.

Voltage and current waveform are examined for impedance/capacitance measurement and 5 mV is chosen as the optimal applied potential for correct measurement of impedance/capacitance. Frequency 10 Hz is chosen for glucose measurement.

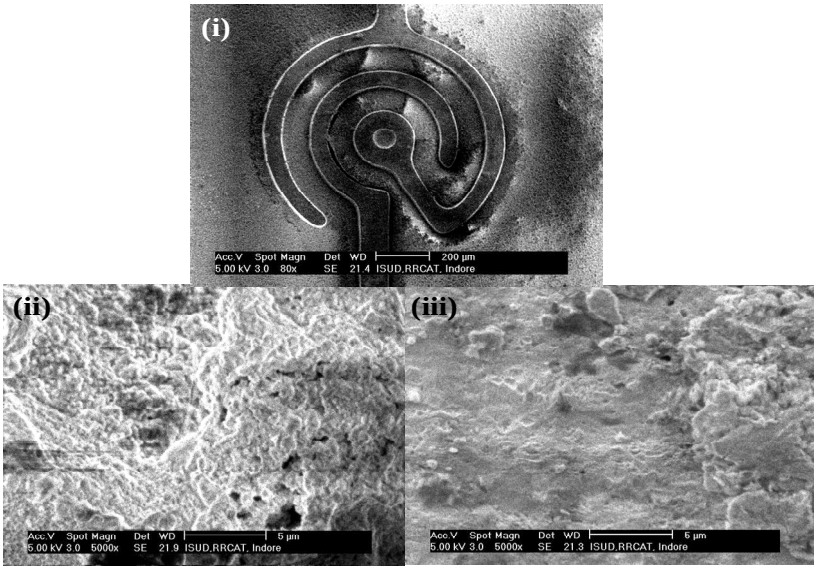

Figure 5. 4 : **Shows the SEM micrograph of (i) the bare Cu electrode of CMEA at magnification 80×; (ii) the 11-MUA modified electrode surface at magnification 5000×; (iii) GOD immobilized electrode surface at magnification 5000×.**

5.3.2 Surface characterization of Cu CMEA

Surface morphology studies

The surface of the Cu-CMEA is characterised by SEM. Figure 5.4 (i) shows the SEM micrograph of the bare Cu electrode of CMEA at magnification 80× and Figure 5.4 (ii) and (iii) shows electrode surface after surface modification by 11-MUA and after immobilization of enzymes at magnification 5000× respectively. After treating with 11-MUA, the Cu electrodes possess a high rough surface topography. Whereas, after enzyme immobilization, the surface of the Cu electrodes became relatively smooth than the surface treated with 11-MUA. The attachment of GOD to a SAMs of 11-MUA on Cu-CMEA surface is achieved

using water soluble EDC/NHS as coupling agents. The carbodiimide cross-linking reaction to form the 11-MUA - GOD conjugated structure is confirmed by ATR FT-IR.

5.3.3 EIS study of glucose biosensor

For the analysis of glucose as a target analyte, enzyme GOD is immobilised on the modified CMEA electrode by physical adsorption. Subsequently, a series of known concentration of glucose are sequentially injected on the surface of Cu-CMEA. The impedance is measured at the frequency range of 10 Hz to 10 kHz at the applied potential of 5 mV. The total impedance is contributed for interfacial electrode impedance and dominated by capacitance, as the measurement is nonfaradic. The capacitance, which is the imaginary part of the measured impedance, is shown in figure 5.5. In this case the change in capacitance is due to the reaction of glucose and GOD, resulting ions was observed at low frequency of 10 Hz. The capacitance increased according to the absorbed ions as the concentration of glucose increases.

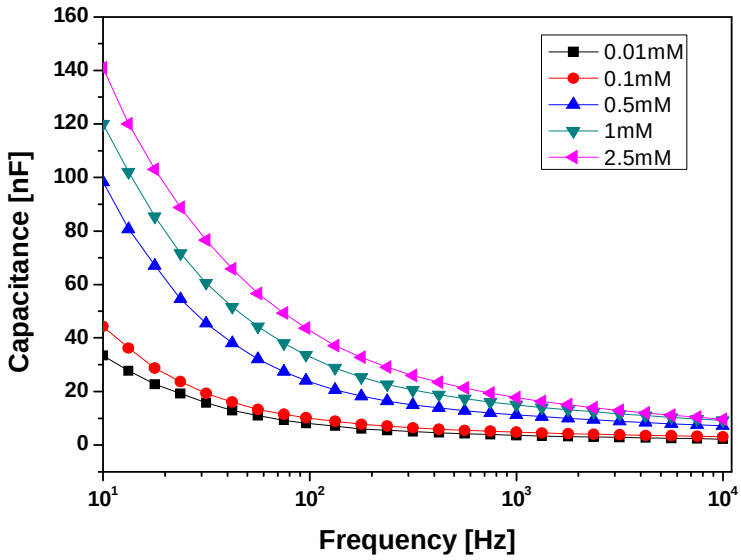

Figure 5. 5 : Capacitive spectra for various concentrations of glucose. EIS: 10 Hz to 10 kHz, 5 mV ac potential.

5.3.4 Effect of surface modification

Capacitance data are recorded for the functionalized Cu-CMEA after exposing it to increasing glucose concentration (0.01 mM– 2.5 mM). A frequency of 10 Hz at applied ac potential 5 mV is selected for analysis. The electrochemical reaction between glucose and GOD give rise to an overall increase in capacitance change from baseline response at the electrode/solution interface for glucose concentration. The resulting calibration curve is presented in figure 5.6. The calibration for *physisorped* GOD is found to be linear in the range of 0.01 mM to 2.5 mM (R^2 = 0.98, n = 5) with an RSD of 5.73 ± 0.7 (The linear equation is y = 0.11755 + 0.05589x (mM)). LOD and LOQ are determined as 0.01 mM and 2.5 mM.

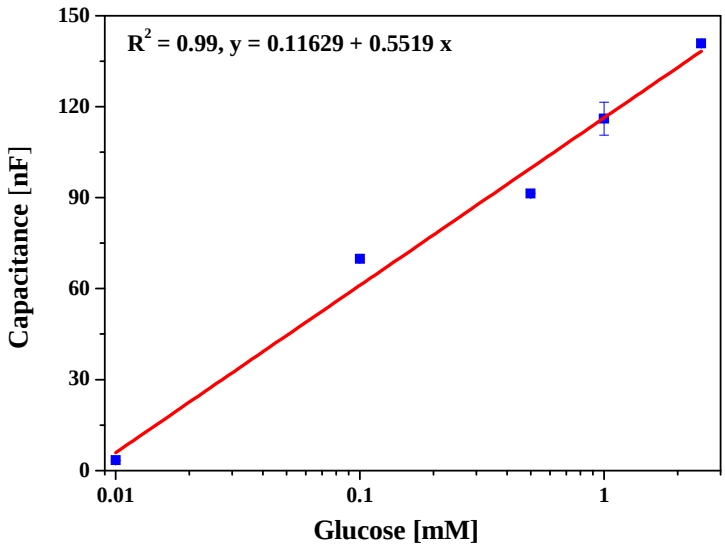

Figure 5. 6 : Calibration curve for different glucose concentrations obtained for physisorbed enzyme on Cu electrode of CMEA.

The results from covalently bonded GOD on Cu-CMEA are encouraging. The results are planned to put as a patent and with revised device dimension. The figures of merit of model glucose biosensor are compared with other recent reported methods and are presented in Table 5.1.

Table 5. 1 : Comparison of design, measurement technique and limit of detection in various established (reported) electrochemical sensor for glucose.

S. No.	Reaction principle using GOD	Design	Measurement technique	Linear range(mM)	Reference
1	Based on ionic enzyme products between GOD and substrate	Three electrode system, (Au-MSA SAM) working electrode	Impedimetric	0-40	Shervedani 2007 [214]
2	Based on ionic enzyme products between GOD and substrate	Three electrode system, Au working electrode	Impedimetric	2.8-22	Pradhan 2013 [224]
3	Based on ionic enzyme products between GOD and substrate	GOD coated ZnO nanowires on Ag wire microelectrode	Potentiometry	0.0005-10	Ali 2010 [225]
4	Electron shuttling from enzyme to electrode via ferrocene	MEMS fabricated Pt electrode coated with polypyrrole, ferrocene and GOx	Amperometry	0–25	Pesántez 2012 [226]
5	Based on ionic enzyme products between GOD and substrate	Coil micro electrode array UV and X-ray lithography	Impedimetric	0.01-2.5	This work 2014.

In conclusion, Cu-CMEA based biosensor chip is fabricated using combinational process of UV and X-ray lithography. The Cu microelectrode has played a pivotal role for detection of glucose based on the enzyme-glucose interaction process. The developed biosensor behaves linearly for wide glucose concentrations covering range of 0.01 mM – 2.5 mM. The biochip is demonstrated in terms of reusability with short analysis time of 2 mins.

Chapter 6

Conclusions

6.1 Summary

This thesis achieved a successful implementation of X-ray lithography technique at Indus-2. The thesis presents, a. design, development and commissioning of XRL beamline facility, b. characterisation and optimization of processing condition of X-ray resist on SDXRL beamline, c. HAR microfabrication in X-ray resist, and d. some other extremely important technologies, such as development of X-ray mask. XRL beamline and accumulated knowledge of various processing technologies have been used to develop the two important technologies/devices, (1) X-ray refractive lenses, and (2) Biosensor. The availability of this first and unique facility in the country has paved a way to fabricate variety of microstructure on many types of substrates having different dimensions and depths which may be useful in wider science and engineering fields.

X-ray lithography beamline facility on Indus-2 is successfully built for HAR microfabrication. The major design goals set during design phase is achieved. Various beamline components including the two diagnostic setup, X-ray mirror system and X-ray scanner system are developed. The role of each beamline component and its utility for fabrication of HAR microstructure using X-ray lithography is explained. The salient features

of beamline components, their offline testing procedures are also explained. SDXRL beamline is installed on Indus-2 and commissioned. Two diagnostic systems are used to define the stability of the source and obtain profile of the beam from two mirror system. A technique to quickly align the two mirror system with the help of WPS in accuracy of 10 μrad is proposed. The utility of XBPM is demonstrated by measuring the beam stability of Indus-2. SDXRL beamline operation is demonstrated in pink beam and white beam modes. Mirrors are used to choose the energy spectrum between 2-24 keV. Critical parameters defined in the beamline design are related with measured HAR microstructures. The beam profiles and beam sizes are determined for various energy spectra at scanner1 and scanner2. X-ray exposures are carried out in air and vacuum mode of operation. The power density transported by the beamline from the source to experimental station, in various spectral ranges are measured using in-house developed Cu calorimeter. This study is used to estimate the exposure dose rate / time for fabrication of microstructures. The vertical beam profiles in different energy ranges and horizontal beam uniformity in one energy range are measured. WPS is also helpful to track the changes in the photon flux or exposure dose rate. The performance of X-ray scanner is also evaluated. The role of X-ray scanner towards maintaining the integrity of the microstructure during the exposure is described.

The major requirement for performing X-ray lithography is to ensure the availability of high quality X-ray mask. The bottleneck here is to not only fabricate good quality of X-ray mask but also to make sustain a thicker gold on membrane. The technology for fabrication of X-ray mask is developed during the present work. The requirement and characteristics of X-ray mask is described. Membrane based and metal foil based X-ray masks are prepared. X-ray mask is fabricated using UV lithography and Au electrodeposition techniques. The minimum feature size of ~10 μm is produced in X-ray masks with a Au thickness of ~15 μm. This thickness of the Au is sufficient to give a good exposure contrast for fabrication of

microstructure in ~2000-3000 μm thick resist layer. Two X-ray sensitive resists, PMMA and SU-8 are used for fabrication of devices and test patterns. Effect of X-ray exposure on PMMA is explored in this work and irradiation effects of PMMA have been explored using Raman and FTIR spectroscopy techniques, optical microscopy and X-ray diffraction technique. A study is carried out to determine the dissolution rate of PMMA irradiated at various exposure dose values. These studies are helpful in determining the development rate of HAR microstructure by establishing the relationship between the exposure dose given by the SDXRL beamline and obtained depth in CLAREX PMMA sheet. The processing conditions of very thick SU-8 resist for HAR microfabrication is optimized for the SDXRL beamline. This includes the optimization of coating parameters, soft baking, exposure and post exposure bake for typical thickness ranging between 100-1200 μm. Test microstructures are fabricated to demonstrate the capabilities of the developed XRL system. In 6 mm thick PMMA sheet, the tallest structure with aspect ratio of ~100 is fabricated. X-ray exposure dose profile is varied in PMMA to obtain 3-D HAR microstructures. The effect of horizontal intensity uniformity on the performance of microstructural feature sizes (100-500 μm) development in PMMA along horizontal direction has been demonstrated. As a function of time, depth is recorded and depth uniformity along horizontal width of the beam is found within ± 10 % for ± 7% measured beam intensity variation. The sidewall roughness of PMMA and SU-8 microstructures is measured using COM. The measured average surface roughness of PMMA sidewall is 1.6 nm (peak to valley 12.6 nm) and for SU-8 is 5.2 nm (peak to valley 38.4 nm). The cross sectional view of developed structure is studied and the vertical sidewall slope error of <1 mrad is achieved. The profile of the microstructures in lateral direction is investigated using COM and variation of ~0.1 to 1.0 % in defined feature dimensions are observed.

CRLs are developed in PMMA and SU-8 materials. The use of CRLs has been described by showing their successful application in microimaging and high pressure microXRD experiments. The development of these lenses was accompanied by the search of suitable lens material which can perform better than PMMA in higher radiation resistance and SU-8 in respect to higher transmission and effective aperture. SUEX having similar properties like SU-8 but absence of Sb impurity atom has not been tried earlier as lens material and it is used first time in this thesis for development of X-ray lens. X-ray refractive lenses are developed in PMMA, SU-8 and SUEX with an aim to use them for microfocussing X-rays and collecting the sample data in various X-ray techniques. The lenses are designed for 8-20 keV with focal lengths 0.3-1 m. However, they can be used at higher energies and will give higher focal length. X-ray lenses with cylindrically symmetric parabolic profiles are fabricated with radius of curvatures 25 μm, 50 μm and 100 μm. Around ~4000 X-ray lenses are integrated in a single Si chip which can be used for focusing different X-ray energies to desired focal lengths. Physical profiles and mechanical dimensions of X-ray lenses are investigated using COM. X-ray lenses are characterized on Indus-2 and Diamond by measuring the focus size, transmission and effective aperture of SU-8 and SUEX X-ray lenses. At Indus-2, the X-ray characterisation facility is setup at BL-16. The role of two SR sources in characterisation of manufactured X-ray lenses is explored by comparing the predicted and measured performance. The minimum focus spot (FWHM) of 3.2 μm and 0.8 μm is obtained at Indus-2 and Diamond respectively. By considering the source sizes and demagnification of optics, the obtained spot sizes are in very close agreements with the estimated focus sizes. The transmission efficiency and effective aperture of a few representative lenses are also shown. The transmission efficiency greater than 50% and effective aperture more than 200 μm is obtained for SUEX X-ray lenses. SU-8 X-ray lenses are also used to obtain the 2-D focus

spot with significant gain at Indus-2 and Diamond. X-ray lenses have been deployed at Indus-2 for micro imaging and micro XRD experiments. Absorption X-ray imaging is performed to see the projection image of Cu grid structure on X-ray CCD. Due to high depth of the field, X-ray lenses can also be used in tomography application. A high pressure XRD data of CeO_2 is recorded by 2-D focusing spot inside DAC. The diffraction data obtained with X-ray lenses focused beam has shown no peaks of Tungsten gasket. The advantages of Indus-2 and Diamond for microfocusing experiments are described. The vis-a-vis advantage of three X-ray lens materials are given.

A monolithic Cu-CMEA is fabricated using UV and X-ray lithography techniques. The application of the developed Cu-CMEA Biochip for use in glucose biosensing is demonstrated. Using EIS technique, detection for glucose (0.01 – 2.5 mM) is achieved on glucose oxidase immobilized CMEA device. Lower detection limit is achieved but not reported in this theis. The use of Cu microelectrode has played a pivotal role for detection of glucose based on the enzyme-glucose interaction process. The present biochip has the potential to detect glucose with a short analysis time of 2 minutes and low sample volume (0.4 μL). An important feature of the biochip device is its reusability that makes it an attractive feature over existing disposable devices.

6.2 Future studies

HAR microfabrication of X-ray lenses with lower radius of curvatures (5-10 μm) out of SUEX material is planned. SUEX has shown more transmission than SU-8. The radiation resistance evaluation of SUEX is planned at very high value (> 2 MJ/cm^3) of exposure dose. The characterisation of SUEX lenses at above Sb K edge is proposed. This will allow us to project SUEX as replacement of SU-8 lens material.

The operation of the beamline in lower energy is planned by operating the beamline in windowless mode or using thin (15-25 μm) Be-window. This will enable the fabrication of submicron structures with shallow depths (< 20 μm). The 3-D microfabrication attachment is prepared and fabrication of 3-D microstructures (eg. microcoils) are also planned. The X-ray mask technology is limited to UV mask and UV photolithography. X-ray mask development with small features and better structure fidelity is planned to develop using e-beam pattern generator. In future, we propose facility augmentation and make HAR microstructures with lower feature sizes.

The characterisation of X-ray lenses reported in this work is carried out at BL-16 using monochromatic beam. A standalone micro optics test bench facility for characterisation of X-ray lenses is required where not only monochromatic but also pink and white beam should available. This test bench will be setup at BL-07.

The sensitivity of EIS biosensor can be increased by lowering the inter-electrode spacing and its width. The fabrication of device with reduced electrode spacing and with enhanced low detection traceability is planned.

In summary, next stage involves, smaller lateral dimensions X-ray mask making, HAR microstructure fabrication of lower feature sizes and comprehensive test bench facility for characterisation of micro optics in monochromatic, pink and white beam at BL-07, Indus-2.

References

1. M. J. Madou, “Fundamentals of Microfabrication and Nanotechnology”, *CRC Press* 1-3 (2012).
2. W. Ehrfeld and D. Müenchmeyer, “Three-dimensional microfabrication using synchrotron radiation”, *Nucl. Instrum. Methods Phys. Res. A* 303, 523–531 (1991).
3. D. W. L. Tolfree, “Microfabrication using synchrotron radiation”, *Rep. Prog. Phys*. 61, 313-351 (1998).
4. E. Di Fabrizio, M. Gentili, L. Grella, M. Baciocchi, A. Krasnoperova, F. Cerrina, W. Yun, B. Lai and E. Gluskin, “High-performance multilevel blazed x-ray microscopy Fresnel zone plates: Fabricated using X-ray lithography”, *J. Vac. Sci. Technol. B* 12, 3979 (1994).
5. V. Nazmov, L. Shabelnikov, FJ. Pantenburg, J. Mohr, E. Reznikova, A. Snigirev, I. Snigireva, S. Kouznetsov and M. DiMichiel, “Kinoform X-ray lens creation in polymer materials by deep X-ray lithography”, *Nucl. Instrum. Methods Phys. Res*. B 217, 409–416 (2004).
6. T. Liu, R. Simon, D. Batchelor, V. Nazmov and M. Hagelstein, “A desktop X-ray monochromator for synchrotron radiation based on refraction in mosaic prism lenses”, *J. Synchtrotron Rad*.19, 191-197 (2012).
7. W. Ehrfeld and E. Lehr, “Deep X-ray lithography for the production of three-dimensional microstructures from metals, polymers and ceramics”, *Radiat. Phys. Chem*. 45(3), 349-365 (1995).
8. S. P. Heussler, H. O. Moser and S. M. P. Kalaiselvi, “3D deep X-ray lithography for producing a multi-channel Fourier transform interferometer”, *Microsys. Technol*. 19, 335-341 (2013).
9. L. Businaro, F. Romanato, P. Candeloro, E. Di Fabrizio, M. Patrini, M. Galli, C. Andreani, A. Passaseo and M. De Vittorio,“High-resolution complex structures for two-dimensional photonic crystals realized by X-ray diffraction lithography”, *J. Vac. Sci. Technol. B* 21, 748 (2003).

10. R. Rinaldi, C. Turco, N. Lovergine, R. Cingolani, L. Vasanelli, E. Di Fabrizio, L. Grella, M. Gentili, L. DeCaro and L. Tapfer, “Free-standing ZnSe/ZnS quantum wires with high luminescence efficiency”, *Appl. Phys. Lett*. 71, 3770 (1997).
11. W. Ehrfeld, V. Hessel, H. Löwe, C. Schulzand L. Weber, “Materials of LIGA technology”, *Microsys. Technol*. 5, 105 (1999).
12. C. Cuisin, Y. Chen, D. Decanini, A. Chelnokov, F. Carcenac, A. Madouri, J. M. Lourtioz and H. Launois, “Fabrication of three-dimensional microstructures by high resolution X-ray lithography”, *J. Vac. Sci. Technol. B* 17, 3444 (1999).
13. O. Tabata, K. Terasoma, N. Agawa and K. Yamamoto, “Moving mask LIGA (M^2 LIGA) process for control of side wall inclination”, *IEEE Proc. MEMS*, 252 (1999).
14. U. Wallrabe, P. Bley, B. Krevet, W. Menz, and J. Mohr, “Design rules and test of electrostatic micromotors made by the LIGA process”, *J. Micromech. Microeng*. 4, 40–45 (1994).
15. B. Loechel, J. Goettert, G. Gruetzner, M. Bednarzik, C. Waberski, G. Ahrens, R. Engelke, V. Singh, R. Degen and U.Kirsch, “Extreme aspect ratio NiFe gear wheels for the production of commercially available Micro Harmonic Drive® gears”, *Microsys. Technol*. 14, 1675-1681 (2008).
16. D. M. Klymyshyn, M. Börner, D.T. Haluzan, E.G. Santosa, M. Schaffer, S. Achenbach and Jurgen Mohr, “Verticle high-Q RF-MEMS devices for reactive lumped-element circuits” *IEEE Trans. on Microwave The. and Tech.* 58, 2976-2986 (2010).
17. D. M. Klymyshyn, H.C. Jayatilaka, M. Borner and Jurgen Mohr, “High aspect-ratio coplanar waveguide wideband bandpass filter with compact unit cells”, *IEEE Trans. on Microwave The. and Tech.* 7, 2753-2760 (2009).
18. E. Spiller, R. Feder, J. Topalian, E. Catellani, L. Romankiw and M. Heritage, "X-ray Lithography for Bubble Devices”, *Solid State Technol.* 62-68 (1976).
19. J. Guo, Q. Leonard, F. Cerrina, E. Di Fabrizio, L. Luciani, M. Gentili and D. Gerold, “Experimental and theoretical study of image bias in x-ray lithography”, *J. Vac. Sci. Technol. B* 10, 3150 (1992).
20. J. W. Goodman, “Introduction to Fourier Optics”, McGraw-Hill, New York (1968).

21. E. W. Becker, W. Ehrfeld, D. Münchmeyer, H. Betz , A. Heuberger, S. Pongratz, W. Glashauser, H. J. Michel, and R. Siemens, “Production of separation - nozzle systems for uranium enrichment by a combination of X - ray lithography and galvanoplastics”, *Naturwissenschaften* 69, 520 – 3 (1982).
22. S. J. Chung, H. Hein, J. Mohr, F. J. Pantenburg, J. Schulz, and U. Wallrabe, “LIGA technology today and its industrial Applications”, *Proc. SPIE* 4194 (2000).
23. S. K. Deb, G. Singh and P. D. Gupta, “Indus-2 Synchrotron Radiation Source: current status and utilization”, *J. Phys*. Conf. Ser. 425, doi:10.1088/1742-6596/425/7/072009 (2013).
24. E. Di. Fabrizio, R. Fillipo, S. Cabrini, R. Kumar, F. Perennes, M. Altissimo, L. Businaro, D. Cojac, L. Vaccari, M. Prasciolu and P. Candeloro, “X-ray lithography for micro- and nano-fabrication at ELETTRA for interdisciplinary applications”, *J. Phys. Condens. Matter* 16, S3517–S353 (2004).
25. F. Pérennés, F. De Bona and F. J. Pantenburg, “Deep X-ray lithography beamline at ELETTRA”, *Nucl. Instrum. Methods Phys. Res. A* 467–468, 1274–1278 (2001).
26. https://www.anka.kit.edu/984.php (2014).
27. https://www.anka.kit.edu/985.php (2014).
28. https://www.anka.kit.edu/986.php (2014).
29. http://140.110.203.42/manage/fck_fileimage/file/bldoc/18BLIGA (2014).
30. http://140.110.203.42/manage/fck_fileimage/file/bldoc/19ALitho.htm (2014).
31. http://pal.postech.ac.kr/paleng/bl/9D/ (2014).
32. Y. Utsumi, T. Kishimoto, T. Hattori and H. Hara, “Large Area X-ray Lithography System for LIGA Process Operating in Wide Energy Range of Synchrotron Radiation”, *Japanese J. App. Phys.*, 44 (7B), 5500-5504 (2005).
33. http://www.camd.lsu.edu/xrlm/xrlm.htm#xrlm1 (2014).
34. http://www-als.lbl.gov/index.php/beamlines/beamlines-directory.html (2014).
35. B. P. Lai, D. C. Mancini, W. Yun and E. S. Gluskin, “Beamline and exposure station for deep x-ray lithography at the advanced photon source”, *SPIE* 2880, 171 (1996).
36. http://mems.ustc.edu.cn/EN/introduction.php?type=mems (2014).
37. http://www.ritsumei.ac.jp/acd/re/src/kankobutsu/vol.14/p181.pdf (2012)

38. M. Bednarzik, H.-U. Scheunemann, A. Barth, D. Schondelmaier, and B. Loechel, "First results in patterning of ultra high aspect ratio microstructures by a 4T wave length shifter at BESSY", *Proc. International Conf. on MEMS, NANO and Smart Systems 2003*, 177-180 DOI: 10.1109/ICMENS.2003.1221989 (2003).
39. A. N. Artemiev, I. N. Bushev, V. A. Kolyasnikov, G. A. Kovachov, O. E. Latish, V. V. Martynenko, V. P. Moryakov, B. I. Nikitin, D. G. Odintsov, S. S. Peredkov, T. Y. Rakhimbabaev, V. G. Stankevitch, E. S. Tzvid, M. Schmidt, A. Schmidt and G. Feiertag, "A Deep X-ray Lithography beamline at the Kurchatov Synchrotron Radiation Source: First results", *Nucl. Instrum. Methods Phys. Res.* A 405 (2–3) 496–499 (1998).
40. http://www.lightsource.ca/beamlines/sylmand.php (2014).
41. V. P. Dhamgaye and G. S. Lodha, "Indus-2 X-ray lithography beamline for X-ray optics and material science applications", *AIP Conf. Proc*. 1591, 7 (2014).
42. Jens Als-Nielsen and Des McMorrow, "Elements of Modern X-ray Physics", *2nd Edition John Wiley & Sons Ltd* (2011).
43. Data is taken from NIST website; http://physics.nist.gov/PhysRefData/Xcom/html/xcom1.html
44. D. Attwood, "Soft X-rays and Extreme Ultraviolet Radiation Principles and Applications", *Cambridge University Press* (1999).
45 Eugene Hecht, "Optics", *Addison-Wesley* (2002).
46. A. El-Kholi, P. Bley, J. Götert, and J. Mohr, "Examination of the solubility and molecular weight distribution of PMMA in view of an optimised resist system in deep etch X-ray lithography", *Mic. Electr. Eng*. 21, 271-274 (1993).
47. Lorenz, H., M. Despont, N. Fahrni, N. LaBianca, P. Renaud, and P. Vettiger, "SU-8: A low-cost negative resist for MEMS",*J. Micromech.Microeng.* 7(3), 121-124 (1997).
48. W. C. Röentgen, "Uber eine neue Art von Strahlen", *Sitzungsberichte der physikalisch-medizinischen Gesellschaft zu Wurzburg*, Berlin, (1895/1896).
49. A. H. Compton and S. K. Allison, "X-rays in Theory and Experiment", *D. Van Nostrand Company, Inc.*, New York (1954).

50. H. Mimura, H. Yumoto, S. Matsuyama, Y. Sano, K. Yamamura, Y. Mori, M. Yabashi, Y. Nishino, K. Tamasaku, T. Ishikawa, and K. Yamauchi, *Appl. Phys. Lett.* 90, 051903 (2007).
51. K. Yamauchi, H. Mimura, T.Kimura, H. Yumoto, S. Handa, S. Matsuyama, K. Arima, Y. Sano, K. Yamamura, K. Inagaki, H. Nakamori, J. Kim, K. Tamasaku, Y. Nishino, M. Yabashi and T. Ishikawa, "Single-nanometer focusing of hard X-rays by Kirkpatrick–Baez mirrors", *J. Phys.: Condens. Matter* 23 394206 (2011).
52. O. Hignette, P. Cloetens, C. Morawe, C. Borel, W. Ludwig, P. Bernard, A. Rommeveaux and S. Bohic, "Nanofocusing at ESRF using graded multilayer mirrors", *AIP Conf. Proc*. 879, 792 (2007).
53. D. H. Bilderback, S. A. Hoffman and D. J. Thiel, "Nanometer spatial resolution achieved in hard X-ray imaging and Laue diffraction experiments", *Science* 263, 201 (1994).
54. C. Bergemann, H. Keymeulen, and J. F. van der Veen, "Focusing X-ray beams to nanometer dimensions", *Phys. Rev. Lett*. 91, 204801 (2003).
55. A. Snigirev, A. Bjeoumikhov, A. Erko, I. Snigireva, M. Grigoriev, M. Erkoand S. Bjeoumikhova, "Two-step hard X-ray focusing combining Fresnel zone plate and single-bounce ellipsoidal capillary", *J. Synchrotron Radiat.* 14, 227 (2007).
56. A. Jarre, C. Fuhse, C. Ollinger, J. Seeger, R. Tucoulou, T. Salditt, "Two-dimensional hard x-ray beam compression by combined focusing and waveguide optics", *Phys. Rev. Lett*. 94, 074801 (2005).
57. M. J. Zwanenburg, J. H. H. Bongaerts, J. F. Peters, D. Riese, and J. F. van der Veen, "Focusing of coherent X-rays in a tapered planar waveguide", *Physica B* 283, 285 (2000).
58. G.-C. Yin, Y.-F. Song, M.-T. Tang, F.-R. Chen, K. S. Liang, F. W. Duewer, M. Feser, W. Yun, and H.-P. D. Shieh, "30nm resolution x-ray imaging at 8keV using third order diffraction of a zone plate lens objective in a transmission microscope", *Appl. Phys. Lett.* 89, 221122 (2006).
59. H. C. Kang, H. Yan, R. P. Winarski, M. V. Holt, J. Maser, C. Liu, R.Conley, S. Vogt, A. T. Macrander and G. B. Stephenson, "Focusing of hard X-rays to 16 nanometers with a multilayer Laue lens", *Appl. Phys. Lett*. 92, 221114 (2008).

60. C. G. Schroer, O. Kurapova, J. Patommel, P. Boye, J. Feldkamp, B. Lengeler, M. Burghammer, C. Riekel, L. Vincze, A. van der Hart, and M. Küchler, "Hard X-ray nanoprobe based on refractive X-ray lenses", *Appl. Phys. Lett.* 87, 124103 (2005).
61. D. J. Beebe, G. A. Mensing and G. M. Walker, "Physics and applications of microfluidics in biology", *Annu. Rev. Biomed. Eng.* 4, 261–286 (2002).
62. J. C. McDonald and G. M. Whitesides, "Poly (dimethylsiloxane) as a material for fabricating microfluidic devices", *Acc. Chem. Res.* 35, 491–499 (2002).
63. J. Cooper and Tony Cass editors, "Biosensors", *2nd edition Oxford University Press* (2004)
64. H. Y. Tan, W. K. Loke, Y. T. Tan and N. T. Nguyen, "A lab-on-a-chip for detection of nerve agent sarin in blood", *Lab on a Chip* 8(6), 885-891(2008).
65. M. S. Chiriacò, E. Primiceri, A. G. Monteduro, A. Bove, S. Leporatti, M. Capello, S. Ferri-Borgogno, R. Rinaldi, F. Novellibc and G. Maruccio , "Towards pancreatic cancer diagnosis using EIS biochips", *Lab on a Chip* 13, 730-734 (2013).
66. Y. Qin, M. R. Matiar, M. Howlader, J. Deen, Y. M. Haddara and P. R. Selvaganapathy, "Polymer integration for packaging of implantable sensors", *Sens. and Actuat. B: Chem.* 202, 758–778 (2014).
67. A. de Mello, "FOCUS On-chip chromatography: the last twenty years", *Lab on a Chip* 2(3), 48N-54N (2002).
68. J. Zhang, K. L. Tan, G. D. Hong, L. J. Yang and H. Gong, "Polymerization optimization of SU-8 PR and its applications in microfluidic systems and MEMS", *J. Micromech. Microeng.* 11, 20–26 (2001).
69. A. A. Adams, P. I. Okagbare, J. Feng, M. L. Hupert, D. Patterson, J. Göttert, R. L. McCarley, D. Nikitopoulos, M. C. Murphy and S. A. Soper, "Highly Efficient Circulating Tumor Cell Isolation from Whole Blood and Label-Free Enumeration Using Polymer-Based Microfluidics with an Integrated Conductivity Sensor", *J. Am. Chem. Soc*. 130(27), 8633–8641 (2008).
70. T. Hattori, H. Mekaru and Y. Utsumi, "An approach to three dimensional microstrusture fabrication utilizing hard X-ray lithography of synchrotron radiation", *Rev. Sci. Inst*. 73, 1376 (2002).

71. F. Yi, J. Zhang, C. Xie, D. Wang and D. Chen, "Activities of LIGA and NANO LIGA technologies at BSRF", *J. Phys. Conf. Ser*. 34, 865-869 (2006).
72. F. Romanato, E. DiFabrizio, L. Vaccari, M. Altissimo, D. Cojoc, L. Businaro and S. Cabrini, "LILIT beamline for soft and deep X-ray lithography", *Elettra. Microelectron Eng*. 101, 57–58 (2001).
73. http://www.camd.lsu.edu/xrlm/xrlm.htm#xrlm1
74. Y. Utsumi and T.Kishimoto, "Large area and wide dimension range X-ray lithography for Lithographite, Galvanoformung, and Abformung process using Energy variable synchrotron radiation", *J. Vac. Sci. Technol. B* 23, 2903(2005).
75. B. Lai and F. Cerrina, "SHADOW: A synchrotron radiation ray tracing program", *Nucl. Instr. Method. A* 246, 337 (1986).
76. M. Sanchez del Rio and R. J. Dejus, "XOP: Recent developments", *SPIE* 3448, 340-345 (1998).
77. F. Schafers, *Bessy Internal Report*, TB 202/96 (1996).
78. G. S. Lodha, V. P. Dhamgaye, M. H. Modi, M. Nayak, A. K. Sinha and R. V. Nandedkar, "Beamlines on Indus-1 and Indus-2 for X-ray Multilayer Optics and Micro Fabrication Research", *AIP Conf. Proc*. 879, 1474-1477 (2007).
79. S. Goto, T. Taguchi, T. Osada, S. Okamura, and T. Hisatsugu, "Synchrotron radiation beamline for x-ray lithography", *J. Vac. Sci. Technol. B* 11, 286 (1993).
80. M. Khan, F. Cerrina and E. Toyota, "Pattern resolution of an x-ray beamline with a wide exposure field", *J. Vac. Sci. Technol. B*, 17, 3433-3438 (1999).
81. V. P. Dhamgaye, G. S. Lodha, B. Gowri Sankar and C. Kant, "BL07 Beamline at Indus-2: A Facility for Microfabrication Research", *J. Synch. Rad*. 21, 259-263 (2014).
82. V. P. Dhamgaye, "Design of Indus-2 X-ray lithography beamline", *ISUD internal report* (2007).
83. Del Rio M. Sanchez and Marcelli, *Nucl. Instr. Method. A* 319, 170-77 (1992).
84. V. P. Dhamgaye and G. S. Lodha, "Selection of mirror coating for SDXRL beamline", *ISUD internal report* (2010).
85 P. Tischer and E. Hundt, "Influence of photoelectrons on the exposure of resists by X-rays", *J. Vac. Sci. Technol.* 15, 1009 (1978).

86 W. B. Peatman and K. Holldack, “Diagnostic front end for BESSY II”, *J. Synchroton Rad.* 5, 639-641 (1998).

87 V. P. Dhamgaye, M. N. Singh, K. J. S. Sawhney and R. V. Nandedkar, “Beam Position Monitor for Synchrotron Radiation: Calibration and Testing”, *DAE-Solid State Physics Symposium- 2003*, Gwalior, 285 (2003).

88 J. J. Yeh, “Atomic Calculations of Photoionization cross-sections and asymmetry parameters”, *Gordon and Beach Publishers*, USA, 73 (1993).

89 Frankoptics, Germany (www.*frank*-optik-products.de).

90 K. Holldack, D. Ponwitz and W. B. Peatman, “Beam stability of undulator and dipole radiation on BESSY II obtained by synchrotron radiation monitors”, *Nucl. Instr. Method. A* 467-468, 213 (2001).

91. E. van Garderen, J. Krempaský , M. Böge, J. Chrin , V. Schlott, T. Schmidt and A. Streun, “Characterisation of the Systematic Effects of the Insertion Devices with Photon Beam Position Monitors”, *Proc.8th European Workshop on Beam Diagnostics and Instrumentation for Particle Accelerators, DIPAC 2007*, Venice, Italy, 126 (2007).

92. O. Tabata, H. You, N. Matsuzuka, T. Yamaji, S. Uemura, and I. Dama, “Moving mask deep X-ray lithography system with multi stage for 3-D microfabrication”Microsystem Technologies 8, 93-98 (2002).

93. A. Saraf, *M. Tech. Thesis*, RRCAT (2013).

94. K. J. S. Sawhney, V. K. Raghuvanshi, V. P. Dhamgaye, S. R. Kane and C. K. Garg, “Indus-2 Frontend”, *Proc. DAE-BRNS InPAC*-2003, CAT, 26 (2003).

95. V. K. Raghuvanshi, V. P. Dhamgaye, A. K. Singh and R. V. Nandedkar, “Design and Development of Front-end components of Indus-2 Bending Magnet Beamlines”, *AIP Conf. Proc*. 879, 631 (2007) .

96. V. K. Raghuvanshi, V. Dhamgaye, A. Kumar and S. K. Deb, “Design and Fabrication of Safety Shutter for Indus-2 Synchrotron Front-ends”, *AIP Conf. Proc*. 1234, 732 (2010).

97. T. Kaneko, Y. Saitoh, S. Itabashi and H. J. Yoshihara, “High efficiency beamline for synchrotron radiation lithography”, *J. Vac. Sci. Technol. B* 9(5), 3214-3217(1991).

98. U. Flechsig, J. Als-Nielsen, A. Jaggi, J. Krempaský, P. Oberta, S. Spielmann and J. F. van der Veen, “X-ray Experiments for Students at the SLS Optics Beamline”, *10th international conf. on synchrotron rad. instrum.*, CP 1234, 653 (2010).
99. M. A. McCord, R. Viswanathan, F. J. Hohn, A. D. Wilson, R. Naumann and T. H. Newman, “100 kV thermal field emission electron beam lithography tool for high-resolution X-ray mask patterning”, *J. Vac. Sci. Technol*. B 10, 2764 (1992).
100. The Centre for X-ray Optics. http://henke.lbl.gov/optical_constants/
101. S. Achenbach, M. Boerner, S. Kinuta, W. Bacher, J. Mohr, V. Saile, and Y. Saotome, “Structure quality in deep X-ray lithography applying commercial polyimide-based masks”, *Microsyst. Technol.* 13, 349–353 (2007).
102. S. Cabrini, F. Pérennès, B. Marmiroli, A. Olivo, A. Carpentiero, R. Kumar, P. Candeloro and E. Di. Fabrizio, *Microsyst. Technol.* 11, 370-373 (2005)
103. S. Kinuta, Y. Saita, M. Kobayashi, M. Boerner, V. Saile and S. Hosaka, “Polyimide-based X-ray masks with advanced performance of pattern accuracy and thermal stability”, *Microsyst. Technol.* 16, 1299–1302 (2010).
104. D. Allen, “5. Photochemical Machining”, *Ullmann's Encyclopedia of Industrial Chemistry* Wiley-VCH Verlag GmbH & Co. KGaA (2011).
105. A. Wisitsoraat, S. Mongpraneet, R. Phatthanakun, N. Chomnawang, D. Phokharatkul, V. Patthanasettakul and A. Tuantranont, “Low-cost and high-resolution X-ray lithography utilizing a lift-off sputtered lead film mask on a Mylar substrate”, *J. Micromech. Microeng.* 20, 075026 (2010).
106. E. Becker, W. Ehrfeld, P. Hagmann, A. Maner and D. Müenchmeyer, “Fabrication of microstructures with high aspect ratios and great structural heights by synchrotron radiation lithography, galvanoforming, and plastic moulding (LIGA process)”, *Microelect. Eng.* 4, 520-523 (1986).
107. E. H. Anderson, D.P. Kern, and H. I. Smith, “Fabrication by tri-level electron beam lithography of X-ray masks with 50nm linewidths, and replication by X-ray nanolithography ”, *Microelect. Eng.* 6, 541–546 (1987).
108. http://www.bwfoundry.com/
109. http://www.ceeri.res.in/

110. B. L. Henke, P. Lee, T. J. Tanaka, R. L. Shimabukuro and B. K. Fujikawa, “Low energy X-ray interaction coefficients, photoabsorption, scattering reflection”, *Atomic Data and Nucl. Data Tables* 27 (1), 1–144 (1982).

111. A. Charlesby (Ed.), “Atomic Radiation and Polymers, Radiation Effects in Materials”, Vol. 1, Pergamon Press, Oxford, New York (1960).

112. J. O. Choi, J. A. Moore, J. C. Corelli, J. P. Silverman and H. Bakhru, “Degradation of poly(methylmethacrylate) by deep ultraviolet, x-ray, electron beam, and proton beam irradiations”, *J. Vac. Sci. Technol. B* 6, 2286 (1988).

113. L. F. Thompson, C. G. Willson and J. M. J. Fréchet, Eds “Materials for microlithography: Radiation-sensitive polymers”, *Amer Chem Soc book series no* 266 (1984).

114. L. A. Wall and D. W. Brown, “Chemical activity of gamma-irradiated polymethylmethacrylate”, *J. Res. Natl. Bur. Stand*. 57(3), 131 (1956).

115. O. Schmalz, M. Hess and R. Kosfeld, “Structural changes in poly(methyl methacrylate) during deep-etch X-ray synchrotron radiation lithography, Part II: Radiation effects on PMMA”, *Die Angew. Makromol. Chem*. 239, 79-91 (1996).

116. J. Zanghellini, “Das Entwicklungsverhalten von röntgenempfindlichen Polymerresists”, Diplomarbeit Bonn University (1995).

117. P. Meyer, A. El-Kholi, J. Mohr, C. Cremers, F. Bouamrane and S. Megtert , “Study of the development behaviour of irradiated foils and microstructure”, *SPIE* 3874, 312-320 (1999).

118. P. Meyer, J. Schulz, and L. Hahn, “DoseSim: Microsoft-Windows graphical user interface for using synchrotron X-ray exposure and subsequent development in the LIGA process”, *Rev. Sci. Instrum*. 74 (2), 1113 (2003).

119. http://physics.nist.gov/PhysRefData/XrayMassCoef/ComTab/pmma.html

120. P. Meyer, “Fast and accurate X-ray lithography simulation enabled by using Monte Carlo method, New version of DoseSim: a software dedicated to deep X-ray lithography (LIGA)”. *Microsyst. Technol*. 18, 1971–1980 (2012).

121. S. Hafizovic, Y. Hirai, O. Tabata, and J. G. Korvink, "X3-D: 3-D X-ray lithography and development simulation for MEMS", *Proc.12th Int. Conf. on Solid-State Sensors Actuators and Microsystems*, 1570 -1573 (2003).

122. Y. Hirai, S. Hafizovic, N. Matsuzuka, J. G. Korvink and O. Tabata, "Validation of X-ray lithography and development simulation system for moving mask deep X-ray lithography", *J. Microelectromech. Sys.* 15(1), 159–168 (2006).

123. O. Schmalz, M. Hess and R. Kosfeld, "Structural changes in poly(methy1 methacrylate) during deep-etch X-ray synchrotron radiation lithography, Part I: Degradation of the molar mass", *Die Angew. Makromol. Chemie.* 239, 63-77 (1996).

124. A. C. Henry, R. L. McCarley, S. Das, C. Khan Malek and D. S. Poche, "Structural changes in PMMA under hard X-ray irradiation", *Microsys. Technol*. 4(3), 104-109 (1998).

125. S. Iqbal, M. S. Rafique, , S. Anjum, , A. Hayat and N. Iqbal, "Impact of X-ray irradiation on PMMA thin films", *Appl. Surface Sci*. 259, 853-860 (2012).

126. P. Tiwari, A. K. Srivastava, B. Q. Khattak, S. Verma, A. Upadhyay, A. K. Sinha, T. Ganguli, G. S. Lodha and S. K. Deb, "Structural modification of poly (methyl methacrylate) due to electron irradiation", *Measurement* 51, 1–8 (2014).

127. J. L. Koeing, "Spectroscopy of Polymers", Elsevier, New York (1999).

128. R. Zwarich, J. Smolarek and L. Goodman, "Assignment of out-of-plane vibrational modes in benzaldehyde", *J. Mol. Spectro.* 38, 336(1971).

129. J. H. S. Green and D. J. Harrison, "Vibrational spectra of benzene derivatives—XVI. Benzaldehyde and mono-substituted benzaldehydes", *Spectrochim. Acta.* 32, 1265 (1976).

130. SU-8 DataSheet, http://microchem.com/pdf/SU-82000DataSheet2025thru2075Ver4.pdf (2014).

131. A. del Campo and C. Greiner, "SU-8: a photoresist for high-aspect-ratio and 3D submicron lithography", *J. Micromech. Microeng*. 17, R81–R95 (2007).

132. W. H. Teh, U. Dürig, U. Drechsler, C. G. Smith and H.-J. Güntherodt, "Effect of low numerical-aperture femtosecond two-photon absorption on (SU-8) resist for ultrahigh-aspect-ratio microstereolithography", *J. Appl. Phys*. 97, 054907 (2005).

133. O. Vladimirsky, G. Calderon, Y. Vladimirsky, and H. Manohara, "Thick PMMA layer formation as an X-ray imaging medium for micromaching", *SPIE* 2723, 360-371 (1996).

134. PMMA datasheet, http://microchem.com/pdf/PMMA_Data_Sheet.pdf

135. J. Mohr, W. Ehrfeld, D. Münchmeyer and A. Stutz, "Resist technology for deep-etch synchrotron radiation lithography", *Macromol. Chem, Macromol. Symp.* (1989).

136. H. Guckel, "LIGA and LIGA-like processing with high energy photons", *Microsys. Technol.* 2, 153-156 (1996).

137. C. M. Khan and S. Das, "Swelling behaviour of poly(methylmethacrylate)thick resist layers in deep X-ray lithography", *J. Synchrotron Rad*. 10, 272 -279 (2003).

138. V. Ghica and W. Glashauser, Deutsche Offenlegungsschrift, Patent no. 3039110 (1982).

139. A. Stutz, Thesis, Karlsruhe University (1986).

140. B. A. Miller-Chou and J. L. Koenig, "A review of polymer dissolution", *Prog. Polym. Sci.* 28, 1223-1270 (2003).

141. E. E. Parsonage, N. A. Peppas and P. I. Lee, "Properties of positive resists.II. Dissolution characteristics of irradiated poly(methyl methacrylate) and poly(methyl methacrylate-co-maleic anhydride)", *J. Vac. Sci. Technol. B* 5(2), 538-45(1987).

142. A. C. Ouano and F. A. Carothers, "Dissolution dynamics of some polymers: solvent–polymer boundaries", *Polym. Eng. Sci.* 20(2), 160–6 (1980).

143. O. Schmalz, M. Hess and R. Kosfeld, "Structural changes in poly(methy1 methacrylate)during deep-etch X-ray synchrotron radiation lithography, Part III: Mode of action of the developer", *Die Angew. Makromol. Chemie.* 239, 93-106 (1996).

144. F. J. Pantenburg, S. Achenbach and J. Mohr, "Influence of developer temperature and resist material on the structure quality in deep X-ray lithography", *J. Vac. Sci. Technol. B* 6(16), 3547–3551 (1998).

145. F. J. Pantenburg, S. Achenbach and J. Mohr, "Characterisation of defects in very high deep-etch X-ray lithography microstructures", *Microsyst. Technol*. 4, 89–93 (1998).

146. A. El-Kholi, J. Mohr and R. Stransky, "Ultrasonic supported development of irradiated micro-structures", *Microelect. Eng*. 23, 219–222 (1994).

147. J. Zanghellini, A. El-Kholi, J. Mohr and F.J. Pantenburg, “New strategies for HAR microstructure”, *Microsyt. Technol*. 4, 94–97 (1998).

148. P. Meyer, A. El-Kholi and J. Schulz, “Investigations of the development rate of irradiated PMMA microstructures in deep X-ray lithography”, *Microelect. Eng.* 63, 319–328 (2002).

149. K. Ueberreiter, “The solution process” *Diffusion in Polymers*, edited by J. Crank and G. Park, *Academic Press*, New York (1968).

150. J. S. Greeneich, “Developer characteristics of poly(methyl methacrylate) electron resist”, *J. Electrochem. Soc*. 122, 970-976 (1975).

151. Z. Liu, F. Bouamrane, M. Rouillay and R. K. Kupka, “Resist dissolution rate and inclined-wall structures in deep X-ray lithography”, *J. Micromech. Microeng.* 8 (4), 293-300 (1998).

152. R. L. Barber, M. K. Ghantasala, R. Divan, K. D. Vora, E. C. Harvey and D. C. Mancini, “Optimization of SU-8 processing parameters for deep X-ray lithography”, *Microsyst. Technol*. 11, 303–10 (2005).

153. C. Becnel, Yohannes Desta and Kevin Kelly, “Ultra-deep X-ray lithography of densely packed SU-8 features: II. Process performance as a function of dose, feature height and post exposure bake temperature”, *J. Micromech. Microeng.* 15, 1249–59 (2005).

154. A. L. Bogdanov and S. S. Peredkov, “Use of SU-8 PR for very high aspect ratio X-ray lithography”, *Microelectron. Eng.* 53, 493–6 (2000).

155. S. Suehiro, H. Miyaji and H. Hayashi, “Refractive lens for X-ray focus”, *Nature* 352, 385 (1991).

156. T Tomie, *Japanese Patent* 2, 526 409 (1994).

157. A. Snigirev, V. Kohn, I. Snigireva and B. Lengeler, “A compound refractive lens for focussing high energy X-rays”, *Nature* 384, 49–51 (1996).

158. C. Schroer, M. Kuhlmann, U. T. Hunger, T. F. Günzler, O. Kurapova, S. Feste, F. Frehse and B. Lengeler, “Nanofocusing parabolic refractive X-ray lenses”, *Appl. Phys. Lett*. 82, 1485 (2003).

159. B. Lengeler, C. G. Schroer, M. Richwin, J. Tümmler, M. Drakopoulos, A. Snigirev and I. Snigireva, “A microscope for hard x rays based on parabolic compound refractive lenses”, *Appl. Phys. Lett*. 74, 3924 (1999).

160. A. Schropp, R. Hoppe, J. Patommel, D. Samberg, F. Seiboth, S. Stephan, G. Wellenreuther, G. Falkenberg and C. G. Schroer, “Hard X-ray scanning microscopy with coherent radiation: Beyond the resolution of conventional X-ray microscopes”, *Appl. Phys. Lett.* 100, 253112 (2012).

161. B. Lengeler, C. G. Schroer, M. Kuhlmann, B. Benner, T. F. Günzler, O. Kurapova, F. Zontone, A. Snigirev and I. Snigireva, “Refractive X-ray lenses”, *J. Phys.* D. doi:10.1088/0022-3727/38/10A/042 (2005).

162. H. Fukui, M. Simon, V. Nazmov, J. Mohr, K. Evans-Lutterodt, A. Stein and A. Q. R. Baron, “Large-aperture refractive lenses for momentum-resolved spectroscopy with hard X-rays”, *J. Synchrotron Rad*. 20, 591-595 (2013).

163. M. K. Tiwari, L. Alianelli, I. P. Dolbnya and K. J. S. Sawhney, “Application of kinoform lens for X-ray reflectivity analysis”, *J. Synchrotron Rad*. 17, 237-242 (2010).

164. T. Weitkamp, O. Chubar, M. Drakopoulos, A. Souvorov, I. Snigireva, A. Snigirev, T.Günzler, C. Schroer and B. Lengeler, “Refractive lenses as a beam diagnostics tool for high-energy synchrotron radiation”, *Nucl. Instru. and Meth.in Phy. Res. A* 467–468, 248–251 (2001).

165. A. Schropp, R. Hoppe, V. Meier, J. Patommel, F. Seiboth, H. J. Lee, B. Nagler, E. C. Galtier, B. Arnold, U. Zastrau, J. B. Hastings, D. Nilsson, F. Uhlen, U. Vogt, H. M. Hertz and C. G. Schroer, “Full spatial characterization of a nanofocused X-ray free-electron laser beam by ptychographic imaging”, *Scientific Rep.* 3, 1633 (2013).

166. I. Snigireva, A. Snigirev, M. Drakopoulos, V. Kohn, V. Nazmov, E. Reznikova, J. Mohr and V. Saile “Near-diffraction limited coherent X-ray focusing using planar refractive lenses made of epoxy SU-8 resist”, *SPIE* 5539, 20-30 (2004).

167. B. Lengeler, J. Tümmler, A. Snigirev, I. Snigireva and C. Raven, “Transmission and gain of singly and doubly focusing refractive X-ray lenses”, *J. Appl. Phys.* 84, 5855-5861 (1998).

168. B. Lengeler, C. Schroer, J. Tümmler, B. Benner, M. Richwin, A. Snigirev, I. Snigireva, and M. Drakopoulos, “Imaging by parabolic refractive lenses in the hard X-ray range”, *J. Synchrotron Rad*. 6, 1153-1167 (1999).

169. B. Lengeler, C. G. Schroer, B. Benner, T. Florian Günzler, M. Kuhlmann, J. Tümmler, A. S. Simionovici, M. Drakopoulos, A. Snigirev and I. Snigirev, “Parabolic refractive X-ray lenses: a breakthrough in X-ray optics”, *Nucl. Instru. and Meth.in Phy. Res. A* 467–468, 944–950 (2001).

170. C. G. Schroer, M. Kuhlmann, B. Lengeler, T. F. Gunzler, O. Kurapova, B. Benner, C. Rau, A. S. Simionovici, A. Snigirev and I. Snigireva, “Beryllium parabolic refractive X-ray lenses”, *SPIE* 4783, 10 (2002).

171. B. Lengeler, C. G. Schroer, M. Kuhlmann, B. Benner, T. F. Gunzler, O. Kurapova, F. Zontone, A. Snigirev and I. Snigireva, “Beryllium parabolic refractive X-ray lenses”, *SPIE* 5539, 1 (2004).

172. B. Nöhammer, J. Hoszowska, A. K. Freund and C. David, “Diamond planar refractive lenses for third and fourth-generation X-ray sources”, *J. Synchrotron Rad.* 10, 168 (2003).

173. L. Alianelli, K. J. S. Sawhney, A. Malik, O. J. L. Fox, P. W. May, R. Stevens, I. M. Loader and M. C. Wilson, “A planar refractive X-ray lens made of nanocrystalline diamond”, *J. of App. Phys.* 108, 123107 (2010).

174. A.N. Artemiev, A. Snigirev, V. Kohn, I. Snigireva, N. Artemieva, M. Grigoriev, S. Peredkov, L. Glikin, M. Levtonov, V. Kvardakov, A. Zabelin and A. Maevskiy, “Planar parabolic X-ray refractive lens made of glassy carbon”, *Nucl. Instru. and Meth.in Phy. Res. A* 543, 322–325(2005).

175. N. R. Pereira, E. M. Dufresne, R. Clarke and D. A. Arms, “Parabolic lithium refractive optics for x rays”, *Rev. of Scien. Instru.* 75, 37 (2004).

176. A. Andrejczuk, M. Nagamine, Y. Sakurai and M. Itou, “A planar parabolic refractive nickel lens for high-energy X-rays”, *J. Synchrotron Rad*. 21(1), 57-60 (2014).

177. V. Nazmov, E. Reznikova, A. Snigirev, I. Snigireva, M. DiMichiel, M. Grigoriev, J. Mohr, B. Matthis, V. Saile, “LIGA fabrication of X-ray Nickel lenses”, *Microsys. Technol.* 11, 292–297(2005).

178. D. C. Mancini, N. A. Moldovan, R.Divan, F. DeCarlo and J. Yaeger, “X-ray lenses fabricated by deep X-ray lithography”, *SPIE* 4783, 28 (2002).

179. Y. Zhang, T. Katoh, Y. Kagoshima, J. Matui, and Y. Tsusaka, “Focusing hard X-ray with a single lens”, *Jap. J. of App. Phys. Part 2* 40, L75-L77 (2001).

180. V. P. Dhamgaye, M. K. Tiwari, K. J. S. Sawhney and G. S. Lodha, “Microfocussing of synchrotron X-rays using X-ray refractive lens developed at Indus-2 deep X-ray lithography beamline”, *Pramana J. Phys.* 83(1), 119–129 (2014).

181. V. Aristov, M. Grigoriev, S. Kuznetsov, L. Shabelnikov, V. Yunkin, T. Weitkamp, C. Rau, I. Snigireva, A. Snigireva, M. Hoffmann and E. Voges. “X-ray refractive planar lens with minimized absorption”, *Appl. Phys. Lett.* 77, 4058 (2000).

182. C. G. Schroer, O. Kurapova, J. Patommel, P. Boye, J. Feldkamp, B. Lengeler, M. Burghammer, C. Riekel, L. Vincze, A. van der Hart and M. Küchler, “Hard X-ray nanoprobe based on refractive X-ray lenses”, *Appl. Phys. Lett.* 87(12), 124103 (2005).

183. V. Nazmov, E. Reznikova, J. Mohr, A. Snigirev, I. Snigireva, S. Achenbach, V. Saile, *Microsyst. Technol.* 10 (2004) 716.

184. V. Nazmov, E. Reznikova, J. Mohr, V. Saile, L. Vincze, B. Vekemans, S. Bohic and A. Somogyi, “Parabolic crossed planar polymeric X-ray Lenses” *J. Micromech. Microeng.* 21, 015020(2011).

185. V. P. Dhamgaye, M. K. Tiwari, C. K. Garg, P. Tiwari, K. J. S. Sawhney, G. S. Lodha, “Development of high aspect ratio X-ray parabolic compound refractive lens at Indus-2 using X-ray lithography”, *Microsys. Technol.* 10-11, 2055 (2014).

186. B. Lengeler, J. Tümmler, A. Snigirev, I. Snigireva andC. Raven, “Transmission and gain of singly and doubly focusing refractive X-ray lenses”, *J. Appl. Phys.* 84, 5855-5861 (1998).

187. C. G. Schroer, B. Lengeler, B. Benner, T. F. Günzler, M. Kuhlmann, A. S. Simionovici, S. Bohic, M. Drakopoulos, A. Snigirev, I. Snigireva and W. H. Schroder, “Microbeam

production using compound refractive lenses: beam characterization and applications", *SPIE* 4499, 52-63 (2001).

188. D. Johnson, J. Goettert, F. Dawan, Z. Ling and W. Dai, "Preliminary Studies of Thick SU-8 Laminate for Ultra-Deep X-ray Lithography", *Proc. HARMST 2007*, Besancon (2007).
189. D. W. Johnson, J. Goettert, V. Singh and D. Yemane, "SUEX Process Optimization for Ultra Thick High Aspect Ratio LIGA Imaging", *SPIE* 7972, 79722U (2011).
190. M. K. Tiwari, P. Gupta, A. K. Sinha, S. R. Kane, A. K. Singh, S. R. Garg, C. K. Garg, G. S. Lodha and S. K. Deb, "A microfocus X-ray fluorescence beamline at Indus-2 synchrotron radiation facility", *J. Synchrotron Rad*. 20, 386-389 (2013).
191. K. J. S. Sawhney, I. P. Dolbnya, M. K. Tiwari, L. Alianelli, S. M. Scott, G. M. Preece, U. K. Pedersen and R. D. Walton, *AIP Conf. Proc.* 1234, 387 (2010).
192. http://www.diamond.ac.uk/Beamlines/Engineering-and-Environment/I12.html
193. V. Nazmov, E. Reznikova, M. Boerner, J. Mohr, V. Saile, A. Snigirev, I. Snigireva, M. DiMichiel, M. Drakopoulos, R. Simon and M. Grigoriev, "Refractive lenses fabricated by deep SR lithography and LIGA technology for X-ray energies from 1 keV to 1 MeV", *AIP Conf. Proc*. 705, 752 (2004) .
194. I. Snigireva, A. Snigirev, M. Drakopoulos, V. Kohn, V.Nazmov, E.Reznikova, J.Mohr, V.Saile, "Near-diffraction limited coherent X-ray focusing using planar refractive lenses made of epoxy SU-8 resist", *SPIE* 5539, 20-30 (2004).
195. A. Snigirev, I. Snigireva, M. Drakopoulos, V. Nazmov, E. Reznikova, S. Kuznetsov, M. Grigoriev, J. Mohr and V. Saile, "Focusing properties of X-ray polymer refractive lenses from SU-8 resist layer", *SPIE* 5195, 21-31 (2003).
196. K. K. Pandey, H. K. Poswal, A. K. Mishra, A. Dwivedi, R. Vasanthi, N. Garg and S. M. Sharma, "Energy-dispersive X-ray diffraction beamline at Indus-2 synchrotron source", *Pramana J. Phys*. 80(4), 607-619 (2013).
197. H. Craighead, "Future lab-on-a-chip technologies for interrogating individual molecules", *Nature* 442, 387-393 (2006).
198. E. Akyilmaz and M. Turemis, "An inhibition type alkaline phosphatise biosensor for amperometric determination of caffeine", *Electrochim. Acta* 55, 5195-5199 (2010).

199. M. Zougagh and Á. Ríos, “Micro-electromechanical sensors in the analytical field”, *Analyst* 134(7), 1274-1290 (2009).

200. A. Guiseppi-Elie, A. A. Rahman and N. K. Shukla, “SAM modified microdisc electrode arrays (MDEAs) with functionalized carbon nanotubes”, *Electrochim. Acta* 55, 4247-4255 (2010).

201. C. Shan, H. Yang, J. Song, D. Han, A. Ivaska and L. Niu, “Direct electrochemistry of glucose oxidase and biosensing for glucose based on grapheme”, *Anal. Chem*. 81(6), 2378–2382 (2009).

202. A. Crew, D. Lonsdale, N. Byrd, R. Pittson and J. P. Hart, “A screen printed, amperometric biosensor array incorporated into a novel automated system for the simultaneous determination of organophosphate pesticides”, *Biosens. Bioelectron.* 26(6), 2847-2851 (2011).

203. S. Haas, H. G. Jahnke, M. Glass, R. Azendorf, S. Schmidt and A. A. Robitzki, “Real-time monitoring of relaxation and contractility of smooth muscle cells on a novel biohybrid chip”, *Lab on a Chip* 10(21), 2965-2971 (2010).

204. A. J. Bard and L. R. Faulkner,Eds., “Electrochemical Methods: Fundamental and Applications”, *Wiley*, New York, USA (1980).

205.R. Hintsche, M. Paeschke and U. Wollenberger, “Microelectrode arrays and application to biosensing devices”, *Biosens. Bioelectron*. 9, 697-705 (1994).

206.K. Balasubramanian, “Challenges in the use of 1D nanostructures for on-chip biosensing and diagnostics: a review”, *Biosens. Bioelectron*. 26, 1195-1204 (2010).

207.A. A. Rahman, G. Justin and A. Guiseppi-Elie, “Towards an implantable biochip for glucose and lactate monitoring using microdisc electrode arrays (MDEAs)”, *Biomed. Microdevices* 11(1), 75-85 (2009).

208.G. Y. Lee, Y. H. Choi, H. W. Chung, H. Ko, S. Cho and J. C. Pyun, “Capacitive immunoaffinity biosensor based on vertically paired ring-electrode”, *Biosens. Bioelectron*. 40, 227-232 (2013).

209. Q. Xue, C. Bian, J. Tong, J. Sun, H. Zhang and S. Xia, “Fabrication of a 3D interdigitated double-coil microelectrode chip by MEMS technique”, *Microchim. Acta.* 177, 491–496 (2012).

210. S. Vaddiraju, I. Tomazos and D. J. Burgess, “Emerging Synergy between Nanotechnology and Implantable Biosensors: A Review”, *Biosens. Bioelectron*. 25, 1553-1565 (2010).

211. J. D. Newman, and A. P. F. Turner, “Home blood glucose biosensors: A commercial perspective”, *Biosens. Bioelectron*. 20, 2435-2453 (2005).

212. P. W. Barone, R. S. Parker, and M. S. Strano, “In vivo fluorescence detection of glucose using a single-walled carbon nanotube optical sensor: design, fluorophore properties, advantages, and disadvantages”, *Anal. Chem*. 77, 7556-7562 (2005).

213. N. A. Morris, M. F. Cardosi and B. J. Birch, “An electrochemical capillary fill device for the analysis of glucose incorporating glucose oxidase and ruthenium (III) hexamine as mediator”, *Electroanal*. 4, 1-9 (1992).

214. R. K. Shervedani and A. Hatefi-Mehrjardi, “Electrochemical characterization of directly immobilized glucose oxidase on gold mercaptosuccinic anhydride self-assembled monolayer ”, *Sens. Actuators B: Chem*. 126, 415-423 (2007).

215. C. Clark, and C. Lyons, “Electrode systems for continuous monitoring in cardiovascular surgery”*Annals of the New York Academy of Sciences* 102, 29-45 (1962).

216. J. Wang, “Electrochemical glucose biosensors”, *Chemical reviews,* 108, 814-25, (2008).

217. H. M. Huang, P. K. Huang, and W. H. Kuo, “Sol-gel immobilized enzymatic glucose biosensor on gold interdigitated array (IDA) microelectrode”, *J. Sol-Gel Sci. Technol*. 67, 492-500 (2013).

218. T. Merke, M. Graeber and L. Pagel, “A new technology for fluidic microsystems based on PCB technology”, *Sens. and Actuat.* 77, 98–105 (1999).

219. S. Tong, H. Jin and D. Zheng, “Investigations on copper-titanate intercalation materials for amperometric sensor”, *Biosens. Bioelectron*. 24, 2404-2409 (2009).

220. H. Y. Ding, Y. Zhou and S. J. Zhang, “Preparation of Nano-Copper Modified Glassy Carbon Electrode and Its Catalytic Oxidation to Glucose”, *Chin. J. Anal. Chem*. 36, 839-842 (2008).

221. P. G. Ganesan, A. Kumar, and G. Ramanath, “Surface oxide reduction and bilayer molecular assembly of a thiol-terminated organosilane on Cu”, *Appl. Phys.Lett*. 87, 011905 (2005).

222. F. Caprioli, M. Beccari and A. Martinelli , “A multi-technique approach to the analysis of SAMs of aromatic thiols on copper”, *Phys. Chem. Chem. Phys*. 11, 11624-11630 (2009).

223. G. Bacher, S. Pal, L. Kanungo and S. Bhand, “A label-free silver wire based impedimetric immunosensor for detection of aflatoxin M1 in milk”, *Sens. Actuators B: Chem.* 168, 223-30 (2012).

224. R. Pradhan, A. Mitra and S. Das, “Impedimetric characterization of human blood using three-electrode based ECIS devices”, *J. Electr. Bioimp.* 4, 73-77 (2013).

225. S. M. Usman Ali, O. Nur, and M. Willander, “A fast and sensitive potentiometric glucose microsensor based on glucose oxidase coated ZnO nanowires grown on a thin silver wire”, *Sens. Actuators B: Chem.* 145, 869-74 (2010).

226. D. E. Pesántez, J. Castracane, and A. P. Gadre, “Continuous glucose microsensor with a nanoscale conducting matrix and redox mediator”, *Electrochimica Acta* 65, 196-203 (2012).